arXiv:2603.21152v1 [physics.geo-ph] 22 Mar 2026

TRACE: A Multi-Agent System for Autonomous Physical Reasoning in Seismological Science

Feng Liu[1,2], Jian Xu[3], Xin Cui[4], Xinghao Wang[2,5], Zijie Guo[2], Jiong Wang[2], S. Mostafa Mousavi[5], Xinyu Gu[2], Hao Chen[2], Ben Fei[2], Lihua Fang[6], Fenghua Ling[2*], Zefeng Li[4*], Lei Bai[2*]

[1]School of Electronic Information and Electrical Engineering, Shanghai Jiao Tong University, Shanghai, China.

[2]Shanghai Artificial Intelligence Laboratory, Shanghai, China.

[3]Department of Geography,McGill University, Montreal, Canada.

[4]School of Earth and Space Sciences, University of Science and Technology of China, Hefei, China.

[5]Earth and planetary sciences, Harvard university, Cambridge, United States of America.

[6]Institute of Earthquake Forecasting, China Earthquake Administration, Beijing, China.

*Corresponding author(s). E-mail(s): lingfenghua@pjlab.org.cn; zefengli@ustc.edu.cn; bailei@pjlab.org.cn;

Abstract

Inferring the physical mechanisms that govern earthquake sequences from indirect geophysical observations remains difficult, particularly across tectonically distinct environments where similar seismic patterns can reflect different underlying processes. Current interpretations rely heavily on the expert synthesis of catalogs, spatiotemporal statistics, and candidate physical models, limiting reproducibility and the systematic transfer of insight across settings. Here we present TRACE (Trans-perspective Reasoning and Automated Comprehensive Evaluator), a multi-agent system that combines large language model planning with formal seismological constraints to derive auditable, physically grounded mechanistic inference from raw observations. Applied to the 2019 Ridgecrest sequence, TRACE autonomously identifies stress-perturbation-induced delayed triggering, resolving the cascading interaction between the Mw 6.4 and Mw 7.1 mainshocks; in the Santorini-Kolumbo case, the system identifies a structurally guided intrusion model, distinguishing fault-channeled episodic migration from the continuous propagation expected in homogeneous crustal failure. By providing a generalizable logical infrastructure for interpreting heterogeneous seismic phenomena, TRACE advances the field from expert-dependent analysis toward knowledge-guided autonomous discovery in Earth sciences.

1 Introduction

Seismology seeks to infer the complex, unobservable dynamics of the Earth's interior from sparse and indirect surface recordings [1]. In recent years, advances in earthquake detection and catalog construction have dramatically increased the volume and resolution of observed seismicity [2, 3]. Yet translating these growing observations into mechanistic understanding of earthquake sequence evolution remains a persistent challenge [4, 5]. Across tectonically diverse settings, researchers continue to rely heavily on expert interpretation to connect statistical patterns with candidate physical processes, including stress transfer and fluid migration [6–9]. This case-by-case approach limits reproducibility and hinders the accumulation of transferable mechanistic insight across heterogeneous environments.

Bridging raw waveform recordings and mechanistic interpretation is currently constrained by two structural challenges. First, constructing high-quality earthquake catalogs with a low magnitude of completeness and high location precision requires a sequence of tightly coupled processing steps spanning detection, phase picking, association and location, where sensitivities or biases introduced at any step can propagate throughout the workflow, ultimately influencing subsequent physical interpretations [10, 11]. Second, translating discrete aspects of seismic features (e.g., spatiotemporal evolution) and statistical patterns (e.g., event clustering) into coherent physical explanations relies heavily on tacit tectonic knowledge and subjective judgment [12, 13]. Although deep-learning models now exceed human performance in specific perception tasks, such as seismic phase picking [10, 14], these advances improve only individual steps of the seismic analysis workflow. Inferring earthquake processes, however, requires coordinated reasoning across multiple processing and interpretation stages. Consequently, artificial intelligence has not yet achieved systematic mechanistic inference, owing to limited long-horizon reasoning capabilities and the absence of rigorous domain-specific physical constraints [15, 16].

To address this gap, we developed TRACE (Trans-perspective Reasoning and Automated Comprehensive Evaluator), a framework for converting seismic observations into auditable, physically grounded mechanistic interpretations. TRACE combines large language model reasoning with formal seismological constraints to orchestrate the entire analysis pipeline [15, 17, 18]. By automatically generating, testing, and refining candidate explanations, it lowers the barrier for expert-independent interpretation, ensures reproducible results, and adapts workflow steps and parameters to diverse seismic contexts. To demonstrate its capability, we applied TRACE to two seismological settings chosen for their scientific significance, data availability, and contrasting seismic regimes: an intraplate faulting zone (Eastern California Shear Zone) and an active volcanic zone (Santorini–Kolumbo volcanic system, Aegean Sea). In the 2019 Ridgecrest sequence [5, 19], TRACE systematically identifies stress-triggering as the dominant mechanism controlling aftershock evolution, reproducing previous expert analyses while supplementing them with more complete catalog-based evidence. In the Santorini–Kolumbo volcanic crisis [20], TRACE autonomously resolves the staged evolution of magma and high-pressure fluid intrusion, and reveals the interactions between volcanic activity and pre-existing structural weaknesses. Together, these results show that TRACE transforms fragmented statistical evidence into coherent physical interpretation, providing a unified logical framework for mechanistic understanding across heterogeneous Earth science datasets and advancing a shift toward knowledge-guided autonomous scientific discovery.

2 Results

2.1 TRACE: An autonomous framework for end-to-end seismological discovery

TRACE provides an autonomous framework for mechanistic inference in seismology that systematically integrates the full seismological research workflow, from hypothesis generation and multidimensional evidence evaluation to dynamical interpretation (Fig. 1a). In contrast to conventional processing and interpretation governed by rigid procedural rules [4, 10, 11], TRACE formalizes and expands expert reasoning within a unified framework. By coupling a reasoning engine grounded in structured knowledge representations with domain-specific seismological priors and an extensive library of over 2,200 specialized analytical modules, the framework establishes a physically constrained system that structures scientific inquiry into three sequential stages.

During the Hypothesis Planning stage, TRACE translates open-ended inquiries into geophysically constrained analytical strategies using semantically encoded scientific principles. Candidate hypotheses are subjected to immediate theoretical consistency checks to ensure physical plausibility. In the subsequent Empirical Execution and Diagnostics stage, these strategies are instantiated as coupled computational workflows. A closed-loop diagnostic mechanism monitors intermediate results, detects computational anomalies or physical divergences, and adaptively refines the workflow through logical backtracking. In the final Interpretive Synthesis stage, TRACE integrates multidimensional analysis results into causally constrained mechanistic interpretations. By continuously incorporating validated analytical pathways, the framework enables cross-task transfer of reasoning strategies and maintains robust performance even in previously unseen tectonic contexts.

To assess scientific validity, we developed a multi-level benchmarking protocol spanning elementary tasks to complex analytical chains. Across end-to-end pipelines—including continuous waveform analysis, phase association, hypocenter relocation, and statistical modeling—TRACE exhibits greater stability and internal consistency than both manual interpretation and rule-based automated workflows. These results confirm that TRACE enables robust, autonomous scientific reasoning across heterogeneous tectonic environments. Detailed implementation and evaluation procedures are described in the Methods section.

2.2 Delayed cascading triggering in the Ridgecrest Mw 6.4-7.1 sequence

The 2019 Ridgecrest earthquake sequence comprises an Mw 6.4 event followed approximately 34 hours later by the Mw 7.1 mainshock [5]. Both events produced ruptures along geometrically and kinematically compatible fault systems, offering a natural experiment for investigating the interactions between large earthquakes within a multi-fault network. Although prior studies have analyzed this sequence using seismic catalogs, stress modeling, and geodetic data, it remains uncertain whether a testable causal triggering chain can be reconstructed exclusively from a self-consistent seismic catalog, without invoking external constraints. To address this question, we constructed a high-resolution earthquake catalog directly from continuous waveform data and used it to jointly constrain the spatiotemporal organization, statistical evolution, and fault-scale coupling of seismicity during the inter-mainshock period.

High-resolution earthquake catalog construction

Identifying triggering mechanisms requires both high hypocentral precision and catalog completeness. For the Ridgecrest sequence, TRACE automatically implemented an end-to-end processing framework to generate a high-resolution earthquake catalog from continuous waveforms. Given the predefined study region and time window, the system retrieved multi-component data from the Southern California Earthquake Data Center and applied a standardized preprocessing pipeline, including quality control, detrending, instrument response correction, and resampling. Informed by regional context and analytical objectives, TRACE selected PhaseNet for phase picking through a retrieval-augmented strategy, identifying more than 1.59 million P- and 1.66 million S-wave arrivals [14]. Multi-station phase picks were associated into candidate events using clustering-based algorithms, followed by initial hypocenter determination and double-difference relocation with HypoDD [21, 22]. This workflow yielded over 90,000 precisely relocated earthquakes (Fig. 2).

Catalog construction did not rely on a single algorithm or manual parameter tuning. Instead, preprocessing, phase identification, event association, and high-precision relocation were integrated into a unified and traceable framework. All processing steps, parameter settings, and intermediate outputs were systematically recorded, ensuring reproducibility and facilitating transfer to other regions or time intervals. The resulting catalog provides a robust empirical basis for analyzing the Ridgecrest triggering process and establishes a scalable paradigm for unified investigation of complex seismic sequences. More details of each processing step can be found in Section A of the Supplementary Information.

Spatiotemporal organization of inter-mainshock seismicity

Using the relocated catalog, we examined the spatiotemporal evolution of seismicity between the Mw 6.4 and Mw 7.1 events to elucidate their triggering relationship (Fig. 3). Multidimensional spatial statistical analyses consistently indicate that the Mw 6.4 earthquake did not induce near-synchronous regional activation. Instead, it generated a multi-branch aftershock system strongly constrained by fault geometry. Temporal epicentral slices, kernel density estimation, and along-strike projections show that nearly all events were concentrated along mapped fault structures. Seismicity preferentially evolved along pre-existing strike-slip faults rather than diffusing isotropically into the surrounding crust. Directional Ripley's function analysis confirms pronounced structural anisotropy, demonstrating that spatial organization was controlled by fault orientation. Grid-based activation timing and fault-segment–scale analyses further reveal that this structure developed asynchronously. The SW–NE–trending rupture zone associated with the Mw 6.4 event was activated rapidly and almost synchronously. In contrast, the NW–SE–trending fault system connecting the Mw 6.4 and Mw 7.1 epicenters exhibited progressive expansion during the approximately 34-hour inter-mainshock interval. Activation within this segment was sequential, with diffuse onset times and no clearly defined migration front, indicating structurally controlled and asymmetric seismic evolution preceding the Mw 7.1 mainshock.

Superimposed on this organized corridor, statistical behavior departs from classical aftershock decay. Seismicity rate analysis and Omori–Utsu parameter inversion reveal distinct dynamics across fault segments. The SW–NE-trending rupture zone displays a high Omori exponent and rapid decay characteristic of typical aftershock sequences. By contrast, the NW–SE-trending rupture zone that later hosted the Mw 7.1 mainshock exhibits delayed acceleration beginning approximately 18 hours after the Mw 6.4 event, with a reduced Omori exponent of about 0.5 and sustained positive seismicity-rate residuals. This acceleration coincides temporally with an intervening Mw 5.4 earthquake. Prior to the Mw 7.1 rupture, a narrow low–b-value corridor progressively emerged along the future rupture zone. This feature is geometrically confined by the fault system and spatially coincident with the delayed acceleration region. Although persistent temporal low–b-value anomalies are not observed, the localized spatial anomaly indicates that the NW–SE segment was already in a relatively high-stress and mechanically unstable state before failure. Together, these observations suggest that the Mw 6.4 earthquake did not instantaneously trigger the Mw 7.1 rupture through dynamic perturbation. Rather, it progressively organized a structurally controlled seismic corridor that established favorable mechanical conditions for subsequent large rupture. Detailed analyses for each perspective are provided in Supplementary Information Section B.

Static-stress-mediated cascading triggering

The inter-mainshock seismicity exhibits a delayed and spatially organized activation along the NW–SE fault segment linking the M_w 6.4 and M_w 7.1 epicenters. Unlike the near-instantaneous response characteristic of dynamic triggering, seismicity within this segment accelerated only after $\sim$18 hours. This delay was accompanied by the emergence of a localized low–b-value corridor along the eventual M_w 7.1 rupture zone, indicating that the structure was progressively driven toward a mechanically critical

state. Such asynchronous evolution is consistent with positive static Coulomb stress transfer from the M_w 6.4 rupture onto geometrically compatible fault planes. This process, governed by rate-and-state frictional nucleation and potentially modulated by aseismic slip, enabled localized rupture patches to approach failure gradually rather than instantaneously. By integrating spatial focusing, temporal delays, and statistical deviations from standard aftershock decay, we interpret the Ridgecrest sequence represents as a near-field cascading process. In this framework, static stress loading acts as the primary driver, mediating a structurally constrained nucleation phase that dictated the ∼1.4-day interval between the two mainshocks.

2.3 Dynamic decoupling of structural control and seismic failure during volcanic crisis

Seismic migration during volcanic crisis is widely interpreted as the surface expression of propagating magma or high-pressure fluid fronts and is therefore used to infer intrusion direction and propagation rate. In tectonically segmented back-arc systems, however, pre-existing structural weaknesses may strongly influence the spatial organization of seismicity. Under such conditions, it remains unclear whether observed migration patterns primarily reflect the dynamics of magma intrusion or the reactivation of inherited fault structures. Although different intrusion scenarios are expected to produce distinct signatures in epicenter-cloud geometry, migration stability, depth evolution, and seismic statistics, the reliability and limitations of these diagnostic indicators have rarely been systematically evaluated during a single volcanic crisis. The 2025 Santorini–Kolumbo unrest provides an unusually well-resolved seismic dataset that enables quantitative assessment of both the interpretative value and the physical limitations of seismic migration as a proxy for intrusion dynamics.

High-resolution seismic characterization of intrusion geometry

During the Santorini–Kolumbo volcanic crisis, TRACE automatically constructed a high-resolution earthquake catalog spanning approximately 50 days of activity using continuous waveform data from 15 seismic stations (Fig. 4a). Based on this catalog, the system quantified the morphology of the earthquake cloud, the temporal evolution of principal-axis orientation, centroid migration patterns, and magnitude–frequency statistics to evaluate whether the observed seismicity is consistent with the classical model of a laterally propagating intrusion opening new pathways within relatively homogeneous crust (Fig. 4b-f).

Throughout the crisis, seismicity remained confined to a narrow and nearly linear three-dimensional volume rather than forming diffuse or radially expanding clusters. The earthquake cloud maintained a stable NE–SW orientation with minimal variation in principal-axis direction and spatially coincided with the regional Astypalaea–Anafi fault system. Most events were concentrated along mapped fault structures, indicating strong structural control on the spatial distribution of seismicity. Within this tectonic corridor, earthquake centroids exhibited multi-stage, coherent along-strike migration accompanied by systematic deep-to-shallow adjustments. However, the migration occurred through episodic pulses rather than a continuous, steadily advancing front. In particular, the seismicity pattern does not reveal the narrow, laterally continuous front that would be expected if earthquakes were systematically triggered at the tip of a propagating magma intrusion. Independent constraints from seismic statistics

further support this interpretation. The temporal evolution and spatial distribution of the b-value display stage-dependent variations, indicating a dynamic reorganization of stress within the fault corridor. In addition, larger magnitude earthquakes do not systematically occur near the inferred migration front and exhibit only weak forward offsets relative to the overall seismicity distribution. These observations are inconsistent with models in which a migrating intrusion tip directly nucleates the largest events, thereby arguing against interpretations that equate swarm migration with progressive rupture at an advancing intrusion front.

Structure-guided episodic intrusion and its separation from single-event failure

Taken together, the geometric, kinematic, and statistical observations suggest that the Santorini–Kolumbo unrest is best explained by episodic intrusion guided by pre-existing tectonic structures. The NE–SW fault network acts as a stable structural corridor that governs the orientation, morphology, and migration pathway of the earthquake cloud. Rather than propagating freely through relatively homogeneous crust, the intrusion evolves through repeated pressure redistribution and fault reactivation within this inherited structural framework. Within this structure-controlled system, however, the occurrence of larger individual earthquakes is not directly determined by the instantaneous position or propagation rate of the migrating seismicity. Instead, these events are primarily controlled by local mechanical conditions, including fault strength, stress accumulation, and failure thresholds. The observations therefore reveal a fundamental mechanistic decoupling: structural architecture constrains the spatial corridor and collective migration of seismic unrest, whereas individual earthquake failure is governed by localized mechanical processes. Recognizing this decoupling between structure-guided migration and single-event rupture dynamics is critical for interpreting seismic swarms during volcanic crises and for assessing associated seismic hazards in tectonically complex volcanic arcs.

3 Discussion

TRACE provides a foundational architecture that reconciles the intrinsic heterogeneity of seismic observations across disparate tectonic environments. Historically, seismological inquiry has been constrained by expert-driven synthesis, which often results in idiosyncratic inference pathways that lack portability across regions or scientific domains. In contrast, TRACE formalizes cross-perspective reasoning by integrating statistical feature extraction and physical constraints within a unified, autonomous logical framework. This approach enables a systematic deconstruction of seismic phenomena guided by consistent causal principles. By reconciling two fundamentally distinct settings, specifically the intraplate faulting of the Eastern California Shear Zone and the active Santorini–Kolumbo volcanic system in the Aegean Sea, TRACE uncovers two potential physical mechanisms. Such a unified representation marks a paradigm shift from reliance on individualized expertise toward a scalable and verifiable foundation for comparative Earth system analysis.

This transition toward a unified representation necessitates a fundamental restructuring of seismological investigations, which have long been characterized by multi-stage workflows heavily reliant on tacit expertise. Such "expert intuition" and subjective procedural choices frequently propagate into divergent physical

interpretations. We argue that this expertise is fundamentally rooted in the implicit recognition of recurrence regimes and the ability to discern deviations from established geophysical expectations. By formalizing these cognitive reasoning chains, TRACE translates subjective intuition into transparent and reproducible computational logic through structured research planning and closed-loop diagnostic oversight. The system autonomously orchestrates specialized analytical tools to synthesize fragmented evidence into coherent, multi-dimensional scientific conclusions. Beyond the integration of discrete evidence, the framework enables a high-level comparative analysis between its findings and the existing corpus of scientific knowledge. This analytical depth allows for the systematic identification of commonalities that reinforce established theories as well as critical discrepancies that challenge current understandings. By explicitly highlighting these cognitive misalignments, TRACE serves as a catalyst for deeper investigation into the origins of such deviations, effectively pushing the scientific frontier. Consequently, this democratization of complex seismic analysis mitigates individual confirmation bias and facilitates a transition from fragmented, case-specific studies toward integrated, systematic scientific reasoning. As evidenced by our global earthquake catalog analysis (Supplementary Information Section C), the explicit formalization of inference protocols ensures that these dynamic characteristics remain statistically coherent across broader tectonic regimes, effectively decoupling scientific progress from individual intuition to anchor it within a verifiable, scalable logical architecture.

The efficacy of this systematic reasoning emerges from the synergistic integration of the reasoning engine, formalized semantic protocols, and an extensible analytical tool-chain. Rather than serving as mere instructions, these protocols function as computational scientific standards that enforce physical constraints and logical invariance throughout protracted reasoning trajectories. Our evaluation reveals that the performance of TRACE is governed by a dual-ceiling effect: while the precision of seismological tools defines the operational baseline, the ultimate scientific rigor is dictated by the semantic alignment and cross-domain reasoning depth of the underlying large language model (Fig. 5b, c). In addition, TRACE incorporates self-diagnostic and validation modules that emulate expert evaluation under uncertainty and low signal-to-noise conditions, maintaining inference stability through iterative logical feedback. Elucidating the sources and boundaries of this robustness is essential for assessing the reliability and applicability of AI-assisted scientific reasoning frameworks within the geophysical sciences.

Despite these advancements, the efficacy of TRACE remains intrinsically bounded by the fidelity of underlying physical models and the computational cost of high-fidelity simulations. Furthermore, its performance under extreme or data-sparse seismic events requires further validation through the integration of real-time observational streams and adaptive learning algorithms. Nevertheless, the synergy between high-level semantic reasoning and rigorous physical tool-chains provides a blueprint that transcends the traditional boundaries of seismology. The capacity of the system to evaluate new data against the established corpus of scientific knowledge allows it to autonomously identify observations inconsistent with existing paradigms, thereby highlighting high-value targets for further investigation. This modular architecture is readily adaptable to other Earth system domains, such as planetary geophysics or oceanographic monitoring, where data heterogeneity and procedural complexity pose similar barriers to discovery. Ultimately, the progression from automated tools to

autonomous scientific agents heralds a shift toward human-AI collaborative inquiry, which will be instrumental in addressing the most pressing challenges of our dynamic planet.

References

[1] Aki, K., Richards, P.G.: Quantitative Seismology, 2nd Ed., 2. ed edn. Univ Science Books, Sausalito, Calif (2002)

[2] Beroza, G.C., Segou, M., Mostafa Mousavi, S.: Machine learning and earthquake forecasting—next steps. Nature Communications **12**(1), 4761 (2021) https://doi.org/10.1038/s41467-021-24952-6

[3] Mousavi, S.M., Beroza, G.C.: Deep-learning seismology. Science **377**(6607), 4470 (2022) https://doi.org/10.1126/science.abm4470

[4] Peng, Z., Zhao, P.: Migration of early aftershocks following the 2004 Parkfield earthquake. Nature Geoscience **2**(12), 877–881 (2009) https://doi.org/10.1038/ngeo697

[5] Ross, Z.E., Idini, B., Jia, Z., Stephenson, O.L., Zhong, M., Wang, X., Zhan, Z., Simons, M., Fielding, E.J., Yun, S.-H., Hauksson, E., Moore, A.W., Liu, Z., Jung, J.: Hierarchical interlocked orthogonal faulting in the 2019 Ridgecrest earthquake sequence. Science **366**(6463), 346–351 (2019) https://doi.org/10.1126/science.aaz0109

[6] Gutenberg, B., Richter, C.F.: Magnitude and Energy of Earthquakes. Nature **176**(4486), 795–795 (1955) https://doi.org/10.1038/176795a0

[7] Ogata, Y.: Statistical Models for Earthquake Occurrences and Residual Analysis for Point Processes. Journal of the American Statistical Association **83**(401), 9–27 (1988) https://doi.org/10.1080/01621459.1988.10478560

[8] Stein, R.S.: The role of stress transfer in earthquake occurrence. Nature **402**(6762), 605–609 (1999) https://doi.org/10.1038/45144

[9] Shapiro, S.A., Huenges, E., Borm, G.: Estimating the crust permeability from fluid-injection-induced seismic emission at the KTB site. Geophysical Journal International **131**(2), 15–18 (1997) https://doi.org/10.1111/j.1365-246X.1997.tb01215.x

[10] Mousavi, S.M., Ellsworth, W.L., Zhu, W., Chuang, L.Y., Beroza, G.C.: Earthquake transformer—an attentive deep-learning model for simultaneous earthquake detection and phase picking. Nature Communications **11**(1), 3952 (2020) https://doi.org/10.1038/s41467-020-17591-w

[11] Zhang, M., Liu, M., Feng, T., Wang, R., Zhu, W.: LOC-FLOW: An End-to-End Machine Learning-Based High-Precision Earthquake Location Workflow. Seismological Research Letters **93**(5), 2426–2438 (2022) https://doi.org/10.1785/0220220019

[12] Frodeman, R.: Geological reasoning: Geology as an interpretive and historical science. Geological Society of America Bulletin **107**(8), 960–0968 (1995) https://doi.org/10.1130/0016-7606(1995)107⟨0960:GRGAAI⟩2.3.CO;2

[13] Bond, C.E., Gibbs, A.D., Shipton, Z.K., Jones, S.: What do you think this is?

"Conceptual uncertainty" in geoscience interpretation. GSA Today **17**(11), 4 (2007) https://doi.org/10.1130/GSAT01711A.1

[14] Zhu, W., Beroza, G.C.: PhaseNet: A Deep-Neural-Network-Based Seismic Arrival Time Picking Method. Geophysical Journal International (2018) https://doi.org/10.1093/gji/ggy423

[15] Wei, J., Wang, X., Schuurmans, D., Bosma, M., Ichter, B., Xia, F., Chi, E., Le, Q., Zhou, D.: Chain-of-Thought Prompting Elicits Reasoning in Large Language Models. arXiv (2022). https://doi.org/10.48550/ARXIV.2201.11903

[16] Bubeck, S., Chandrasekaran, V., Eldan, R., Gehrke, J., Horvitz, E., Kamar, E., Lee, P., Lee, Y.T., Li, Y., Lundberg, S., Nori, H., Palangi, H., Ribeiro, M.T., Zhang, Y.: Sparks of Artificial General Intelligence: Early Experiments with GPT-4. arXiv (2023). https://doi.org/10.48550/ARXIV.2303.12712

[17] Jumper, J., Evans, R., Pritzel, A., Green, T., Figurnov, M., Ronneberger, O., Tunyasuvunakool, K., Bates, R., Žídek, A., Potapenko, A., Bridgland, A., Meyer, C., Kohl, S.A.A., Ballard, A.J., Cowie, A., Romera-Paredes, B., Nikolov, S., Jain, R., Adler, J., Back, T., Petersen, S., Reiman, D., Clancy, E., Zielinski, M., Steinegger, M., Pacholska, M., Berghammer, T., Bodenstein, S., Silver, D., Vinyals, O., Senior, A.W., Kavukcuoglu, K., Kohli, P., Hassabis, D.: Highly accurate protein structure prediction with AlphaFold. Nature **596**(7873), 583–589 (2021) https://doi.org/10.1038/s41586-021-03819-2

[18] Guo, Z., Wang, J., Yue, X., Wei, W., Jiang, Z., Xu, W., Fei, B., Zhang, W., Gu, X., Cheng, L., Luo, J.-J., Li, C., Wang, Y., Chen, T., Ouyang, W., Ling, F., Bai, L.: EarthLink: A Self-Evolving AI Agent for Climate Science. arXiv (2025). https://doi.org/10.48550/arXiv.2507.17311

[19] Sheng, S., Meng, L.: Stress Field Variation During the 2019 Ridgecrest Earthquake Sequence. Geophysical Research Letters **47**(15), 2020–087722 (2020) https://doi.org/10.1029/2020GL087722

[20] Isken, M.P., Karstens, J., Nomikou, P., Parks, M.M., Drouin, V., Rivalta, E., Crutchley, G.J., Haghighi, M.H., Hooft, E.E.E., Cesca, S., Walter, T.R., Hainzl, S., Saul, J., Anastasiou, D., Raptakis, K., Shapiro, N.M., Münchmeyer, J., Higueret, Q., Soubestre, J., Brenguier, F., Hufstetler, R.S., Autumn, K.R., Tsakiri, M., Lange, D., Kopp, H., Urlaub, M., Blanch Jover, M., Preine, J., Hübscher, C., Motagh, M., Müller, D., Dahm, T., Berndt, C.: Volcanic crisis reveals coupled magma system at Santorini and Kolumbo. Nature **645**(8082), 939–945 (2025) https://doi.org/10.1038/s41586-025-09525-7

[21] Waldhauser, F.: A Double-Difference Earthquake Location Algorithm: Method and Application to the Northern Hayward Fault, California. Bulletin of the Seismological Society of America **90**(6), 1353–1368 (2000) https://doi.org/10.1785/0120000006

[22] Zhu, W., McBrearty, I.W., Mousavi, S.M., Ellsworth, W.L., Beroza, G.C.: Earthquake Phase Association Using a Bayesian Gaussian Mixture Model. Journal of Geophysical Research: Solid Earth **127**(5), 2021–023249 (2022) https://doi.org/10.1029/2021JB023249 arXiv:2109.09008 [physics]

[23] Beyreuther, M., Barsch, R., Krischer, L., Megies, T., Behr, Y., Wassermann, J.:

ObsPy: A Python Toolbox for Seismology. Seismological Research Letters **81**(3), 530–533 (2010) https://doi.org/10.1785/gssrl.81.3.530

[24] Woollam, J., Münchmeyer, J., Tilmann, F., Rietbrock, A., Lange, D., Bornstein, T., Diehl, T., Giunchi, C., Haslinger, F., Jozinović, D., Michelini, A., Saul, J., Soto, H.: SeisBench—A Toolbox for Machine Learning in Seismology. Seismological Research Letters **93**(3), 1695–1709 (2022) https://doi.org/10.1785/0220210324 arXiv:2111.00786 [physics]

[25] Hu, M., Li, Z.: DASPy: A Python Toolbox for DAS Seismology. Seismological Research Letters **95**(5), 3055–3066 (2024) https://doi.org/10.1785/0220240124

[26] Chamberlain, C.J., Hopp, C.J., Boese, C.M., Warren-Smith, E., Chambers, D., Chu, S.X., Michailos, K., Townend, J.: EQcorrscan: Repeating and Near-Repeating Earthquake Detection and Analysis in Python. Seismological Research Letters **89**(1), 173–181 (2018) https://doi.org/10.1785/0220170151

[27] Mirwald, A., Schmid, N., Mizrahi, L., Han, M., Rohnacher, A., Ritz, V.A., Wiemer, S.: SeismoStats: A Python Package for Statistical Seismology. arXiv (2025). https://doi.org/10.48550/arXiv.2511.04521

[28] SCEDC: Southern California Earthquake Center. Caltech (2013). https://doi.org/10.7909/C3WD3XH1

[29] National Observatory Of Athens, Institute Of Geodynamics, Athens: International Federation of Digital Seismograph Networks. International Federation of Digital Seismograph Networks (1975). https://doi.org/10.7914/SN/HL

[30] Aristotle University Of Thessaloniki: International Federation of Digital Seismograph Networks. International Federation of Digital Seismograph Networks (1981). https://doi.org/10.7914/SN/HT

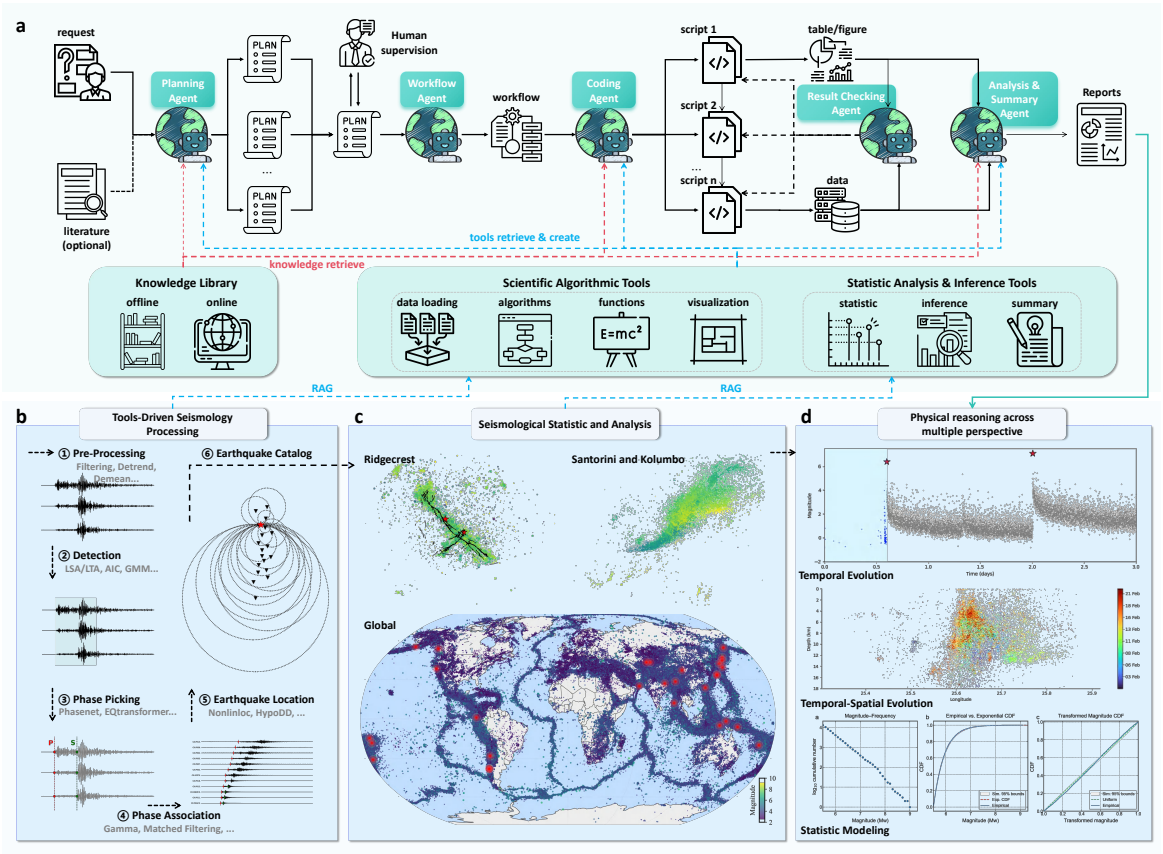


Fig. 1 The TRACE multi-agent framework for autonomous seismic discovery and end-to-end scientific reasoning. a, Schematic architecture of the TRACE autonomous reasoning system. The workflow translates an open-ended scientific request, augmented by a domain-specific knowledge library, into physically constrained analytical strategies. A specialized Planning Agent decomposes the request into structured protocols, which are overseen by human supervision to ensure scientific alignment. The Workflow Agent then instantiates these plans into executable task sequences. Subsequently, a Coding Agent generates modular scripts by linking a suite of seismological algorithms and statistical inference libraries. A Result Checking Agent performs real-time diagnostics to verify physical consistency, while the Analysis & Summary Agent synthesizes multidimensional evidence into mechanistic scientific reports. **b**, Tool-driven long-chain seismology processing. This module demonstrates the automated execution of a complete seismic pipeline, comprising waveform pre-processing, event detection, phase picking, association, high-precision hypocenter relocation, and the construction of a final earthquake catalog. **c**, Multi-scale statistical analysis and cross-regional application. The framework exhibits scalability across diverse tectonic settings, illustrated here by high-resolution seismicity catalogs for the Ridgecrest shear zone, the Santorini-Kolumbo volcanic system, and global-scale seismic monitoring. **d**, Mechanistic reasoning across multiple perspectives. TRACE integrates statistical modeling with spatiotemporal evolution analysis to perform causal inference. By evaluating magnitude-frequency distributions and transformed magnitude cumulative distributions, the system bridges raw observational data with physically constrained interpretations of tectonic processes.

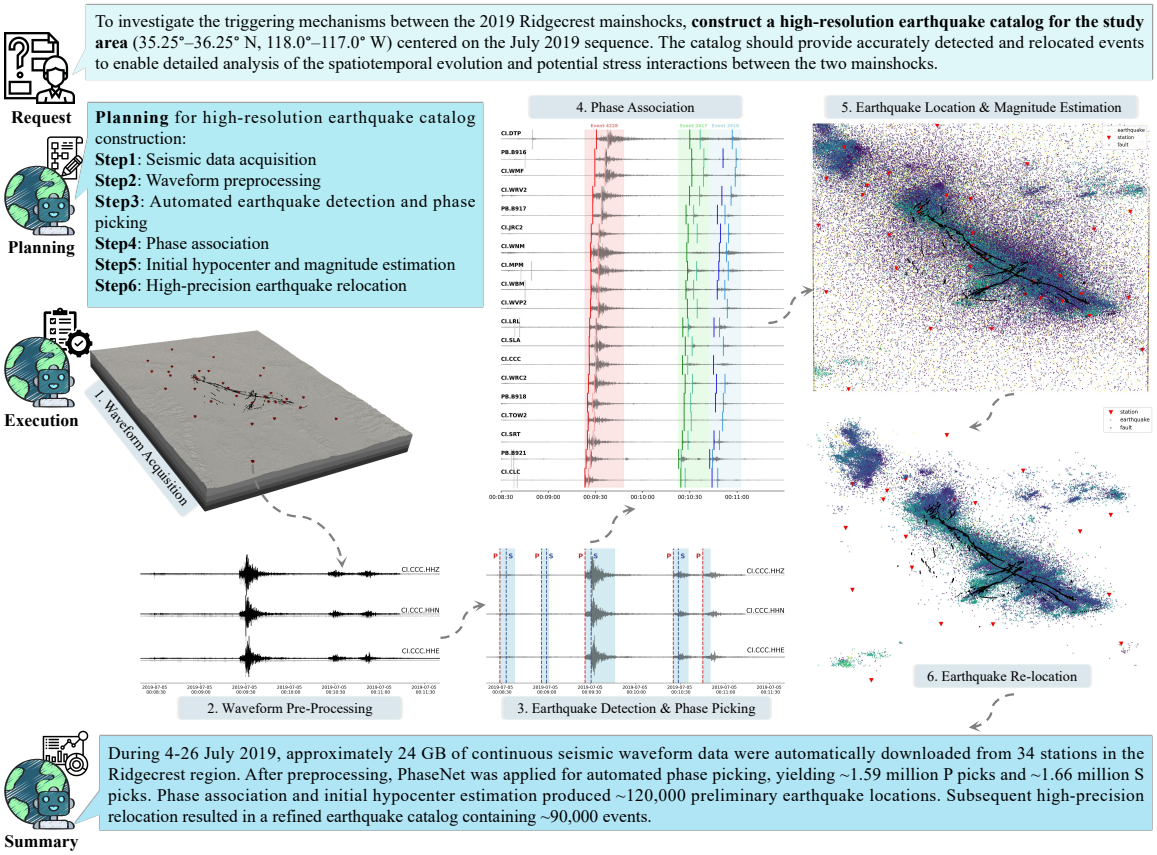


Fig. 2 High-resolution earthquake catalog construction using the multi-agent system TRACE. TRACE generates a high-resolution earthquake catalog for the 2019 Ridgecrest seismic sequence within the study area (35.25°–36.25° N, 118.0°–117.0° W). The workflow integrates six sequential processing stages, comprising (1) continuous waveform acquisition from regional networks such as CI, GS, and PB; (2) waveform preprocessing; (3) deep-learning-based earthquake detection combined with P and S phase picking; (4) phase association; (5) initial hypocenter location and magnitude estimation; and (6) high-precision relocation to resolve fine-scale seismogenic structures. The resulting catalog provides the basis for analyzing the spatiotemporal evolution and stress interactions between the M_{w} 6.4 and M_{w} 7.1 mainshocks.

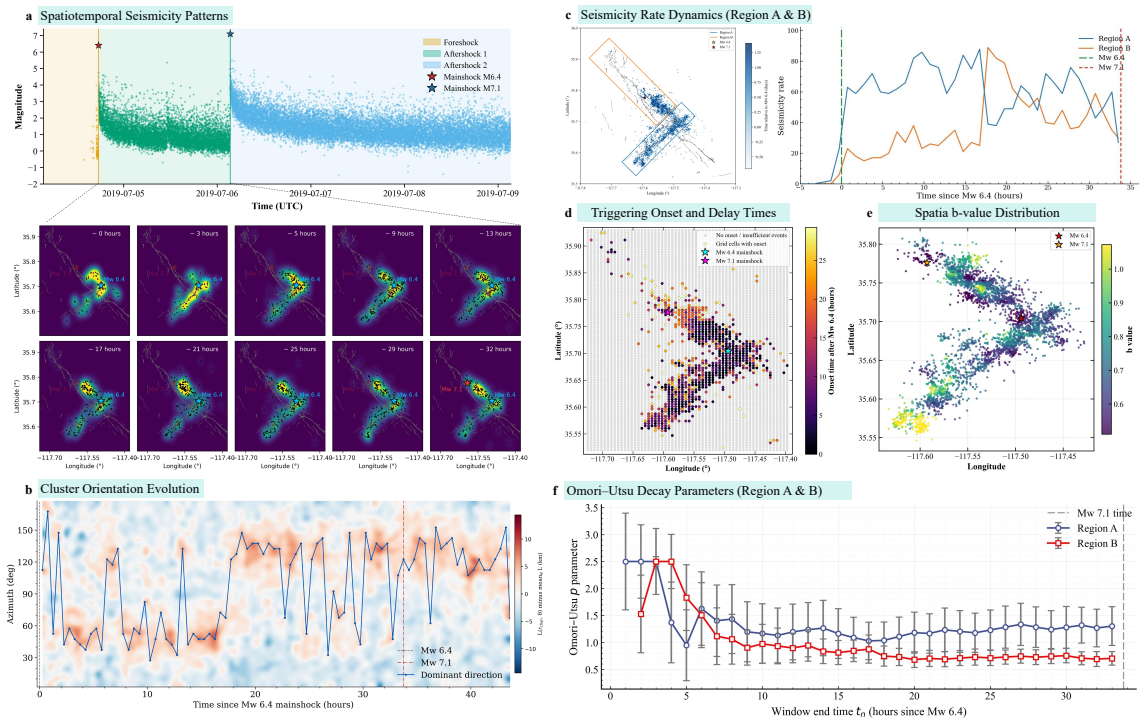


Fig. 3 Spatiotemporal organization of seismicity between the Ridgecrest mainshocks. High-resolution analysis of the TRACE-derived earthquake catalog reveals the progressive and structurally controlled evolution of seismicity bridging the M_w 6.4 and M_w 7.1 events. **a**, Spatiotemporal evolution of seismicity between the M_w 6.4 (blue star) and M_w 7.1 (red star) mainshocks, characterized by kernel density estimation (KDE) maps. **b**, Temporal evolution of seismicity orientations, revealing directional organization and shifts in dominant alignment consistent with orthogonal fault structures. **c**, Spatial delineation of Regions A and B and their respective seismicity rate evolution, highlighting contrasting temporal behaviors across fault segments. **d**, Spatial distribution of activation onset times relative to the M_w 6.4 event, indicating rapid activation along the SW–NE rupture zone followed by delayed expansion along the NW–SE fault system linking the two mainshocks. **e**, Spatial distribution of b-values, where localized low-b anomalies emerge along the future rupture zone, suggesting relatively elevated stress levels. **f**, Omori–Utsu decay parameters (p-values) for Regions A and B, indicating rapid aftershock decay along the SW–NE rupture zone and delayed seismic acceleration along the NW–SE segment. Together, these observations indicate that the M_w 6.4 earthquake did not instantaneously trigger the M_w 7.1 rupture, but progressively organized a structurally controlled seismic corridor preceding the second mainshock.

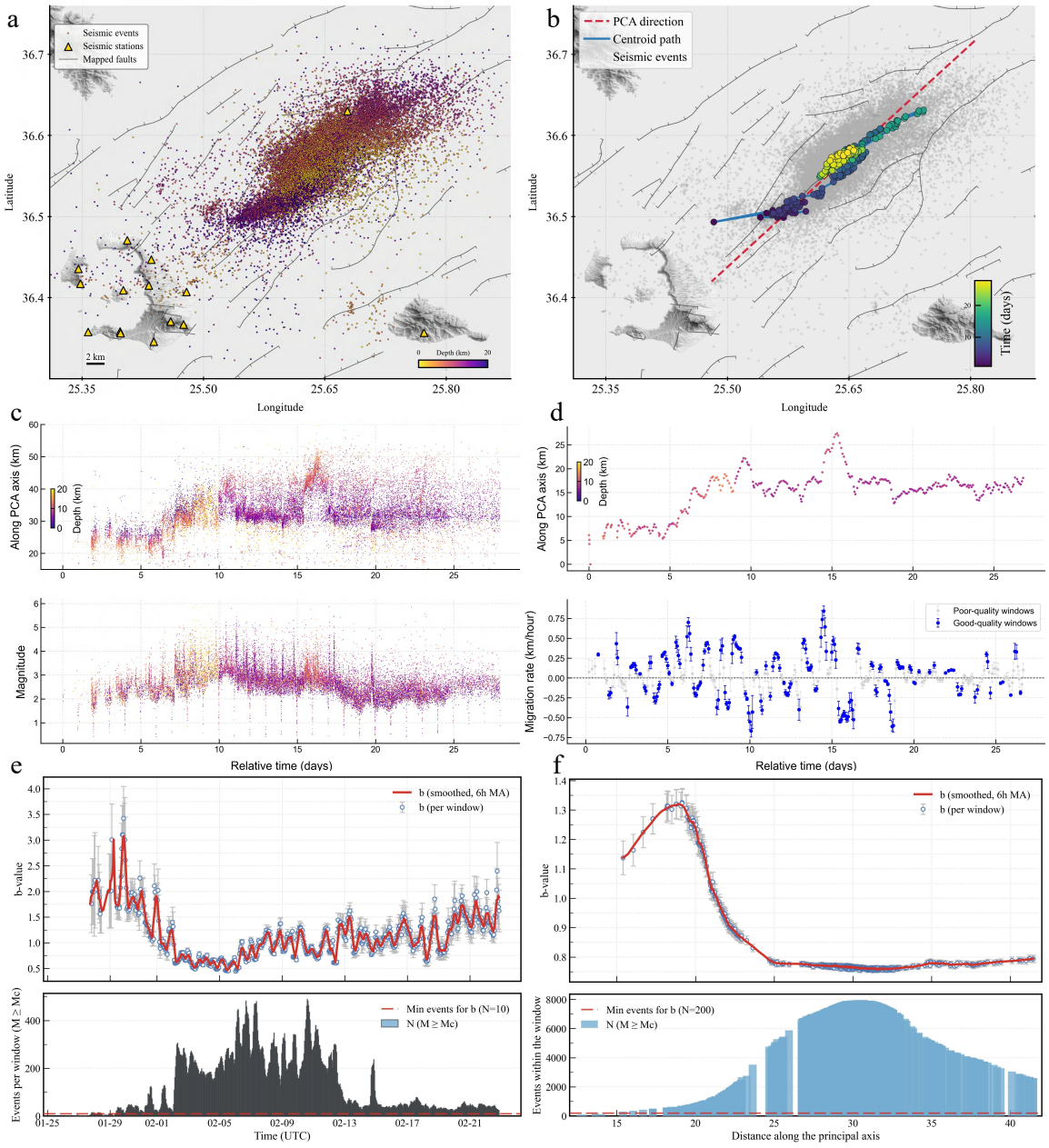


Fig. 4 Structural control and mechanistic decoupling of seismic migration during the 2025 Santorini–Kolumbo volcanic crisis. a, High-resolution earthquake catalog (colored circles, color-coded by depth) automatically constructed using TRACE from 15 seismic stations (yellow triangles). Grey lines indicate mapped regional faults, highlighting the alignment of seismicity with the NE–SW trending fault system. **b**, Geometry and centroid evolution of the earthquake cloud. The red line represents the principal axis (PCA) orientation. Colored circles show the centroid trajectory calculated in 6-hour moving windows, indicating a structure-guided migration path along the tectonic corridor. **c**, Spatiotemporal evolution of seismicity. Top: projection of earthquake hypocenters along the PCA axis as a function of time. Bottom: magnitude versus relative time. Both panels are color-coded by depth, showing episodic along-strike migration and systematic depth adjustments. **d**, Kinematic analysis of the migration. Top: centroid position along the PCA axis over time. Bottom: calculated migration rate (km h^{-1}). Migration occurs in episodic pulses rather than as a continuous steady advance. **e**, Temporal evolution of seismic statistics. Top: *b*-value calculated in 6-hour windows (red line indicates moving average). Bottom: frequency of events with $M \geq M_c$ (completeness magnitude). **f**, Spatial distribution of seismic characteristics. Top: *b*-value distribution (smoothed 6-h moving average) as a function of distance along the PCA axis. Bottom: seismic event density within a 5-km radius of the moving centroid. The spatial heterogeneity of *b*-values and the weak correspondence between the migration front and the largest events indicate a decoupling between structure-guided migration and localized mechanical failure.

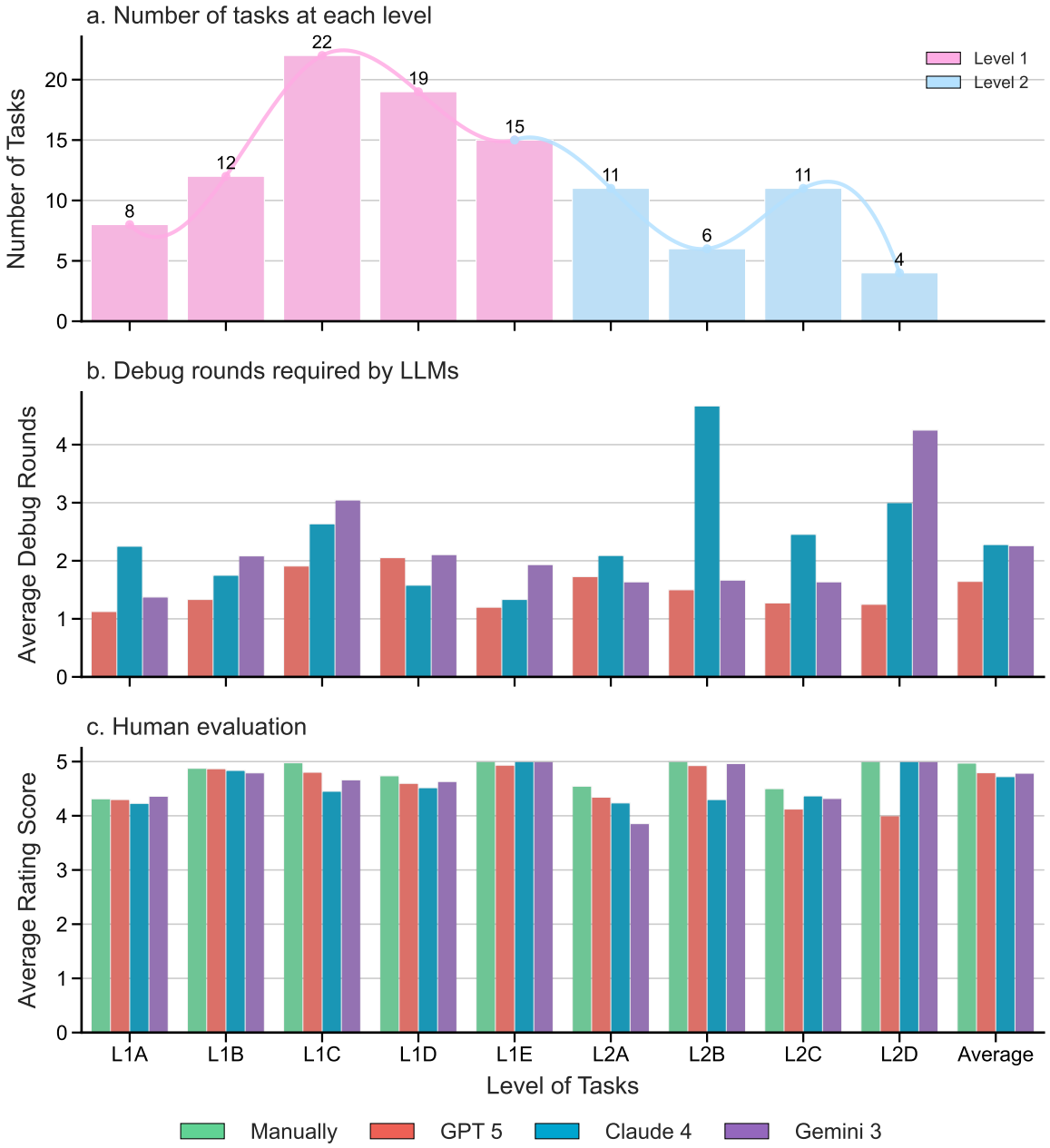


Fig. 5 Performance and distribution of the TRACE benchmark across task hierarchies. **a**, Distribution of tasks across two distinct complexity levels: atomic tasks (Level 1, green bars, $L1A$–$L1E$) and multi-step analytical tasks (Level 2, blue bars, $L2A$–$L2D$). Sub-levels correspond to representative task categories (Level 1: data retrieval, data formatting, signal processing, feature analysis, and scientific visualization; Level 2: sequential workflows, heuristic branching, batch processing, and parameter-space exploration). The vertical axis represents the absolute number of tasks categorized within each sub-level, with Level 1C ($n = 22$) constituting the largest task group. **b**, Evaluation of debugging efficiency across task levels for different large language models (LLMs). The vertical axis displays the average number of debug rounds required to achieve task completion. **c**, Average performance scores for human experts, GPT-5, Claude-4, and Gemini-3 across all task categories. Scores are normalized on a scale of 1 to 5, reflecting overall task performance across different levels of analytical complexity.

4 Methods

4.1 Implementation of TRACE

4.1.1 System overview and design principles

TRACE is an automated multi-agent reasoning framework designed for seismological analysis (Fig. 1a). It integrates general scientific reasoning capabilities with domain-specific seismological knowledge and validated computational tools to enable structured modeling, experimental execution, and interpretation of complex scientific problems. Unlike conventional research paradigms that rely on expert-driven integration of heterogeneous observations and analytical tools, TRACE formalizes scientific analysis as executable reasoning and computational workflows, allowing complex seismological problems to be systematically addressed within a unified analytical framework.

The framework is organized around the logical structure of scientific investigation and decomposes seismological analytical tasks into a hierarchical architecture composed of multiple cooperative functional modules. The *Planning and Task Decomposition Module* first performs semantic interpretation and structured representation of high-level scientific questions. By jointly considering research objectives, physical constraints, and data availability, this module generates executable experimental designs. *The Automated Execution and Validation Module* subsequently invokes or synthesizes appropriate computational and statistical analysis tools according to the generated plans. It performs observational data processing and experimental execution while validating intermediate and final outputs through consistency diagnostics and physical plausibility constraints. Finally, the *Scientific Integration and Inference Module* evaluates analytical results across multiple dimensions, including statistical distribution characteristics, spatial structural patterns, and geodynamic constraints, thereby producing physically interpretable and scientifically consistent conclusions.

At the system implementation level, TRACE maps these analytical functions onto agents or agent ensembles with clearly defined reasoning responsibilities. Standardized task interfaces and state representation mechanisms enable coordinated information exchange and inference across modules. During execution, agents dynamically access an integrated structured knowledge base and validated computational tool libraries, allowing automatic construction and adaptive refinement of scientific analysis workflows. This design ensures reproducibility, scalability, and methodological extensibility of scientific investigations.

4.1.2 Core agent-based modules

Planning and Task Decomposition Module

The *Planning and Task Decomposition Module* converts scientific queries, typically expressed in natural language, into structured and executable analytical strategies, thereby initiating TRACE 's automated scientific reasoning pipeline. This module explicitly integrates semantic interpretation, domain knowledge constraints, and analytical method selection to systematically map complex seismological questions into executable scientific workflows.

Specifically, the **Planning Agent** first performs semantic parsing of the input query Q to extract key task descriptors, analytical objectives, and relevant physical and data constraints. When additional contextual information is required to constrain

the analysis space, user-provided literature L may be optionally incorporated to guide the reasoning process within established scientific frameworks. The Planning Agent then queries the *Structured Knowledge Library*, which encodes validated analytical workflows, theoretical domain knowledge, and interface descriptions of computational and statistical analysis tools. This allows planning to be conducted under established methodological and theoretical constraints. Based on this information, the Planning Agent generates a set of candidate analytical plans:

$$\mathcal{P} = \{p_1, p_2, \ldots, p_m\}, \tag{1}$$

where each candidate plan is represented as an ordered sequence of analytical operations corresponding to a candidate scientific reasoning and computational pathway.

To reduce redundancy and enhance scientific validity, the candidate plans are subsequently evaluated by a **Plan Aggregation Agent**. This agent merges semantically similar or structurally equivalent analytical pathways and filters candidate plans according to feasibility, data availability, methodological consistency, and physical plausibility. When key assumptions remain uncertain or multiple scientific interpretations are viable, an optional human-in-the-loop supervision mechanism $\mathcal{H}$ may be introduced to confirm or refine analytical strategies, thereby improving interpretability and analytical robustness. The selected optimal analytical plan $p^\star$ is formalized as an executable workflow that drives subsequent automated execution:

$$\mathcal{P} = \mathcal{G}(Q, L), \quad p^\star = \mathcal{A}(\mathcal{P} \mid \mathcal{H}), \tag{2}$$

where $\mathcal{G}$ denotes candidate plan generation and $\mathcal{A}$ denotes plan aggregation and selection under optional human supervision.

Automated Execution and Validation Module

Before execution, abstract analytical plans must be translated into workflows with explicit computational semantics. TRACE introduces a **Workflow Agent** that converts the optimal analytical plan $p^\star$ into a machine-executable workflow representation:

$$w = \mathcal{W}(p^\star). \tag{3}$$

This workflow representation serves as the primary intermediate abstraction for automated execution and validation. It adopts a hierarchical organization of scientific tasks. At the task level, workflows consist of abstract scientific operations, including seismic data preprocessing, phase picking and earthquake location. At the operation level, each task is decomposed into specific computational procedures and function calls. For example, data preprocessing may include detrending, instrument response correction, and noise suppression. Task dependencies and data-flow constraints are explicitly encoded within the workflow, ensuring logical consistency and methodological reproducibility across execution stages.

The standardized workflow drives automated code synthesis, execution, and validation. Task dependencies are parsed to determine execution scheduling strategies. Tasks with sequential dependencies are executed serially to preserve causal consistency, whereas independent tasks are parallelized to enhance computational efficiency. For each task, a **Coding Agent** dynamically generates executable code by integrating workflow-defined operational semantics, validated computational functions from the

Tools Library, and task examples and documentation stored in the *Knowledge Library*. These tools support data acquisition, preprocessing, numerical simulation, statistical analysis, and scientific visualization.

To ensure reliability and physical consistency, TRACE implements a feedback-driven validation mechanism. A **Result Checking Agent** performs runtime diagnostics to detect statistical anomalies and violations of physical constraints. An **Image Feedback Agent** evaluates visualization outputs for structural consistency and interpretability, identifying anomalous or physically implausible patterns. When inconsistencies or failures are detected, TRACE initiates automated error recovery through parameter adjustment, function restructuring, or tool substitution. This execution-validation loop iterates until outputs satisfy predefined task-specific success criteria. Verified workflows and execution scripts are archived in the knowledge and tool libraries to support reuse and continuous system evolution.

The execution-validation process is formalized as:

$$O^{(k+1)} = \mathcal{E}\left(\mathcal{M}\big(\mathcal{F}(w \mid \mathcal{T}, L)^{(k)}\big)\right), \quad \text{s.t. } \mathcal{V}(O^{(k+1)}) = 1, \tag{4}$$

where k denotes the iteration index, $\mathcal{F}$ denotes code instantiation, $\mathcal{M}$ denotes error correction, $\mathcal{E}$ denotes program execution, and $\mathcal{V}$ denotes validation. $\mathcal{T}$ denotes available computational tools and L denotes the structured knowledge base.

Scientific Integration and Inference Module

Following workflow execution and automated validation, TRACE performs scientific interpretation through the *Scientific Integration and Inference Module*. This module conducts perspective-specific scientific analyses and optionally enables cross-perspective reasoning for problems involving complex or multi-source observations.

Perspective-specific **Analysis Agents** interpret workflow outputs from predefined or dynamically identified scientific perspectives. Each perspective represents an interpretative framework within which system behaviour is evaluated through one or multiple analytical dimensions. For example, a spatiotemporal perspective may characterise migration behaviour, clustering organisation, seismicity rate evolution, and spatial density variations to constrain underlying triggering and transport processes. For perspective v, TRACE extracts structured evidence from workflow outputs O through a perspective-dependent evidence extraction operator E_v:

$$S_v = E_v(O). \tag{5}$$

During this process, TRACE simultaneously constructs a provenance record linking scientific conclusions to experimental design, workflow structure, task-level code, and output data, ensuring transparency and auditability of scientific interpretations.

For problems involving heterogeneous observations or strongly coupled geodynamic processes, TRACE can optionally activate a Cross-Perspective Analysis Agent. This agent integrates perspective-specific conclusions $S_v v \in \mathcal{V}$ by evaluating evidence consistency, complementarity, and constraint relationships to construct multi-source evidence chains and identify potential causal structures:

$$S^\star = \mathcal{I}(\{S_v\}_{v\in\mathcal{V}}), \tag{6}$$

where $\mathcal{I}$ denotes cross-perspective evidence fusion and scientific inference, and $S^\star$ represents the integrated scientific interpretation.

4.1.3 Foundational reasoning engine and LLM configuration

TRACE employs a state-of-the-art foundation large language model (LLM) as its central reasoning engine to perform semantic parsing of scientific queries, workflow synthesis, autonomous code generation, and multi-dimensional scientific interpretation. To mitigate stochasticity and ensure methodological rigor, LLM-driven reasoning is strictly constrained by structured knowledge libraries, validated computational tool interfaces, and specialized system-level control prompts.

Comparative evaluations across multiple LLM backbones (see Fig. 5) demonstrate that GPT-5 consistently achieves superior performance metrics across varying levels of task complexity, specifically in terms of algorithmic correctness and convergence speed (requiring the fewest debugging iterations). Given its robust balance between complex scientific reasoning and code synthesis efficiency, GPT-5 is implemented as the primary foundation model for all constituent agents within the TRACE framework. This standardized backbone ensures cross-module compatibility and maximizes the overall success rate of end-to-end seismological workflows.

4.1.4 Resource library

To support reproducible, auditable, and adaptive scientific reasoning, TRACE establishes a robust resource infrastructure that bridges high-level methodological knowledge with executable computational capabilities. This layer provides the essential constraints and functional implementations for automated workflows, acting as the foundational substrate for the planning, execution, and validation modules. The infrastructure comprises two synergistic components: a *Structured Knowledge Library* and a *Validated Scientific Tools Library*.

Structured Knowledge Library

The Structured Knowledge Library serves as the cognitive core of TRACE , encoding methodological expertise, parameterization strategies, and analytical paradigms derived from established seismological practices. Unlike the Tools Library, which facilitates execution, the Knowledge Library focuses on the underlying logic and heuristic rules of scientific inquiry. This enables TRACE to autonomously select optimal research strategies and method-selection criteria based on the nuanced requirements of a given query.

The library organizes domain knowledge through hierarchical structuring and semantic indexing. It incorporates workflow templates for diverse analytical scenarios, including algorithm applicability constraints, recommended hyperparameter ranges, and documented failure modes, thereby providing interpretable guidance for workflow synthesis. Furthermore, it integrates comprehensive documentation for seismic signal processing and earthquake catalog analysis, ensuring precise semantic parsing of function calls. Beyond static curated resources, the library maintains online retrieval capabilities to dynamically ingest recent literature and updated API specifications, allowing TRACE to evolve alongside the rapidly advancing seismological community.

Validated Scientific Tools Library

The Validated Scientific Tools Library aggregates a comprehensive suite of open-source software and expert-developed algorithmic modules, providing the functional implementation for seismic data acquisition, preprocessing, and multi-scale analysis. The library incorporates widely used seismological software packages such as ObsPy [23], SeisBench [24], DASPy [25], GaMMA [22], and HypoDD [21], as well as earthquake catalog statistical analysis toolkits including EQcorrscan [26], SeismoStats [27], and ETAS. TRACE further integrates general scientific computing libraries including xarray, cartopy, iris, eofs, and scikit-learn to support multidimensional data processing and statistical modeling.

To ensure interoperability within a heterogeneous software ecosystem, TRACE utilizes an LLM-orchestrated code synthesis mechanism that adapts analytical procedures from legacy R, MATLAB, or Fortran environments into standardized Pythonic workflows. This unified interface allows for consistent task scheduling and rigorous error handling. Each tool is encapsulated with descriptive metadata—defining operational boundaries, input-output schematics, and physical constraints—to enable precise autonomous task-tool matching. This modular architecture ensures the library remains extensible, allowing the seamless integration of emerging community-standard algorithms while maintaining a robust foundation for automated seismological research.

4.2 Evaluation framework

4.2.1 Scientific task design and benchmarking scenarios

To systematically quantify the analytical capabilities of TRACE , we established a hierarchical evaluation benchmark that tracks performance progression from fundamental tool execution to autonomous scientific reasoning. This benchmark categorizes seismological workflows into three complexity levels, reflecting increasing cognitive demands and analytical depth (Extended Data Table 1).

Level 1: Atomic task capability. This level evaluates the accuracy and procedural reliability of TRACE in executing fundamental seismological operations at the level of individual analytical functions, focusing on its ability to correctly invoke standard toolchains and perform routine data-processing procedures. Tasks include representative categories such as data retrieval, data formatting, signal processing, feature analysis, and scientific visualization. Level 1 comprises 76 tasks and is designed to assess computational consistency and execution robustness in basic seismic data processing and signal analysis workflows.

Level 2: Multi-step analytical capability. This level focuses on multi-stage scientific workflows at the workflow level, requiring coordinated use of multiple analytical tools. It evaluates TRACE's ability to organize workflow-level task dependencies, manage intermediate computational states, and adaptively select analytical pathways. Tasks represent common seismological workflow patterns, including sequential workflows, heuristic branching, batch processing, and parameter-space exploration. Level 2 includes 32 tasks and evaluates workflow consistency, adaptive decision-making, and complex tool orchestration in long-chain analytical processes.

Level 3: Integrated scientific analysis capability. This level evaluates TRACE's ability to perform end-to-end scientific investigations under realistic research

conditions. These tasks involve cross-module data processing, multi-perspective scientific analysis, and integrative reasoning, simulating the complete research process in which seismologists formulate hypotheses, integrate multi-source evidence, and construct scientific interpretations. Two complex research tasks are included at this level, designed as representative real-world case studies (corresponding to the Ridgecrest inter-event and Santorini–Kolumbo volcanic crisis cases presented in Results), with evaluation focusing on the coherence of scientific reasoning, integration across tasks, and validity of the generated interpretations.

This hierarchical evaluation framework enables systematic characterization of TRACE's performance boundaries across varying levels of scientific complexity and provides a quantitative reference for assessing the progression of autonomous scientific agents from tool execution toward self-directed scientific reasoning.

4.2.2 Basic evaluation and scoring criteria

To ensure reproducible and scientifically consistent performance assessment, we developed a dual-track evaluation protocol that distinguishes between tasks with deterministic quantitative outputs and tasks involving open-ended scientific analysis. For tasks with deterministic numerical outputs, system results were quantitatively compared with reference solutions generated through expert-designed control experiments. Discrepancies between TRACE outputs and reference results were evaluated using standard statistical metrics, including Root Mean Square Error (RMSE) and correlation coefficients, to assess numerical accuracy and computational stability.

For tasks involving scientific visualization, experimental workflow design, or code-based analytical workflows, evaluation was conducted using structured expert scoring. Each task was independently assessed across three dimensions: 1) Experimental planning and methodological design, evaluating the scientific validity, logical completeness, and practical feasibility of the analytical workflow; 2) Code implementation quality, evaluating syntactic correctness, functional completeness, and consistency between generated scripts and proposed analytical plans; 3) Result synthesis and scientific communication, evaluating interpretability, visualization quality, and completeness of scientific reporting. To mitigate subjective bias, evaluations were conducted independently and aggregated across multiple reviewers following standardized scoring guidelines.

Based on the aggregated scores, task performance was categorized into three levels: scores above 4.0 were classified as expert-level performance; scores between 2.5 and 4.0 as research-ready with limited supervision; and scores below 2.5 as indicating substantial methodological or technical deficiencies requiring extensive expert intervention. Detailed scoring definitions are provided in Extended Data Table 2.

Data availability

All datasets used in this study are publicly available and accessible through the sources described below. Continuous waveform data for EH and HH channels within 80 km of the Ridgecrest mainshock were obtained from the Southern California Earthquake Data Center (SCEDC) [28]. Seismic waveform data for the Santorini–Kolumbo case

were accessed via the EIDA node (https://eida.gein.noa.gr/), using network codes HL [29] and HT [30].

Code availability

The code of TRACE will be publicly available at https://github.com/OpenEarthLab/TRACE.

Acknowledgments

This work was supported by a locally commissioned task from the Shanghai Municipal Government.

Author contribution

F.L. designed the study, performed the experiments, and wrote the original manuscript. F.Lin., Z.L., and L.B. led and supervised this work. J.X., X.C., X.G., H.C., and B.F. contributed to the methodology and revised the manuscript. X.W., Z.G., and J.W. performed data collection and processing. S.M.M., Z.L. and L.F. contributed to the interpretation of results and provided professional guidance. All authors discussed the results and commented on the manuscript.

Conflict of Interest

The authors declare no competing interests.

Extended Data

Extended Data Table 1 The task complexity levels and representative capabilities of the TRACE in the seismological evaluation framework.

Levels	Description	Number of Tasks
Level 1: Atomic task capability	Performs fundamental seismological operations with procedural correctness and execution stability, including seismic data acquisition, format conversion, preprocessing, signal feature extraction, and scientific visualization. Emphasizes accurate tool invocation, parameter handling, and computational consistency in routine seismic data processing workflows.	76
Level 2: Multi-step analytical capability	Solves workflow-level seismological problems requiring coordinated multi-tool orchestration and dependency management. Integrates sequential toolchains, heuristic branching strategies, large-scale batch scanning, and parameter-space exploration under physical constraints. Evaluates adaptive pathway selection, intermediate state management, and long-chain analytical coherence.	32
Level 3: Integrated scientific analysis capability	Conducts end-to-end scientific investigations under realistic research scenarios. Integrates cross-module data processing, multi-perspective analysis, hypothesis formulation, and evidence synthesis to generate scientifically valid interpretations. Assesses global reasoning coherence, cross-task integration, and interpretative rigor in complex seismological studies.	2

Extended Data Table 2 Result-Oriented Evaluation Reference Table (Full Score 5 Points).

Score	Quantitative Accuracy	Scientific Correctness	Visualization and Reporting Quality
5 points	Numerical outputs match reference solutions with negligible deviation under predefined statistical thresholds. Results are stable and reproducible.	All results are scientifically valid, logically consistent, and fully aligned with task objectives. No conceptual or methodological errors.	Figures are accurate, clearly labeled (axes, units, scales), and publication-ready. Visual design enhances interpretability. Text and figures are fully consistent.
4 points	Minor numerical deviations from reference results but within acceptable tolerance. No impact on overall conclusions.	Results are scientifically correct with only minor interpretative omissions or limited analytical depth.	Figures are correct and interpretable, but minor issues exist (e.g., formatting inconsistencies, limited annotations). Overall presentation is clear.
3 points	Moderate deviation from reference values, but core trends or magnitudes remain correct.	Partial correctness: main scientific conclusion is identifiable, but secondary errors or incomplete interpretation exist.	Figures are understandable but contain noticeable labeling issues, limited clarity, or insufficient explanation.
2 points	Significant numerical errors or unstable results that affect reliability.	Results contain conceptual misunderstandings or incorrect scientific interpretations.	Figures are poorly constructed or partially incorrect, limiting interpretability.
1 point and below	Numerical results are incorrect or fail to match reference benchmarks.	Scientific conclusions are invalid or inconsistent with task requirements.	No meaningful figures or coherent result presentation provided.

Supplementary Information

TRACE: A Multi-Agent System for Autonomous Physical Reasoning in Seismological Science

Table of contents

A High-resolution earthquake catalog construction using TRACE 3

A.1 Study region, time window, and data acquisition . . . 3
A.2 Automated waveform preprocessing pipeline . . . 9
A.3 Event detection and phase picking strategy . . . 14
A.4 Multi-Station association and initial hypocenter determination . . . 19
A.5 Double-difference relocation with HypoDD . . . 25

B Spatiotemporal organization of Ridgecrest inter-mainshock seismicity 30

B.1 Spatiotemporal Coupling Structure of Inter-Mainshock Seismicity . . . 31
B.1.1 Spatiotemporal evolution of epicenters . . . 31
B.1.2 Onset Time Distribution of Regional Earthquake Activation . . . 39
B.2 Fault-Geometry Constraints and Branching Structure Identification . . . 47
B.2.1 Fault Correlation and Strike-Directional Unfolding Characteristics 47
B.2.2 Triggered Stratification and Fault Segment Response . . . 55
B.2.3 Geometric Evolution and Structure-Guiding Effects in high-Density Regions . . . 63
B.3 Migration Directionality and Seismicity Rate Evolution . . . 71
B.3.1 Temporal Evolution of Directional Clusters . . . 71
B.3.2 Quantitative Analysis of Fault Segmentation: Differences in Propagation at the Fault Scale . . . 78
B.4 Magnitude-Frequency Distribution and Temporal Variability of the b Value 88
B.4.1 Spatial b-value structure and stress transfer . . . 88
B.4.2 Time Evolution and Comparative Analysis of the Mw 7.1 Epicenter Region . . . 97
B.5 Stage-Dependent Behavior of the Omori-Utsu Decay Relation . . . 104
B.6 Multi-Perspective Synthesis and Agent-Based Integrated Assessment . . . 113

C Global Seismicity Characterization through Structured TRACE Reasoning 121

C.1 Spatiotemporal Evolution of Catalog Completeness and Observational Capacity . . . 121
C.2 Magnitude–Frequency Scaling and Multi-dimensional *b*-value Heterogeneity . . . 128
C.2.1 Magnitude-Frequency Modeling . . . 128
C.2.2 Multi-dimensional b-value Heterogeneity . . . 133

C.3 Temporal Seismicity Dynamics and Stochastic Point-Process Characterization 139
C.4 Spatial Distribution Patterns and Plate-Tectonic Modulation 145
C.4.1 Epicenter Coupling with Plate Boundaries 145
C.4.2 Tectonic Modulation of b-values 151
C.5 Vertical Structure of Global Seismicity and Discrimination of Depth Artifacts 156

A High-resolution earthquake catalog construction using TRACE

This section presents the complete technical workflow and implementation details by which TRACE constructs a high-resolution earthquake catalogue under conditions of complex seismic activity. Using the 2019 Ridgecrest earthquake sequence as a representative case [1, 2], we demonstrate how an end-to-end catalogue can be derived from continuous waveform data under observational conditions characterized by intense aftershock clustering, rapidly varying signal-to-noise ratios, and heterogeneous data quality.

Given predefined constraints on study region, time window, and data type, TRACE orchestrates the full processing chain through a unified control framework, including continuous waveform acquisition and preprocessing, event detection and phase picking, multi-station association, initial hypocenter determination, and double-difference relocation. Key parameters and quality-control thresholds may incorporate expert constraints when necessary, maintaining a balance between automated execution and established seismological practice. All intermediate decisions, parameter configurations, and outputs are systematically archived to ensure reproducibility and traceability.

A.1 Study region, time window, and data acquisition

At 03:19:53 UTC on 6 July 2019, an Mw 7.1 earthquake struck the Ridgecrest region of eastern California, USA, initiating a prolonged and spatially complex aftershock sequence. Owing to its well-characterized tectonic setting, high seismicity rate, and dense regional seismic network coverage, this sequence has become a benchmark dataset for evaluating automated monitoring and earthquake catalogue construction methodologies. We therefore selected this sequence to assess the end-to-end waveform monitoring capability of TRACE under conditions of intense aftershock activity.

The study region spans longitudes -118.0 to -117.0 and latitudes 35.25 to 36.25, with a temporal window from 4 July to 27 July 2019. Continuous waveform data were automatically retrieved from the Southern California Earthquake Data Center, comprising records from 34 stations and a total data volume of approximately 23.36 GB. All data consist of routinely acquired multi-component continuous recordings, without prior event selection or manual intervention, and constitute the sole input to the subsequent automated processing workflow.

Box A.1.1 User Request

```
Acquire the station and waveform data with following
    requirements
Requirements:
1. Region settings
- Providers: "SCEDC"
- Network: "*" (all networks)
- Station: "*" (all stations)
- Location: "*" (all locations)
- Channels: "EH*", "HH*" (three-component seismometers)
- Time Range: 2019-07-04T00:00:00 to 2019-07-27T00:00:00 (23
    days)
- Station Geographic Range:
    - minlatitude = 35.25
```

```
    - maxlatitude = 36.25
    - minlongitude = -118.0
    - maxlongitude = -117.0
2. Waveform Data Statistic and visualization: for each
   waveform file, statistic the file infomation and the data
   completeness. Plot a figure to overview the waveform data.
3. Station Data Loading and Statistics: load and visualize
   the station distribution (longitude-latitude) with a large
    region = [31.0, 40.00, -124.0, -112.00] and a smaller
   region = [35.1, 36.35, -118.0, -117.15].
```

Box A.1.2 Final Experimental Plan

```
Experimental Plan: Data preparation and statistics for the
   Ridgecrest Mw7.1 earthquake.
1. Top-level Plans: Obtain station metadata and 22 days of
   three-component seismic waveform data from SCEDC for all
   stations inside the geographic rectangle (lat 35.25-36.25,
    lon -118.0--117.0) for the time window 2019-07-04T00
   :00:00 → 2019-07-27T00:00:00. Save the station inventory
   in StationXML, download waveforms in MiniSEED using
   parallel download. Generate comprehensive file-level and
   station-day completeness statistics for continuous seismic
    waveforms, produce diagnostic plots of data coverage and
   waveform overviews, and extract and map station metadata.

2. download stations: query SCEDC for stations that satisfy
   time + channel + geographic filters, save StationXML,
   export a station table.
- Query SCEDC station service (ObsPy FDSN client) with
   precise filters:
    - provider: "SCEDC"
    - network: "*" ; station: "*" ; location: "*"
    - channel patterns: "EH*", "HH*"
    - time window: starttime = 2019-07-04T00:00:00 UTC,
       endtime = 2019-07-27T00:00:00 UTC
    - geographic bounding box: minlatitude = 35.25,
       maxlatitude = 36.25, minlongitude = -118.0,
       maxlongitude = -117.0
    - request level that includes channels (e.g., level="
       response" / channel info) so downstream selection is
       accurate
- Filter returned Inventory:
    - collapse duplicates and record available location codes
       per station
- Save filtered Inventory

3. download waveforms: read the StationXML / CSV produced by
   previously script, build a restricted download list,
   download MiniSEED waveform data in parallel, save files,
   show progress.
- Read station list:
    - Prefer the CSV to build an explicit download list of
       network, station, location and available channel names
       or patterns.
    - If CSV missing, fall back to parsing the StationXML.
- Construct download requests (per station):
```

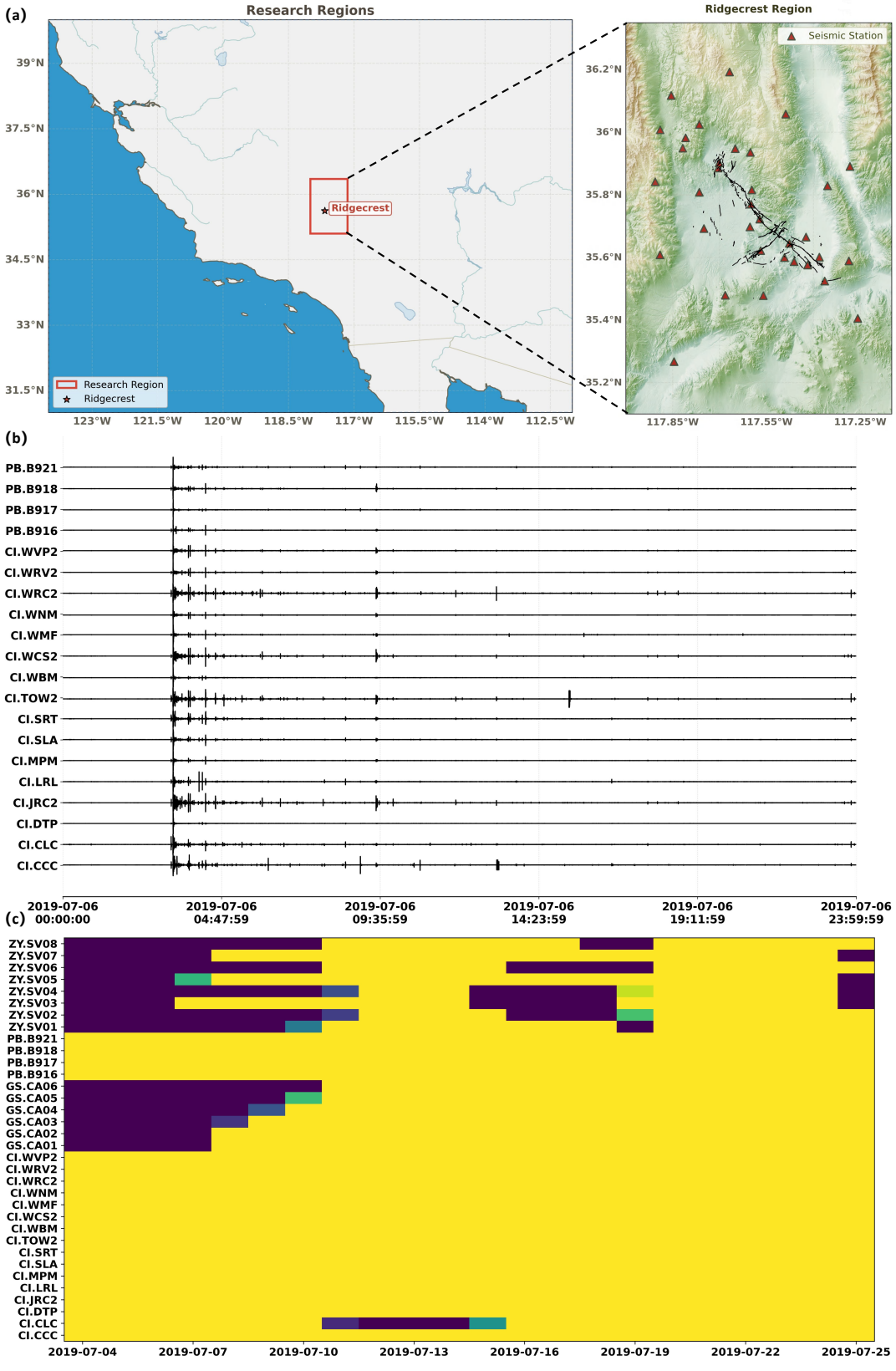
```
    - For each network.station.location group, request
      channels matching the available channel list filtered
      for EH* and hH*; if channel names unknown, request
      channel wildcard list ["EH*", "HH*"] but limit by
      station list to avoid unrelated servers.

4. statistic the waveform file: Discover all MiniSEED files,
   extract file metadata (size, time span, sampling rate,
   sample count), compute per-station, per-day completeness
   ratios and Save results to CSVs
- File Discovery
    - Recursively traverse base directory and identify files
      matching `*.mseed` and parse filename tokens: network
      (e.g., CI), station (e.g., CCC), location, channel (
      HHN/HH1, hHE/HH2, hHZ, EHN, EHE, EHZ), start_time (`
      YYYYMMDDThhmmssZ`), end_time
    - Record file path and file size (bytes)
- File-Level Metadata Extraction
    - For each file, call ObsPy `read(headonly=True)` to
      extract: starttime, endtime (UTCDateTime) and
      sampling_rate (Hz), npts (number of samples)
    - Compute duration_seconds = endtime - starttime
    - Compute completeness_ratio = npts / (duration_seconds ×
      sampling_rate)
    - Catch/read errors, log file path and error message, and
      continue
- Save File-Level Statistics
    - Aggregate all records into a table
- Station-Day Completeness Computation
    - From waveform file statistics, for each unique network.
      station and each calendar day covered by the data:
        - Group records by station and UTCDateTime(starttime)
          .date()
        - Sum total recorded seconds per day (npts /
          sampling_rate)
        - Expected_seconds_per_day = 86400
        - daily_completeness = total_recorded_seconds /
          Expected_seconds_per_day
    - Build station_daily_completeness.csv with columns:
      network, station, date (YYYY-MM-DD),
      total_recorded_seconds, daily_completeness

5. waveform visualize: visualize station-day data coverage as
   a heatmap, and plot vertical-component (Z) waveforms for
   all stations over 2019-07-06→2019-07-07
- Station-Coverage-By-Day heatmap
    - Read station daily completeness data into pandas
    - Pivot to matrix: rows = sorted network.station, columns
      = date, values = daily_completeness
    - Plot matrix as a color grid with completeness ratio
      [0,1]
    - Label x-axis with date strings (YYYY-MM-DD), y-axis
      with station codes
    - Save figure as station_day_coverage.png
- Single-Day Z-Component Waveform Overview
    - Define time window: t0 = UTCDateTime("2019-07-06T00
      :00:00Z"), t1 = UTCDateTime("2019-07-07T00:00:00Z")
    - For each station in pivot matrix:
```

```
52          - Identify MiniSEED file(s) whose channel ∈ {HHZ, EHZ
                } and whose header times overlap [t0, t1]
53          - Read full data segment with ObsPy `read(...).slice(
                t0, t1)` (headonly=False)
54      - Use multiprocessing (up to 64 processes) with a tqdm
            progress bar for file loading
55      - Plot stacked time-series traces: one horizontal panel
            per station, aligned on the same UTC axis
56          - X-ticks set directly to UTCDateTime labels (e.g., "
                2019-07-06T00:00", "2019-07-06T06:00",..)
57          - Do not downsample; display full resolution
58      - Save figure as daily_waveform_overview.png
59
60  6. research region visualize
61  - Load StationXML
62  - Filter Relevant Stations
63      - List subdirectories under waveform base dir, parse
            network.station codes
64      - For each code, find matching Network/Station in
            inventory
65      - If a code is missing, log a warning
66  - Extract and Save Metadata
67  - Plot station locations over two geographic extents
68      - Large region: minlat=31.0, maxlat=40.0, minlon=-124.0,
            maxlon=-112.0
69      - Small region: minlat=35.1, maxlat=36.35, minlon=-118.0,
            maxlon=-117.15
```

Box A.1.3 Main Visualization Results (Raw Output)



Box A.1.4 Analysis Summary

```
Summary of data download and statistics for Ridgecrest Mw7.1.
1. Records
- high file-level and daily completeness at core stations (e.g., B916, B917, B918, B921, DTP, JRC2, LRL, MPM, SLA, SRT, WBM, WCS2, WMF, WNM, WRC2, WRV2, WVP2) with completeness ratios ≈ 1 across the 22-day period
- Z-component waveforms exhibit uninterrupted full-resolution records for most sites, with minor gaps (<1 h) at CLC, SV02, SV04, TOW2 and transient high-amplitude spikes around ~06:00 UTC and ~18:00 UTC.
- Complete extraction of 34 station coordinates matching waveform directories, confirming network deployment concentrated in eastern California (35.27-36.19° N, -124.0 to -112.0° W)

2. Overview and method context
- We implement a two-stage data-acquisition pipeline.
    - The first stage queries the SCEDC FDSN station service (network="", station="", location="", channel patterns "EH", "HH*") within the geographic box and time window t0=2019-07-04T00:00:00 to t1=2019-07-26T23:59:99; it filters channels active in [t0, t1], and saves the StationXML and a CSV summary.
    - The second stage reads the CSV/StationXML, constructs explicit per-(NET, STA, LOC, CHAN) download requests for the same interval, and configures the ObsPy MassDownloader with concurrency=32 and chunk_length=600 s.
    - It then streams MiniSEED files to disk using a deterministic filename template, validates each saved file by re-reading, logs per-request status, and builds a manifest. Finally, a parallelized pipeline was implemented to: 1) discover and read MiniSEED headers across approximately 3,000 files; 2) compute per-file metadata (start/end times, fs, npts) and completeness ratios; 3) aggregate results to station-day completeness; 4) visualize heatmaps and full-day Z-component stacks;parse StationXML to extract station latitudes/longitudes; 5)map station distributions over large and small extents.

3. Summary of figure-based results
Diagnostic A - Station Distribution - Large Region
- All stations lie within a narrow band of eastern California, between roughly 31°-40° N latitude and 124°-112° W longitude.
- The entire array is concentrated around the Ridgecrest seismic zone (approx. 35.5°-36° N, 118°-117° W).

Diagnostic B - Station Distribution - Small Region
- Zooming into 35.2°-36.25° N and 117.9°-117.2° W highlights detailed station placement.
- There are minor under-covered corners (northwest and southeast), but overall coverage is dense.

Diagnostic C - Analysis of Z-component Waveforms (2019-07-06 to 2019-07-07)
```

```
- Stacked Z-component traces for all stations over the 24 h
  window from 2019-07-06T00:00Z to 2019-07-07T00:00Z. Each
  horizontal panel corresponds to one station's hHZ/EHZ
  channel, plotted at full instrument sampling rate and
  aligned on a common UTC time axis.
- Overall noise levels appear low and consistent, with no
  large, network-wide events dominating the 24 h record.

Diagnostic D - Daily Completeness heatmap (2019-07-04 to 2019
  -07-26)
- heatmap of daily data completeness per station. Color scale
   runs from purple (0 % completeness) through green (~50-80
   %) to yellow (100 %). Gray cells indicate entirely
  missing data for that station-day.
- Stations PB.B921, PB.B918, PB.B917, PB.B916 and all CI.*
  stations (e.g., CI.WVP2, CI.WRC2, etc.) show full data
  availability (coverage fraction ≃ 1.0) for every day in
  the period. These stations provide a stable backbone for
  continuous monitoring.
- ZY.* stations (ZY.SV01-ZY.SV08) and GS.* stations (GS.CA01-
  GS.CA06) begin recording around July 6-8, ramp up to full-
  day coverage by July 9-10, then continue mostly
  uninterrupted until the end of the window.
- Station CI.CCC has a delayed start (~July 11) and reaches
  full-day coverage by July 15.
- ZY.SV06 and ZY.SV05 show intermittent gaps around July 6-8
  before achieving full coverage.
- GS.CA03 and GS.CA04 exhibit partial coverage on July 7-9,
  indicating possible maintenance or data dropouts during
  that interval.
- ZY.SV02 and ZY.SV07 have minor coverage dips around mid-
  July, suggesting short outages.
- The PB.* and CI.* networks operate continuously with no
  detectable daily gaps, making them reliable for long-term
  trend analysis.
```

A.2 Automated waveform preprocessing pipeline

Continuous waveform data obtained as described above were subjected to a unified automated preprocessing procedure designed to produce standardized waveform representations under constraints of temporal continuity, physical unit consistency, and comparable spectral characteristics. Continuous MiniSEED records were first merged by station and UTC day and trimmed to complete 24-hour segments. Missing or masked intervals were filled to preserve temporal continuity and prevent boundary effects during sliding-window analyses. Detrending, demeaning, and tapering were applied sequentially to suppress baseline drift, followed by removal of the instrument response to convert the data into physical ground displacement. Band-pass filter parameters were selected according to the target magnitude range to attenuate non-seismic frequency components and enhance phase coherence within the relevant frequency band. For three-component records, channel alignment and sampling-rate standardization were performed automatically, with resampling applied when necessary to ensure cross-station comparability in temporal sampling and spectral resolution. The resulting dataset comprises temporally continuous, spatially consistent three-component waveforms with explicitly documented processing parameters, minimizing

implicit assumptions and ensuring methodological reproducibility. All preprocessing steps, filter bands, and response correction parameters were structurally recorded to eliminate ambiguities commonly associated with ad hoc script-based workflows.

Box A.2.1 User Request

```
Preprocess and analysize the seismic data below:
Requirements:
1. Data Sources
- Continuous Seismic Waveform Data locate at:`./data/waveforms_raw`
- Station Metadata locate at:`./data/stationxml`
2. Extract and reformat the station information for three-component channels, including: `network.station,latitude,longitude,elevation,gain`
3. Waveform Data Aggregation and Standardization
- For each station, each full UTC day in used data range:
    - Load all waveform files covering that day and for that station from the base directory.
    - For each file, check the trace completeness and merge the split trace
    - For each station-day, assemble the three-component waveform and check the three-component waveform completeness: if all three components are present, proceed to the preprocessing step; if two components are present, duplicate an existing component to fill the missing one (Z component is preferred); if only one component is present: duplicate Z to N and E if Z component exist, otherwise skip and log this as warning
4. Per-trace Waveform Preprocessing: for each three-component waveform in each station-day, designed a preprocessing pipeline, including: Detrend linear, demean, taper (max 1%, hann), remove instrument response (output to displacement), resample to 100 hz if not already, and other commonly used preprocessing steps in seismic data preprocessing.
5. Preprocessing Visualization: plot a figure to show the preprocessing process for the saved preprocessing data of one station-day.
6. Output requirements: save processed three-component waveform per station-day as format: `YYYYMMDD/{network}.{station}.{starttime}.{endtime}.processed.mseed`
```

Box A.2.2 Final Experimental Plan

```
Experimental Plan: Seismic Data Preprocessing for Monitoring and Analysis
1. Top-level Plans: Standardize and preprocess continuous three-component seismic waveform data: 1) Extract and format station metadata for all stations active between 2019-07-04 and 2019-07-26. 2)Standardize and preprocess continuous three-component seismic waveforms over the given time window. 3)Assemble clean three-component Waveforms per station-day and save in MiniSEED. 4)Select one representative station-day to record intermediate preprocessing outputs. 5)Visualize the full preprocessing pipeline for that example station-day.

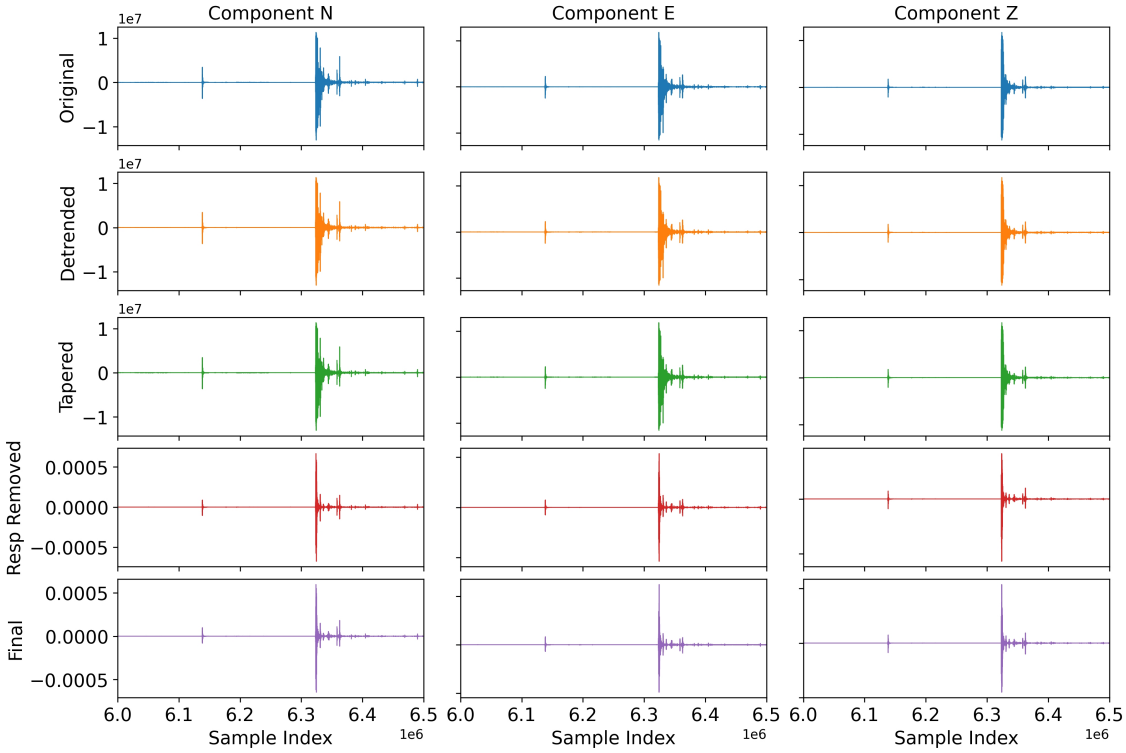
```

```
2. extract station metadata: build a CSV table of station parameters for all stations with data in the target date range.
- Define constants
  - BASE_WF_DIR = "./data/waveforms_raw"
  - STAXML_DIR  = "./data/stationxml"
  - START_DATE  = UTCDateTime("2019-07-04T00:00:00")
  - END_DATE    = UTCDateTime("2019-07-26T23:59:59")
- Discover stations
  - List all subdirectories of BASE_WF_DIR; parse names: "network.station".
  - Filter only those with any files overlapping [START_DATE, END_DATE].
- Parse StationXML for each station
  - For each network.station:
    - Load its inventory via obspy.read_inventory(f"{STAXML_DIR}/{network}.{station}.xml").
    - Identify three high-gain channels per component, priority hH* over EH*:
      - N-component candidates: hHN, hH1, EHN
      - E-component candidates: hHE, hH2, EHE
      - Z-component candidates: hHZ, EHZ
    - Extract station latitude, longitude (6 decimals) and elevation in meters (1 decimal) from the chosen channel.
    - For those three channels, read instrument gain (from PAZ zeros/poles or instrument sensitivity), compute their average (round to 1 decimal).
- Write station.sta: network.station,latitude,longitude,elevation,gain

3. preprocess waveforms: for each station-day in the given windows, load raw MiniSEEDs, apply a standard preprocessing pipeline to each component, assemble or skip according to completeness rules, save three-component MiniSEEDs, and capture one example station-day's intermediate data.
- Define constants and load station.sta
  - BASE_WF_DIR, STAXML_DIR, START_DATE, END_DATE (same as Script 1)
  - PRE_FILT   = [1.0, 5.0, 40.0, 45.0]
  - TARGET_FS  = 100.0
  - OUTPUT_ROOT = "./processed_waveforms"
  - MAX_WORKERS = 64
- Load station inventory dict
  - Read station.sta, re-load each StationXML into a dict for remove_response.
- Build station-day tasks
  - For each station in station.sta and for each UTC day D in {2019-07-04, 2019-07-26}:
    - DAY_START = UTCDateTime(D+"T00:00:00")
    - DAY_END   = DAY_START + 24*3600 - 1e-3
- Parallel processing pool (up to MAX_WORKERS). Each worker processes one (station, DAY_START) pair:
    A. Discover raw files
      - List all files under BASE_WF_DIR/network.station/ matching "*.mseed".
```

```
40              - Parse filenames' start/end times; select those
                  overlapping [DAY_START, DAY_END].
41              - Read each selected file with obspy.read();
                  append resulting Stream to a list.
42          B. Merge & trim per component
43            For each Stream in the list:
44              1. stream.merge(method="fill", fill_value=None)
45              2. stream.trim(starttime=DAY_START, endtime=
                   DAY_END, pad=False)
46              3. For each Trace, if isinstance(data,
                   MaskedArray), fill masked regions with zeros.
47          C. Preprocessing pipeline on each Trace
48            For each merged Trace:
49              1. detrend(type="linear"); detrend(type="demean")
50              2. taper(max_percentage=0.01, type="hann")
51              3. remove_response(inventory=station_inventory,
                   pre_filt=PRE_FILT, output="DISP")
52              4. if trace.stats.sampling_rate != TARGET_FS:
                   resample(TARGET_FS)
53              5. bandpass(1.0, 40.0, corners=4, zerophase=True)
54          D. Three-component assembly
55              1. Identify available components by priority
                   lists (N, E, Z).
56              2. Cases:
57                  a. Exactly three → assemble Stream([N,E,Z]).
58                  b. Two → if Z present, duplicate Z into
                       missing; else duplicate whichever exists
                       into missing. Log WARNING.
59                  c. One → if that is Z → duplicate to N and E;
                        else skip entire station-day (log WARNING
                       ).
60              3. Detect any remaining gaps: fill by linear
                   interpolation to the trace's mean; log WARNING
                   .
61              4. If any component is all zeros after processing
                    → skip station-day (log WARNING).
62          E. Save outputs
63              - If this is the first successful station-day and
                   example not yet saved → For each processing
                   step (original, detrended, tapered,
                   response_removed, bandpassed) and each
                   component, save the Trace.data array as NumPy
                   .npy in "./example_pipeline/" with clear names
                   .
64              - Always write final three-component Stream to
                   MiniSEED:
65                Path: OUTPUT_ROOT/YYYYMMDD/
66                Filename: "{network}.{station}.{YYYYMMDD}T000000Z
                     .{YYYYMMDD}T235959Z.processed.mseed"
67
68  4. visualize pipeline: plot the five major preprocessing
       stages for the example station-day's three components.
69  - Load intermediate arrays
70  - Define plot configuration
71  - Generate multi-panel figure
72  - Save figure: "preprocessing_pipeline_example.png"
```

Box A.2.3 Main Visualization Results (Raw Output)



Box A.2.4 Analysis Summary

```
Summary of data download and statistics for Ridgecrest Mw7.1.
1. Results Summary
- A comprehensive station metadata file (‘station.sta‘) was
    generated for 34 stations active between 2019-07-04 and
    2019-07-26.
- The preprocessing pipeline produced gap-filled, three-
    component daily MiniSEEDs at 100 hz for each station-day
    with uniform instrument-response removal. Raw streams were
     merged and trimmed per day, masked data filled with zeros
    , then processed by detrending, tapering, deconvolution of
     instrument poles/zeros (pre_filt=[1,5,40,45] hz) and
    bandpass filtering.
- Visualization confirms that the sequence of detrend, taper,
     response removal and 1-40 hz bandpass preserves phase
    coherence across N/E/Z components and greatly enhances
    signal-to-noise for seismic arrivals. Linear detrend
    removes baseline drift; 1% hann taper confines edge
    artifacts; response removal converts counts to physical
    displacement; zero-phase bandpass isolates seismic band
    without phase distortion.

2. Overview and method context
```

```
- We first extract station metadata from StationXML files and
    save key parameters to a CSV. Next, for each station and
    UTC day (2019-07-04 to 2019-07-26), we load raw MiniSEED
    streams, merge and trim to exact 24 h windows, fill masked
    samples with zeros, then apply a preprocessing chain:
    linear detrend, demean, 1% hann taper, instrument-response
    removal (pre_filt = [1,5,40,45] hz) to obtain
    displacement, resample to 100 hz, and bandpass filter
    between 1-45 hz. We serialize one fully complete station-
    day's intermediate states for visualization. In parallel,
    we then assemble three-component streams per station-day,
    handling missing and gap-filled channels, and write final
    processed MiniSEED files. Finally, we generate a figure
    illustrating all five preprocessing stages for N, E, Z
    components without datetime conversion on the x-axis.

3. Summary of figure-based results
Diagnostic A - Preprocessing Pipeline Visualization
- The figure below shows the full preprocessing workflow
    applied to one station-day of seismic data, for all three
    components (N, E, Z). Each row represents a sequential
    processing step, from raw counts to the final, band-
    limited displacement time series.
- The preprocessing chain successfully:
    - Removed baseline trends,
    - Eliminated instrument response effects,
    - Produced physically meaningful displacements, and
    - Applied band-limited filtering to highlight seismic
        phases.
- The single, impulsive event is clearly visible and coherent
    across N, E, and Z components after each step.
- Final waveforms have low noise levels (<10^-5 m) before and
    after the event, demonstrating robust data conditioning.
- This pipeline is suitable for automated phase picking and
    downstream seismic monitoring tasks.
```

A.3 Event detection and phase picking strategy

Within the end-to-end monitoring framework, event detection and phase picking transform continuous waveform data into structured observations suitable for source inversion. In the context of densely clustered aftershocks and temporally and spatially variable signal-to-noise ratios, conventional fixed-threshold or single-feature approaches often fail to balance detection completeness and stability. We therefore employed a mature deep-learning-based phase picker to process continuous waveforms automatically. Specifically, the convolutional neural network model PhaseNet was used for inference on continuous data streams [3]. Daily MiniSEED files were assembled by station, and a pre-trained model was executed in a GPU environment using sliding time windows for continuous inference. P- and S-phase arrival times and associated confidence scores were extracted simultaneously, along with corresponding waveform amplitude information. All model parameters, window lengths, and threshold settings were explicitly recorded to ensure procedural consistency. Continuous data from 4 July to 26 July 2019 were processed on a daily basis. For example, approximately 31,000 phase picks were generated on 4 July and more than 100,000 on 5 July. Statistical analysis indicates that P-phase picks remain comparatively stable across varying

amplitude conditions, whereas S-phase picks exhibit greater sensitivity to threshold selection under low signal-to-noise conditions. These statistical characteristics were incorporated into quality-control criteria during subsequent association. All picks were exported in standardized tabular format with complete parameter logs to ensure reproducibility and traceability of the phase catalogue.

Box A.3.1 User Request

```
Perform seismic phase picking using PhaseNet (deep learning) for efficient and reproducible seismological analysis.
Requirements:
1. Continuous Seismic Waveform Data (MiniSEED): Located at: `./processed_data`
    - Directory Structure: Subfolders organized by start date, each containing processed MiniSEED files for specific 24-hour windows.
    - Naming Convention: Files follow the format `{network}.{station}.{start_time}.{end_time}.processed.mseed`.
2. Station Information: Located at`./processed_data/station.sta`, contains the infomation of `network.station,latitude,longitude,elevation,gain`
3. Load and perform phase picking using PhaseNet (a deep learning method), utilizing the "original" version of the pretrained model and CUDA GPU acceleration for fast inference.
4. Output requirements: extract P and S picks from the PhaseNet model output, determine the waveform amplitude at each pick time, and save all picks from the same day to a CSV file named `picks_YYYYMMDD.csv`
5. Visualization: plot a figure to demonstrate a representative example of the picking results.
```

Box A.3.2 Final Experimental Plan

```
Experimental Plan: Modular Single-Script Workflow for PhaseNet-Based Seismic Phase Picking

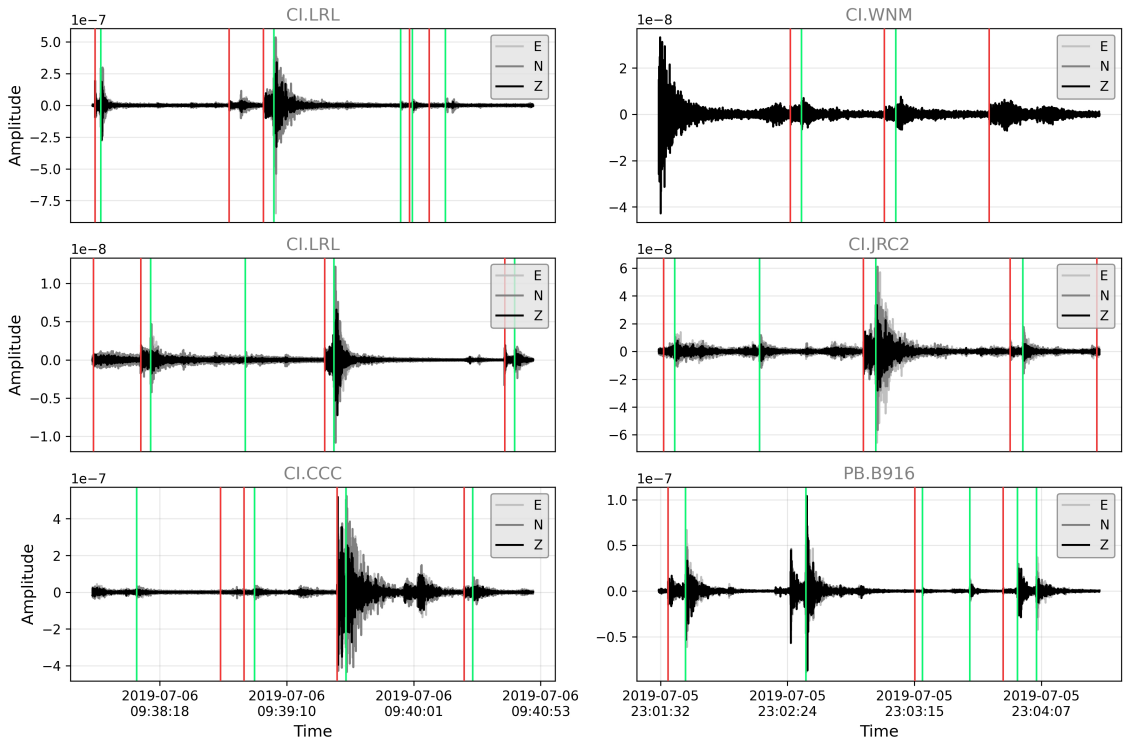
1. Top-level Plans: Automatically detect and extract P- and S-phase arrivals from 23 days (2019-07-04 to 2019-07-26) of continuous, pre-processed MiniSEED waveforms using the PhaseNet deep-learning picker on GPU. Produce one CSV "picks_YYYYMMDD.csv" per day and a summary figur of example picks.

2. Phase Picking using Phasenet: This single Python script is organized into clearly separated functions ("modules") with a final `main()` orchestrator.  It uses ObsPy for I/O, SeisBench's PhaseNet implementation for inference, pandas for tabular output, and matplotlib for visualization. All parameters (paths, time windows, model settings) are defined up front for scalability.
A. Imports & Configuration
    - Define time-window variables using ObsPy UTCDateTime:
        - START_TIME = UTCDateTime("2019-07-04T00:00:00.000Z")
        - END_TIME   = UTCDateTime("2019-07-26T23:59:99.000Z")
    - Define data paths:
        - BASE_DIR = "./data/processed_data"
```

```
12          - STATION_FILE = BASE_DIR + "/station.sta"
13      - PhaseNet model settings (from retriever):
14          - NETWORK_MODEL_PATH = ".../library/ai_module/
              phase_picking/model/phasenet.py"
15          - PRETRAINED_MODEL_PATH =  ".../library/ai_module/
              phase_picking/pretrained/v3/phasenet/original.pt.
              v2"
16          - INFERENCE_EXAMPLE_PATH =  ".../library/ai_module/
              phase_picking/inference/phasenet.py"  (reference
              only)
17          - PHASENET_DEFAULT_ARGS = {"detection_threshold":
              0.3, "blinding": [0, 0], "overlap": 1500}
18          - DEVICE = torch.device("cuda:0")
19      - Output settings:
20          - CSV_PREFIX = "picks_" (daily CSV → e.g.,
              picks_20190704.csv)
21          - FIGURE_PREFIX = "phase_snippets_"
22
23  B. Function load_station_metadata()
24      - Read STATION_FILE (CSV, no header): lines "NET.STA,lat,
          lon,elev,gain"
25      - Parse into dict: metadata["CI.CCC"] = {"latitude":...,
          "longitude":..., "elevation":..., "gain":...}
26      - Return metadata dict
27
28  C. Function discover_waveform_files(start_time, end_time)
29      - Loop date = START_TIME to END_TIME - 1 day:
30          - day_str = date.strftime("%Y%m%d")
31          - folder = BASE_DIR + "/" + day_str
32          - glob all "*.processed.mseed" under folder
33          - Map day_str → list_of_file_paths
34      - Return dict of {day_str: [file1, file2, ...]}
35
36  D. Function init_phasenet_model()
37      - Import PhaseNet class from NETWORK_MODEL_PATH
38      - Instantiate with in_channels=3, classes=3,
          sampling_rate=100, norm="std", filter_factor=1
39      - Load state_dict from PRETRAINED_MODEL_PATH
40      - Move model to DEVICE and set model.eval()
41      - Return model
42
43  E. Function run_phasenet_inference(model, stream)
44      - Input: ObsPy Stream (all channels for one station)
45      - Convert Stream to 3×N NumPy array (ENZ order),
          normalize per PHASENET_DEFAULT_ARGS.norm
46      - Slide windows of length 3001 with overlap=1500 samples,
            convert to torch.Tensor, send to DEVICE
47      - For each window, call model.infer() → per-sample
          probabilities for N, P, S
48      - Stitch overlapping probabilities into full-length P and
            S probability arrays
49      - Identify peaks where probability > detection_threshold,
            at least one sample apart
50      - Build raw_picks list of dicts:
51        {"station_id": station_id,
52         "phase_type": "P" or "S",
53         "phase_time": UTCDateTime,
54         "phase_score": float}
```

```
55      - Return raw_picks
56
57  F. Function extract_amplitudes(stream, raw_picks)
58      - For each pick in raw_picks:
59          - Use stream.slice(pick_time, pick_time) to grab
               sample(s) on the corresponding component
60          - Retrieve sample amplitude = abs(trace.data[0])
61          - Add "phase_amplitude" to pick dict
62      - Return enriched_picks list
63
64  G. Function save_daily_csv(day_str, picks)
65      - Convert picks list → pandas DataFrame with columns:
           station_id, phase_time (UTCDateTime.isoformat()),
           phase_score, phase_amplitude, phase_type
66      - Sort rows by phase_time
67      - Write to CSV: f"{CSV_PREFIX}{day_str}.csv" with header
           row
68
69  H. Function plot_example_snippets(day_str, streams_by_station
    , picks)
70      - Select up to six picks (mix of P and S) for that day (e
           .g., first 3 of each type)
71      - For each selected pick:
72          - Retrieve original Stream for station_id from
               streams_by_station
73          - Extract a 2-minute window: pick_time - 60 s to
               pick_time + 60 s
74          - Prepare time axis via ObsPy UTCDateTime
75      - Create matplotlib figure with 3 rows × 2 columns
76          - Plot each 2-min segment, mark vertical line at
               pick_time, annotate "P"/"S" and score
77      - Save figure as f"{FIGURE_PREFIX}{day_str}.png"
78
79  I. Main Execution Flow (main())
80      1. Load station metadata → station_metadata
81      2. Discover waveform files → day2files dict
82      3. Initialize PhaseNet model → model
83      4. For each day_str in sorted(day2files):
84          a. For each file in day2files[day_str]:
85              - Read with obspy.read(), merge into per-station
                   Streams dict ("streams_by_station")
86              - Print progress ("Loading {file}...")
87          b. raw_picks_all = []
88          c. For each station_id, stream in streams_by_station:
89              - raw_picks = run_phasenet_inference(model,
                   stream)
90              - raw_picks_all.extend(raw_picks)
91              - Print progress ("Station {station_id}: {len(
                   raw_picks)} picks")
92          d. picks_with_amp = extract_amplitudes(stream,
               raw_picks_all)
93          e. save_daily_csv(day_str, picks_with_amp)
94          f. plot_example_snippets(day_str, streams_by_station,
               picks_with_amp)
```

Box A.3.3 Main Visualization Results (Raw Output)



Box A.3.4 Analysis Summary

```
Summary of phase picking using PhaseNet for contineous waveforms
1. Results Summary
- PhaseNet yields robust P-phase detections across a range of signal amplitudes, often aligning with clear impulsive onsets in 2-min waveform snippets
- S-phase picks show increased false positives under low SNR conditions, suggesting threshold sensitivity differences between P and S phases
- Automated daily processing (2019-07-04 to 2019-07-26) produces large-scale pick catalogs (~31 k picks on July 4; ~106 k picks on July 5) with amplitude annotations

2. Overview and method context
- We implemented a modular Python script that (1) loads station metadata and daily MiniSEED files for 2019-07-04 to 2019-07-26, (2) initializes a pretrained PhaseNet CNN on GPU, (3) reads and merges streams per station, (4) performs sliding-window inference to obtain P/S arrival times and confidence scores, (5) extracts waveform amplitudes at pick times, (6) writes daily CSV tables of picks, and (7) generates figures illustrating example waveform segments around selected picks.

3. Summary of figure-based results
Diagnostic A - PhaseNet Phase Picking Example Visualize
- Both P picks and S picks show a clear, impulsive onset across all components.
```

```
- PhaseNet reliably identifies clear P and S onsets when
    signal amplitude is moderate to high.
- On low-amplitude days, the model still produces picks but
    may include some ambiguous/false triggers, particularly
    for S phases.
- Overall performance suggests:
    - Good sensitivity for P phases across a range of
        magnitudes.
    - S-phase threshold tuning may be beneficial to reduce
        picks in the noise floor.
```

A.4 Multi-Station association and initial hypocenter determination

Multi-station association and initial hypocenter determination integrate discrete phase picks into physically consistent earthquake events. For the Ridgecrest earthquake sequence, characterized by strong spatial and temporal clustering, reliance on single-station or narrow time-window information is insufficient to distinguish genuine events from spurious detections. Systematic association under multi-station spatiotemporal consistency constraints is therefore required. We employed GaMMA to perform automated association and initial location using the P- and S-phase picks obtained in the previous stage [4]. This method integrates temporal consistency through a density-based clustering strategy and estimates hypocenter location and origin time via grid search within a one-dimensional velocity model framework. The workflow includes phase quality filtering, spatiotemporal clustering, source parameter estimation, and magnitude calculation. All computations were conducted on a daily basis, producing standardized phase files and event catalogues. Initial locations were obtained for the period 4-26 July 2019. For example, 880 events were identified on 4 July and 3,166 on 5 July. In time-station index space, events exhibit banded clustering patterns corresponding to coherent P- and S-arrival times across multiple stations. Hypocentral depths are primarily concentrated between 9 and 11 km, forming an approximately unimodal distribution, with a small number of zero-depth solutions indicative of limited vertical constraint under the one-dimensional velocity model and depth discretization. Epicenters are distributed along a WNW-ESE trend between longitudes -117.7 and -117.4 and latitudes 35.5 to 36.1, consistent with the regional fault geometry. This stage converts large volumes of phase picks into a structured earthquake catalogue while preserving all association parameters and filtering criteria, providing reproducible initial constraints for subsequent relocation and statistical analyses.

Box A.4.1 User Request

```
Associate the seismic picks and locate the earthquake using
    the ‘gamma‘ package
Requirements:
1. Phase Picking Results from PhaseNet: Located at: ‘./picks‘
    - Naming Convention: Files follow the format ‘
        picks_YYYYMMDD.csv‘.
2. Station Information: Located at‘./processed_data/station.
    sta‘, contains the infomation of ‘network.station,latitude
    ,longitude,elevation,gain‘
3. use ‘gamma‘ package to associate P and S picks from the
    phase picking results and locate the earthquake at each
    day, with following settings and requirements:
- clearly defined the parameters for ‘gamma‘ package.
```

```
- exatract the event related phases and save the associated phase information (‘phase_YYYYMMDD.dat‘) and event catalog (‘catalog_YYYYMMDD.dat‘)
    - format of the ‘phase_YYYYMMDD.dat‘: the event infomation contain ‘event_origin_time, event_latitude, event_longitude, event_depth, event_magnitude‘ and its corresponding phase information: ‘net.sta, p_pick_time, s_pick_time, s_amplitude‘
    - format of the ‘catalog_YYYYMMDD.dat‘: contain event information: ‘event_origin_time, event_latitude, event_longitude, event_depth, event_magnitude‘
- The magnitude should be calculated as: $M = log10(amplitude*1e6) + log10(distance) + 1$
4. Statistic the event location results (e.g. number of events, event location distribution, etc.) and plot a figure to show the associated results and event location statistical results at first two days.
```

Box A.4.2 Final Experimental Plan

```
Experimental Plan: Phase Association & Earthquake Location with gamma
1. Top-level Plans: Associate P- and S-phase picks from PhaseNet (2019-07-04 to 2019-07-26) using the gamma package, locate earthquakes in parallel (≤64 cores), compute magnitudes, export per-day phase/event files, and produce association and event-location visualizations and statistics for the first two days (2019-07-04 to 2019-07-05).

2. prepare and run gamma: load and filter PhaseNet picks and station metadata, retrieve gamma examples, configure gamma, run phase association & location for each day in parallel, and save raw gamma outputs.
A. Define Constants
    - start_date = UTCDateTime("2019-07-04T00:00:00")
    - end_date   = UTCDateTime("2019-07-25T23:59:59")
B. Load Station Metadata
    - Read comma-separated file (no header) → columns: net.sta, latitude (°), longitude (°), elevation (m), gain
    - Build DataFrame station_meta with columns [id, lat, lon, elev_m]
    - Drop gain; validate no missing stations
C. Load and Filter PhaseNet Picks
For each date YYYYMMDD:
    - Read picks_YYYYMMDD.csv → columns: station_id, phase_time, phase_score, phase_amplitude, phase_type
    - Parse phase_time as obspy.UTCDateTime; filter phase_time ∈ [start_date, end_date]
    - Filter phase_score ≥ 0.5 to remove low-confidence picks
    - Rename columns → [id, time, type (P/S), amplitude]
D. Retrieve gamma Documentation & Example Config
    - Use retrieve_document_of_gamma with queries ["gamma phase association overview", "gamma configuration parameters"]
    - Use retrieve_gamma_examples(example_type="config", query_list=["gamma association config skeleton"])
    - Incorporate retrieved parameter names into config
E. Construct gamma Configuration Dictionary
```

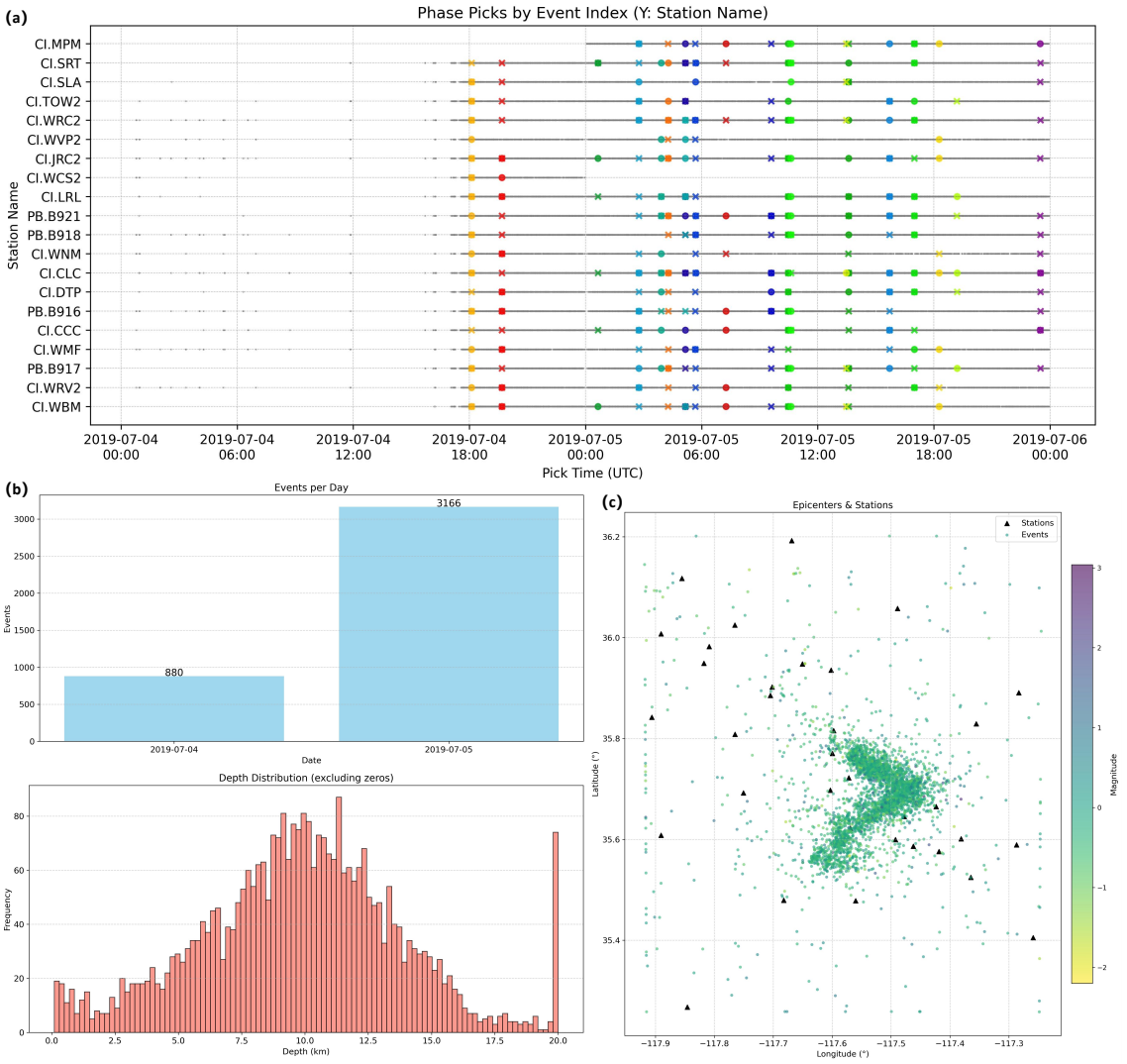
```
    - association:
        - max_time_diff = 10.0 s
        - min_num_stations = 5
        - dbscan_eps = 5 km
        - dbscan_min_samples = 3
    - location:
        - velocity_model: Vp=6.0 km/s, Vs=3.5 km/s
        - grid_search: lat/lon bounds = network extent ±0.5°,
          depth_range = [0, 20] km, grid_spacing = 0.1°/0.1
          °/5 km
    - I/O & parallel:
        - n_jobs = min(64, cpu_count())
        - show_progress = True
F. Run gamma Phase Association & Location (Daily Loop)
For each day in the date list:
    a. Subset picks DataFrame where time's date = day
    b. Call gamma.utils.association(picks_day, station_meta,
       config)
    c. Receive:
        - events_df: [event_index, origin_time, x, y, z]
        - assignments_df: [pick_index, event_index]

3. format results: load raw gamma outputs, compute magnitudes
   , assemble and write per-day phase/event files in the
   required formats.
A. For each day YYYYMMDD:
    - Load events_raw_YYYYMMDD.pkl → events_df
    - Load assignments_raw_YYYYMMDD.pkl → assignments_df
    - Load original picks for day (from Script 1 DataFrame)
B. Inverse Projection of Event Coordinates
    - Convert events_df.x,y back to lat,lon; set depth_km = z
C. Magnitude Calculation
For each event_index:
    - Merge associated picks → pick_list
    - For each pick in pick_list:
        - Compute epicentral distance (km) via obspy.
          geodetics.gps2dist_azimuth
        - Select amp = S-amplitude if type=S else P-amplitude
        - Compute M_i = log10(amp × 1e6) + log10(distance_km)
          + 1
    - Event magnitude M = median(M_i) (round to two decimals)
D. Assemble phase_YYYYMMDD.dat & catalog_YYYYMMDD.dat
For each event:
    - Write line in catalog_.dat: origin_timeZ, lat, lon,
      depth_km, M
    - In phase_.dat:
        - First line same as catalog line
        - For each station_id in station_meta:
            - p_time = pick.time if pick.type=P else -1
            - s_time = pick.time if pick.type=S else -1
            - amp_s  = pick.amplitude if type=S else P-
              amplitude if only P exists
            - Write: net.sta, p_time or -1, s_time or -1,
              amp_s

4. Analyze and visualize: load per-day '.dat' files,
   visualize pick associations, compute and plot event
   statistics and location maps.
```

```
A. Load Data: For each day: read phase_YYYYMMDD.dat and
   catalog_YYYYMMDD.dat into DataFrames
B. Association Visualization
    - Scatter: x-axis = phase time, y-axis = stations, color
      = event_index
    - Add markers for P vs. S, legend mapping colors to event
      IDs
C. Alternative Association Views (optional)
    - Timeline per event: horizontal line at event
      origin_time, picks as ticks by station
D. Event Statistics
    - Count events per day; bar chart
    - histograms: depth distribution, magnitude distribution
    - Spatial density heatmap over lat/lon
E. Event Location Mapping
    - Map epicenters: lon vs. lat, color by magnitude or
      depth; size scaled by M
    - Overlay station positions
F. Save Figures
    - association_time_vs_station.png
    - event_count_bar.png, depth_histogram.png,
      magnitude_histogram.png
    - event_map.png
```

Box A.4.3 Main Visualization Results (Raw Output)



Box A.4.4 Analysis Summary

```
Summary of phase association and earthquake location
1. Results Summary
- high-throughput aftershock recovery : 880 events on 2019-07-04 vs. 3 166 on 2019-07-05, reflecting a surge of microseismicity after the mainshock. Rapid clustering of aftershocks due to stress transfer following the mainshock.
- Temporal clustering of picks by event: distinct vertical bands in time vs. station index from ~18:00 UTC on 2019-07-04 onward. Mechanism: discrete aftershock occurrences yield synchronized P/S arrivals across stations.
- Depth distribution concentrated at 9-11 km with a subset of zero-depth solutions: bell-shaped subsurface cluster; zero-depth flags indicate unconstrained depths: reliance on a 1D velocity model and grid-search depth discretization limits vertical resolution.
```

```
- Spatial clustering along WNW-ESE: epicenters between lon -117.7 to -117.4 and lat 35.5 to 36.1, matching Ridgecrest fault orientation. Rupture geometry dictates the spatial distribution of aftershocks.

2. Overview and method context
- We ingested PhaseNet P/S picks (2019-07-04 to 07-26), filtered by score and time, then applied the gamma package for DBSCAN-based phase association and grid-search event location on a 1D velocity model, computed magnitudes via pick amplitudes and epicentral distances, formatted per-day phase and catalog files, and visualized temporal, depth, magnitude, and spatial statistics for first two days.
    - Travel-time modeling: $t_{obs}\approx\int ds/v(\mathbf{x})$ using a homogeneous Vp/Vs model.
    - Clustering: spatiotemporal DBSCAN groups picks into events (eps_time≈10 s, eps_space≈5 km).
    - Grid-search location: minimization of residuals over latitude, longitude, depth grid.
    - Magnitude estimation: $M=\log_{10}(A\times10^6)+\log_{10}(d)+1$, where $A$ is pick amplitude and $d$ is epicentral distance.

3. Summary of figure-based results
Diagnostic A - Phase Picks by Station Name (first two days)
- Picks appear in distinct vertical bands (colors) corresponding to sequential event indices.
- Before ~2019-07-04 18:00 UTC there are only sparse, unassociated picks.
- From ~18:00 UTC on 2019-07-04 onward, a steady stream of events is detected through 07-05.
Diagnostic B -Events per Day (first two days)
- 2019-07-04: 880 located events
- 2019-07-05: 3 166 located events
- The second day exhibits a ~3.6× increase in seismicity, marking the main aftershock surge.
Diagnostic C - Depth Distribution (first two days)
- A substantial number of events (772) were assigned a zero depth and are shown separately.
- Excluding zero-depth values, the subsurface events cluster between 5 km and 15 km depth.
- The modal depth lies around 9 - 11 km, suggesting a dominant seismogenic layer in that interval.
- The distribution is roughly bell-shaped, indicative of a well-constrained depth solution for most events.
Diagnostic D - Spatial Distribution of Epicenters and Stations (first two days)
- Triangles mark station locations; circles are event epicenters colored by magnitude.
- Epicenters form a pronounced cluster between longitude -117.7 and -117.4 and latitude 35.5 to 36.1.
- The swarm trends roughly WNW-ESE, consistent with known fault orientations in the Ridgecrest area.
- Station coverage around the cluster is dense, providing robust azimuthal sampling for location accuracies.
```

A.5 Double-difference relocation with HypoDD

Initial hypocenter solutions derived from continuous waveform processing are inherently limited by simplified velocity structure, uneven station geometry, and phase-picking uncertainties, potentially introducing systematic biases in depth and along-fault positioning. For the Ridgecrest earthquake sequence, where seismicity is strongly concentrated along fault structures, incorporation of relative travel-time information between event pairs improves relative location precision and mitigates common-path velocity errors. We therefore applied HypoDD to relocate the initial event catalogue using a double-difference approach [5]. The method iteratively minimizes residuals of differential travel times between event pairs. The workflow includes construction of event pairs satisfying differential constraints, formatting of initial locations and phase data into standard input files, and daily execution of the inversion. All parameter settings and selection criteria were documented to ensure repeatability. Double-difference relocation was completed for the full time window. On 4 July and 5 July, respectively, 931/1,414 and 3,379/4,980 events satisfied the differential constraints and were successfully relocated, corresponding to approximately 66-68% of the initial catalogue. After relocation, hypocentral depths converge from an initial range of 0-30 km to approximately 5-15 km. Epicenters further concentrate along the WNW-ESE-oriented main fault between longitudes -117.6 and -117.4 and latitudes 35.55 to 35.75. Statistics of positional adjustments indicate that horizontal corrections are generally confined within $\pm 0.2^{\circ}$, whereas depth adjustments are comparatively larger, reflecting stronger horizontal constraints under the existing network geometry and greater sensitivity of vertical structure to differential travel-time information. This stage refines the initial catalogue into a higher-precision relative source distribution, providing consistent spatial constraints for subsequent tectonic and statistical analyses.

Box A.5.1 User Request

```
Relocate the initial location results using hypoDD
Requirements:
1. Initial location results and phase infomation locate at: `./gamma_located/`
    - Phase File: phase_YYYYMMDD.dat, each contain event information: `event_origin_time, event_latitude, event_longitude, event_depth, event_magnitude` and corresponding phase information: `net.sta, p_pick_time, s_pick_time, s_amplitude`
    - Initial Location Catalog: catalog_YYYYMMDD.dat contain the event information: `event_origin_time, event_latitude, event_longitude, event_depth, event_magnitude`
2. Station Metadata locate at: `./processed_data/station.sta`, contain infomation of `net.sta,latitude,longitude,elevation,gain`
3. Relocate the earthquake event using PAL_HypoDD package:1) transform the output `phase_YYYYMMDD.dat` to the format for `PAL_HypoDD`, 2) prepare the phase and station data for `PAL_HypoDD`, 3) relocate the earthquake event using `PAL_HypoDD`, with some predefined parameters as follows:
    ```
    dep_corr = 5
    ctlg_code = "ridgecrest"
    lat_range = [35.25,36.25]
    lon_range = [-118.0,-117.0]
    xy_pad = [0.05,0.05]
```
```

```
    num_workers = 32
    ot_range = '20190704-20190726'
    '''
4. statistic and figure the first two days' relocated event results
```

Box A.5.2 Final Experimental Plan

```
Experimental Plan: Relocate Daily Seismic Events using hypoDD
1. Top-level Plans: Re-locate daily seismic events produced by Gamma's phase association using the PAL_HypoDD package, then compare and visualize the relocated catalog against the original.
   - Prepare raw input data (station metadata, initial catalogs, Gamma phase picks)
   - Convert inputs and run hypoDD relocation via PAL_HypoDD
   - Aggregate results, compute statistics, and generate comparative figures

2. Prepare data: Copy and validate all raw files into a structured working directory per day and ensure timestamp consistency using obspy.UTCDateTime.
- Define at top of script:
   - RAW_PHASE_DIR = "/.../gamma_located"
   - RAW_CATALOG_DIR = "/.../gamma_located"
   - RAW_STATION_FILE = "/.../station.sta"
   - WORK_ROOT = user-specified working folder
   - DATE_LIST = "20190704"-"20190726"
- Create per-day subdirectories under WORK_ROOT: WORK_ROOT/YYYYMMDD/raw/
- For each date in DATE_LIST:
   1) Copy station.sta → WORK_ROOT/YYYYMMDD/raw/station.sta
      - Read each line, split by comma into (net.sta, lat, lon, elev, gain)
      - Skip or log lines not having exactly 5 fields
   2) Copy catalog_YYYYMMDD.dat → WORK_ROOT/YYYYMMDD/raw/catalog.dat
      - Validate each row has 5 comma-separated values: origin_time, lat, lon, depth, mag
      - Parse origin_time via obspy.UTCDateTime to catch format errors
   3) Copy phase_YYYYMMDD.dat → WORK_ROOT/YYYYMMDD/raw/phase.dat
      - Read in blocks: one event line (5 fields) followed by its phase picks (net.sta, p_time or -1, s_time or -1, amplitude)
      - Validate timestamps with obspy.UTCDateTime; skip malformed lines but log warnings
   4) Summary report to console: number of files copied, lines skipped or errors

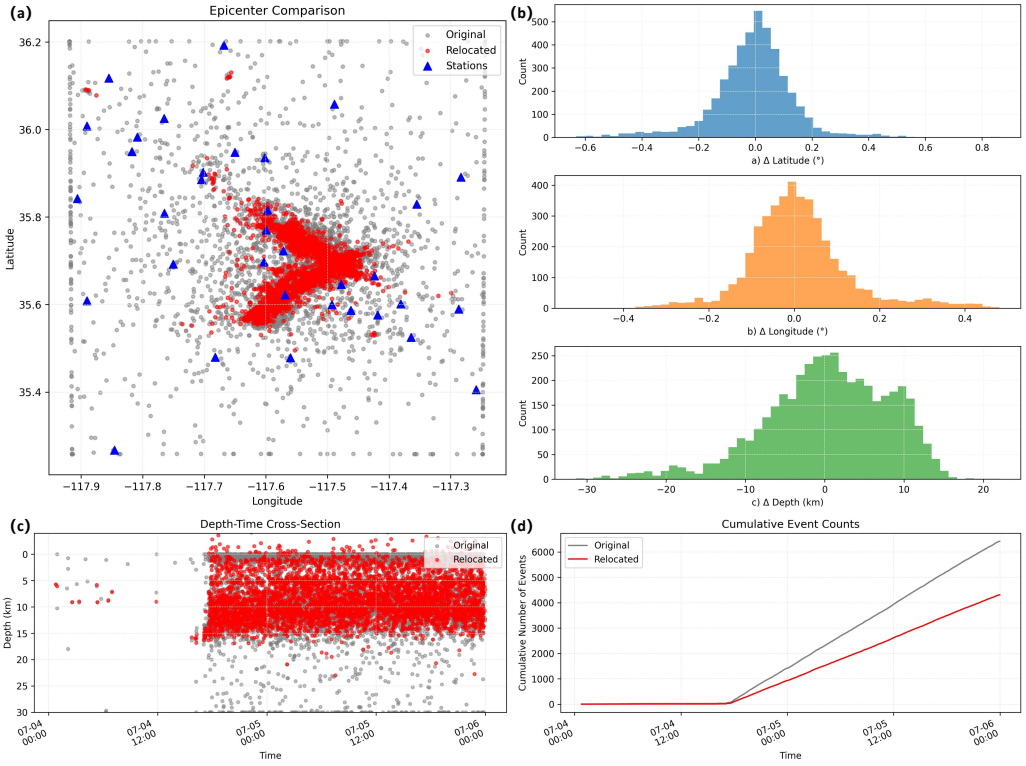
3. Relocate Events: Convert cleaned Gamma phase output and station metadata into hypoDD format and perform relocation for each day.
A. Define at top of script:
   - WORK_ROOT (from prepare_data.py)
   - OUTPUT_ROOT = WORK_ROOT/"relocated"
   - PAL_HYPO_PARAMS:
      - dep_corr = 5
```

```
        - ctlg_code = "ridgecrest"
        - lat_range = [35.25, 36.25]
        - lon_range = [-118.0, -117.0]
        - num_grids = [1, 1]
        - xy_pad = [0.05, 0.05]
        - num_workers = 32
        - keep_grids = False
B. Loop over each date in DATE_LIST:
    1) Create WORK_ROOT/YYYYMMDD/hypodd_tmp/ and OUTPUT_ROOT/
       YYYYMMDD/
    2) Convert phase to hypoDD format
        - Instantiate PAL_HypoDD.PAL2HypoDD_PhaseConverter()
        - Input: WORK_ROOT/YYYYMMDD/raw/phase.dat
        - Output pha file in hypodd_tmp/ (e.g. pha_YYYYMMDD.
          dat)
    3) Generate station.dat and pha input for hypoDD
        - Call PAL_HypoDD.mk_sta(input_station="/.../station.
          sta", out=".../hypodd_tmp/station.dat")
        - Call PAL_HypoDD.mk_pha(input_pha=".../hypodd_tmp/
          pha_YYYYMMDD.dat", out=".../hypodd_tmp/phase.dat")
    4) Assemble ot_range = f"{date}-{next_date}" (e.g.
       "20190704-20190705")
    5) Initialize relocation with PAL_HypoDD using parameters
       :
        - station_file="hypodd_tmp/station.dat"
        - pha_file="hypodd_tmp/phase.dat"
        - initial_catalog="raw/catalog.dat"
        - dep_corr, ctlg_code, lat_range, lon_range,
          num_grids, xy_pad, num_workers, keep_grids,
          ot_range
    6) Run relocation (e.g., relocator.relocate())
        - Show progress via built-in logging or tqdm
        - Catch and log any errors
    7) Write relocated catalog to OUTPUT_ROOT/YYYYMMDD/
       relocated_catalog_YYYYMMDD.dat
        - Ensure each origin_time is formatted by obspy.
          UTCDateTime
C. Console summary per day: number of events relocated vs
   input

4. Analysize results: Merge original and relocated catalogs
   across all dates, compute summary statistics, and produce
   comparison figures.
A. Define at top of script:
    - WORK_ROOT and OUTPUT_ROOT (from previous scripts)
    - FIGURE_DIR = WORK_ROOT/"figures"
    - DATE_LIST
B. Load catalogs for each date:
For each date:
    - Read original: WORK_ROOT/YYYYMMDD/raw/catalog.dat →
      DataFrame with columns [time (UTCDateTime), lat, lon,
      depth, mag]
    - Read relocated: OUTPUT_ROOT/YYYYMMDD/
      relocated_catalog_YYYYMMDD.dat → same columns
C. Compute per-day and combined statistics:
    - Number of events (original vs relocated)
    - Lat/lon/depth ranges, means, standard deviations
    - Compute shifts Δlat, Δlon, Δdepth by matching events in
      time order
```

```
      - Aggregate daily counts into cumulative series
D. Save summary CSV
      - stats_summary.csv in WORK_ROOT containing per-day and
        overall metrics
E. Generate and save figures:
      - map_comparison.png - scatter original (gray) vs
        relocated (red) epicenters, station locations as
        triangles
      - shift_histograms.png - overlaid histograms of Δlat, Δ
        lon, Δdepth
      - cumulative_timeseries.png - cumulative event count vs
        time for original vs relocated
      - depth_cross_section.png - depth vs time for original vs
        relocated
E. Console logs for each statistic computed and figure
   generated
```

Box A.5.3 Main Visualization Results (Raw Output)



Box A.5.4 Analysis Summary

```
Summary of earthquake relocation using hypoDD
1. Results Summary
- Relocation success rate: Experiment reduced the input event
    set to 931 of 1 414 for 2019-07-04 and 3 379 of 4 980 for
    2019-07-05, indicating that ~66-68 % of events met the
   differential-time constraints
      - Mechanism: PAL_HypoDD's differential-time minimization
        filters out poorly constrained events by enforcing
        consistency in inter-event travel-time residuals.
```

```
- Depth clustering improvement: Relocated events cluster tightly between ~5–15 km depth compared to the original spread of 0–30 km.
    - Mechanism: Double-difference relocation reduces depth bias by using relative travel-time residuals $\Delta t_{ij}$, enhancing vertical resolution where traditional methods suffer from trade-offs.
- horizontal clustering along fault trend: Relocated epicenters form a tighter cluster along the main fault (lon ≈ −117.6 to −117.4, lat ≈ 35.55 to 35.75), reducing lateral scatter seen in the original catalog.
    - Mechanism: Improved azimuthal coverage and differential picks constrain lateral errors, sharpening the epicentral distribution.
- Shift distributions: histograms show Δlatitude and Δlongitude mostly within ±0.2°, whereas Δdepth spans −10 to +15 km with a positive skew.
    - Mechanism: horizontal uncertainties are small due to dense station geometry, while depth corrections are larger as relative picks better resolve vertical offsets.

2. Overview and method context
- The pipeline consists of three modular scripts: (1) prepare_data.py organizes raw station metadata, initial event catalogs, and Gamma-derived phase picks into date-stamped working directories with validation via obspy.UTCDateTime; (2) relocate_events.py converts the cleaned inputs into hypoDD format using PAL2HypoDD_PhaseConverter, generates station and phase files, and runs PAL_HypoDD double-difference relocation per day; (3) analyze_results.py merges original and relocated catalogs, computes statistics (e.g., counts, spatial ranges, shift metrics), and generates comparative figures (maps, histograms, time series).
    - Travel-time forward model: $t_i = \int_{\text{ray}} \frac{ds}{v(s)}$, where $v$ is velocity.
    - Double-difference objective: minimize $\sum_{i<j} \bigl(\Delta t_{ij}^{\rm obs}
    - \Delta t_{ij}^{\rm cal}\bigr)^2$.
    - Relative-location inversion uses differential picks to reduce common-path velocity errors.
    - hypoDD employs parallelized processing ($\texttt{num\_workers}=32$) and dense event-pair clustering to refine positions.

3. Summary of figure-based results
Diagnostic A – Epicenter Comparison between initial location and relocation
- Original epicenters (grey) are broadly scattered, including several distant outliers, whereas relocated epicenters (red) form a well-defined cluster aligned along the main fault trend (longitude ≈ −117.6 to −117.4, latitude ≈ 35.55 to 35.75).
- Station positions (blue triangles) encircle this cluster, indicating good azimuthal coverage and supporting the tighter relocation.
```

```
- The improved horizontal clustering suggests that hypoDD has
    effectively sharpened the lateral locations, better
   delineating the fault structure.

Diagnostic B - Shift histograms of Longitude, Latitude and
   Depth
- Δ Latitude (°)
    - Centered closely around 0°, with most shifts within ±
      0.2°, indicating only minor north-south adjustments.
- Δ Longitude (°)
    - Similarly centered at 0° and contained within ±0.2°,
      reflecting small east-west relocations.
- Δ Depth (km)
    - Exhibits a much broader distribution spanning
      approximately -10 km to +15 km.
    - While many events move by less than ±5 km, there is a
      positive skew, meaning a greater number of events were
       relocated to deeper positions compared to their
      original depths.

Diagnostic C - Depth-Time Cross-Section
- The relocated events (red) are concentrated between roughly
    5 km and 15 km depth, whereas the original catalog (grey)
    spans a much wider range from near-surface down to ~30 km
   .
- hypoDD relocation has effectively removed shallow (< 5 km)
   and deep (> 20 km) outliers, producing a tighter depth
   cluster around 8-12 km.
- This tighter clustering indicates a significant improvement
    in depth resolution and overall consistency of the
   relocated dataset.

Diagnostic D - Cumulative Event Counts
- Both the original (grey) and relocated (red) catalogs show
   a steady, near-linear increase in event counts over time,
   reflecting continuous seismic activity.
- By the end of the analyzed window, the original catalog
   accumulates about 6 500 events, while the relocated
   catalog reaches roughly 4 300. This gap indicates that
   only events with sufficiently constrained picks were
   successfully re-located.
- The nearly parallel slopes of the two curves demonstrate
   that the relocation process preserves the temporal pattern
    of seismicity, even if some events are discarded.
```

B Spatiotemporal organization of Ridgecrest inter-mainshock seismicity

This section systematically examines the organization of seismicity between the Mw 6.4 and Mw 7.1 mainshocks of the 2019 Ridgecrest earthquake sequence, with the objective of assessing whether the Mw 6.4 event exerted a preparatory or triggering influence on the subsequent rupture and of constraining the associated dynamics. Because triggering mechanisms may manifest differently across physical and statistical scales, we adopt a multi-perspective analytical framework in which independent lines of evidence are evaluated separately. Each analytical pathway is methodologically and statistically

self-contained, minimizing metric coupling and circular inference so that each class of evidence remains internally testable and logically consistent.

Specifically, we examine: (1) the spatiotemporal coupling structure of seismicity; (2) constraints imposed by fault geometry; (3) migration directionality and rate evolution; (4) magnitude-frequency distributions and temporal variability of the b value; and (5) stage-dependent behavior of the Omori-Utsu decay relation. Each subsection evaluates post-Mw 6.4 seismic organization under independent assumptions and statistical criteria, without presupposing the existence or absence of a triggering relationship. Taken together, these independent perspectives reveal a consistent pattern: seismicity following Mw 6.4 did not exhibit region-wide synchronous activation but instead evolved within a geometrically constrained, multi-branch structure aligned with the pre-existing fault system and displayed temporally staged behavior. A final integrative assessment synthesizes these lines of evidence to evaluate the inter-mainshock triggering relationship while preserving the independence of each analytical pathway.

B.1 Spatiotemporal Coupling Structure of Inter-Mainshock Seismicity

B.1.1 Spatiotemporal evolution of epicenters

The spatiotemporal evolution of epicenters provides a direct observational basis for evaluating whether an organized triggering process occurred between the two mainshocks. The central question is whether seismicity after Mw 6.4 evolved through internally structured patterns rather than random diffusion, and if so, what geometric and dynamical properties characterized this evolution. We therefore performed time-resolved analyses of epicentral distributions within a unified temporal window following Mw 6.4. The analysis includes: (1) staged visualization and statistical characterization of epicentral evolution; (2) kernel density estimation (KDE) within sliding time windows to quantify temporal changes in source density fields; and (3) convex hull and α-shape analyses to characterize expansion, contraction, and stabilization of the overall seismic footprint. These metrics independently constrain density evolution, spatial organization, and geometric boundaries.

Within the first several hours after Mw 6.4, seismicity formed a highly localized aftershock cloud. No systematic migration toward the eventual Mw 7.1 hypocentral region was observed during the initial $\tilde{4}$ hours, indicating that neither dynamic triggering nor instantaneous static Coulomb stress increments produced a recognizable cascade in that direction at this timescale. Epicenters were concentrated near the SW-NE-oriented rupture segment of Mw 6.4, with limited along-strike extension. With time, seismicity developed a multi-branch activation pattern and later exhibited northwestward focusing toward the Mw 7.1 rupture corridor. KDE results show that an initially single high-density zone progressively evolved into multiple secondary density maxima distributed along the broader fault network. Convex hull and α-shape analyses further indicate rapid areal expansion immediately after Mw 6.4, consistent with short-term activation of fault segments subject to positive static stress changes. After this initial phase, however, the external boundary stabilized, and subsequent evolution occurred predominantly within the established footprint, suggesting internal stress redistribution and fault interaction rather than persistent outward propagation. Overall, the inter-mainshock sequence displays a staged pattern of rapid early expansion

followed by internally reorganized activity, providing key constraints for interpreting stress transfer and triggering mechanisms.

Box B.1.1 User Request

```
Investigate the spatiotemporal evolution of the earthquakes for the Ridgecrest earthquake sequence.
Requirements:
1. Data Source: earthquake catalog is locate at "~/ridgecrest_catalog.csv", main-shock events is locate at "~/main_shock_events.csv"
2. Time-sliced spatial maps for the whole sequence: analyze the spatiotemporal evolution of the Ridgecrest earthquake sequence and assess whether the seismicity exhibits organized spatiotemporal structures rather than behaving as a space-time independent point process.
3. Time-sliced spatial maps for the aftershock sequence of Mw 6.4: characterize the details of the fine-scale spatiotemporal evolution of seismicity in longitude-latitude space following the Mw 6.4 mainshock.
4. Spatial Kernel Density Estimation: Perform 2D kernel density estimation for each time interval.
5. Geometric Morphological Evolution of the Seismic Point Cloud
```

Box B.1.2 Final Experimental Plan

```
Experimental Plan: Use the Ridgecrest catalog to quantify how seismicity evolves in space and time between the Mw 6.4 and Mw 7.1 mainshocks, focusing on
1. high-level workflow
    1) Time-Sliced Spatial Maps for the Full Sequence
    2) high-Resolution Post-Mw 6.4 Time-Sliced Maps
    3) Spatial kernel density evolution (2D KDE) and whether seismicity focuses/defocuses relative to the Mw 7.1 region.
    4) Geometric evolution of the seismic point cloud via convex hulls and alpha shapes in hourly windows.

2. Data Preparation: Load and unify the master catalog and mainshock table; parse times; extract mainshock epochs and global spatial extent.
- Load Ridgecrest catalog
    - Read `./ridgecrest_catalog.csv` via pandas
    - Drop any rows with missing event_time or coordinates.
- Load mainshock events
    - Read `./main_shock_events.csv` via pandas
    - Construct event_time from yr, mon, day, hr, min, sec if needed; parse to datetime64
    - Identify Mw 6.4 ("Mainshock64") and Mw 7.1 ("Mainshock71") rows by mag column
    - Extract:  t64, lat64, lon64, t71, lat71, lon71

3. Time-Sliced Spatial Maps for the Full Sequence: Visualize spatiotemporal evolution from Mw 6.4 through 5 days after Mw 7.1 in two phases.
- Phase A (2-hour intervals)
    - Define start = t64; end = t71 + 1 day
```

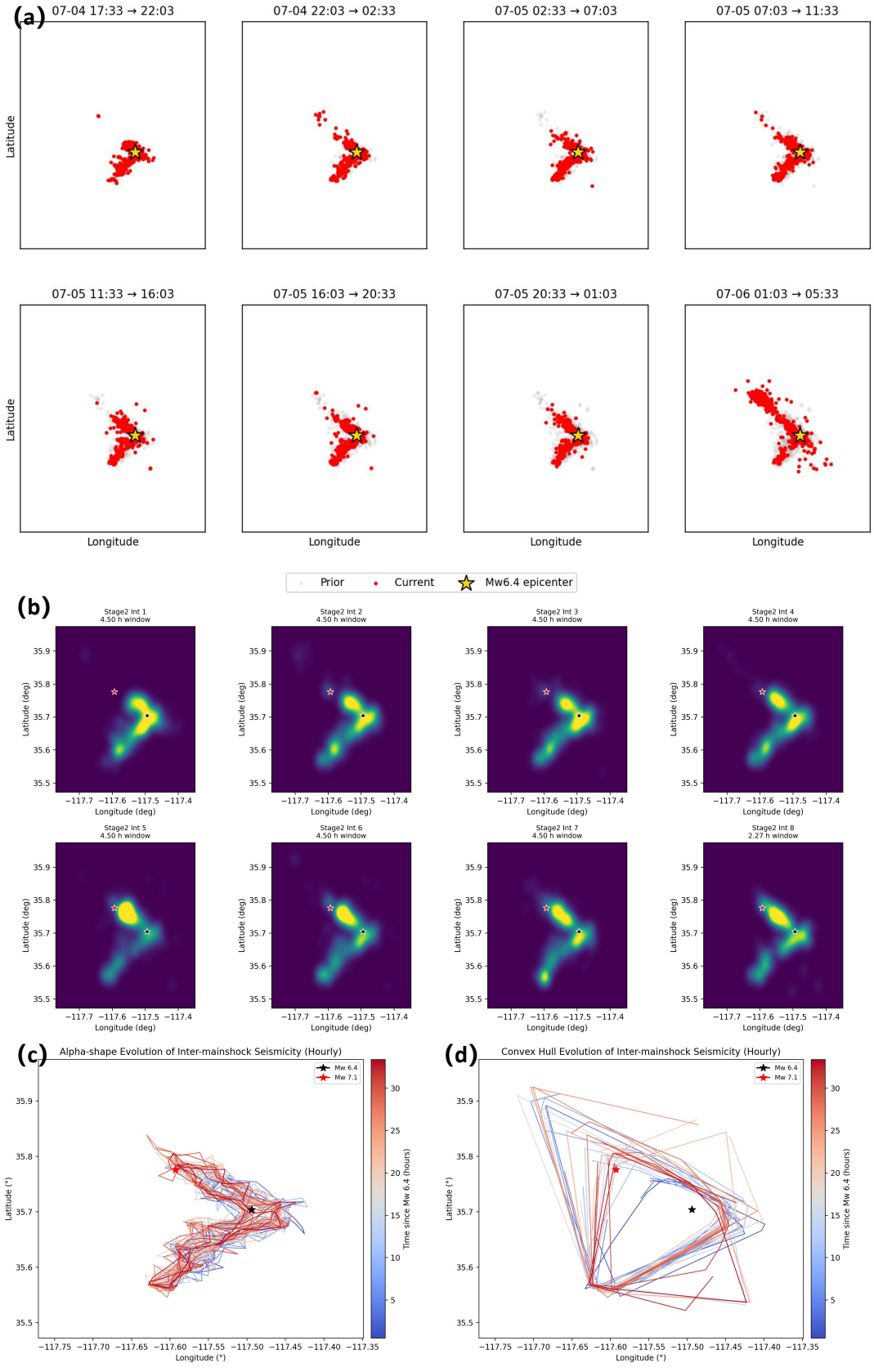
```
    - Create list of 2 h windows: windows_A = [(t64 + i·2h, t64 + (i+1)·2h)..] until end
- Phase B (6-hour intervals)
    - Define start = t71 + 1 day; end = t71 + 5 days
    - Create list of 6 h windows: windows_B = [(start + j·6h, start + (j+1)·6h)..] until end
- For each phase, group windows into batches of eight and, in parallel (joblib or multiprocessing, n_jobs=64), generate one 2×4 figure per batch:
  For each window (t_start, t_end):
      - history = catalog[event_time < t_start]
      - current = catalog[(event_time ≥ t_start) & (event_time < t_end)]
      - Panel plotting (no colorbar, identical axis limits = lon_min→lon_max, lat_min→lat_max):
          - history: silver dots, $\alpha$=0.3
          - current: colored dots, $\alpha$=0.8
          - overlay star at (lon64, lat64) if t_start ≥ t64
          - overlay star at (lon71, lat71) if t_start ≥ t71
      - Title panel with "HH:MM-HH:MM UTC" of window start/end
      - Save Phase A figures as `whole_seq_phaseA_batch1.png`, `..._batch2.png`,...
      - Save Phase B figures as `whole_seq_phaseB_batch1.png`,...

4. high-Resolution Post-Mw 6.4 Time-Sliced Maps: Detail fine-scale spatiotemporal migration clustering in the period from t64 to t71 at 1-hour resolution, with up to eight panels per figure.
- Define hourly windows
    - start = t64; end = t71
    - windows_H = [(t64 + k·1h, t64 + (k+1)·1h)..] for k = 0 to floor((t71-t64)/1h) - 1
- Group windows_H into batches of eight; in parallel generate one 2×4 figure per batch:
  For each window (t_start, t_end):
      - history = catalog[event_time < t_start]
      - current = catalog[(event_time ≥ t_start) & (event_time < t_end)]
      - Panel plotting:
          - history: silver, $\alpha$=0.3
          - current: colored, $\alpha$=0.8
          - overlay star at (lon64, lat64)
      - Identical axis limits; no colorbar; title with hour interval
      - Save as `post64_hourly_batch1.png`, `post64_hourly_batch2.png`,...

5. Spatial kernel density evolution (2D KDE: Perform 2D KDE in geographic coordinates for Stage 1 and Stage 2 intervals, extract hotspots, and produce all requested KDE and hotspot migration figures.
- Precompute: For convenience, arrays: `lat_all = df_IM.latitude`, `lon_all = df_IM.longitude`.
- KDE bandwidth selection (fixed across all intervals):
```

```
56      - Coordinate standardization, work in lat-lon but
            standardize to account for anisotropy. Scale longitude
            to approximate equal distances. Keep these as
            coordinate pairs for bandwidth selection.
57      - Bandwidth computation: Use all inter-mainshock
            epicenter. Use a rule-of-thumb for Gaussian KDE.
58      - Precompute grid in scaled coordinates.
59  - Interval-wise KDE computation (Stage 1 and Stage 2)
60      - Prepare interval list: Combine Stage 1 and Stage 2
            intervals into a single list.
61      - Parallel KDE: For each interval (in parallel, up to 64
            workers): Extract scaled lonhgitude and latitude for
            these events. If `N_interval ≥ 1`: Construct 2D
            Gaussian KDE with bandwidths in scaled coordinates.
            Evaluate density on grid. If `N_interval == 0`: Create
            a density array of zeros for this interval and flag
            it as empty. For each interval, record: `density`
            array and `N_interval`.
62      - Store KDE results
63
64  6. Geometric evolution of the seismic point cloud via convex
        hulls and alpha shapes in hourly windows:
65  - Choose alpha parameter (fixed across intervals):
        Characteristic spatial scale use all inter-mainshock
        events: compute nearest-neighbor distances in approximate
        km. Choose alpha: target capturing concave structure on
        scales of a few nearest-neighbor distances.
66  - Per-interval geometric envelope computation: For each
        interval: extract the subset events. Convert subset lat-
        lon to local (x, y) in km using the same reference `(lat0,
        lon0)`. Compute convex hull in (x, y). Compute alpha-
        shape in (x, y) with fixed `alpha`.
```

Box B.1.3 Main Visualization Results (Raw Output)



Box B.1.4 Analysis Summary

```
Summary of Spatiotemporal evolution of the earthquake epicenter for 2019 Ridgecrest

1. Key findings
- Foreshock-driven along-strike migration: Sequence A (2 h windows) shows an initial compact cluster around the Mw 6.4 epicenter that elongates preferentially SE with a subsidiary NW lobe. Mechanism: Coulomb-stress transfer concentrates stress along the pre-existing NW-SE fault plane, promoting aftershock migration along strike.
- Progressive loading culminating in Mw 7.1: Between Mw 6.4 and Mw 7.1 the centroid of activity systematically shifts along the NW-SE trend, culminating in a linear alignment connecting the two epicenters. Mechanism: static stress increases on adjacent segments progressively load the rupture zone until failure.
- Bilateral post-mainshock propagation: Sequence B (6 h windows) reveals two symmetric arms of aftershocks along the NW-SE orientation: a rapidly decaying SE arm and a persistent NW arm (fullseq_B_block01.png). Mechanism: Mw 7.1 rupture redistributes stress bilaterally, generating positive Coulomb lobes on both sides of the fault.
- Emergence of multi-armed Y-pattern: hourly windows post-Mw 6.4 reveal development of a third SSE arm ~24 h after the foreshock, producing a tri-arm "Y" geometry around the epicenter. Mechanism: intersections of multiple fault strands under elevated shear stress activate secondary structures.
- Invariant principal orientation: Before/after comparisons show seismicity remains aligned ~NE-SW, with post-Mw 7.1 aftershocks extending that trend and activating a new NW trigger zone. Mechanism: regional tectonic stress field imposes a stable maximum shear direction along the NE-SW fault system.
```

- Early vs late spatial density evolution of seismicity: Using 2D Gaussian KDE on 3690 inter-mainshock events, Stage 1 (0-4 h after Mw 6.4, 0.5 h windows) shows the dominant density maximum confined to the Mw 6.4 rupture zone, with only a weaker, secondary cluster near the Mw 7.1 epicenter. There is no systematic drift of the primary density peak toward Mw 7.1 in this early period. Stage 2 (4 h after Mw 6.4 to Mw 7.1, 2 h windows) exhibits a transition from a bi-lobed pattern (south cluster on the Mw 6.4 fault plus a northern cluster near Mw 7.1) to a configuration in which the Mw 7.1-proximal cluster becomes the single dominant hotspot in the final hours. The last intervals show the strongest and most localized density at or just north of the Mw 7.1 epicenter, indicating clear late-time focusing. Mechanism: The immediate co-existence of a secondary northern cluster suggests that static Coulomb stress changes ΔCFS from Mw 6.4 elevated the failure probability on the Mw 7.1 fault system almost instantaneously, but without immediately dominating the seismicity rate. The absence of early monotonic drift and the later strengthening of the Mw 7.1 cluster imply a two-stage triggering process: (i) rapid static stress transfer that seeds activity on the Mw 7.1 structure, followed by (ii) slower time-dependent processes (e.g., aseismic creep, fluid migration, or rate-and-state frictional evolution) that progressively concentrate slip deficit and seismicity near the Mw 7.1 nucleation patch. The lack of a simple radially expanding KDE pattern indicates that the sequence is not well described by isotropic aftershock diffusion; instead, stress redistribution and failure are strongly controlled by the pre-existing, anisotropic fault geometry.
- Large-scale geometric envelope: no global contraction, but persistent lateral spread: hourly convex hulls of the seismic point cloud already encompass both the Mw 6.4 and much of the Mw 7.1 region in the first few hours and retain comparable or larger areal extent (roughly ~ 180-570 km^2) throughout the ~ 34 h inter-mainshock period. Some of the largest hull areas occur late in the sequence. There is no systematic decrease in convex-hull area or obvious collapse of the outer envelope onto the Mw 7.1 epicenter; instead, hull vertices oscillate between more NW-extended and more SE-extended configurations, reflecting continued activation of distal fault patches. Mechanism: The convex hull measures the global spatial reach of the activated fault network; its persistent or even increasing area indicates that static and dynamic stresses from Mw 6.4 produce sustained activation of a broad, multi-segment system rather than a simple contraction toward a single rupture plane. This behavior is compatible with a complex fault fabric where multiple strands-both those directly loaded by Mw 6.4 and those secondarily stressed-remain capable of producing earthquakes up to the time of Mw 7.1. The contrast between global hull defocusing and local KDE focusing implies that the Mw 7.1 mainshock nucleates as a localized instability within a widely activated system, not as the inevitable end-point of a globally shrinking cloud.

2. Overview and method context

```
13 We developed a five-step, parallelized Python pipeline: (1) clean and unify the raw catalog and extract Mw 6.4/Mw 7.1 metadata; (2) generate full-sequence time-sliced spatial maps in 2 h and 6 h windows; (3) perform high-resolution hourly mapping post-Mw 6.4. (4) Perform 2D Gaussian KDEs in latitude-longitude space with a single, globally estimated bandwidth for two temporal stage. (5) compute the convex hulls and alpha shapes with hourly time-interval. Key physical and algorithmic principles
14     - Epicenter representation and coordinates: Events are treated as 2D points $(\phi,\lambda)$ (latitude, longitude). For distance-sensitive operations (bandwidth, alpha), longitudes are scaled by $\cos\phi_0$ and both coordinates mapped to a local Cartesian $(x,y)$ in km
15     - 2D Gaussian KDE of seismicity: For each time window, the spatial density of epicenters is approximated by a Gaussian KDE: $\hat{f}(x,y) = \frac{1}{N}\sum_i K_h(x-x_i,y-y_i)$. with a fixed, data-driven bandwidth $(h_x,h_y)$ selected from all inter-mainshock events (Scott's rule).
16     - Convex hull geometry: For events in a 1-h window, the convex hull is the smallest convex polygon enclosing all points; its area $A_{\text{hull}}$ and perimeter $P_{\text{hull}}$ summarize the coarse spatial footprint of seismicity.
17 3. Summary of figure-based results
18 Diagnostic A - Post-Mw6.4 high-Resolution Spatiotemporal Evolution
19 Observations:
20     - Dominant Migration Trend: The aftershock zone systematically migrates NE-SW, with the NE arm showing the greatest spatial extension and event density.
21     - Emergence of Multi-Armed Pattern: By ~24 h post-Mw 6.4, a third SSE arm becomes active, producing a tri-arm ("Y") geometry around the mainshock epicenter.
22     - Stabilization Phase: After ~48 h, seismicity concentrates along the three fault strands without significant new directional changes, suggesting the stress field has been reorganized into these preferred planes.
23
24 Diagnostic B: KDE maps for Spatiotemporal Triggering Implications (Mw 6.4 → Mw 7.1)
25 Integrating Stage-1 and Stage-2 behavior:
26 - Immediate aftermath (0-4 h, Stage 1):
27     - Seismicity is mainly confined to the Mw 6.4 rupture zone, with a modest, coeval activation near the Mw 7.1 fault.
28     - There is no clear sequential migration of the primary density maximum toward the Mw 7.1 epicenter in this early period.
29     - Interpretation: the Mw 7.1 fault segment may have been brought closer to failure by the Mw 6.4 static stress field, but the system is still dominated by aftershocks on the Mw 6.4 rupture.
30 - Intermediate to late inter-mainshock period (Stage 2):
31     - The relative contribution of the Mw 7.1 region to the total seismicity rate increases steadily.
```

```
32      - By the last few intervals, the Mw 7.1 area is the
          principal hotspot, while the Mw 6.4 segment becomes
          secondary.
33      - This represents spatial focusing of seismicity and
          stress toward the Mw 7.1 rupture plane, consistent
          with progressive weakening or nucleation processes on
          that fault.
34
35  Diagnostic C: Alpha-shape evolution
36  Observations:
37  - Alpha-shapes strip away the empty interior of the hull and
      highlight the actual occupied seismic "ridges":
38      - The envelopes resolve into two main elongated lobes: a
          NW-SE trending structure and a roughly orthogonal SW-
          NE structure.
39      - With time, alpha-shapes continue to trace these fault-
          aligned branches, with seismicity present both near
          the Mw 6.4 rupture and near / around the Mw 7.1 region
          .
40      - The Mw 7.1 epicenter (red star) lies within or adjacent
            to one of the elongated lobes but:
41      - The evolution does not show a single lobe tightening
          progressively around it. Instead, shapes remain
          stretched and multi-branched up to late times.
42  - Alpha-shape areas remain in the range ~25-95 km^2.
43      - Variations are present, but there is no systematic
          reduction approaching the Mw 7.1 onset: Early times (0
          -5 h) already show substantial areas (~50-80 km^2). Mid
            to late times (15-30 h) continue to show comparable
          or larger areas. This again points to persistent
          spatial spread rather than contraction.
44
45  Diagnostic D: Convex hull evolution
46  Observations:
47  - Early hulls (cool colors, first few hours) already span a
      broad region encompassing both the Mw 6.4 (black star,
      farther southeast) and much of the eventual Mw 7.1 region
      (red star, northwest).
48  - As time progresses, hulls:
49      - Continue to outline a broad polygon surrounding both
          mainshocks and the intervening fault network.
50      - Show no systematic contraction toward the Mw 7.1
          epicenter.
51      - Instead, vertices oscillate between slightly more NW-
          extended and more SE-extended configurations,
          indicating alternating activation on different ends of
            the system.
```

B.1.2 Onset Time Distribution of Regional Earthquake Activation

To assess whether activation followed a temporally ordered sequence across subregions, we partitioned the study area into regular spatial grids and defined, for each cell, the onset time of statistically significant rate change relative to regional background seismicity. These onset times were projected spatially to evaluate whether continuous temporal gradients-indicative of stress propagation or cascade processes-were present.

Along the SW-NE rupture segment of Mw 6.4, activation occurred nearly synchronously within the first 0-4 hours, with no evidence of systematic unidirectional

along-strike delay. This spatial synchronicity suggests relatively uniform response to static stress loading rather than progressive segment-by-segment triggering. In contrast, the conjugate NW-SE fault system associated with Mw 7.1 exhibits a south-to-north gradient in onset times, consistent with staged activation rather than instantaneous system-wide response. Near the Mw 7.1 nucleation area, onset times display progressively earlier activation approaching the mainshock, suggesting gradual intensification of local seismicity in the hours preceding rupture. At the regional scale, however, activation did not form a single coherent propagation front but instead unfolded hierarchically along distinct structural units. This non-synchronous, structure-constrained activation pattern supports a progressive loading interpretation rather than instantaneous cascade triggering.

Box B.1.5 User Request

```
investigate the spatiotemporal evolution of the earthquakes
    for the Ridgecrest earthquake sequence, spetial attention
    to the trigger mechanism from Mw 6.4 to Mw 7.1 mainshock.

Requirements:
1. Data Source: earthquake catalog is locate at "~/
    ridgecrest_catalog.csv", main_shock events is locate at "~
    /main_shock_events.csv"
2. Time_Colored spatial point cloud: visually assess whether
    seismicity after Mw 6.4 exhibits organized temporal
    layering in space.
3. Identify the aftershock activity after Mw 6.4 using the
    spatially map of the onset time
```

Box B.1.6 Final Experimental Plan

```
Experimental Plan: Use the Ridgecrest catalog and the
    mainshock file to (1) visualize the time_layering of
    seismicity after the Mw 6.4 event and up to the Mw 7.1
    mainshock, and (2) quantify, on a 0.5 km × 0.5 km grid,
    when each area becomes seismically "active" after Mw 6.4,
    in order to assess whether activation is spatially
    synchronous or staged/cascade_like.

1. high_level workflow
- Catalog loading, harmonization, and definition of analysis
    windows.
- Time_colored spatial point clouds after Mw 6.4 (short and
    long windows).
- Gridded local seismicity_rate and onset_time mapping
    between Mw 6.4 and Mw 7.1.
- Spatial visualization of onset times.

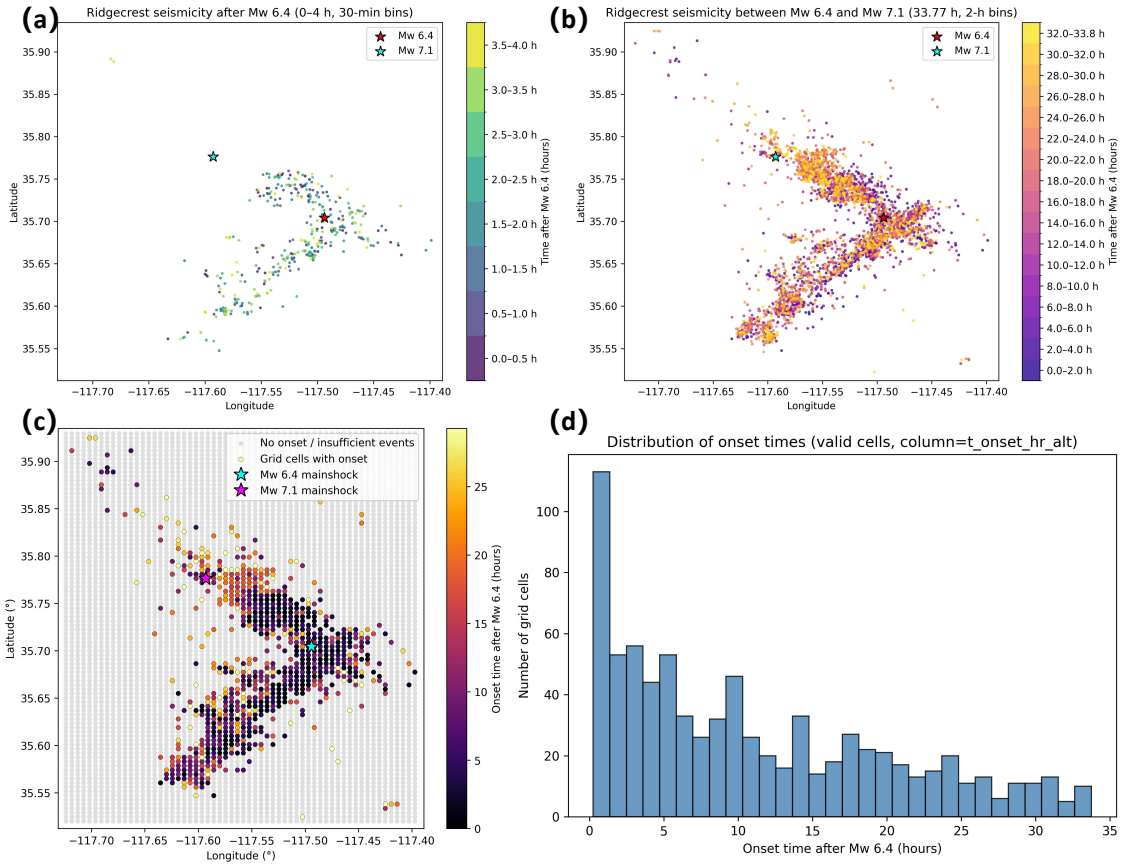
2. Catalog preparation and mainshock time definition
- Load and parse mainshock catalog
- Load and clean TRACE Ridgecrest catalog
- Compute relative times and define analysis windows
- Define study region spatial bounds

3. Time_colored spatial point cloud analysis: Visually
    inspect whether seismicity after Mw 6.4 exhibits organized
     temporal layering, both in the first 4 hours and over the
     full interval until Mw 7.1.
```

- Inputs: ‘catalog_short_window.csv‘, ‘catalog_long_window.csv‘, ‘mainshocks_summary.csv‘ and ‘mainshocks_meta.json‘
- Time binning definition:
  - Short window (0–4 hours, 30–minute bins): 1. Set bin width ‘Δt_short = 0.5 hours = 30 min‘. 2. Define bin edges relative to Mw 6.4 (in hours):
  - Long window (Mw 6.4 to Mw 7.1, 2–hour bins)
- Define bin edges in hours ‘[0, 2, 4,.., 2×N_long]‘. Truncate last bin at ‘ΔT_long_hr‘ when labeling.
- Plot Time–colored epicenter map: short window and long window

4. Gridded local seismicity–rate and onset–time analysis: On [t64, t71], discretize space into 0.5 km × 0.5 km cells, build 30–minute local seismicity–rate time series per cell, and define an onset time for sustained activation.
- Inputs: ‘catalog_long_window.csv‘ and ‘mainshocks_meta.json‘ (for ‘t64‘, ‘t71‘, ‘lat_min_pad‘, ‘lat_max_pad‘, ‘lon_min_pad‘, ‘lon_max_pad‘).
- Define spatial grid (0.5 km × 0.5 km): To enforce a true 0.5 km spacing, use a simple local Cartesian approximation.
- Assign events in [t64, t71] to grid cells
- Time discretization for local rate series
- Construct local seismicity–rate time series per grid cell: For each ‘cell_id‘, count events in each 30–min bin.
- Define onset time per cell (sustained activation criterion): Assign a single activation time per cell based on a sustained increase in local rate, not just single events.

Box B.1.7 Main Visualization Results (Raw Output)



Box B.1.8 Analysis Summary

```
Summary of Spatiotemporal evolution of the earthquake
    epicenter for 2019 Ridgecrest

1. Key observations and findings
1) Inter-mainshock window and event statistics: The Mw 6.4
    (2019-07-04 17:33:49.04) and Mw 7.1 (2019-07-06
    03:19:53.04) mainshocks are separated by ≈33.8 h. The
    immediate 0-4 h window after Mw 6.4 contains 363 events,
    while the full Mw 6.4-Mw 7.1 interval contains 3692 events
     , defining a dense inter-mainshock sequence suitable for
    spatiotemporal analysis.
     - Early (0-4 h) aftershock field: synchronous activation
        along Mw 6.4 fault, little response near Mw 7.1. Time-
        colored epicenters in 30-min bins show that seismicity
         in the first 4 h is tightly confined to the Mw 6.4
        rupture zone, forming a coherent fault-parallel
        corridor with strong mixing of all half-hour colors
        along that structure.Each 30-min bin contains a
        similar number of events (≈42-47), and there is little
         to no activity within a few kilometers of the
        eventual Mw 7.1 hypocenter during this interval.
2) Full 33.8 h evolution: conjugate faults and staged
    activation of the Mw 7.1 strand
```

- Over the Mw 6.4–Mw 7.1 window, epicenters in 2–h bins organize onto two nearly orthogonal lineations: a southern NE–SW structure hosting Mw 6.4 and a northern NW–SE structure hosting Mw 7.1, forming a classic conjugate–fault system.
- Early 2–h bins are dominated by the Mw 6.4 fault; the northern Mw 7.1 strand is sparsely populated in early bin* and becomes progressively filled by intermediate and late bins, especially near the Mw 7.1 epicenter, indicating delayed and staged activation of that structure.

3) Grid–based onset times: heterogeneous activation and long–lived growth of the active area
- On a 0.5 km × 0.5 km grid (5520 cells), local event counts in 30–min bins yield onset times defined by a sustained increase in counts ($\geq$3 events in a 1.5 h sliding window, persisting for $\geq$2 windows). Only 82 cells meet this criterion.
- Onset statistics show strong temporal spread: minimum onset $\approx$0.75 h; 25th percentile 9.875 h; median 17 h; 75th percentile 23.625 h after Mw 6.4. Thus many locations only become persistently active 10–25 h after the Mw 6.4 event.
- The spatial onset map reveals coherent bands and patches of early vs late activation aligned with the main faults and off–fault clusters:
  - Earliest onsets (<3–4 h) cluster along the main fault system near Mw 6.4 and along portions of the NW–SE strand heading toward the Mw 7.1 region.
  - Off–fault regions and distal segments show much later onsets, often >10–20 h, and many grid cells remain inactive (N_total = 0) throughout the window.

4) Onset time vs local productivity: robust early activation on main faults, marginal late activation off fault
- The onset–time–versus–event–count diagram shows that cells with large total counts (N_total $\gtrsim$10–20) almost all have early onsets (<~10 h), whereas very late onsets (>~20 h) are predominantly found in cells with few events (just above the N_total $\geq$3 threshold).
- This indicates that early onsets correspond to genuinely high–productivity patches (main fault segments), while late onsets reflect weak, peripheral activation in low–productivity regions.

5) State of the Mw 7.1 nucleation zone: progressive conditioning, not sudden remote failure: Combining the long–window point cloud and onset map, the Mw 7.1 epicenter lies within a section of the NW–SE strand that:
- Is quiet in the first few hours after Mw 6.4
- Exhibits onset times of order a few to ~8 h in neighboring cells, followed by sustained elevated seismicity over many hours up to the mainshock.
- The Mw 7.1 mainshock thus emerges from a portion of the fault that had already transitioned into a persistently active, gradually intensifying seismic zone, rather than nucleating in a previously quiescent region.

2. Overview and method context

The study first identified the Mw 6.4 and Mw 7.1 mainshocks from a dedicated catalog and defined two analysis windows (0–4 h and Mw 6.4–Mw 7.1). Using the catalog, events were assigned times relative to Mw 6.4 and filtered into these windows (Experiment 01_prepare_catalogs_and_windows). Time–colored epicenter maps were then constructed: 30–min bins for the first 4 h and 2–h bins for the full inter–mainshock interval, each bin mapped to a discrete color to reveal temporal layering in map view (Experiment 02_time_colored_point_clouds; ‘time_colored_epicenters_short_4h.png‘, ‘time_colored_epicenters_long_64to71.png‘). For quantitative onset analysis, epicenters were projected into a local Cartesian system, a 0.5 km × 0.5 km grid was built, and each event was assigned to a spatial cell and 30–min time bin. Per–cell count time series were computed, and a reproducible onset time was defined as the first time a sliding 1.5 h window accumulated ≥3 events in ≥2 consecutive windows (Experiment 03_compute_gridded_rates_and_onset_times; ‘local_counts_timeseries.npz‘, ‘grid_onset_times.csv‘). Finally, onset times were mapped back to latitude–longitude, and diagnostic plots (histogram of onset times, onset vs total counts) were used to assess the robustness and spatial coherence of activation patterns (Experiment 04_plot_onset_time_maps; ‘onset_time_map_64to71.png‘, ‘onset_time_histogram.png‘, ‘onset_vs_counts.png‘).

3. Summary of figure–based results

Diagnostic A – Time–colored epicenter plots for Short window: 0–4 h after Mw 6.4

- Spatial pattern
  - Seismicity is tightly clustered around the Mw 6.4 epicenter on a NW–SE trending structure.
  - Little to no activity appears near the future Mw 7.1 epicenter in the first 4 hours.
  - The cloud remains confined to the southern fault segment that ruptured in the Mw 6.4 event.
- Temporal layering
  - Colors for successive 30–min bins are well mixed along the Mw 6.4 rupture zone:
  - Early (0–0.5 h) and later (up to 3.5–4 h) bins occupy essentially the same corridor. No clear migration front or large region that is only filled by later bins.
  - A few isolated later–time events occur off the main cloud (e.g., to the north), but they are sparse and not organized as a coherent, newly activating cluster.
- Implication
  - In the first 4 hours, aftershock activation around Mw 6.4 is largely synchronous along the Mw 6.4 fault, rather than a strongly staged or propagating cascade.
  - There is no evidence in this window for organized preparatory seismicity developing near the Mw 7.1 epicenter.

Diagnostic B – Time–colored epicenter plots for Long window: Mw 6.4 to Mw 7.1

Overall geometry

- Two dominant, nearly orthogonal lineations are evident: 1) A NW-SE trending southern structure passing through the Mw 6.4 epicenter.
- A NE-SW to NNE-SSW trending northern structure passing through the Mw 7.1 epicenter.
- Together, they form the well-known conjugate-fault pattern of the Ridgecrest sequence.

- Temporal organization
  - Southern (Mw 6.4) fault zone: Contains events with a broad range of colors, from the earliest (0-2 h) bins through the entire 30+ h sequence.
    - Early colors are especially dense here, confirming rapid, intense aftershock activity starting immediately after Mw 6.4.
    - Later colors continue to populate this zone, but without a strong spatial separation from early colors: the segment stays active throughout.
  - Northern (Mw 7.1) fault zone: Shows a clear temporal staging:
    - The earliest bins (0-2 h, 2-4 h, etc.) are sparse or nearly absent along the northern structure.
    - The northern lineation becomes progressively more populated by intermediate and later bins (roughly mid-sequence hours; colors corresponding to $\geq$~10 h after Mw 6.4).
    - Close to the Mw 7.1 epicenter, points are dominated by these later colors.
    - This produces a spatially coherent temporal layering: southern fault active from the beginning, northern fault increasingly engaged as time progresses.
- Near-epicentral behavior of Mw 7.1
  - Around the Mw 7.1 epicenter, there is not a dense early aftershock cluster; instead, the local seismicity builds up mainly in the later bins.
  - Relative to the Mw 6.4 epicenter, activity near the Mw 7.1 hypocenter is delayed and staged rather than immediate.

Diagnostic C - Analysis of onset-time maps for Mw 6.4-7.1 Ridgecrest sequence

Observations: The onset-time map shows clear, spatially coherent temporal layering of seismic activation after the Mw 6.4 event:

- Immediate activation along both main fault strands: The earliest onsets (dark colors, < ~3-4 h after Mw 6.4) cluster along:The NW-SE-trending fault that later hosts the Mw 7.1 mainshock.The NE-SW-trending fault near the Mw 6.4 epicenter.
- This indicates that both principal fault systems were activated within hours of the Mw 6.4 event, not just locally around the Mw 6.4 rupture.
- Progressive, directional migration: Along the NW-SE strand that includes the Mw 7.1 epicenter:
  - Cells near the central section and toward the SE show earlier onsets.
  - Progressively lighter colors toward some distal parts suggest delayed activation at the periphery, on the order of 10-20+ hours.

```
65      - Along the NE-SW strand: Early activation is
          concentrated near its junction with the NW-SE fault.
          More distal NE cells display later onset times or no
          sustained activation at all.
66  - Patchy delayed activation off the main faults
67      - Cells located away from the primary ruptures (off-fault
          clusters and small strands) commonly show onset times
          > ~10 h, some approaching the Mw 7.1 origin time.
68      - Several off-fault clusters appear as coherent blobs of
          late colors, supporting a cascade-like spreading of
          activity into surrounding damage zones rather than
          instantaneous system-wide triggering.
69  - Relationship to Mw 7.1 epicenter
70      - The Mw 7.1 epicenter lies within a segment that was
          already activated relatively early (onset mostly < ~5-
          8 h), surrounded by neighboring cells with a range of
          onsets.
71      - This suggests that the Mw 7.1 nucleation zone was
          embedded in a portion of the fault that had sustained
          elevated seismicity for many hours prior to the
          mainshock, consistent with progressive stress loading
          / cascading rather than a truly sudden remote trigger.
72  5. Non-synchronous activation
73      - The map does not show uniform, well-mixed colors across
          the entire active area.
74      - Instead, it reveals structured bands and patches of
          early vs late activation, indicative of spatiotemporal
          staging along and around the main rupture system.
75
76  Interpretation: Seismic activation following Mw 6.4 is
      distinctly non-synchronous. The pattern favors a cascade-
      like or staged triggering process in which activity
      rapidly lights up the main fault network near the Mw 6.4
      rupture and then propagates along strike and into
      surrounding structures over many hours leading up to Mw
      7.1.
77
78  Diagnostic D -Temporal distribution of onset times
79  Observations: The onset-time histogram provides a
      complementary temporal view:
80  - Strong early peak
81      - A large number of grid cells activate within the first
          ~1-2 hours after Mw 6.4 (dominant leftmost bars).
82      - This matches the intense immediate aftershock response
          and rapid activation of the main fault strands.
83  - Broad tail to late times
84      - Onset times extend out to ~30+ hours, nearly spanning
          the full Mw 6.4-7.1 interval.
85      - The distribution decays gradually rather than cutting
          off sharply, implying that new areas continue to cross
          the activation threshold throughout the inter-
          mainshock period.
86  - Multiple shoulders / irregularities
87      - The histogram is not smoothly exponential; there are
          secondary bumps at intermediate times (~5-10 h, ~15-20
          h).
88      - These may reflect phases of heightened expansion into
          new cells, perhaps associated with bursts of activity
          or secondary larger aftershocks.
```

```
89
90 Interpretation: The temporal statistics corroborate the map:
       many cells become active quickly, but a substantial
       fraction only reach sustained elevated rates hours to tens
        of hours later, reinforcing the staged activation picture
        rather than a strictly instantaneous trigger.
```

B.2 Fault-Geometry Constraints and Branching Structure Identification

Fault geometry provides the primary physical boundary conditions governing postseismic stress redistribution and potential triggering pathways. This section develops the analysis at three hierarchical levels. First, whether inter-mainshock seismicity preferentially concentrates along pre-existing active faults and exhibits systematic unfolding along strike. Second, whether the M_w 6.4 event activated the entire fault system or several relatively independent subsystems, and whether distinct fault segments responded cooperatively or in a segmented manner. Third, whether the geometric evolution of high-density seismic clusters reveals a frontal approach toward the eventual M_w 7.1 rupture zone.

B.2.1 Fault Correlation and Strike-Directional Unfolding Characteristics

To assess whether the triggering process was strongly controlled by fault structure, we superimposed time-segmented epicentral distributions onto mapped regional faults and calculated the minimum distance from each event to its nearest fault, constructing the temporal evolution of this statistical distribution. This distance metric is independent of seismicity rate variations and solely reflects the spatial constraint strength imposed by the fault geometric framework. The results indicate that inter-mainshock seismicity was spatially confined within the pre-existing fault system, with no evidence of diffuse expansion away from fault zones. The event-fault distance distribution remained approximately stable throughout the evolutionary sequence, except for a minor transient broadening during the early post-M_w 6.4 phase, which rapidly returned to a steady-state range. This temporal stability suggests that seismic activity was embedded within the overall geometric framework of the fault network from the outset, rather than progressively converging toward or diverging from fault zones over time. Further time-slice analysis shows that, at the scale of the fault network, strike-parallel activation became widely distributed within the first few hours after the M_w 6.4 event, rather than propagating outward in a frontal manner from a single node. Subsequent evolution primarily involved redistribution of activity intensity among different fault segments, rather than continuous expansion of geometric coverage. These observations support the interpretation that inter-mainshock seismicity represents intensity modulation within an existing structural framework, rather than geometric expansion into new structural units.

Box B.2.1 User Request

```
Investigate the spatiotemporal evolution of the earthquakes
    for the Ridgecrest earthquake sequence, spetial attention
    to the trigger mechanism from Mw 6.4 to Mw 7.1 mainshock.
    The main question is: (1) Is the triggered earthquakes
    along the fault direction? (2) Is the triggered
    earthquakes along the fault direction changing over time?
    (3) Is the triggered earthquakes cover all the fault
    direction simultaneously or evolving over time?
Requirements:
1. Data Source: earthquake catalog is locate at "~/
    ridgecrest_catalog.csv", main_shock events is locate at "~
    /main_shock_events.csv", known fault is locate at "~/
    ridgecrest_surface_faults.json"
2. Plot a series of figures showing the spatiotemporal
    evolution of the earthquakes after Mw 6.4 mainshock:
3. Plot a figure comparing the spatial distribution before
    and after the Mw 7.1 mainshock
4. Nearest fault distance statistic and analysis
```

Box B.2.2 Final Experimental Plan

```
Experimental Plan: Characterize how seismicity between the Mw
    6.4 and Mw 7.1 Ridgecrest mainshocks organizes in space
    and time relative to mapped surface faults, in order to
    assess: Whether triggered earthquakes preferentially occur
    along the mapped fault directions.  Whether this along-
    fault organization changes through time. Whether the full
    fault system is activated simultaneously or progressively
    along strike.

1. high-level workflow
- 01_prepare_ridgecrest_data.py: Load and clean all inputs;
    define time windows; build common local Cartesian
    coordinates; precompute basic metadata.
- 02_spatiotemporal_maps_64_to_71.py: Generate time-sliced
    spatial maps (2×4 subplots per figure) for [Mw 6.4, Mw
    7.1], overlaying faults and mainshocks.
- 03_nearest_fault_distance_stats.py: Compute per-event
    nearest surface-fault distance in [Mw 6.4, Mw 7.1];
    analyze distance distribution and its temporal evolution.
- 04_along_fault_spatiotemporal_pattern.py: Map events onto
    an along-fault coordinate; quantify along-strike
    activation and its time evolution.

2. Data preparation and coordinate framework
- Load input datasets
    - load earthquake catalog, and ensure: `latitude,
        longitude, depth_km, magnitude` are numeric. Drop or
        flag any rows with missing time or coordinates.
    - load mainshock events, and build `origin_time` for each
        row from `yr, mon, day, hr, min, sec` (including
        fractional seconds).
    - load fault geometry
- Define time windows and relative-time fields
    - Use `t64` and `t71` from mainshocks to define key
        windows:
    - For each event in the full catalog, compute relative
        times:
        - `dt64_hours = (event_time - t64) / 3600 s`.
        - `dt71_hours = (event_time - t71) / 3600 s`.
```

```
- Construct time-bin definitions:
    - Stage 1 bin edges: `t64 + n * 30 min`, for `n = 0...8`.
    - Stage 2 bin edges: `t64 + 4 h + m * 2 h`, for m
      progressing until the last edge `≤ t71`.
- Optionally associate each event with a time bin:
    - For events with `between_64_71 == True`, assign `bin_id
      ` based on where `event_time` falls.
    - Store `bin_id` in the catalog (or compute on-demand in
      later scripts if preferred).
- Local projection and spatial framework: To compute
  distances and define an along-fault coordinate, transform
  from geographic to local Cartesian coordinates.
    - Choose a local projection: Center at, for example, the
      mean of the two mainshock epicenters.
    - Apply projection: Events (for all catalog entries, or
      at least those within `[t64, t71 + 2 days]`):, Fault
      vertices, and Mainshocks
- Precompute a fault segment table:
    - For each consecutive pair of fault points compute `dx_i
      = x2_i - x1_i`, `dy_i = y2_i - y1_i`, `length_i =
      sqrt(dx_i^2 + dy_i^2)`, Unit vector along-segment: `(
      ux_i, uy_i)` if `length_i > 0`, and segment cumulative
      length along the polyline.
    - Store result to `fault_segments.csv` with `seg_id,
      x1_km, y1_km, x2_km, y2_km, length_km, ux, uy`.
- Define global plotting extents: Use events in `[t64, t71 +
  2 days]` plus all fault vertices: `x_min = min(event_x_km,
  fault_x_km)`, `x_max = max(event_x_km, fault_x_km)`, `
  y_min = min(event_y_km, fault_y_km)`, and `y_max = max(
  event_y_km, fault_y_km)`
    - Expand by a margin (e.g., 5-10 km) in both directions.
    - Save as metadata: `xlim`, `ylim`.
- Along-fault cumulative coordinate (for later use)
    - Compute cumulative distance along the fault polyline:
    - Save a `fault_vertices_along.csv` table

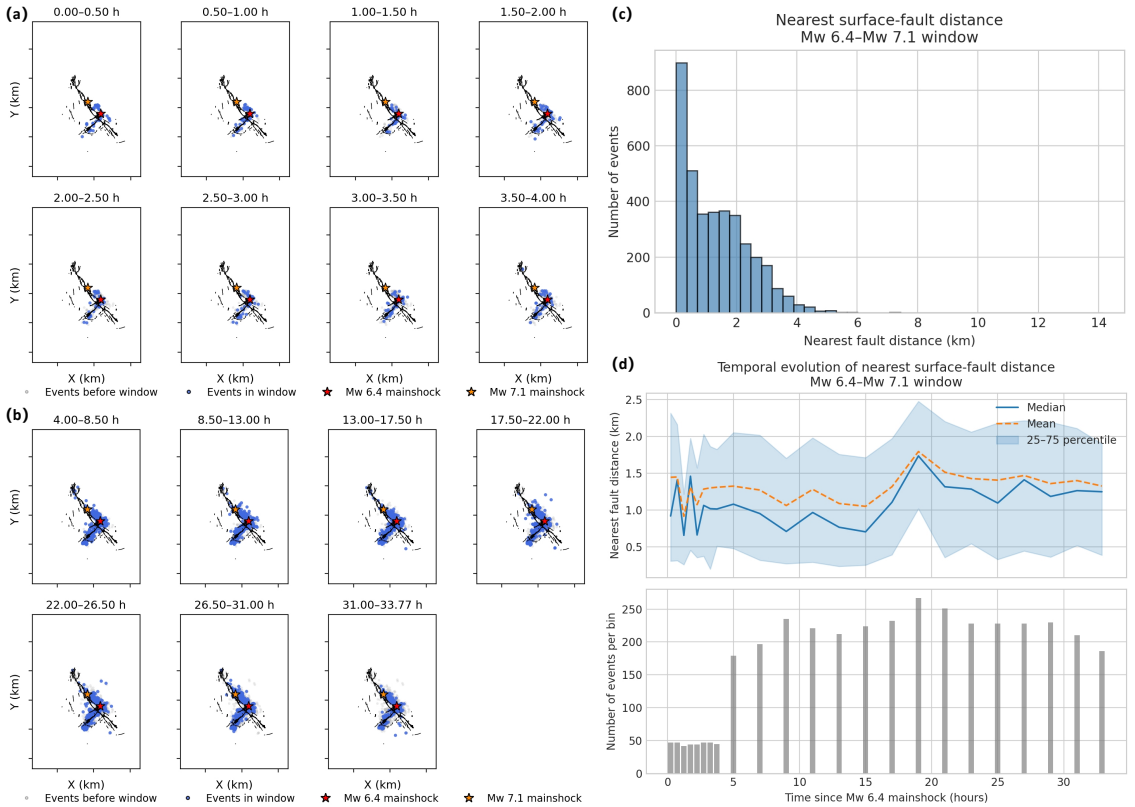
3. Spatiotemporal maps between Mw 6.4 and Mw 7.1
Produce time-sliced maps (2×4 subplots per figure) showing
   seismic evolution between Mw 6.4 and Mw 7.1, relative to
   faults and mainshocks.
- Load prepared data and select events in `[t64, t71]`
- Define time windows for plotting
    - Use `ridgecrest_time_bins.csv`:
    - Order bins chronologically by `t_start`.
    - Group bins into pages of 8 bins each:
- Per-window event subsets, for each bin k with `[t_start_k,
  t_end_k)`:
    - `events_in_bin_k`: `event_time ∈ [t_start_k, t_end_k)`.
    - `events_before_k`:`event_time < t_start_k` and `
      event_time ≥ t64`.
- Figure construction: 2×4 grid, for each page j:
    - Initialize a figure with 2 rows × 4 columns.
    - For each subplot corresponding to bin k

4. Nearest-fault distance statistics
Quantify how close events in [Mw 6.4, Mw 7.1] lie to the
   mapped faults, and how this distance distribution changes
   over time.
```

- Load and prepare dataset
  - Geometry representation: Use ‘fault_segments.csv‘ with segment endpoints ‘(x1_km, y1_km)‘ and ‘(x2_km, y2_km)‘ and precomputed ‘dx, dy, length‘.
  - Build a spatial index: Create a KD-tree or similar index using segment midpoints ‘(x_mid, y_mid)‘ to quickly find candidate segments for each event.
- nearest-fault distance computation
  - For each event: Use the spatial index to find candidate segments within a radius (e.g., 10-20 km) or nearest N segments.
  - For each candidate segment: Compute the point-to-segment distance in 2D:
    - Projection scalar ‘t‘ along the segment.
    - Clamp ‘t‘ to [0, 1].
    - Get closest point ‘P_closest‘.
    - Distance ‘d = sqrt((x_event - x_closest)^2 + (y_event - y_closest)^2)‘.
  - Take minimum ‘d‘ across all candidate segments as ‘dist_fault_km‘ (distance already in km units).
- Overall nearest-fault distance distribution
  - Load ‘events_64_71_with_fault_distance.csv‘.
  - Compute descriptive statistics for ‘dist_fault_km‘:
    - Min, max, mean, median.
    - Selected quantiles (e.g., 10%, 25%, 75%, 90%).
    - Counts of events within thresholds (e.g., ‘<1 km‘, ‘<2 km‘, ‘≥5 km‘).
  - Plot distance distribution:
    - histogram of ‘dist_fault_km‘ (choose bin width based on range).
    - Optionally apply log-scale on x or y if needed.
- Temporal evolution of nearest-fault distance
  - Use time bins defined in ‘ridgecrest_time_bins.csv‘ (Stage 1 & Stage 2).
  - For each bin k, Select events with ‘t_start_k ≤ event_time < t_end_k‘, and extract their ‘dist_fault_km‘. Compute bin-level statistics:
    - ‘median_dist_km‘, ‘p25_dist_km‘, ‘p75_dist_km‘.
    - ‘mean_dist_km‘.
    - ‘count_events‘.
  - Compile into a bin statistics table: ‘bin_id, t_mid_hours_since_64, median_dist_km, p25_dist_km, p75_dist_km, mean_dist_km, count_events‘.
  - Plot temporal evolution

5. Along-fault spatiotemporal pattern
- Load data and Use events with ‘between_64_71 == True‘ and valid ‘dist_fault_km‘.
- Compute along-fault coordinate for each event
- Along-fault vs time: space-time diagrams
- plot 2D density (space-time)
- analysis the temporal evolution of "alignment" with the fault

Box B.2.3 Main Visualization Results (Raw Output)



Box B.2.4 Analysis Summary

```
Summary of Spatiotemporal evolution of the earthquake
    epicenter for 2019 Ridgecrest

1. Key observations and findings
- persistent close alignment: The narrow, time-stable
    distribution of nearest-fault and fault-normal distances
    is consistent with a triggering process dominated by
    stress changes on and very near pre-existing fault planes.
     Static Coulomb stress changes \Delta CFS from the Mw 6.4
    rupture, compounded by subsequent aftershocks, are
    expected to concentrate on favorably oriented, high-shear
    regions within a damage zone of order 1-2 km wide. The
    lack of progressive drift away from the faults argues
    against a scenario where early, more diffuse off-fault
    failure gradually migrates onto the main faults; instead,
    the fault system appears to be the primary locus of
    failure from the outset.
```

```
- progressive local along-strike expansion and preconditioning of Mw 7.1): Within the immediate Mw 6.4-Mw 7.1 corridor, the observed sequence-initial activation near Mw 6.4, followed by stepwise expansion and eventual dense microseismicity around the Mw 7.1 epicentral area-is consistent with static stress transfer along strike and/or progressive weakening (e.g., damage growth, pore-pressure diffusion) on contiguous segments. The emergence of intense microseismicity in the future Mw 7.1 rupture zone suggests that this segment underwent significant stressing and was brought closer to failure over several to tens of hours, supporting a triggering link from Mw 6.4 to Mw 7.1 via along-fault stress loading.
- early network-wide activation without a simple propagating front:The rapid attainment of a large along-fault span and the persistence of multiple active along-fault bands imply that the Mw 6.4 static and dynamic stress perturbations affected a broad regional fault network almost immediately, activating segments that were already near failure. Rather than a single rupture front advancing along strike, these data favor a picture of *multi-segment, stress-shadow-modulated triggering*: different segments respond quasi-independently depending on their local stress state, while remaining confined within a narrow corridor around the mapped faults.
- post-Mw 7.1 reorganization and lengthening:The substantial increase in along-strike extent and the sharpening of the NW-SE trend after Mw 7.1 reflect the much larger static stress changes and dynamic shaking from the Mw 7.1 rupture. This event appears to have fully engaged a long, coherent NW-SE fault structure, extending and reinforcing the inter-mainshock pattern that had already developed between and around the two mainshocks. The contrast between the pre- and post-7.1 patterns underscores that the Mw 6.4 sequence partially illuminated and loaded the eventual rupture area, whereas the Mw 7.1 mainshock completed and extended that activation along the main fault.

2. Overview and method context
```

```
10 - A single catalog of 2019 Ridgecrest for July 4-25, 2019 and high-precision locations of the Mw 6.4 and Mw 7.1 mainshocks were first standardized and projected into a common local Cartesian frame (‘01_prepare_ridgecrest_data‘). Time windows and bins relative to Mw 6.4 and Mw 7.1 were defined, and each event was assigned a time bin. Mapped surface faults were converted from geographic polylines into fault-segment tables with along-fault cumulative distance. Using this framework, time-sliced epicentral maps between Mw 6.4 and Mw 7.1 were generated (‘02_spatiotemporal_maps_64_to_71‘), followed by a direct spatial comparison of inter- vs post-Mw 7.1 seismicity (‘03_pre_post_71_spatial_comparison‘). For the inter-mainshock window, nearest-fault distances were computed by projecting each event onto its closest surface-fault segment, enabling both global and time-binned distance statistics (‘04_nearest_fault_distance_stats‘). Finally, each event was mapped to an along-fault coordinate s_{\rm fault} and a signed normal offset d_{\rm normal}, from which along-fault space-time density, alignment metrics, and activation extent were derived (‘05_along_fault_spatiotemporal_pattern‘). All geometry-intensive steps (event-fault distances, binwise statistics) used parallel computation to handle thousands of events and >200,000 fault vertices efficiently.   - Key physical and algorithmic principles
11      - Local projection and distance geometry: Geographic coordinates (\phi,\lambda) were mapped to a local Cartesian frame (x,y) (km) so that Euclidean distances approximate horizontal distances on the Earth’s surface. Surface faults are represented as polylines; each segment has endpoints (x_1,y_1), (x_2,y_2), length L_i, and unit tangent \mathbf{u}_i. The nearest-fault distance is the minimum point-to-segment distance over all segments.
12      - Along-fault and fault-normal coordinates: An along-fault coordinate s_{\rm fault} is defined by cumulative arc length along the polyline, giving a 1-D parameterization of the fault system. For an event projected onto its nearest segment, the local projection parameter t \in [0,1] gives the along-segment position; the global along-fault position is s_{\rm event}=s_{\rm start,i}+t\,L_i. A local normal unit vector \mathbf{n}_i (perpendicular to \mathbf{u}_i) yields the signed normal distance d_{\rm normal}=(\mathbf{x}_{\rm evt}-\mathbf{x}_{\rm proj})\cdot\mathbf{n}_i. |d_{\rm normal}| measures how tightly events cluster around the fault core.
13      - Time binning and space-time density: The inter-mainshock interval is divided into short (30-min) and longer (2-h) bins; for each bin k, statistics (median, mean, quantiles) of nearest-fault distance and |d_{\rm normal}| are computed. A 2D density grid in (time, s_{\rm fault}) is constructed by counting events in each bin, producing space-time diagrams of along-strike activation.
14
15 3. Summary of figure-based results
```

```
Diagnostic A & B – Spatiotemporal evolution between Mw 6.4 and Mw 7.1
Observations:
– Early stage (0–4 h, page 1, bins 0–7): Blue events cluster tightly around the mapped fault traces immediately after the Mw 6.4.
    – The epicenters form two dominant linear belts: striking belt passing through the Mw 6.4 epicenter; a conjugate, more NNW–SSE / N–S belt to the northwest.
    – Off–fault seismicity is sparse; most events lie within a narrow corridor around the surface traces.
– Later stage (4–34 h, pages 2, bins 8–16)
    – As the sequence grows denser, the same two principal lineations persist.
    – New events largely fill in along these preexisting strands rather than forming diffuse clouds away from mapped faults
– Across all time bins, the majority of triggered earthquakes are clearly organized along the known fault directions. The spatial pattern is strongly fault–controlled rather than isotropic.
– The orientation of seismicity relative to the faults is stable, but the extent and relative emphasis along strike change with time. Early activity is more localized around Mw 6.4; later activity increasingly occupies the full length between the Mw 6.4 and Mw 7.1 hypocenters and strengthens both conjugate strands.
– The activated region grows progressively along strike, rather than the entire fault system being triggered instantaneously. however, this growth is relatively fast ( hours to <1 day), and by the time of the Mw 7.1 almost the whole mapped fault network in the window is already seismically active.

Diagnostic C – nearest–fault distance distribution
Observations:
    – The distribution is strongly peaked at small distances (<1 km).
    – Event counts are highest in the 0–0.5 km bin (≈900 events) and remain high up to about 2 km.
    – Counts decrease roughly monotonically beyond 2 km and become very small by 4–5 km.
    – A few outliers occur between 5–7 km, and there is essentially no seismicity farther than ~7 km from the mapped surface faults.
Interpretation:
    – The bulk of the Mw 6.4–Mw 7.1 seismicity is closely associated with the mapped surface fault traces.
    – Only a minor fraction of earthquakes occur more than a few kilometers from the mapped faults, indicating that triggered events predominantly nucleate within the fault zone or its immediate damage zone.
    – This supports the idea that the fault system provides the main structural control on aftershock locations, rather than widespread off–fault distributed deformation.

Diagnostic D – Temporal evolution of nearest–fault distance
```

```
Top panel: time series of nearest-fault distance statistics (median, mean, and 25-75th percentile band) versus time since the Mw 6.4 mainshock. Bottom panel: number of events per time bin (showing the change from early 30-min bins to later 2-hr bins).
Observations:
    - Median distances in the early bins are around 0.7-1.2 km, with some variability in the first hour.
    - The 25-75% range is roughly 0.3-1.8 km, i.e., most events are still within ~2 km of the faults.
    - Mean distances are slightly higher than the median (≈ 1.1-1.3 km), reflecting a small tail of more distant events.
    - Event counts per bin are modest but stable (~40-50 events per 30-min bin).
Interpretation:
    - Immediately after the Mw 6.4 mainshock, aftershocks are already tightly clustered around the mapped faults.
    - There is no evidence that very early events are systematically farther from the faults; the structure-controlled pattern is present from the beginning.
```

B.2.2 Triggered Stratification and Fault Segment Response

To examine whether the M_w 6.4 event activated the entire fault system, seismic events were assigned to their nearest mapped fault (threshold ¡ 5 km), and onset time profiles were constructed for each fault segment to characterize the timing of their first significant activation. The results demonstrate that fault segments along the same strike did not exhibit instantaneous cooperative responses. Instead, activation was temporally dispersed and non-synchronous. The distribution of "illumination" times across segments displays pronounced diffusivity, indicating a staged and multi-phase triggering process rather than a system-wide coherent response. Structurally, early activation was concentrated on fault segments oblique or conjugate to the M_w 6.4 rupture plane. Subsequently, the activity centroid progressively shifted toward NW-SE trending segments aligned with the eventual M_w 7.1 rupture. This evolutionary pattern indicates that triggering did not propagate continuously along a single dominant strike, but instead developed through branching cascades across multiple structural units. Overall, while seismicity remained spatially confined within the fault belt, its along-strike distribution was patchy and segmented, rather than forming a coherent advancing rupture front. This structural stratification provides geometric evidence for stress redistribution pathways within the fault network.

Box B.2.5 User Request

```
Investigate the spatiotemporal evolution of the earthquakes for the Ridgecrest earthquake sequence, spetial attention to the trigger mechanism from Mw 6.4 to Mw 7.1 mainshock. The main question is: (1) Is the activation of the earthquakes along the fault direction synchronous? (2) Is the activation of the earthquakes along the fault direction staged or cascade-like or more complex?
Requirements:
```

```
1. Data Source: earthquake catalog is locate at "~/
   ridgecrest_catalog.csv", main_shock events is locate at "~
   /main_shock_events.csv", known fault is locate at "~/
   ridgecrest_surface_faults.json"
2. Discretize each mapped fault polyline into contiguous
   fault segments of fixed arclength (e.g., 1 km per segment)
    if longer than the arclength, otherwise keep the original
    and end points. And then do the earthquake_to_fault_
   segment association for each earhtquake (nearest distance
   < 3 km). Statistic the fault_segment_level seismicity time
    series and calculate the fault_segment activation time.
   Finally visualize the results.
```

Box B.2.6 Final Experimental Plan

```
Experimental Plan: Quantitatively characterize how seismicity
    between the Mw 6.4 and Mw 7.1 Ridgecrest mainshocks
   activated in space and along mapped faults, and provide
   diagnostics to assess: Whether activation along the fault
   direction is approximately synchronous or clearly time_
   structured. Whether activation is staged or cascade_like
   along individual faults and across the fault network, or
   more complex.

1. high_level workflow
- 01_prep_catalog_mainshocks_faults.py: Load and standardize
   all inputs; define time window [Mw 6.4, Mw 7.1]; project
   to local coordinates; define expanded study region.
- 02_grid_activation_analysis.py: Build 1 km × 1 km grid over
    expanded fault region; construct 30_min local seismicity
   rate time series; define robust, sustained_rate onset time
    per cell; generate onset maps.
- 03_fault_segmentation_and_association.py: Segment faults
   into ~1 km segments; compute segment geometry and strike;
   associate events to segments (≤3 km); build 30_min segment
    time series.
- 04_activation_visualization_and_triggering_diagnostics.py:
    Define segment activation times (rate > 10 events/h);
   visualize fault_segment activation; build activation
   density vs. time and strike×time maps; construct time_
   distance diagrams and quantitative metrics for synchronous
    vs cascade_like activation.

2. Catalog, mainshock, and fault preparation
- Load mainshocks and define time window
    - Load‘main_shock_events.csv‘ and Define analysis window:
       ‘time_start = t64‘ and ‘time_end = t71‘.
    - Load fault polylines.
- Coordinate projection and study region: To avoid
   distortions in distances and 1 km binning, work in a local
    Cartesian system.
    - Define local projection.
    - Project all coordinates to (x, y) in kilometers.
    - Define spatial study region from faults.

```

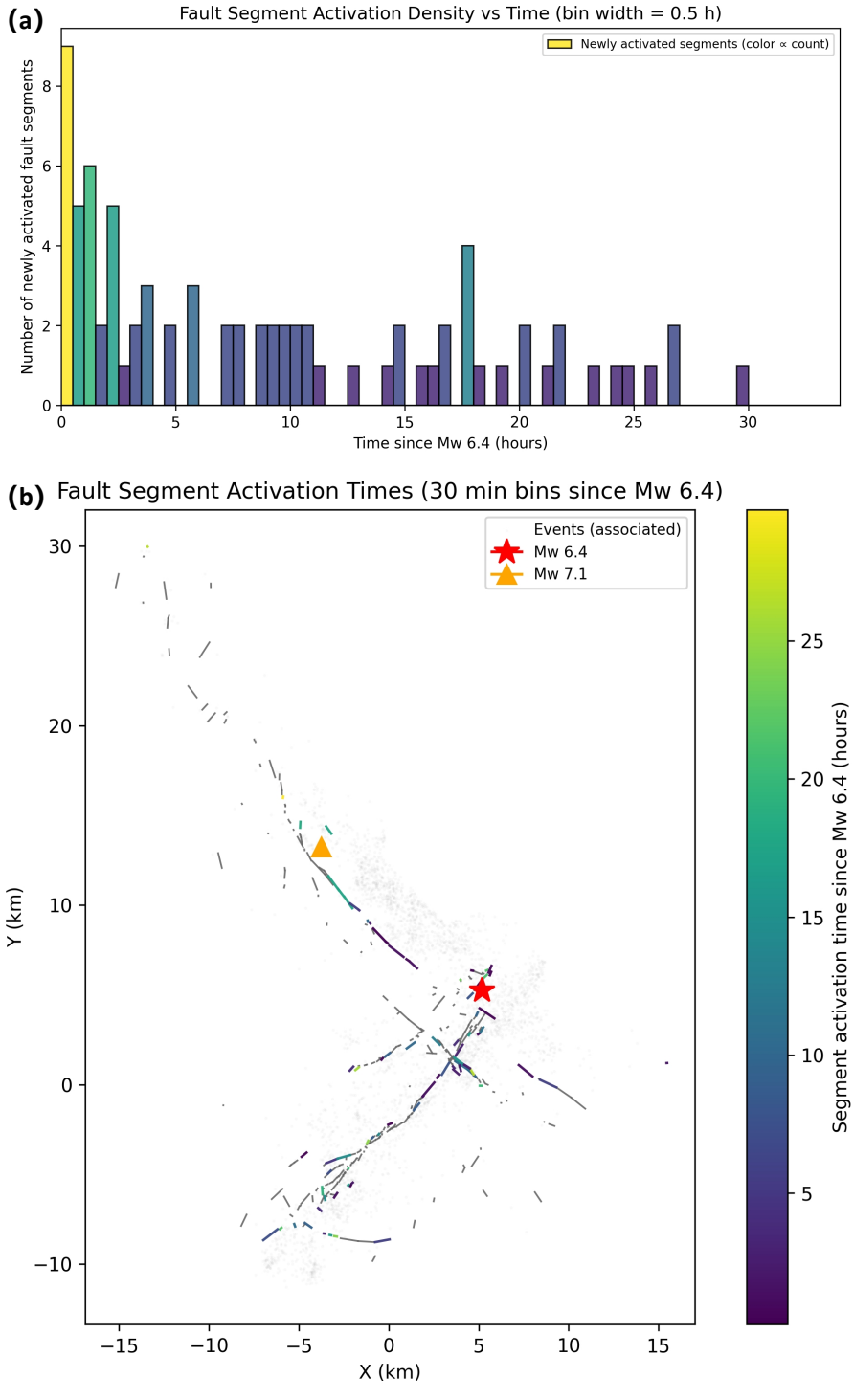
3. Grid-based activation analysis: build a 1 km × 1 km grid around the faults, derive 30-min local seismicity rate time series per cell, and define a physically interpretable activation onset time per cell based on sustained rate increase.
- Grid definition and event-to-cell assignment
  - Construct 1 km grid
  - Assign each event to a grid cell
- Time binning and per-cell seismicity rate
  - Define time bins:
  - Assign events to time bins:
  - Build counts and rates:
- Activation onset definition per grid cell (robust, sustained)
  - Extract rate series `r_k = rate[cell_id, k]` for `k = 0..Nt-1`.
  - Define a baseline: Compute `r_bg = median(r_k for k in 0..Nb_bg-1)`.
  - Define activation threshold
  - Enforce persistence via moving average
  - Assign activation time
- Spatial mapping of grid onset times
  - Build a 2D grid of onset times
  - Plot in projected coordinates

4. Fault segmentation and event association: discretize mapped faults into ~1 km segments, then associate each event to its nearest segment if within 3 km, and build per-segment 30-min time series.
- Fault segmentation into ~1 km segments
  - Preprocess polylines: For each polyline compute cumulative arclength from first vertex and segment length between consecutive vertices `ds_i = sqrt(dx^2 + dy^2)`. Cumulative `s_i = Σ ds_i`.
  - Segmenting by arc length.
  - Compute segment attributes: `line_id`: original polyline index.`segment_id`: index along that line.` global_id`: contiguous ID over all segments.Endpoints: `x1, y1`, `x2, y2`.Midpoint: `xm, ym`.Length ` L_seg_km`.
- Earthquake-to-fault-segment association
  - Build spatial index for segments.
  - For each event: retrieve candidate segments within a local search radius (e.g., 5 km).
- Segment-level 30-min time series
  - For each segment `s`: Collect its associated events (distance $\leq$ 3 km). For those events, obtain their ` t_rel_64_hours`.
  - histogram per segment

5. Activation visualization & triggering diagnostics: define segment activation times using your 10 events/hour threshold; visualize activation sequence; construct diagnostic plots to test synchronous vs staged/cascade-like activation.
- Fault-segment activation time
  - Apply activation definition.
  - Merge with segment geometry

```
- Fault-segment activation map
  - Prepare map geometry.
  - Plot Each segment as a line with color = `t_act_seg_rel_hours`:
- Segment activation density vs time
  - Build activation density series.
  - Plot: x-axis: `t_rel_64_hours` (bin centers); y-axis: `N_activated_seg[k]` (segments per 30 min).
- Strike × activation time density map
  - Prepare strike-time data: For each activated segment: Use `strike_deg` and `t_act_seg_rel_hours`.
  - Bin time and strike.
  - Build 2D histogram:`H[time_bin, strike_bin] = number of segments activating in that bin`.
  - Plot: x-axis: activation time (hours since Mw 6.4). y-axis: strike (or strike_rel).
- Time-distance diagrams along main fault direction
  - Define a principal fault axis: Compute a principal strike for the main Mw 7.1 strand: Define an axis passing through Mw 7.1 epicenter with this orientation. Using local projection, define unit vector `u` along this axis.
  - Project segment midpoints: For each segment midpoint `(xm, ym)`: Compute signed distance along axis: `s_seg = ( (xm - x71_km, ym - y71_km) · u )` in km.
  - Segment activation time-distance plot: Scatter x-axis: `s_seg` (km along axis, positive in one direction). y-axis: `t_act_seg_rel_hours`.
```

Box B.2.7 Main Visualization Results (Raw Output)



Box B.2.8 Analysis Summary

```
To characterize fault-controlled triggering behavior, we
    quantify the spatiotemporal association between seismicity
     and mapped fault structures.

1. Key observations and findings
```

- Temporal spread and non-synchronous activation along strike:
  - Observations:Activation of both grid cells and fault segments spans most of the ~34 h between Mw 6.4 and Mw 7.1, rather than occurring in a short co-active window. Central 10-90% of activation times extend over ≈21.5 h for segments and ≈26.3 h for grid cells, corresponding to relative spans of ≈0.64 and ≈0.78 of the Mw 6.4-7.1 interval.
  - Mechanistic interpretation: The broad temporal spread is consistent with a heterogeneous stress field and variable fault strength following the Mw 6.4 rupture. Static Coulomb stress changes from Mw 6.4 and its early aftershocks likely brought some patches immediately close to failure, while others required additional loading (e.g., cumulative stress transfer from intervening events or aseismic slip) before reaching their own failure thresholds. Rate-and-state friction predicts such delayed failure on positively stressed but not yet critically loaded patches, naturally producing extended, non-synchronous activation along strike.
- Staged, multi-phase activation rather than instantaneous co-activation:
  - Observations: Grid-cell activation times show a multi-peaked distribution from near 0 h to >30 h after Mw 6.4, with distinct clusters around early (<2 h), intermediate (~10-20 h), and late (~27-32 h) times. The number of newly activated cells per 30-min bin exhibits a strong initial burst immediately after Mw 6.4, followed by quieter intervals and secondary bursts, especially around ~18-19 h.
  - Mechanistic interpretation: The temporal clustering indicates a staged triggering process. The initial burst reflects direct dynamic and static stress effects from Mw 6.4 on nearby cells. Subsequent bursts likely arise when stress changes from earlier aftershocks and local aseismic processes (e.g., creep on some strands) accumulate sufficiently to trigger additional patches. This behaviour is compatible with a cascade of interacting sources, where each stage modifies the stress field and failure clock of neighbouring regions rather than a single, instantaneous network-wide adjustment.
- Orientation-dependent activation:
  - Observations: early oblique/conjugate faults, later Mw 7.1-oriented segments: The strike-time density diagram shows that early-activated segments ($t \lesssim 4$ h) cluster at corrected strikes strongly oblique or conjugate to the Mw 7.1 fault (e.g., ~+75-80° and -10 to -20° relative to the principal Mw 7.1 orientation). Segments whose strike is aligned with the Mw 7.1 rupture (corrected strike ≈ 0-10°) tend to activate later, commonly around ~15-20 h after Mw 6.4.

- Mechanistic interpretation: Static Coulomb stress changes from the Mw 6.4 rupture are highly orientation dependent: faults optimally oriented for right-lateral slip in the Mw 6.4 stress field (often conjugate or oblique to the subsequent Mw 7.1 fault) receive larger immediate shear-stress increases and thus fail earlier. The main Mw 7.1-oriented fault, while central to the later event, may initially see smaller net stress change or even mixed positive/negative lobes, requiring additional stress transfer from intervening seismicity to reach failure. This produces a fault-family sequence: early activation on conjugate/oblique structures, followed by delayed engagement of the Mw 7.1-aligned strands.
- Spatially localized but patchy along-fault cascade, not a coherent rupture-front:
  - Observations: Grid-based onset maps show activation tightly concentrated along the mapped fault system, with later onset times at increasing along-fault distances, but without a single smooth front. Segment-level activation times vs distance along a principal axis show a weak overall trend (apparent migration of order ~2-3 km/h) but with large scatter; segments at similar distances activate across ~0-30+ h. Many fault segments are never "activated" at the high-rate threshold despite recording some events, indicating localized high-rate patches interspersed with only weakly active segments.
  - Mechanistic interpretation: This pattern is more consistent with a patchy, multi-patch cascade than with a coherent diffusive or rupture-front propagation. Static and dynamic stress transfer from individual moderate-size events redistribute stress in a spatially irregular way, controlled by fault geometry, segmentation, and local frictional properties, so that some patches respond quickly while others remain below the imposed rate threshold. The modest regression-inferred migration velocity likely reflects an ensemble average drift of activity rather than a physical front.
- Mw 7.1 nucleation region is not an anomalously early or strongly activated patch:
  - Observations: Grid cells in the immediate vicinity of the Mw 7.1 epicenter show intermediate activation times (~10-20 h), not among the earliest or latest cells. The fault segment closest to the Mw 7.1 nucleation point (~0.85 km) does not reach the 10 events/h activation threshold.

- Mechanistic interpretation: The Mw 7.1 mainshock nucleated on a region that was moderately but not anomalously active, and whose nearest mapped segment never attained the high-rate threshold imposed in this analysis. This suggests that nucleation did not require prior extreme foreshock clustering on the exact nucleation segment, but instead occurred in a volume that had been gradually brought closer to failure by distributed stressing on the surrounding network, including on nearby but not exactly coincident segments. This is consistent with nucleation controlled by local stress heterogeneity and small-scale asperities rather than by being embedded in the single most highly activated patch.

2. Overview and method context

- The study integrated a high-resolution 2019 Ridgecrest catalog, relocated Mw 6.4 and Mw 7.1 mainshock metadata, and dense surface fault polylines for the Ridgecrest region. First, all earthquakes between the Mw 6.4 and Mw 7.1 origin times were extracted and projected, together with faults and mainshocks, into a local Cartesian system, and an expanded fault-bounded study region was defined (01_prep_catalog_mainshocks_faults). Within this region, a 1 km × 1 km grid was constructed; events were binned into 30-minute intervals to form local seismicity-rate and cumulative-count time series per cell, from which robust activation onsets were identified using a baseline-relative, smoothed threshold criterion (02_grid_activation_analysis). In parallel, mapped faults were segmented into ~1 km elements, each assigned a strike and midpoint, and earthquakes were associated to the nearest segment within 3 km to build segment-level 30-minute count, rate, and cumulative series (03_fault_segmentation_and_association). Finally, fault-segment activation times were defined via a 10 events/hour criterion; activation maps, activation density vs time, strike-time histograms, and time-distance diagrams along a principal fault axis were generated, and quantitative metrics for temporal spread, along-fault migration, clustering, and the Mw 7.1 nucleation segment were extracted (04_activation_visualization_and_triggering_diagnostics).

3. Summary of figure-based results

Diagnostic A - Fault-segment activation density vs time

Observations:

- histogram of the number of newly activated segments per 30-min bin (color $\propto$ count).
- The window spans about 33 h between Mw 6.4 (t=0) and Mw 7.1.
- Behaviour:
  - A strong initial burst: the first few hours host the highest activation rates (up to ~9 segments/bins very close to t=0-0.5 h, then several bins with 4-6 segments).
  - After ~4-5 h, activation continues at lower but non-zero rates.
  - Additional small "pulses" occur at later times (e.g., ~17-20 h), well before Mw 7.1.

```
        - Activation events are scattered up to almost the
          end of the window.
- Implication: the system shows a front-loaded but clearly
  time-extended activation. It is neither a single, near-
  instantaneous network-wide step nor a smooth, uniformly
  progressive rate-rather, a sequence of bursts.

Diagnostic B  - Fault-segment activation map
Observations:
    - Colors show activation time of each fault segment (
      threshold: ≥10 events/hour in 30-min bins) relative to
       Mw 6.4.
    - The Mw 6.4 epicenter lies on the southern right-lateral
       fault; Mw 7.1 is on the NW-striking main fault to the
       NW.
    - Key observations:
    - Earliest activation (dark colors, <~2-3 h) is strongly
      concentrated on:
        - The immediate vicinity of the Mw 6.4 rupture.
        - A limited section of the central NW-striking fault
          zone.
    - Progressively later activation appears:
        - Northward along the main NW-striking fault,
          approaching the Mw 7.1 epicentral area.
        - Southward and into adjacent ENE-WSW or more complex
          cross-faults.
    - Several peripheral faults and small strands show no
      activation at this threshold (grey segments), even
      though background events scatter nearby.
- Implication: activation is not synchronous across the
  mapped fault system. Instead, a subset of segments near
  the Mw 6.4 rupture activate early; other parts of the
  network, including the Mw 7.1 region, reach high
  seismicity rates only later.
```

B.2.3 Geometric Evolution and Structure-Guiding Effects in high-Density Regions

By integrating kernel density estimation time slices with mapped fault distributions, we further analyzed the geometric morphology and evolving outer boundaries of high-density seismic clusters, with particular emphasis on whether a frontal advance toward the M_w 7.1 rupture zone was present. The analysis shows that during the early inter-mainshock stage, seismic activity was primarily confined near the fault intersection zone associated with the M_w 6.4 rupture, without a clear migration trend toward the M_w 7.1 source region. Approximately four hours after the M_w 6.4 event, activity gradually focused along the NW-SE fault corridor connecting the two mainshocks. Thereafter, the high-density region progressively intensified along this corridor and eventually became anchored near the nucleation area of the M_w 7.1 event. Importantly, this along-strike progressive focusing did not manifest as continuous outward expansion of the external spatial boundary. Instead, it remained nested within the multi-lobed seismic envelope established during the early stage. In other words, the overall spatial footprint was largely determined early in the sequence, and subsequent evolution mainly reflected internal reorganization and directional intensification constrained by fault geometry. These geometric evolution characteristics suggest that the occurrence of the M_w 7.1

mainshock is more consistent with a progressively prepared triggering process guided by structural constraints, rather than an independent instability arising at a random location. The fault network provided a well-defined spatial conduit during the inter-mainshock phase, enabling stress loading and microfracturing activity to progressively concentrate along pre-existing structures toward the eventual nucleation zone.

Box B.2.9 User Request

```
Investigate the spatiotemporal evolution of the earthquakes
    for the Ridgecrest earthquake sequence, spetial attention
    to the trigger mechanism from Mw 6.4 to Mw 7.1 mainshock.

Requirements:
1. Data Source: earthquake catalog is locate at "~/
    ridgecrest_catalog.csv", main_shock events is locate at "~
    /main_shock_events.csv", known fault is locate at "~/
    ridgecrest_surface_faults.json"
2. Spatial Kernel Density Estimation Migration Analysis and
    Geometric Morphological Evolution of the Seismic Point
    Cloud to answer the question of : Whether the seismic
    culster transfer to the Mw 7.1 is progressive spatial
    focusing, or progressive spatial spreading or bifurcation
```

Box B.2.10 Final Experimental Plan

```
Experimental Plan: Use the provided Ridgecrest 2019 catalogs
    and surface fault geometry to characterize, between the Mw
     6.4 and Mw 7.1 mainshocks:
     1. how seismicity density migrates in space and time (KDE
         + hotspot tracking).
     2. how the overall geometry of the seismic point cloud
        evolves (convex hulls vs alpha-shapes).

1. high-level workflow
- 01_prep_ridgecrest_data.py: Load catalogs and faults,
    identify mainshocks, define time windows, define a local
    coordinate system and spatial grid, estimate KDE bandwidth
     and alpha parameter, and save standardized data.
- 02_kde_spatiotemporal_evolution.py: Compute 2D KDE maps for
     Stage 1 and Stage 2 intervals on a fixed grid and
    bandwidth; generate 2×4 panel figures with consistent
    extent and color scale.
- 03_hotspot_tracking.py: From the KDE grids, extract primary
     hotspots per interval; generate hotspot migration maps
    for Stage 1 and Stage 2.
- 04_geometric_envelope_evolution.py: Compute convex hull and
     alpha-shape envelopes for 1-hour intervals; visualize the
     evolution of envelope boundaries with time-encoded colors
    .

2. Data & geometry preparation: Standardize input catalogs
    and geometry, define the inter-mainshock subset and all
    time windows, and set a physically meaningful local
    coordinate system and spatial grid.
- Load input catalogs and faults
- Define global temporal windows and subset catalog
```

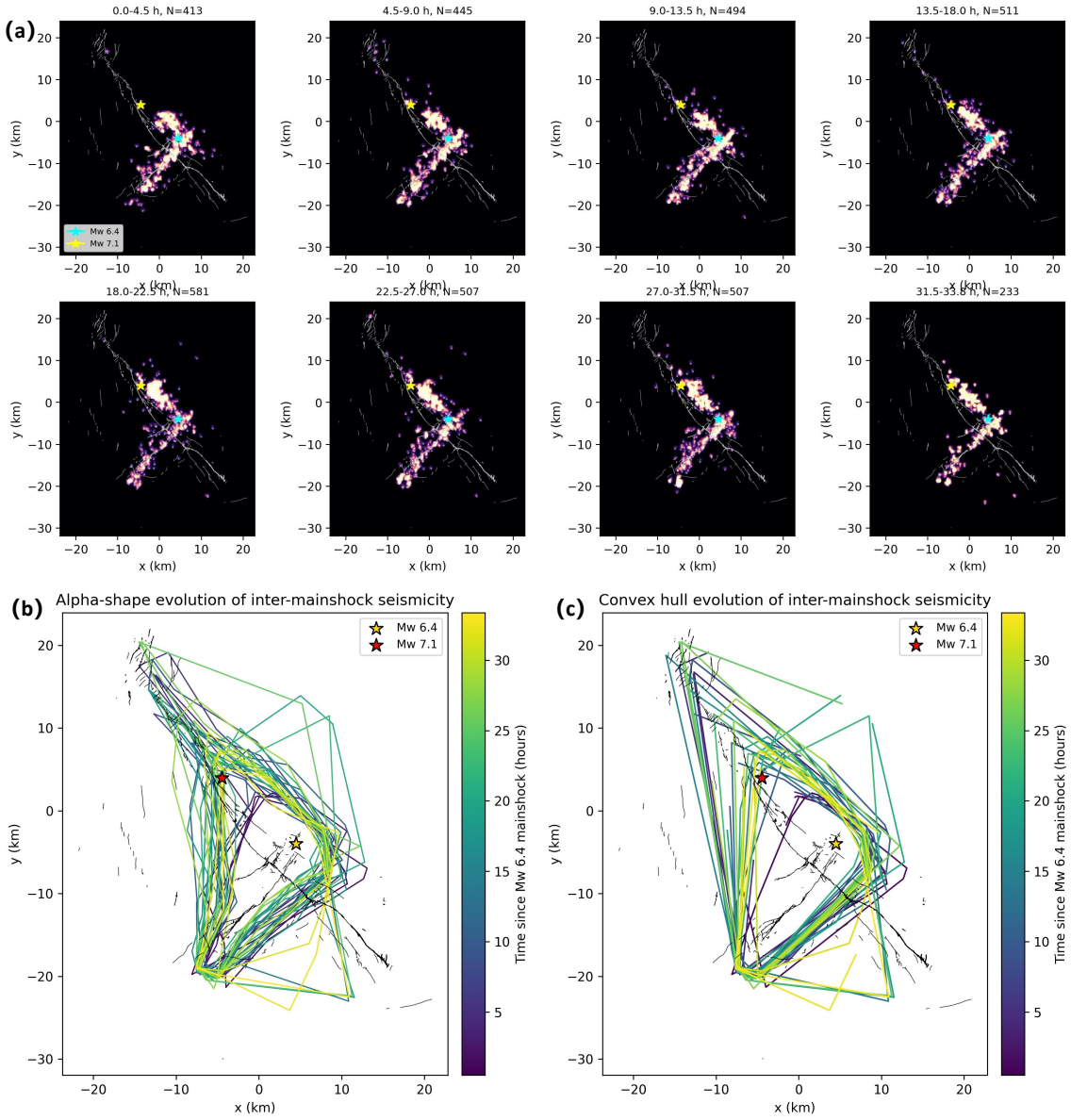
```
14 - Local coordinate system (for metric operations): KDE and
     alpha-shape computations are best done in metric
     coordinates, but the user requested KDE in geographic
     coordinates.
15     - Reference point use midpoint between mainshock
         epicenters
16     - Approximate projection
17     - Store both coordinate systems
18 - Spatial extent and grid
19     - Compute spatial extent in local (x, y)
20     - Define local grid for KDE
21     - Corresponding geographic grid (for plotting)
22 - Time interval definitions (consistent with user's
     specification)
23     - Stage 1 - 30 min intervals
24     - Stage 2 - 2 h intervals
25     - Envelope analysis - 1 h intervals
26 - Preselect global KDE bandwidth and alpha parameter
27     - KDE bandwidth (in km)
28     - Alpha-shape parameter
29
30 3. KDE spatiotemporal evolution: Compute 2D KDE for each
     Stage 1 and Stage 2 interval on a fixed x-y grid, then
     visualize density evolution in 2×4 multi-panel maps with
     consistent color scales and overlays.
31 - Interval-wise event selection
32     - Load inter-mainshock arrays `event_time`, `x`, `y`.
33     - For Stage 1 and Stage 2:
34         - For each interval (from CSV), select events with `
             t_start ≤ event_time < t_end`.
35         - Keep counts per interval for logging and later
             annotations.
36 - KDE computation (x-y coordinates, same bandwidth and grid)
37     - KDE setup
38         - Use Gaussian KDE in 2D.
39         - Bandwidth: `bandwidth_km` from `analysis_parameters.
             json`.
40         - Coordinate system: (x, y) in km.
41         - Evaluation grid: `X`, `Y` from `grid_metadata.json`.
42     - Parallel computation
43         - Treat each interval as an independent task.
44         - Use a pool with up to 64 workers.
45         - For each interval:
46           - Input: `(x_i, y_i)` for that interval.
47           - Output: `Z_interval` (2D array of KDE values on
               grid).
48         - Use a progress bar or logging to show interval
             completion and timing.
49 - handling sparse intervals
50 - Visualization - KDE evolution maps
51
52 4. hotspot tracking: For each interval, identify the location
     of the primary KDE maximum (hotspot) and visualize its
     migration for Stage 1 and Stage 2.
53 - hotspot extraction per interval
54     - Load `X`, `Y` grid from `grid_metadata.json`.
```

```
    - For each interval in Stage 1 and Stage 2:
      - Take `Z` field.
      - Compute global maximum index `(i_max, j_max)` where `Z` is largest.
      - Coordinates: x_hot = X[i_max, j_max]`, `y_hot = Y[i_max, j_max]`.
      - Convert to approximate lat-lon using inverse of projection: `lat_hot = y_hot / 110.57 + lat0`, `lon_hot = x_hot / (111.32 * cos(lat0)) + lon0`.
      - Record also `max_density = Z[i_max, j_max]`.
    - Assemble hotspot tables:
- hotspot migration visualization

5. Geometric envelope evolution: For 1-hour intervals within `[t64, t71]`, compute convex hull and alpha-shape envelopes (in x-y) and visualize their boundary evolution to assess contraction, expansion, and multi-lobed structure.
- Interval-wise point sets
    - Load `event_time`, `x`, `y` from `inter_mainshock_events.npz`.
    - From `intervals_env.csv`:
      - For each 1-hour interval: Select events `t_start ≤ event_time < t_end`. Store `x_i`, `y_i` and their count.
    - Log the number of intervals with very few events (e.g., `N < 3`) as they will not produce valid polygons.
- Convex hull calculation (per interval, parallelized)
    - For each interval with `N ≥ 3` points:
      - Compute convex hull in (x, y) using a standard algorithm.
      - Extract ordered hull vertices `(x_hull, y_hull)` forming a closed polygon.
      - Optionally compute: hull area and Perimeter length.
    - For intervals with `N < 3`: Mark hull as invalid or empty; record in metadata.
- Alpha-shape calculation (per interval, parallelized)
    - Alpha parameter
      - Load `alpha_param` from `analysis_parameters.json`.
      - It must be the same for all intervals.
    - For each interval with sufficient points (N threshold depends on alpha-shape implementation, typically `N ≥ 4`):
      - Compute alpha-shape of the point set in (x, y) using the fixed `alpha_param`.
      - Extract outer boundaries: Single polygon or multiple polygons.
      - For each interval, represent alpha-shape as: A list of polygons, each with arrays `(x_poly_j, y_poly_j)`.
- handle degenerate cases:
    - If alpha-shape degenerates into a line or point: Mark as degenerate; optionally skip plotting or represent as a minimal polygon.
    - For intervals with too few points: Mark as no alpha-shape.
- Visualization - Convex hull evolution
```

```
88 - Visualization - Alpha-shape evolution
```

Box B.2.11 Main Visualization Results (Raw Output)



Box B.2.12 Analysis Summary

```
1 To characterize fault-controlled triggering behavior, we
    quantify the spatiotemporal association between seismicity
     and mapped fault structures.
2
3 1. Key observations and findings
4 - Early inter-mainshock seismicity is tightly localized
    around the Mw 6.4 fault junction, with no clear migration
    toward the Mw 7.1 source region
```

- Physical interpretation: Immediately after a Mw 6.4 strike-slip event, static Coulomb stress changes ΔCFS are largest on nearby segments and especially at fault intersections and bends, where stress concentrates and diverse orientations are close to failure. The observed tight clustering near the Mw 6.4 fault junction is consistent with rapid failure of patches brought above the Mohr-Coulomb threshold by ΔCFS, with little time yet for stress redistribution or aseismic slip to influence more distant segments.

- From ~4 h onward, seismicity progressively focuses along the NW-SE fault corridor linking Mw 6.4 and Mw 7.1, with late-time hotspots anchored near the Mw 7.1 nucleation area
  - Physical interpretation: This evolution is characteristic of fault-guided stress transfer and progressive loading: after the initial Mw 6.4 static stress perturbation, stress and/or aseismic slip propagate along mechanically connected, favorably oriented strike-slip segments. Recurrent late-time density maxima near the Mw 7.1 hypocenter suggest that this patch was progressively brought closer to failure-either by increasing ΔCFS from surrounding events or by aseismic creep concentrating stress at locked barriers-culminating in dynamic rupture. The confinement of hotspots to mapped NW-SE traces implies that the triggering is structurally controlled rather than diffusive in the host rock.

- At the scale of the entire aftershock cloud, the spatial envelope expands and becomes multi-lobed, rather than collapsing onto the Mw 7.1 fault segment alone
  - Physical interpretation: The convex-hull expansion reflects network-wide activation of multiple faults that experienced positive ΔCFS from Mw 6.4 and its aftershocks, consistent with a broad, heterogeneous stress perturbation. The multi-lobed alpha-shapes track segment-scale heterogeneity in frictional strength, stress, and fault geometry: activity localizes into several structurally coherent lobes separated by gaps at barriers, bends or low-ΔCFS regions. Thus, while density maxima progressively focus onto the Mw 7.1 segment, the broader system displays geometric defocusing and fragmentation, indicating that Mw 7.1 emerges as one particularly critical lobe within a larger activated network, not as a uniquely isolated focus of seismicity.

- Synthesis of triggering style between Mw 6.4 and Mw 7.1: The Mw 6.4 event initiates a locally concentrated aftershock burst at its fault junction, consistent with static stress concentration. Over tens of hours, the active region expands across the fault network, but within this expanding set, both KDE and hotspots document a net along-strike focusing of the most active patch toward the future Mw 7.1 rupture. This pattern is best described as fault-controlled, along-strike progressive focusing embedded within a globally expanding, multi-lobed seismic envelope-supporting a triggered, structurally guided preparation of the Mw 7.1 mainshock rather than an independent, randomly located failure.

```
2. Overview and method context
- The workflow starts by extracting all catalog events between the Mw 6.4 and Mw 7.1 mainshocks and projecting their locations, together with mapped surface faults and the mainshock epicenters, into a local Cartesian x-y frame (01_prep_ridgecrest_data). Within this frame, a fixed 0.5 km grid and a global isotropic KDE bandwidth of 0.2 km are defined, and three consistent temporal partitions are built: Stage 1 (0-4 h, 30-min), Stage 2 (4 h-t71, 2-h), and 1-h envelopes. Spatial KDE fields are then computed on the fixed grid for all Stage-1 and Stage-2 intervals (02_kde_spatiotemporal_evolution), and interval-wise maxima ("hotspots") are extracted and tracked in time (03_hotspot_tracking). In parallel, for each 1-h interval, convex hulls and alpha-shapes of the event cloud are computed to characterize the evolving geometric envelope (04_geometric_envelope_evolution). All analyses use identical spatial extents and parameters across time so that observed evolution reflects changes in seismicity, not changes in processing.
- Key physical and algorithmic principles
    - Seismicity as a spatiotemporal point process: Earthquakes are treated as discrete points with rate density approximated by a nonparametric KDE estimate: \hat{\lambda}(x,y,t_i) = \sum_j K_h\bigl((x-x_j),(y-y_j)\bigr), where K_h is an isotropic Gaussian kernel with bandwidth h = 0.2\ km and the sum is over events in each time interval t_i.
    - Static stress transfer and Coulomb failure: While not explicitly computed, interpretation relies on the Coulomb failure concept: \Delta CFS = \Delta \tau + \mu' \Delta \sigma_n, where positive ΔCFS on favorably oriented, pre-stressed segments raises failure probability; intersections and bends amplify ΔCFS, explaining early clustering near Mw 6.4, and connected segments along the NW-SE corridor receive sustained positive ΔCFS, favoring later focusing near Mw 7.1.

3. Summary of figure-based results
Diagnostic A - Spatiotemporal evolution between Mw 6.4 and Mw 7.1
Observations:
- At stage1: 0~4 h
    - During the first few hours the sequence exhibits fault-controlled clustering at intersections and bends, but no progressive focusing toward the Mw 7.1 nucleation patch.
    - Triggering at this stage appears dominated by localized stress concentration and structural complexity around the Mw 6.4 rupture.
- At stage2: 4-33.8 h
    - a clear progressive north-northwestward focusing of seismicity from the Mw 6.4 rupture zone toward the Mw 7.1 nucleation area.
    - The migration is fault-guided: density maxima track along the mapped NW-SE fault segment rather than jumping off to new structures.
```

```
    - There is no strong evidence of bifurcation into multiple comparable lobes away from this corridor; secondary clusters on the conjugate system remain subordinate.
Synthesis of Observations:
    - Role of structural complexity: Immediately after the Mw 6.4 event, aftershocks concentrate at fault intersections and bends near the Mw 6.4 rupture and along the southern conjugate fault. This is consistent with static stress concentration and geometric complexity controlling early aftershock nucleation.
    - Spatiotemporal evolution of the main cluster: From ~4 h onward, the dominant aftershock density shifts progressively along strike toward the NW, eventually concentrating around the Mw 7.1 epicenter. The pattern is one of progressive spatial focusing along a single primary fault corridor, not broadening or splitting into independent lobes.
    - Nature of the triggering from Mw 6.4 to Mw 7.1: The Mw 6.4 rupture appears to have activated and loaded the adjacent NW-SE fault segment, promoting increasing seismicity in the zone that later hosted the Mw 7.1. The sustained and intensifying clustering near the Mw 7.1 location in the final ~10-15 h is consistent with a preparatory phase of progressive fault loading and local weakening, rather than a random or purely remote triggering. Because activity remains largely confined to mapped fault traces, the triggering mechanism is best described as fault-controlled progressive along-strike focusing, rather than lateral spreading or complex defocusing.

Diagnostic B - Alpha-shapes evolution of the 2019 ridgecrest catalog
Observations:
    - The alpha-shapes are broadly similar in outer extent to the hulls but reveal internal concavity and segmentation.
    - Early times (dark colors): The alpha-shape is relatively single-lobed, tightly hugging the early aftershocks near the Mw 6.4 epicenter and along its primary rupture trend.
    - Intermediate times: The envelope clearly bifurcates into at least two main lobes: A SW-NE lobe linking the Mw 6.4 region toward the central portion of the fault system. A second, more easterly lobe that tracks activity migrating toward the future Mw 7.1 rupture zone. Concavities open between these lobes, indicating regions with fewer or no events despite the overall hull still covering them.
    - Late times (green-yellow): Alpha-shapes remain multi-lobed, wrapping around fault intersections and step-overs. The lobe including the Mw 7.1 epicentral area becomes more prominent, but other lobes along adjacent fault strands persist; the envelope does not "collapse" solely onto the 7.1 fault.
Implication: The alpha-shapes show multi-lobed, fragmented evolution, consistent with spatially heterogeneous triggering along multiple fault segments, rather than a single, smoothly focusing aftershock front.
```

```
Diagnostic C – Convex hulls evolution of the 2019 ridgecrest catalog
Observations:
    – The earliest hulls (dark/purple curves) are compact and centered near the Mw 6.4 epicenter in the southwest.
    – As time progresses (colors transition to green–yellow), the hulls elongate strongly toward the northeast, ultimately spanning the region between the 6.4 and 7.1 epicenters and beyond.
    – The later hulls wrap around much of the main NW–SE fault system, with vertices extending: SW of the Mw 6.4 event to ~y ≈ –20 km, NE to ~y ≈ +20 km, and across a width of ~30–40 km in x.
    – The hull envelopes do not systematically shrink toward the Mw 7.1 location; instead they remain large and often expand to include additional distal clusters along neighboring fault strands.
Implication: In terms of convex hull geometry, the seismic cloud shows progressive expansion / lateral spreading, not simple geometric contraction toward the Mw 7.1 rupture zone.
```

B.3 Migration Directionality and Seismicity Rate Evolution

In this section, "triggering" is formulated as a quantifiable propagation process. Specifically, we statistically characterize whether seismicity exhibits structured migration through the temporal evolution of directional clustering intensity and occurrence rates. The analysis comprises two components. First, a directionally decomposed Ripley's K/L function is employed to identify the temporal evolution of clustering intensity across azimuths. Second, the study area is partitioned into structurally defined subregions to compare occurrence-rate variations and internal migration patterns across distinct fault units.

B.3.1 Temporal Evolution of Directional Clusters

To determine whether clustering intensifies preferentially along specific directions, we adopt a sector-based directional decomposition of Ripley's K/L function. Under a fixed characteristic radius of $r = 5$ km, a two-dimensional direction-time intensity distribution (direction-time heatmap) is constructed. Directional intensity time series for principal azimuthal bands are then extracted to quantify the temporal evolution of spatial anisotropy. The results show that immediately after the M_w 6.4 event, the clustering structure transitioned rapidly from a near-multidirectional distribution to pronounced anisotropy, progressively aligning with mapped fault strikes. During the first few hours following the mainshock, directional peaks fluctuated across multiple azimuths. Approximately four hours later, the dominant orientation gradually converged toward the NW-SE axis. Under a 0-180° axial definition, this corresponds to azimuthal bands of approximately 40-60° and 120-150°, which are highly consistent with the rupture corridor of the subsequent M_w 7.1 event. Directional intensity time series indicate that clustering strength along the NW-SE direction continuously increased throughout the inter-mainshock stage and reached a stabilized and amplified level several hours prior to the M_w 7.1 event. This evolution was not characterized by instantaneous orientation locking; rather, it reflects a gradual convergence from early multidirectional clustering toward a structurally parallel dominant axis, expressed

as persistent strengthening of directional selectivity. These observations demonstrate that inter-mainshock seismicity was neither randomly distributed nor isotropically expanding. Instead, in a statistical sense, it progressively migrated and focused toward the future M_w 7.1 rupture corridor. The systematic enhancement of directionality provides explicit azimuthal evidence supporting the interpretation of triggering as a measurable propagation process.

Box B.3.1 User Request

```
Investigate the spatiotemporal evolution of the earthquakes
    for the Ridgecrest earthquake sequence, spetial attention
    to the trigger mechanism from Mw 6.4 to Mw 7.1 mainshock.
Requirements:
1. Data Source: earthquake catalog is locate at "~/
    ridgecrest_catalog.csv", main_shock events is locate at "~
    /main_shock_events.csv", known fault is locate at "~/
    ridgecrest_surface_faults.json"
2. Compute sector_based directional Ripley's K_functions for
    the time interval of [mainshock64, mainshock71+10 hours]
```

Box B.3.2 Final Experimental Plan

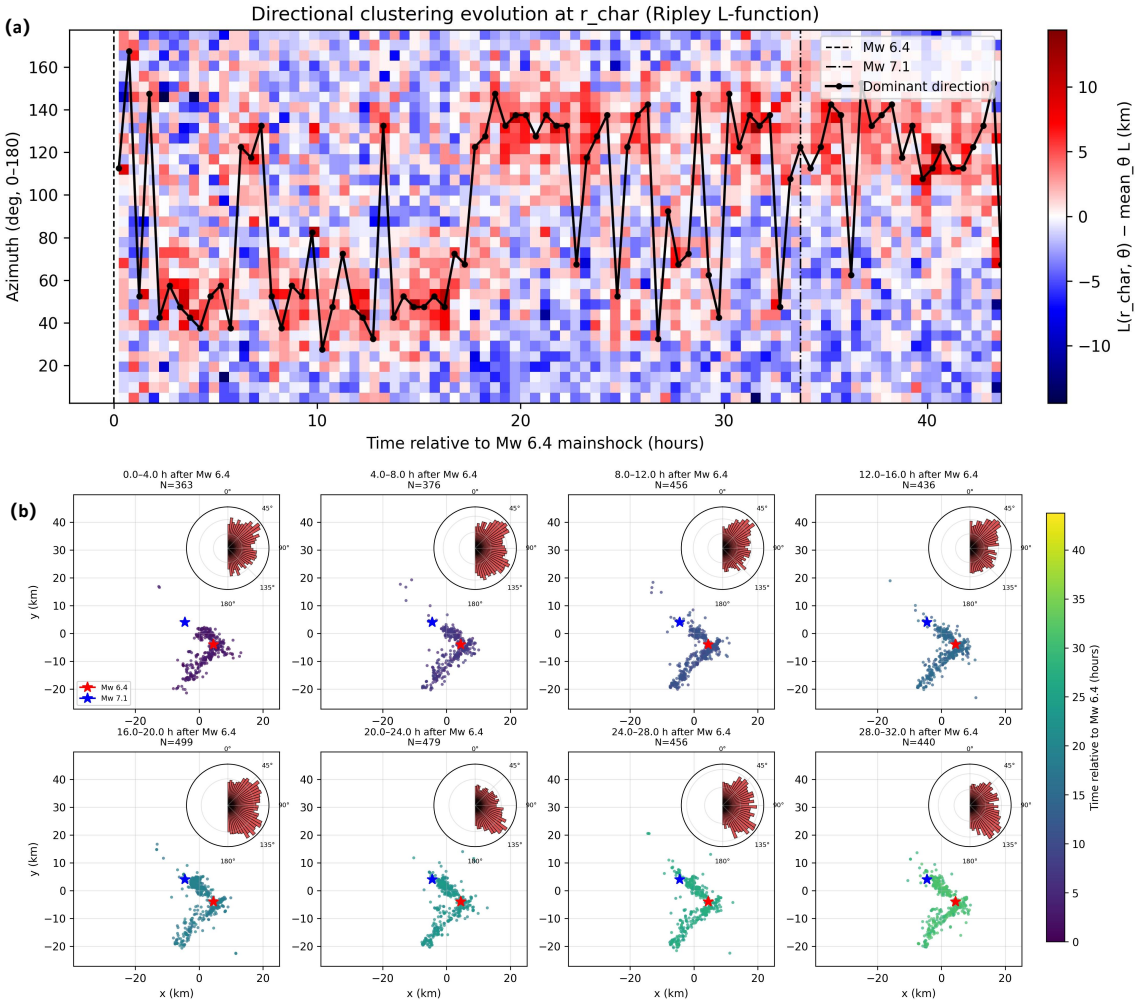
```
Experimental Plan: Quantitatively characterize how the
    spatial clustering and preferred directions of the 2019
    Ridgecrest seismicity evolve between the Mw 6.4 and Mw 7.1
     mainshocks, using sector_based directional Ripley's K/L_
    functions in 30_minute windows, and visualize these
    patterns with a time_direction heatmap and polar_rose/map
    panels.

1. Prepare catalogs, mainshocks, and spatial framework
- Load and harmonize earthquake catalog
- Load and identify mainshocks
- Define time window and 30_minute intervals
- Define spatial reference and project coordinates
- Outputs:
    - `ridgecrest_catalog_prepared.pkl` (or npz): all event
      information (time, relative times, x_km, y_km,
      depth_km, magnitude, interval index).
    - `ridgecrest_intervals_30min.pkl`: list of `(k,
      t_k_start, t_k_end, t_k_mid)`.
    - `ridgecrest_mainshocks.pkl`: mainshock metadata +
      projected coordinates.
    - `ridgecrest_faults_projected.pkl`: fault traces in
      projected coordinates.

2. Compute sector_based directional Ripley's K/L per 30_min
    interval
- Define spatial and directional parameters
    - Distance range: `r_max`: choose to capture fault_scale
      clustering; e.g., 12 km (configurable). `dr`: radial
      step; e.g., 0.5 km or 1 km. `r_values = [dr, 2dr,..,
      r_max]`.
    - Characteristic radius: `r_char`: single radius for
      heatmaps and roses; fix globally, e.g., 3 km or 5 km.
      Ensure `r_char` is exactly one of `r_values` or record
       index of nearest radius.
```

```
18      - Angular sectors: Azimuth range: [0°, 180°), Sector
          width: 5°.
19      - Minimum sample size per interval:
20      - Edge correction (simple, consistent): Use a rectangular
          -window border correction:
21  - Per-interval pairwise distances and orientations
22      - Subset events: Use `cat` where `interval_index == k`.
          Extract arrays `x_km`, `y_km`. `n_k = number of events
          `.
23      -  Compute pairwise separations: Use vectorized or KD-
          tree approach restricted to `d ≤ r_max` to avoid full
          O(n^2) where possible.
24  - Directional K and L estimation: Within each interval `k`
     with sufficient events
25      - Initialize arrays:
26      - Sector mapping:
27      - For each radius index `m` (radius `r_m`) and sector `j
          `: Count pairs with `d_ij ≤ r_m` and sector index = j.
28      - K estimator (no edge correction):
29      - L-function estimation
30      - Extract L at characteristic radius
31  - Aggregate K/L results across all intervals
32
33  3. Build and visualize time-direction heatmap
34  - Prepare data at characteristic scale
35      - Load `L_char_all` [N_intervals, N_theta], `
          time_midpoints`, `theta_centers`, `
          n_events_per_interval`.
36      - Convert `time_midpoints` to hours since `t64`
37      - Decide plotted quantity
38      - Mask low-count intervals
39  - Generate time-direction heatmap
40
41  4. Polar rose diagrams and spatiotemporal panels
42  - Common preparations
43      - Load all data.
44      - Fix a consistent map extent
45      - Decide color scale for event times:
46      - Normalize polar roses
47  - Window definition
48  - Directional L for each 4-hour window
49  - Directional L for catalog after Mw 6.4
```

Box B.3.3 Main Visualization Results (Raw Output)



Box B.3.4 Analysis Summary

```
Quantify analysis of the aftershock of 2019 ridgecrest Mw 6.4
1. Key observations and findings
- Fault architecture and mainshock locations: The 5,114 events within the 43.8-hour analysis window occupy two principal, intersecting lineations: a dominant NW-SE-striking band that hosts the Mw 7.1 mainshock and a shorter, oblique NE-SW-striking band centered on the Mw 6.4 mainshock. Seismicity forms a continuous NW-SE corridor between the two epicenters.
    - Physical interpretation. This geometry is characteristic of a conjugate strike-slip system: the NE-SW Mw 6.4 rupture lies on a secondary conjugate fault, while the NW-SE band corresponds to the primary through-going right-lateral structure that ultimately hosts the Mw 7.1. The continuous corridor of aftershocks implies mechanical connectivity between these faults, providing a ready pathway for stress transfer and rupture propagation.
```

- Directional clustering rapidly becomes anisotropic and fault-parallel after Mw 6.4: Finding. Sector-based Ripley's L at r_{char}=5 km shows that within the first few hours after Mw 6.4, clustering evolves from multi-directional to strongly anisotropic, with a persistent fault-parallel axis equivalent to a NW-SE trend (represented by azimuths in the ~40-60° and ~120-150° bands in the 0-180° axial convention). The dominant orientation fluctuates in the first ≈4 h but then converges toward this NW-SE axis.
    - Physical interpretation. In an initially perturbed stress field following the Mw 6.4 rupture, multiple fracture sets are briefly activated. As static and dynamic stress perturbations relax, slip localizes onto structures that are optimally oriented with respect to the regional shear stress-here, the NW-SE right-lateral system. The emergence of a consistent NW-SE maximum in L(r_{char},\theta) reflects this progressive focusing of shear failure onto the mechanically preferred fault set.
- Progressive migration and focusing of aftershocks onto the future Mw 7.1 rupture corridor: Polar-rose panels for successive 4-h windows and early 30-min windows after Mw 6.4 show that seismicity spatially migrates northwestward from the Mw 6.4 source and progressively fills a NW-SE corridor linking to the Mw 7.1 epicentral region. Throughout this migration, the polar roses increasingly exhibit a sharply peaked NW-SE lobe in L(5 km,\theta); the conjugate NE-SW lobe becomes comparatively weak.
    - Physical interpretation. The joint spatial-directional pattern indicates guided, fault-parallel propagation of seismicity from the Mw 6.4 rupture toward the Mw 7.1 fault. Static Coulomb stress changes from slip on the NE-SW Mw 6.4 fault are expected to increase shear and/or reduce normal stress on adjacent NW-SE right-lateral segments; once activated, those segments further concentrate stress along the through-going structure. The growing NW-SE lobe in the directional L-function captures this incremental loading and localization along the future Mw 7.1 rupture corridor.
- Stable, intensified NW-SE clustering in the hours before Mw 7.1: In the ≈8 hours preceding the Mw 7.1 mainshock, 30-min windows centered on the late part of the sequence show extremely strong and stable NW-SE clustering near the Mw 7.1 epicenter, with L(5 km,\theta) lobes sharply focused around the NW-SE axis and negligible power in other directions. The time-direction heatmap shows that this dominant orientation is already established $\gtrsim$10 hours before Mw 7.1 and persists across its occurrence, rather than rotating or changing abruptly at the mainshock time.

```
10      - Physical interpretation. The long-lived, highly
          anisotropic clustering aligned with the Mw 7.1 rupture
           plane is the signature of a preparatory phase: a
          critically stressed NW-SE fault accumulates slip in
          small events and aseismic deformation until a large
          rupture nucleates. Because the dominant orientation
          does not change at the Mw 7.1 origin time, the
          mainshock is best interpreted as the culmination of
          ongoing fault-parallel stressing and failure rather
          than as an abrupt switch to a new structure. This is
          consistent with a causal triggering chain in which the
           Mw 6.4 sequence progressively loads the Mw 7.1 fault
          through static stress transfer and ongoing aftershock
          activity.
11  2. Overview and method context
12  - A cleaned Ridgecrest catalog was first restricted to the
      interval from the Mw 6.4 origin time to 10 hours after the
       Mw 7.1 (43.8 h, 5,114 events) and projected into a local
      Cartesian (x,y) system together with mapped surface faults
      ; this dataset was segmented into 88 non-overlapping 30-
      min intervals. For each interval, pairwise inter-event
      distances and azimuths were computed up to 12 km, and
      sector-based Ripley's K and L functions were estimated in
      36 directional bins spanning 0-180° with 5° spacing,
      yielding K(r,\theta,t) and L(r,\theta,t) on a 12 (radii) ×
       36 (directions) grid for each time slice. The L-function
      at a characteristic radius r_{char} = 5 km was extracted
      to form L_{char}(\theta,t), which was then mean-centered
      over \theta for visualization as a time-direction heatmap
      and used directly to build polar rose diagrams in selected
       4-h and 30-min time windows, overlaid on event maps and
      surface faults to interpret the evolving relationship
      between clustering orientations, mapped structures, and
      the Mw 6.4-Mw 7.1 mainshocks.
13  - Key physical and algorithmic principles
14      - Directional Ripley's K for a planar point process. For
          events in a fixed study area of size A with n events
          in a given interval, the directional K in sector width
           \Delta\phi is estimated as: \hat{K}(r,\theta) \approx
           \frac{A}{n^2}\,\frac{\pi}{\Delta\phi}\,N_{\text{pairs
          }}\bigl(d_{ij}\le r,\ \theta_{ij}\in \text{sector
          around }\theta\bigr), where N_{\text{pairs}} counts
          inter-event pairs with separation d_{ij} within radius
           r and orientation \theta_{ij} falling in the sector.
          Under a homogeneous, isotropic Poisson process, \hat{K
          }(r,\theta) is independent of \theta; azimuthal
          variations therefore quantify anisotropic clustering.
15      - L-transform as a clustering diagnostic. The scalar L-
          function is defined by: L(r,\theta) = \sqrt{\frac{\hat
          {K}(r,\theta)}{\pi}} - r. For each direction \theta, L
          >0 implies excess clustering relative to a Poisson
          baseline, L<0 indicates inhibition/regularity, and the
           magnitude of L (here up to \sim 10 km) reflects the
          strength of clustering at scale r.
16  3. Summary of figure-based results
17  Diagnostic A - Ridgecrest time direction heatmap
18  Observations:
19  - First few hours (0-~4 h)
20      - Immediately after Mw 6.4, the dominant direction (black
          curve) is highly variable, jumping between:
```

- ~50–60°,
- ~110–170° in the first couple of hours.
- The heatmap colors in this period are patchy, with alternating red/blue in many directions.
- Interpretation:
- This suggests that in the immediate aftermath of the Mw 6.4, seismicity is not yet locked into a single, stable fault-parallel orientation.
- Multiple fracture sets or conjugate fault strands are being activated, consistent with mixed-orientation early aftershocks.
- Transition toward a NW–SE trend (~4–15 h)
- Between roughly 4 and 15 h:
- The black dominant-direction trace oscillates mostly between ~40–60° (lower half of the plot).
- The heatmap shows recurrent red bands near 40–70°, while other azimuths are not consistently red.
- Geological implication:
- A moderately dipping NW–SE oriented cluster (in map view, an oblique direction relative to the cardinal axes) becomes increasingly favored.
- This likely corresponds to one of the principal Ridgecrest fault segments activated by the Mw 6.4 event.
- Intermediate stage before the Mw 7.1 mainshock
- ~15–22 h: Mixed but trending
- In the 15–22 h window, the dominant direction shows a gradual rise from ~40–50° up toward 70–80°, with occasional excursions.
- heatmap:
- Stronger red patches develop between 60–90°,
- Blue patches appear more frequently at very low angles (<30°).
- Interpretation:
- The aftershock field continues to reorganize, with clustering increasingly concentrated along a direction ~70–80°.
- This may signal progressive localization of seismicity onto a particular fault orientation within the complex rupturing zone.
- ~22–34 h: Stabilization on a high azimuth (~120–140°)
- From about 22 h up to the Mw 7.1 mainshock (~34 h):
- The dominant direction locks into higher azimuths, mainly ~120–140°, with relatively small fluctuations.
- The heatmap displays a broad, persistent red band between roughly 110 and 150°, while directions below ~70° are often neutral or blue.
- This pattern is the clearest and most coherent segment in the plot.

Diagnostic B – Directional clustering from polar roses

Observations:

- Early 0–8 h after Mw 6.4: seismicity is concentrated around the Mw 6.4 hypocentral area and along a NW–SE trend extending slightly SE of it.

```
    - 8–16 h: activity begins to extend more clearly toward the NW, along the future Mw 7.1 rupture zone.
    - 16–32 h: a well-defined NW-trending line of events develops that links the Mw 6.4 region to the Mw 7.1 epicentral area.
    - The dominant L(5 km, θ) lobe is consistently oriented ~135°–150°, i.e., a NW–SE lineation (since the azimuths are axial over 0–180°).
    - Secondary, weaker clustering appears in a near-orthogonal band around ~45°–60°, compatible with the conjugate NE–SW faulting seen in the mapped surface ruptures.
    - The strength of the NW–SE lobe increases as time proceeds:
        - 0–4 h: clear but moderate lobe at ~140°.
        - 8–16 h: lobe amplitude grows; clustering is strongly focused along the NW–SE trend cutting through both mainshock epicenters.
        - 16–32 h: the NW–SE lobe dominates the rose diagrams, while orthogonal directions are weak.
Implication: On 4–h scales, the sequence rapidly organizes into a fault-parallel NW–SE cluster that links the Mw 6.4 and Mw 7.1 segments, with directional clustering increasingly aligned with the eventual Mw 7.1 rupture orientation.
```

B.3.2 Quantitative Analysis of Fault Segmentation: Differences in Propagation at the Fault Scale

To further examine whether activation patterns differ across structural units, the study area is divided according to fault geometry into two regions: Region A (NE-SW trending, associated with the M_w 6.4 fault system) and Region B (NW-SE trending, associated with the M_w 7.1 fault system). Within identical temporal windows, seismic occurrence rates, cumulative event counts, and internal migration patterns are quantified separately for each region. The results indicate that at the time of the M_w 6.4 event, initial activation in both regions was nearly synchronous. However, systematic temporal divergence emerged during subsequent evolution. Rate fluctuations in Region B consistently led those in Region A by approximately nine hours, indicating phased response differences. Region A exhibited near-synchronous post-mainshock activation with relatively uniform spatial distribution. No significant distance-ordering effect was observed among grid cells, consistent with cooperative and widespread activation. Its seismic productivity was substantially higher, with occurrence rates reaching 60-80 events per hour, approximately 2-7 times that of Region B within comparable time windows. The cumulative number of inter-mainshock events in Region A was approximately 2100-2200, about 1.6-1.7 times that in Region B. In contrast, Region B displayed stronger spatial concentration and clearer temporal stratification. During the early post-M_w 6.4 stage, activity was concentrated near the epicentral vicinity. Subsequently, peak occurrence rates were progressively delayed with increasing distance, revealing directional propagation from proximal to distal segments. Approximately 17-18 hours after the M_w 6.4 event, Region B experienced a pronounced transient intensification phase, during which its occurrence rate briefly exceeded that of Region A. This episode may reflect localized stress concentration or the reinforcing

effect of moderate-magnitude events along the NW-SE structure, thereby enhancing triggering efficiency on that fault segment.

Overall comparison reveals distinct propagation modes at the fault scale. Region A is characterized by high-frequency, near-synchronous system-level activation, whereas Region B exhibits directionally organized and temporally stratified sequential propagation. Seismicity within Region B progressively concentrated toward the eventual M_w 7.1 nucleation zone, while Region A did not display comparable directional ordering. These differences indicate pronounced propagation heterogeneity during the inter-mainshock stage. Although the M_w 6.4 event triggered a broad regional response, the subsequent evolutionary pathways differed across structural units. The NE-SW fault system primarily manifested cooperative high-frequency activation, whereas the NW-SE fault system underwent a directionally organized and temporally layered propagation process. This contrast provides quantitative constraints on structural coupling and stress transfer mechanisms linking the two mainshocks.

Box B.3.5 User Request

```
Investigate the triggering mechanism of the M7.1 earthquake by the M6.4 earthquake within the Ridgecrest earthquake sequence. with a focus on comparing two fault-oriented regions, by characterizing the spatiotemporal patterns of seismic rate evolution: 1) characterize whether the activation of the two regions following the Mw 6.4 is synchronous or exhibits systematic temporal offsets. 2) identify and quantify systematic differences in the seismic rate evolution and triggering behavior. 3) identify the spatial inhomogeneity and temporal ordering of the triggering process inside each region after the Mw 6.4 mainshock, in order to assess whether fault activation is spatially coherent or directionally evolving
Requirements:
1. Data Source: earthquake catalog is locate at "~/ridgecrest_catalog.csv", main-shock events is locate at "~/main_shock_events.csv", known fault is locate at "~/ridgecrest_surface_faults.json"
2. Regional and Time Window definition
- Time Window: [catalog start time, mainshock71]
- Two rectangular regions are defined along the fault direction:
- Region A: along the NE-SW fault direction, coordinates:
[-117.62120049,   35.52601731],
[-117.66574867,   35.57056548],
[-117.47482793,   35.76148622],
[-117.43027975,   35.71693805]
- Region B: along the NW-SE fault direction, coordinates:
[-117.49103561,   35.7507739 ],
[-117.55467585,   35.68713365],
[-117.77105269,   35.90351049],
[-117.70741244,   35.96715074]
3. Seismic rate statistic and analysis for two regions
4. Grid seismicity rate statistics and analysis for two regions
```

Box B.3.6 Final Experimental Plan

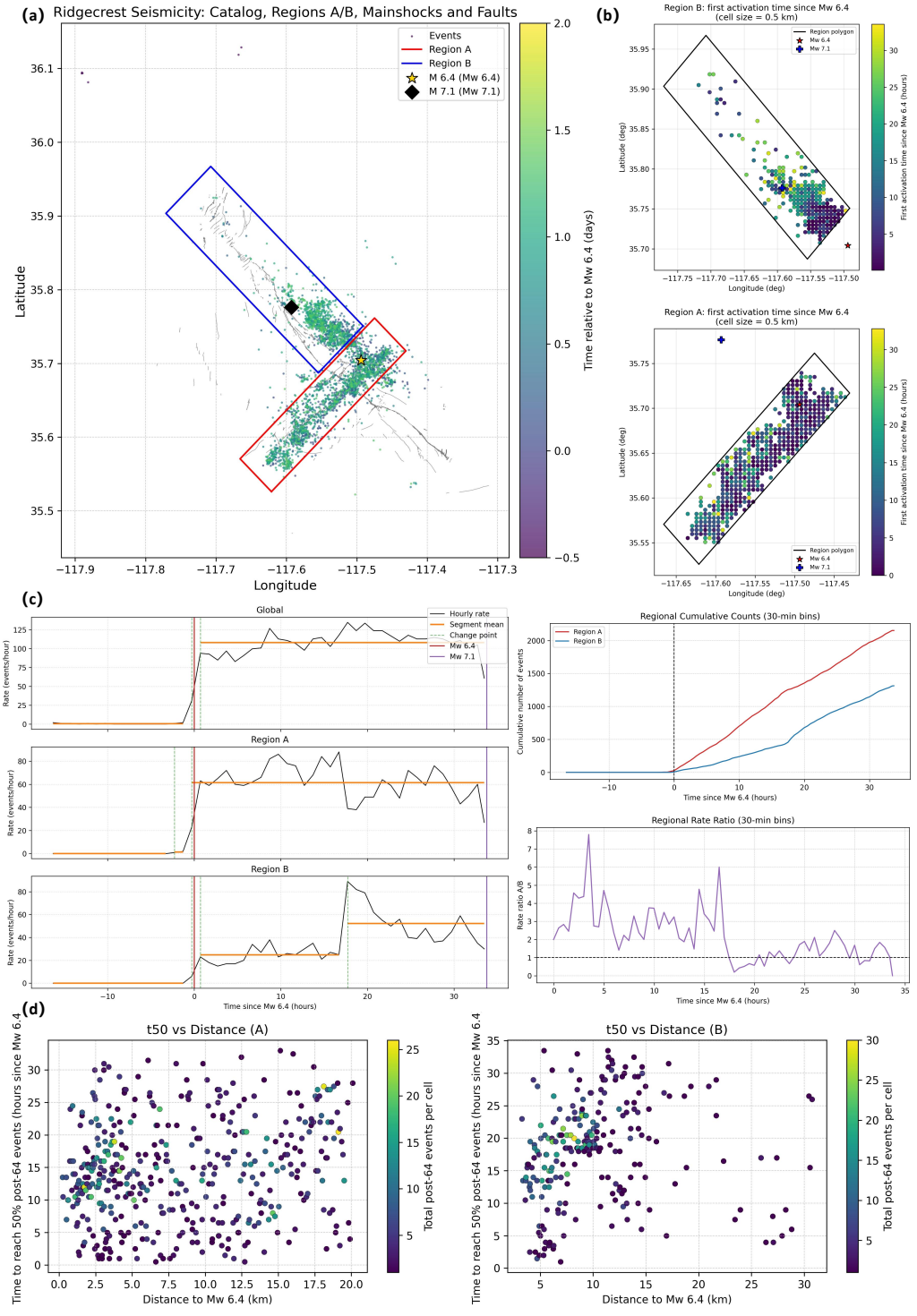
```
Experimental Plan: Use the Ridgecrest 2019 catalog to quantify how the Mw 6.4 event triggered seismicity before the Mw 7.1 mainshock, focusing on two fault-oriented regions (A: NE-SW, B: NW-SE). Specifically: 1) Determine whether activation in A and B after Mw 6.4 is synchronous or exhibits systematic temporal offsets. 2) Identify and quantify systematic differences in seismic rate evolution and triggering behavior between A and B. 3) Within each region, resolve spatial inhomogeneity and temporal ordering of triggering (directional vs spatially coherent activation) using 0.5 km × 0.5 km grids.

0. Top Level tasks
- 01_prep_and_map_ridgecrest.py: Load catalogs and faults; define time window; construct region polygons; assign events to regions; compute times relative to Mw 6.4; produce overview map.
- 02_regional_rate_analysis_AB.py: Using region-tagged catalog, build 30-min and hourly seismic rates for A and B; derive quantitative activation metrics; visualize rates and differences.
- 03_define_grids_and_assign_events.py: Define 0.5 km × 0.5 km grids within each region in a local Cartesian frame, compute cell distances to Mw 6.4, sort indices, and assign events to cells (parallelized).
- 04_grid_rate_analysis_and_spatiotemporal_patterns.py: For each cell, compute 30-min and hourly rates (parallelized), cumulative statistics, and create spatial and time-cell visualizations to assess inhomogeneity and directional triggering.

1. Catalog preparation, region definition, and overview map: Create a time-windowed, region-tagged catalog with times referenced to Mw 6.4, and generate the requested overview map with regions, mainshocks, faults, and time-colored events.
- Load catalogs and mainshocks
    - Read the main catalog with `event_time` parsed as UTC `datetime` (naive).
    - Read the mainshock file; construct a `datetime` for each row from `yr, mon, day, hr, min, sec` (including fractional seconds).
    - Identify: Mainshock64: row with `mag == 6.4`. Mainshock71: row with `mag == 7.1`.
    - Extract: `t64`, `t71`: origin times. `latR_64, lonR_64, depR_64` and `latR_71, lonR_71, depR_71`.
- Define and apply global time window
- Define regions A and B and assign membership
    - Region A (NE-SW oriented polygon):
        - `[-117.62120049, 35.52601731]`
        - `[-117.66574867, 35.57056548]`
        - `[-117.47482793, 35.76148622]`
        - `[-117.43027975, 35.71693805]`
    - Region B (NW-SE oriented polygon):
        - `[-117.49103561, 35.7507739 ]`
        - `[-117.55467585, 35.68713365]`
        - `[-117.77105269, 35.90351049]`
```

```
26          - `[-117.70741244, 35.96715074]`
27  - Load fault traces
28
29  2. Regional seismic rate analysis (A vs B): Construct 30-min
       and hourly seismic rates for regions A and B over the time
        window [catalog start, Mw 7.1], quantify activation
       timing and rate evolution (including possible offsets),
       and provide visual and numerical comparisons.
30  - Load inputs and define time axes
31      - Load catalog; parse times and region flags (`
           in_region_A`, `in_region_B`).
32      - Extract `t_start`, `t64`, `t71` from metadata.
33      - Define common bin edges:
34          - 30-min bins: edges from `t_start` to `t71` with
               step 30 minutes.
35          - 1-hour bins: edges from `t_start` to `t71` with
               step 1 hour.
36      - Compute bin centers and relative times:
37          - `t_mid_30`, `t_mid_60`.
38          - `t_mid_30_rel64 = (t_mid_30 - t64)` in hours.
39          - `t_mid_60_rel64` similarly.
40  - Build regional subsets
41  - Compute regional rates (with simple parallelization)
42  - Activation timing and rate evolution metrics
43  - Visualizations for regional rates
44
45  3. Grid definition and event-to-cell assignment: Subdivide
       regions A and B into 0.5 km × 0.5 km grid cells, compute
       distance from each cell center to Mw 6.4, sort cells by
       this distance, and assign events to cells. This underpins
       cell-based rate and triggering analysis.
46  - Load data and define local projection
47      - Load catalog and metadata.
48      - Establish a local Cartesian coordinate system
49      - Apply this transformation
50  - Define 0.5 × 0.5 km grids within each region
51  - Sort cells by distance to Mw 6.4 and finalize indices
52  - Assign events to grid cells (parallel)
53
54  4. Grid-based rate analysis and spatiotemporal triggering
       patterns: Compute 30-min and hourly seismicity rates for
       each grid cell, derive cumulative and onset metrics, and
       generate spatial and time-cell visualizations to assess
       inhomogeneity and directional ordering of triggering
       within each region.
55  - Load grid and event-cell data
56  - Compute per-cell seismic rates (parallel)
57  - Cumulative counts and cell-level summary metrics
58  - Spatial maps of cumulative seismicity (requested)
59  - Time-cell rate images to reveal directional triggering
60  - Distance vs activation time plots
61  - Optional along-strike analysis (if you want stronger
       directional constraints)
```

Box B.3.7 Main Visualization Results (Raw Output)



Box B.3.8 Analysis Summary

```
1 Quantify analysis of the regional seismicity for aftershock
    of 2019 ridgecrest Mw 6.4
2
3 1. Key observations and findings
```

- Regional activation is near-synchronous at Mw 6.4, but subsequent evolution is time-shifted between Regions A and B. Onset: Activation of Regions A and B is effectively simultaneous at Mw 6.4. Evolution: After onset, fluctuations in Region B's rate systematically lead those in Region A by ~9 h.
    - Physical interpretation: The synchronous jump is consistent with immediate static Coulomb and dynamic stress changes from the Mw 6.4 rupture affecting both the NE-SW and NW-SE fault systems nearly instantaneously. The subsequent ~9 h lead of Region B suggests additional time-dependent processes-such as postseismic slip on the Mw 6.4 fault or evolving stress redistribution-modulate seismicity differently in the two domains, with the NW-SE system (Region B) responding earlier to these secondary stress changes than the NE-SW system (Region A).

- Region A is more productive and more steadily active than Region B: Immediately after Mw 6.4, Region A's rate exceeds Region B by factors of 2-7; A reaches ~60-80 events/h while B is typically <50 events/h in the same window. Over the full Mw 6.4-Mw 7.1 interval, Region A accumulates roughly 1.6-1.7× more events (~2100-2200 vs. ~1300). Region B shows a pronounced transient burst around 17-18 h after Mw 6.4, during which its rate briefly exceeds that of Region A.
    - Physical interpretation: Region A straddles the Mw 6.4 rupture and adjoining NE-SW faulting; it lies within zones of large positive Coulomb stress change, so a high and sustained aftershock productivity is expected. Region B is farther from the Mw 6.4 rupture and partly in a less favorably stressed configuration immediately after the event, explaining lower mean rates. The transient high-rate episode in Region B likely reflects a localized stress concentration and/or moderate events on the NW-SE structure, transiently boosting local triggering and potentially contributing to the preparation of the Mw 7.1 fault patch.

- Within Region A, triggering is spatially widespread and not distance-ordered: Post-Mw 6.4 seismicity is distributed along most of Region A, with per-cell counts generally modest and no single dominant high-rate patch. The time-cell rate image shows that many cells across a broad range of distance-ordered indices become active within the first few hours, without a coherent front migrating outward. Both first-event delays and t50 (time to 50% of post-64 events) span almost the full 0-30+ h range at all distances (0-20 km) from Mw 6.4; early and late activation occurs at both short and long distances.

- Physical interpretation: The absence of a distance trend indicates that Region A experienced a spatially coherent, near-simultaneous stress perturbation from Mw 6.4 that rapidly brought a large fraction of the NE-SW system close to failure. This pattern is characteristic of broad static stress changes and dynamic triggering, rather than a slowly migrating front or localized aseismic slip propagating along the NE-SW fault. Subsequent variability in per-cell rates reflects local heterogeneities in fault strength and small-scale stress, but not a systematic directional triggering process.

- Within Region B, triggering is spatially inhomogeneous and temporally ordered toward the Mw 7.1 nucleation area: Region B exhibits a strongly localized high-productivity cluster near the eventual Mw 7.1 hypocenter; cells closer to the Mw 6.4 epicenter are not the most productive. The time-cell rate image shows that enhanced rates appear first in cells closer to Mw 6.4 / southern Region B, then progressively in more distant cells, culminating in intense activity in a narrow band of cell indices near the Mw 7.1 patch ≈10-20 h after Mw 6.4. First-event time and, to a lesser degree, t50 increase with distance from Mw 6.4: nearer cells (4-8 km) often activate within 0-5 h, whereas more distant ones (>15-20 km) commonly activate >15-20 h after Mw 6.4.
    - Physical interpretation: This distance-ordered and spatially focused activation is consistent with a directional triggering process propagating along the NW-SE fault system toward the Mw 7.1 nucleation zone. A plausible mechanism is progressive stress loading of the NW-SE fault by post-Mw 6.4 processes (e.g., afterslip on the Mw 6.4 fault, viscoelastic relaxation, or cumulative loading from intermediate-magnitude events), which increases Coulomb stress and brings the Mw 7.1 patch to failure over several to tens of hours. The contrast with Region A's non-directional response reinforces the view that the Mw 6.4 event not only triggered widespread aftershocks but also initiated a focused preparatory phase on the NW-SE fault that culminated in the Mw 7.1 mainshock.

- Integrated interpretation: triggering of the Mw 7.1 event by Mw 6.4: Immediate, coherent triggering in both regions at Mw 6.4. Stronger, more diffuse aftershock behavior in Region A, characteristic of typical mainshock-aftershock response on the Mw 6.4 fault system. A structured, distance-ordered intensification in Region B focused near the Mw 7.1 hypocenter, suggesting triggered nucleation of Mw 7.1 rather than an independent, background event. Physically, the Mw 6.4 earthquake appears to have: Directly loaded and fractured the NE-SW system (Region A), generating abundant aftershocks. Simultaneously perturbed the NW-SE right-lateral fault, with subsequent time-dependent stress evolution leading to progressive activation and concentration of seismicity at the Mw 7.1 patch, ultimately promoting rupture.

2. Overview and method context

```
- A unified workflow was implemented in four modular experiments. ‘01_prep_and_map_ridgecrest‘ built a time-windowed catalog (from first catalog event to Mw 7.1) with times referenced to Mw 6.4, tagged events by membership in two fault-oriented polygons (Region A: NE-SW; Region B: NW-SE), and overlaid these on mapped surface faults for structural context. ‘02_regional_rate_analysis_AB‘ converted the region-tagged catalog into 30-min and hourly seismicity rate time series for A and B, quantified activation metrics (onset, peak, pre/post-64 contrasts), and measured the temporal lag between regions by cross-correlating their rate histories. ‘03_define_grids_and_assign_events‘ established a local Cartesian (km) frame centered at Mw 6.4, discretized each region into 0.5×0.5 km cells, ordered cells by distance to Mw 6.4, and assigned events to cells using parallelized event-cell mapping. ‘04_grid_rate_analysis_and_spatiotemporal_patterns‘ then computed per-cell 30-min and hourly counts/rates, cumulative statistics, and cell-level activation times, and synthesized these into spatial cumulative maps, time-cell rate images, and distance-dependent activation metrics to resolve spatial inhomogeneity and directional triggering within each region.

3. Summary of figure-based results
Diagnostic A - Geometry of regions vs. mainshocks and mapped faults
Observations:
    - Region A (red rectangle)
        - Trends roughly NW-SE, centered on the Mw 6.4 epicentral area (yellow star at ~35.71°N, -117.50°E).
        - Encloses the densest early aftershock cloud that aligns with the NE-SW-striking left-lateral fault system mapped in grey.
        - Extends southeastward beyond the Mw 6.4 epicenter, following the mapped surface fault traces.
    - Region B (blue rectangle)
        - Oriented more NNW-SSE (or NE-SW with steeper dip in map view) and is centered on the later Mw 7.1 rupture area (black diamond at ~35.78°N, -117.60°E).
        - Its long axis aligns with the principal right-lateral fault that hosted the Mw 7.1 event.
        - It overlaps the northwestern continuation of the seismicity cloud that emerges after the Mw 6.4.
    - Fault traces, the grey linework shows two main fault trends:
        - A SE-NW left-lateral system in the southern part, consistent with Region A and the Mw 6.4 mainshock.
        - A more NNW-SSE right-lateral system in the north, coinciding with Region B and the Mw 7.1 epicenter.
Implication: The regional boxes are well chosen to isolate the two main structural domains of the sequence: the Mw 6.4 rupture zone (Region A) and the Mw 7.1 rupture zone (Region B).
```

```
Diagnostic B – First activation times: spatial maps for region A & B
Observations:
    Region A:
        – First activation times (in hours since Mw 6.4) are mostly in the 0–10 h range across the entire region.
        – There are scattered pockets with later activation (up to ~30 h), but they are distributed throughout, not confined to one structural end.
        – The cells near both the southern and northern edges of the polygon show early activation; no coherent gradient is apparent along strike.
    Region B:
        – Near the southern part of Region B, around the Mw 7.1 epicenter, first activation times are very early (≈0–5 h).
        – Moving north and northwest along the polygon, first activation times become systematically later (10–25+ h).
        – Cells in the far northern part of the polygon sometimes activate very late or remain inactive (effectively beyond the examined window).
Interpretation:
    – Region A behaves as a spatially coherent block: most of its 0.5 km cells experience their first post–6.4 event within a few hours. The absence of a strong along–strike gradient indicates limited directional migration within this time window; triggering appears to act nearly instantaneously at the scale of this segment.
    – Region B shows a clear temporal gradient: early activation near the Mw 7.1 area and increasingly delayed activation with distance from that zone. This points to a directionally evolving triggering process within Region B, with activity concentrating and intensifying near the eventual Mw 7.1 nucleation area early in the sequence, then gradually involving more distant cells.

Diagnostic C – Seismicity–rate evolution and Bayesian change points
Observations:
    – Global:
        – Rate is essentially zero before Mw 6.4, then jumps sharply in the first hour after Mw 6.4 to ~90 events/h and remains high (>100 events/h for many hours).
        – Bayesian change–point model:
            – One main post–6.4 segment with a nearly constant mean rate ~100 events/h from shortly after Mw 6.4 until just before Mw 7.1.
            – A single change point is picked just after Mw 6.4 (vertical green dashed line slightly to the right of the red Mw 6.4 line).
        – There is no additional global change point close to the time of Mw 7.1 within this pre–7.1 window, implying that the M7.1 did not require a distinct, sequence–wide rate increase in the hours beforehand.
```

```
59      - Region A (NE-SW fault-oriented)
60          - Immediately after Mw 6.4, Region A's rate jumps to
              ~60-80 events/h.
61          - Rate remains elevated and relatively stable
              throughout the 0-34 h window, with moderate
              fluctuations but no long lull.
62          - Bayesian segmentation:
63              - First post-6.4 segment begins essentially at
                  the time of Mw 6.4 (green change-point line
                  nearly coincident with the red line).
64              - The modeled post-6.4 mean rate is ~60 events/h
                  and persists to just before Mw 7.1 (no later
                  regional change point).
65          - Interpretation from the rate series:
66              - Region A is immediately and strongly activated
                  by the Mw 6.4 mainshock.
67              - Its high activity is continuous in the lead-up
                  to Mw 7.1 and does not show a second, discrete
                   rate transition that would signal a late-
                  stage preparatory phase.
68      - Region B (NW-SE fault-oriented)
69          - hourly rate after Mw 6.4:
70              - Increases to ~20-30 events/h within the first
                  few hours.
71              - A second, more pronounced jump to ~80-90 events
                  /h occurs later, around 18 hours after Mw 6.4.
72          - Bayesian segmentation:
73              - First post-6.4 segment: ~25 events/h beginning
                  soon after Mw 6.4.
74              - A clear change point at ~18 h marks transition
                  to a higher-rate segment (~50-55 events/h).
75          - Compared with Region A:
76              - Early post-6.4 rates are systematically lower
                  in Region B.
77              - The substantial rate increase in B is delayed
                  by ~18 h relative to the Mw 6.4 origin,
                  whereas A shows its major rate increase
                  immediately.
78
79  Diagnostic D - time to 50% of post-64 events vs distance
80  Observations:
81      - Region A
82          - t50 values span roughly 0-32 h across the full 0-20
              km distance range.
83          - There is no systematic increase of t50 with
              distance: early and late t50 values occur at all
              distances.
84          - high-productivity cells (bright colors) show t50
              around ~10-20 h, but again distributed over a
              broad distance range.
85      - Region B
86          - For distances ~4-10 km, t50 is clustered mostly
              between ~10-22 h, with higher-productivity cells
              showing t50 around ~15-22 h.
```

```
87          - At larger distances (>15-20 km), many cells have
              t50 values that are either late (>20 h) or poorly
              constrained (few events), and there are fewer high
              -productivity cells.
88          - Compared with first-event times, the t50 pattern is
              somewhat more scattered, but there remains a
              tendency for nearer, productive cells to reach 50%
              of their events earlier than distant, low-
              productivity cells.
89  Implication:
90      - Region A: The build-up of seismicity in Region A is
          temporally scattered and not distance-ordered. half of
          the aftershock productivity in a given cell is
          reached at times that do not depend strongly on how
          far that cell is from Mw 6.4.
91      - Region B's cumulative buildup is more focused and
          somewhat earlier at intermediate distances (the
          concentrated patch near the Mw 7.1 area), reinforcing
          the picture of a progressive concentration of activity
          near that patch.
```

B.4 Magnitude-Frequency Distribution and Temporal Variability of the b Value

Building upon the preceding spatiotemporal structural analysis, this section further constrains stress evolution during the inter-mainshock stage from the perspective of the magnitude-frequency distribution. Within the framework of the Gutenberg-Richter relation, the b value characterizes the relative proportion of events of different magnitudes and is commonly regarded as a statistical proxy for differential stress level, fault surface roughness, and rupture-scale distribution. Accordingly, if an organized stress redistribution process occurred between the two mainshocks, it should leave identifiable signatures in either the spatial structure or temporal evolution of the b value. To address this objective, the analysis is conducted at two levels. First, we examine whether a continuous b-value anomaly belt consistent with fault geometry developed during the inter-mainshock stage. Second, we evaluate the temporal evolution of the b value within the M_w 7.1 source region and compare it with that of the M_w 6.4 rupture zone to assess whether statistically significant pre-nucleation anomalies can be identified.

B.4.1 Spatial b-value structure and stress transfer

Between the M_w 6.4 and M_w 7.1 events, the spatial distribution of b values exhibits pronounced structural heterogeneity. A continuous and narrow low-b corridor (approximately 0.5-0.7) developed along the NW-SE direction. Its geometric extent aligns with the future M_w 7.1 rupture orientation and closely coincides with the principal anisotropic axis identified by the directionally decomposed Ripley's L function. This spatial consistency indicates that the anomaly in the magnitude-frequency distribution is not an isolated statistical fluctuation, but rather embedded within the overall spatial organization governed by fault geometry. The low-b structure traverses the eventual M_w 7.1 nucleation zone, suggesting that the future rupture segment had already exhibited a relative suppression of small events and an enhanced proportion of larger events during the inter-mainshock stage. Such low-b distributions are commonly interpreted as reflecting elevated effective differential

stress or mechanically stronger, more locked fault segments. In contrast, surrounding regions display relatively elevated b values, corresponding to a higher proportion of small events. The overall spatial pattern therefore consists of a low-b core developed along the principal fault corridor, flanked by comparatively higher-b zones. This configuration is inconsistent with uniform postseismic relaxation or random spatial dispersion. Instead, it accords with a model of directional stress redistribution, in which stress was not uniformly dissipated at the regional scale but was maintained or re-concentrated along specific structural units. Consequently, the future M_w 7.1 rupture segment resided within a statistically elevated stress environment during the inter-mainshock stage.

Box B.4.1 User Request

```
Analysis the b-value changes in the Mw 7.1 rupture region
    after the Mw 6.4 mainshock.
Focus on the time window after the Mw 6.4 mainshock: [
    mainshock64, mainshock71].
Requirements:
1. Data Source: earthquake catalog is locate at "~/
    ridgecrest_catalog.csv", main-shock events is locate at "~
    /main_shock_events.csv", known fault is locate at "~/
    ridgecrest_surface_faults.json", and a longtern background
     catalog is located at "~/
    catalog_2year_background_before_64.csv"
2. Long-term reference b-value (qualitative anchor): Estimate
     a regional b-value from the background catalog. Use it
    only to indicate the typical b-value range of the region.
    Do not use it as a baseline for Δb, anomaly amplitude, or
    significance testing. Do not directly compare its
    numerical value with b values from the Mw6.4-Mw7.1 window.
3. Estimate a spatially resolved b-value field to analyze the
     b-value changes in the Mw 7.1 rupture region after the Mw
     6.4 mainshock.
4. b-value anomaly detection: Detect the b-value anomaly
    regions using the smoothed b-value field. Spetially
    attention to the local low-b value regions and large high-
    b value regions. Define a low-b threshold relative to the
    regional reference (e.g., b < b_regional - 1σ). Identify
    spatial clusters of low-b regions. Assess whether low-b
    clusters preferentially align with the future Mw 7.1
    rupture direction.
```

Box B.4.2 Final Experimental Plan

```
Experimental Plan: Estimate how the b-value varies in space
    within the Mw 7.1 rupture region during the interval
    between the Mw 6.4 and Mw 7.1 mainshocks, using an event-
    centered adaptive rectangular-kernel method and a single
    Mc for that window. Use the 2-year background catalog only
     to define a qualitative regional b-value range, not for Δ
    b or formal significance tests. Implement Mc and b
    estimation with SeismoStats, and use parallel computation
    where heavy.

0. Top Level tasks
```

```
- 01_prepare_catalogs_and_coordinates: Load all catalogs; define mainshock times; extract [Mw 6.4, Mw 7.1] window; define local Cartesian coordinates and rupture-direction proxy; save prepared datasets.
- 02_mc_and_reference_bvalues.py: Estimate a single Mc for the [Mw 6.4, Mw 7.1] catalog with SeismoStats. Estimate a long-term regional b-value and its uncertainty from the 2-year background catalog (qualitative anchor). Produce FMD and b-distribution plots.
- 03_event_centered_adaptive_bvalues.py: Implement the event-centered adaptive rectangular kernels for the [6.4-7.1] window. For each valid kernel, estimate local b and bootstrap uncertainty using SeismoStats with fixed Mc. Parallelize over epicenters; output per-event kernel table and quick maps.
- 04_grid_smoothing_and_anomaly_analysis.py: Map event-centered b-values to a spatial grid via kernel footprints. Smooth the b field. Detect low- and high-b anomaly regions relative to the regional *background* b range. Examine low-b cluster alignment with the Mw 7.1 rupture direction. Produce final b-value and anomaly maps.

1. Catalog prep and local coordinates
- Load input catalogs
    - Parse `datetime` as UTC `datetime`. If inconsistent, rebuild from `yr, mon, day, hr, min, sec`.
    - Ensure `latR, lonR, depR, mag` are numeric; drop invalid rows.
    - Retain at least: `datetime, latR, lonR, depR, mag`.
- Extract [Mw 6.4, Mw 7.1] time window
    - Define time window:
    - Filter catalog:
    - QA:
        - Count events (`N_64_71`).
        - Record `M_min`, `M_max`, mean magnitude.
        - Check that at least hundreds of events exist; note in summary.
- Define analysis region and local Cartesian coordinates
    - Region of interest (ROI)
    - Local Cartesian projection (km)
    - Rupture-direction proxy

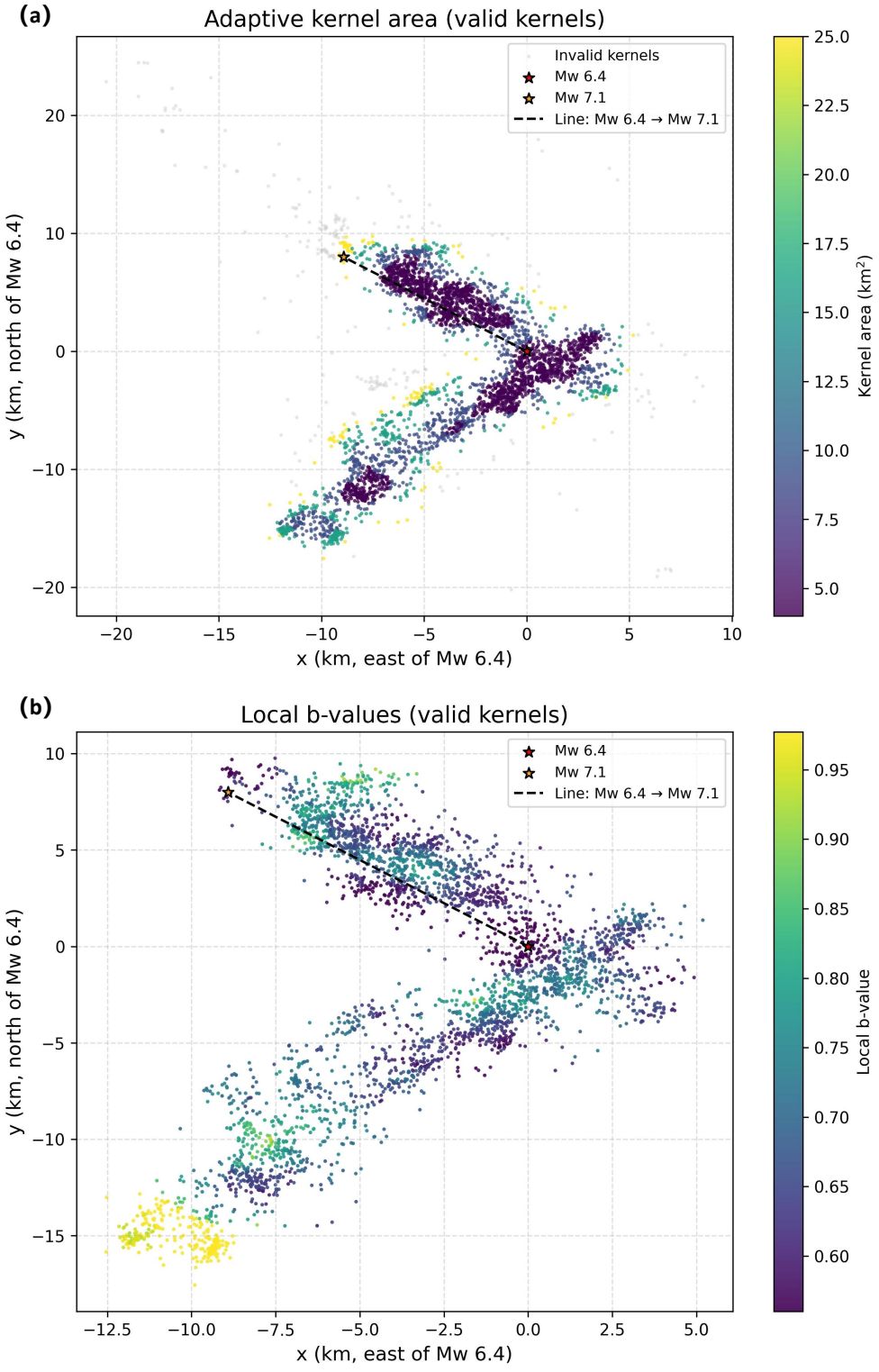
2. Mc and regional b-values: Use SeismoStats for b and Mc estimation.
- SeismoStats catalog for [Mw 6.4, Mw 7.1] window
- Single Mc for [Mw 6.4-Mw 7.1] window (for all kernels)
    - Estimate Mc with Maximum Curvature (primary):
    - Optionally, internally check KS or b-stability (no extra experiment, just internal):
    - Diagnostics:
        - Count events with `magnitude ≥ Mc_64_71`.
        - Ensure that this count is comfortably larger than N_min and enough for spatial subdivision.
- SeismoStats catalog for background (long-term) regional b
    - Load `background_catalog_prepared.csv`.
    - Create SeismoStats `Catalog`
```

```
    - Set same `delta_m = 0.1` and call `cat_bg.bin_magnitudes(delta_m=0.1, inplace=True)`.
- Mc and b for background catalog (qualitative reference)
    - Estimate Mc for background
    - Estimate b for background:
    - Bootstrap uncertainty (for qualitative range)
    - FMD and b-range plots
    - Save background reference

3. Event-centered kernels & local b
- Load data and define parameters
- Prepare arrays for fast access
- Adaptive rectangular-kernel loop, for each event i in `cat_64_71_prepared`:
    - Center coordinates: `x_i = X[i]`, `y_i = Y[i]`.
    - Initialize kernel size:
    - While `h ≤ h_max` and `w ≤ w_max`
        - Define rectangular bounds
        - Identify all events j satisfying the requirements
        - Let `idx_kernel` be indices of these events, `N_total = len(idx_kernel)`.
        - If `N_total ≥ N_min`:
            - Set `valid = True`.
            - Break the loop; record current `h_final = h`, `w_final = w`, `idx_kernel`.
        - Else:
            - Increase kernel size: `h += 1 km`, `w += 1 km`.
    - If the loop exits with `valid = False` (reached `h > h_max` or `w > w_max` and `N_total < N_min`):
        - Mark this epicenter as invalid.
- Local b estimation for valid kernels (using fixed Mc), For each event i with `valid_flag = True`:
    - Magnitude selection
    - Reliability check
    - SeismoStats b estimation
    - Bootstrap uncertainty (per kernel):
    - Store for each epicenter
- Save outputs and basic diagnostics

4. Gridding, smoothing, anomalies
- Load inputs
- Define spatial grid in local x-y
- Assign b-values to grid via kernel footprints
- Grid coverage, masking, and raw map
- Spatial smoothing of b field
- b-value anomaly detection (regional analysis)
```

Box B.4.3 Main Visualization Results (Raw Output)



Box B.4.4 Analysis Summary

```
1 Quantify analysis of the b¯value spatia distribution for
    aftershock of 2019 ridgecrest Mw 6.4
2
3 1. Key observations and findings
```

4 - Catalog preparation and regional b-value characterization: The Mw 6.4-Mw 7.1 inter-mainshock window contains 3692 events (M ≈ 0.14-7.1), clustered along two intersecting fault lineations with a clear NW-SE trend between the Mw 6.4 and Mw 7.1 epicenters. A single completeness magnitude for this window was estimated as Mc ≈ 1.6, with a corresponding bulk b-value of b ≈ 0.71 for M ≥ Mc. The 2-year background catalog yields Mc_bg ≈ 0.8 and a tightly constrained regional reference b_bg ≈ 0.79 ± 0.02 (1σ). This background b is used only as a qualitative range and to define low/high-b anomaly thresholds, not for formal Δb or significance tests.

5 - Physical interpretation: In the Gutenberg-Richter relation, the lower inter-mainshock b (~0.71) indicates a relative enhancement of moderate-to-large events compared with the long-term regional behavior (b_bg ~0.79). This is consistent with a temporarily elevated differential stress or concentration of slip-compatible structures in the Mw 6.4-7.1 interval, while the background catalog reflects a more averaged tectonic state.

6 - Event-centered local b-values: low-b corridor versus high-b periphery: Event-centered adaptive rectangular kernels (initial 1×1 km, up to 5×5 km, N_min = 50) produced local b-values for almost all events in the dense rupture region. Most kernels stabilized at 1-2 km scales, with only a small tail up to 4-5 km, indicating that b is resolved at ~kilometer scales along the main faults. The distribution of local b across the window is unimodal, peaked at b ≈ 0.65-0.75 with a tail up to $\gtrsim$1.2. Spatially, the lowest b-values (≈0.5-0.7) form a continuous NW-SE corridor that passes through the eventual Mw 7.1 epicenter and broadly follows the line joining the Mw 6.4 and Mw 7.1 mainshocks. High-b patches (b $\gtrsim$ 1.0) occur predominantly at the southern extremity and in more distal, off-axis regions, away from the main Mw 7.1 rupture corridor.

7 - Physical interpretation: Low b-values indicate a relative deficit of small events vs larger ones, commonly associated with higher effective stress, stronger asperities, or less damaged, more coherent fault segments. The emergence of a low-b corridor co-located with the eventual Mw 7.1 rupture between the two mainshocks suggests that the future large-rupture patch already behaved as a high-stress, mechanically robust segment during the inter-mainshock period. Conversely, high-b zones at the periphery likely reflect more damaged, heterogeneous, or fluid-affected regions where small fractures dominate.

8

- Gridded/smoothed b-field and anomaly clusters aligned with the Mw 7.1 rupture: Mapping kernel b-values onto a regular grid and smoothing them yields a coherent NW-SE low-b band (b ≈ 0.6-0.7) that crosses the Mw 7.1 epicenter and roughly follows the rupture-direction proxy. Using the background reference (b_bg, σ_b_bg) qualitatively, a major low-b anomaly cluster is identified with mean b_mean ≈ 0.66 and minimum b_min ≈ 0.47, covering ≈348 km^2 and elongated subparallel to the main aftershock trend. This cluster encompasses the Mw 7.1 epicenter. Two high-b anomaly clusters (b_mean ≈ 0.88-0.98) are found at the southern and northern ends of the cloud, each offset from the main Mw 7.1 rupture corridor. A profile along the rupture-direction proxy shows a local minimum in b (~0.66-0.68) in the central segment near and southeast of the Mw 7.1 nucleation area, relative to somewhat higher values (~0.7-0.8) toward both ends. A radial profile around the Mw 7.1 epicenter shows lowest b (~0.53-0.6) within a few kilometers of the epicenter, rising toward b $\gtrsim$ 0.8 at radii of ~20-25 km, where the high-b lobes reside.
    - Physical interpretation: The gridded and profile-based analyses jointly indicate that, between the Mw 6.4 and Mw 7.1 mainshocks, the Mw 7.1 nucleation zone sat within a low-b, high-stress core embedded in an outer high-b halo. This structure is consistent with a stress-concentrated asperity surrounded by a more damaged or dissipative environment. The along-strike minimum in b near the eventual Mw 7.1 rupture section suggests that stress concentration and/or reduced small-scale damage were focused there after the Mw 6.4 event, making that segment more favorable for hosting the subsequent Mw 7.1 rupture.

2. Overview and method context

- The workflow proceeds by (i) extracting the Ridgecrest catalog for the inter-mainshock window [Mw 6.4, Mw 7.1], projecting epicenters into a local Cartesian system and defining a rupture-direction proxy (vector from Mw 6.4 to Mw 7.1); (ii) estimating a single completeness magnitude Mc = 1.6 and bulk b for that window, and a long-term regional Mc_bg = 0.8 and b_bg ≈ 0.79±0.02 from a 2-year background catalog used only as a qualitative reference; (iii) applying event-centered adaptive rectangular kernels (1-5 km, N_min = 50) around each epicenter to estimate local b-values using only events with M ≥ Mc, with bootstrap uncertainties and parallel computation; and (iv) mapping these local b-values onto a spatial grid via kernel footprints, smoothing the field, and identifying low/high-b anomaly clusters relative to the qualitative regional b range, including their orientations and relation to the Mw 7.1 rupture direction.
- Physical principles

```
15 - Gutenberg-Richter scaling: Earthquake magnitudes obey \log_{10} N(M \ge m) = a - b\,m. The b-value parameterizes the relative abundance of small vs large events; low b implies a higher proportion of larger events (often interpreted as higher differential stress or stronger asperities), while high b suggests more numerous small events (often linked to damage, heterogeneity, or fluids).
16 - Magnitude of completeness M_c:Below M_c, catalogs are incomplete; above it, detection is assumed complete. Mc is estimated via maximum curvature of the frequency-magnitude distribution; all b-value estimation is then restricted to M \ge M_c.
17 - Maximum-likelihood b estimation: For magnitudes M_i with M_i \ge M_c, the classical estimator approximates: b \approx \frac{\log_{10} e}{\bar M - (M_c - \Delta M/2)}, where \bar M is the mean magnitude and \Delta M is the bin width. Bootstrap resampling of M_i provides uncertainty estimates (b_{\text{std}}, b_{16}, b_{84}).
18
19 3. Summary of figure-based results
20 Diagnostic A - Spatial distribution of kernel sizes for calculation b-value
21 Observations:
22     - Valid kernels (colored points) follow two main linear trends:
23         - A NW-SE strand passing through the Mw 7.1 epicentral region (roughly along the dashed Mw 6.4 → Mw 7.1 line).
24         - A NE-SW strand to the south, corresponding to the conjugate fault.
25     - Kernel areas are mostly small (dark colors: ~4-10 km$^2$) along the dense parts of both strands.
26     - Larger kernels (yellowish colors, approaching the 25 km$^2$ maximum 5×5 km) occur:
27         - Near the tips and sparser sections of the southern fault.
28         - In scattered peripheral regions off the main fault traces.
29     - Invalid kernels are plotted as grey points; they lie almost exclusively off the main fault strands where seismicity is sparse, indicating that the N_min criterion is generally met along the faults.
30 Conclusion: The adaptive kernels are smallest and best constrained along the two principal fault systems, particularly along the Mw 7.1 rupture trend. Off-fault and peripheral regions often require the largest kernels or fail the N_min test, so subsequent b-value interpretations are primarily controlled by on-fault seismicity.
31
32 Diagnostic B - Spatial pattern of local b-values
33 Observations:
34 - Epicenters between the Mw 6.4 and Mw 7.1 mainshocks organize into two principal, intersecting fault strands, consistent with the conjugate fault system at Ridgecrest:
35     - A NW-SE trending structure passing near both mainshocks.
36     - A SW-NE to WSW-ENE trending structure, particularly prominent south of the Mw 7.1 epicenter.
```

- b-values span roughly 0.5-1.1, with a few spots approaching ~1.2-1.3 at the southern end.
- Low-b zones
  - Along the main NW-SE trend, especially:
    - In the immediate vicinity of the Mw 7.1 epicenter (around x ≈ 4-6 km, y ≈ -5 km), there is a compact concentration of low b-values (~0.5-0.7).
    - A broader low-b band runs NW-SE through the central part of the cloud (y ≈ -2 to -8 km), closely aligned with the line joining the Mw 6.4 and Mw 7.1 epicenters.
  - Near the Mw 6.4 epicenter (x ≈ -4.5 km, y ≈ 4 km), the immediate surroundings are also dominated by relatively low b-values, again mainly 0.5-0.7.
  - These low-b patches are elongated along the same NW-SE direction that approximates the subsequent Mw 7.1 rupture orientation.
  - Interpreting the b-value distribution in a purely spatial sense (without yet invoking the background catalog):
    - The future Mw 7.1 rupture corridor between the Mw 6.4 and Mw 7.1 mainshocks is characterized by systematically lower b-values than much of the surrounding aftershock field during the inter-mainshock period.
    - This suggests that the asperity or high-stress portion of the eventual Mw 7.1 rupture was already a low-b domain after the Mw 6.4 event.
- High-b zones
  - A pronounced cluster of high b-values (>1.0) lies in the southern segment of the aftershock zone (x ≈ -6 to -4 km, y ≈ -18 to -21 km). This is spatially distant from the Mw 7.1 epicenter and from the primary NW-SE rupture path.
  - Additional pockets of moderately elevated b (~0.9-1.0) appear:
    - In the mid-southern area (x ≈ -4 to 1 km, y ≈ -14 to -18 km).
    - Locally near the junction of the conjugate faults, but these are less coherent than the southernmost high-b cluster.
  - These higher b regions are more diffuse and tend to occupy off-rupture or peripheral areas, rather than the core of the future Mw 7.1 rupture.
- Relation to the Mw 6.4 and 7.1 mainshocks
  - Mw 7.1 epicentral area: Low b-values, compact and well defined, indicate a localized zone with relatively higher proportion of larger events (or fewer small events) compared to nearby regions.
  - Along the inferred Mw 7.1 rupture path (between the two mainshocks): b remains systematically low, forming a continuous low-b corridor.
  - Peripheral fault strands and southern extensions: Show higher b-values, implying more "diffuse" seismicity with a larger fraction of small events relative to large ones.

```
In qualitative seismological terms, this pattern is consistent with a concentrated, high-stress, high-strength patch along the eventual Mw 7.1 rupture, embedded in a broader, more damaged, and higher-b environment.
```

B.4.2 Time Evolution and Comparative Analysis of the Mw 7.1 Epicenter Region

Following characterization of the spatial structure, we further analyze the temporal evolution of the b value within the M_w 7.1 source region and compare it with that of the M_w 6.4 rupture zone. The long-term regional mean b value is approximately 0.77-0.79, lower than the global typical value of about 1.0, indicating that the study area as a whole is characterized by a relatively high differential stress background. Within this context, the M_w 6.4 rupture zone exhibited only a brief fluctuation in b value during the early post-mainshock phase, after which it stabilized within the range of 0.8-0.9, without sustained deviation. This behavior suggests that the region returned relatively quickly to a statistical steady state following the strong event. In contrast, the M_w 7.1 source region experienced a distinct high-b phase (b $\simeq$ 1.0-1.25) approximately 0.6-0.4 days prior to the mainshock, characterized by an anomalously elevated proportion of small events. This stage may correspond to distributed microcrack propagation or widespread damage accumulation preceding final instability. Subsequently, within the last few hours before the mainshock, the b value declined from this elevated level to approximately 0.7-0.8, approaching the regional background but not reaching an extreme low-b range significantly below it. Statistical comparison between the two regions indicates that the overall difference in b value between the M_w 7.1 source region and the M_w 6.4 rupture zone is limited. No isolated, statistically significant low-b patch markedly below the regional background is identified within the M_w 7.1 source area. In other words, no "super-background" low-b nucleation anomaly is detected.

Integrating the spatial and temporal results leads to the following interpretation. Spatially, the inter-mainshock stage indeed developed a low-b concentration belt consistent with fault geometry, supporting directional stress loading along specific structural units. Temporally, the M_w 7.1 source region underwent a "high-b plateau followed by relaxation toward background" evolution, but without the emergence of an isolated extreme low-b anomaly. This contrast suggests that stress evolution during the inter-mainshock period more likely reflects a progressively organized preparation process under the combined influence of a regionally elevated stress background and structural control. Its statistical expression is directional loading and staged damage evolution, rather than abrupt nucleation dominated by a single pronounced low-b anomaly patch.

Box B.4.5 User Request

```
Analyze the b-value evolution after Mw 6.4 mainshock for the Mw 6.4 rupture region and the future Mw 7.1 rupture region. Identify and interpolate the b-value change for the Mw 7.1 region after the Mw 6.4 mainshock, specially for the absolute value change and the time approaching the Mw 7.1 mainshock.
Requirements:
```

```
1. Data Source: earthquake catalog is locate at "~/
   ridgecrest_catalog.csv", main-shock events is locate at "~
   /main_shock_events.csv", known fault is locate at "~/
   ridgecrest_surface_faults.json", and a longtern background
    catalog is located at "~/
   catalog_2year_background_before_64.csv"
2. Long-term reference b-value (qualitative anchor): Estimate
    a regional b-value from the background catalog. Use it
   only to indicate the typical b-value range of the region.
   Do not use it as a baseline for Δb, anomaly amplitude, or
   significance testing. Do not directly compare its
   numerical value with b values from the Mw6.4-Mw7.1 window.
3. Time-varying b-value analysis for the Mw 6.4 rupture
   region (control region)
4. Time-varying b-value analysis for the Mw 7.1 rupture
   region (primary target)
```

Box B.4.6 Final Experimental Plan

```
Experimental Plan: Evaluate whether the 2019 Mw 6.4
   Ridgecrest earthquake promoted the Mw 7.1 rupture by
   inducing a localized, persistent low-b-value anomaly in
   the future Mw 7.1 source region, using only catalog data
   and SeismoStats-based Mc/b-value analysis.

0. Top Level tasks
- 01_prepare_catalogs_and_regions.py: load/harmonize catalogs
   ; define t64, t71; compute distances and region flags.
- 02_background_bvalue_reference.py: regional Mc and b from 2
   -year background.
- 03_bvalue_time_series_mw64_region.py: sliding-window Mc/b
   in Mw 6.4 region (control).
- 04_bvalue_time_series_mw71_region.py: sliding-window Mc/b
   in Mw 7.1 region (target).
- 05_interpolate_and_quantify_anomalies.py: interpolation, Δb
    in Mw 7.1 region, timing of changes, comparison to
   control.

1. Catalog preparation and mainshock / region definition
- Load and standardize catalogs
- Compute epicentral distances and region flags
- Basic diagnostics and outputs
- Event-centered kernels & local b
- Load data and define parameters
- Gridding, smoothing, anomalies

2. Regional long-term b-value (qualitative anchor)
- Prepare background catalog
- Estimate Mc via MAXC (SeismoStats)
- Estimate b-value and bootstrap uncertainty
    - Point estimate With SeismoStats:: Use `
      ClassicBValueEstimator` or `catalog.estimate_b(mc=
      Mc_bg, delta_m=0.1)`.
    - Bootstrap
      - Magnitudes restricted to `mag ≥ Mc_bg`.
      - Perform bootstrapping
- Outputs and figures

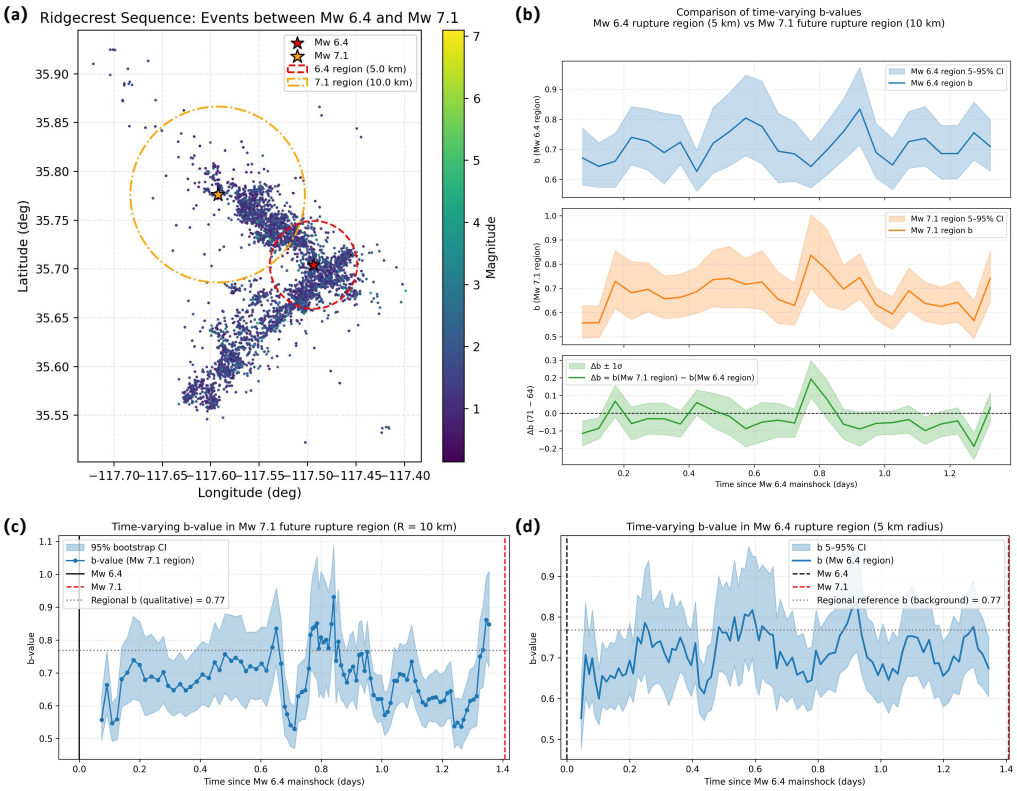
```

```
3. Time-varying b-value for Mw 6.4 rupture region (control)
- Select events in 6.4 region and time window
- Define sliding event windows
  - Window parameters:
    - N=200 events, step=25 events.
  - For events indexed `0..(N_total_64-1)`:
    - For each window k:
      - `start_idx_k = k * 25`
      - `end_idx_k = start_idx_k + 200 - 1`
    - Stop when `end_idx_k ≥ N_total_64`.
  - For each window k:
    - `mags_k = mag[start_idx_k : end_idx_k+1]`
    - `times_k = time[start_idx_k : end_idx_k+1]`
    - `t_start_k = times_k[0]`
    - `t_end_k = times_k[-1]`
    - `t_center_k = (t_start_k + t_end_k)/2`
- Mc estimation per window (MAXC), for each window:
  - Construct a small SeismoStats Catalog with the 200 magnitudes.
  - Call `cat_win.estimate_mc_maxc(fmd_bin=0.1)`:
    - Get `Mc_64_k`.
  - Determine sample size above Mc:
    - `N_above_Mc_64_k = count(mags_k ≥ Mc_64_k)`.
  - Define a quality flag:
    - If `N_above_Mc_64_k < 50`, mark `quality_flag_k = "few_above_Mc"`, still compute b but interpret carefully.
- b-value and bootstrap per window, for each window:
  - Point estimate: use `ClassicBValueEstimator` or `estimate_b`
  - Bootstrap
- Outputs and control-region figures

4. Time-varying b-value for Mw 7.1 rupture region (target)
- Select events in 7.1 region and time window
- Sliding windows and explicit time stamps
- Mc estimation per window (MAXC)
- b-value and bootstrap per window
- Outputs and target-region figures

5. Interpolation, anomaly quantification, and comparison
- Load and align time series
- Define common time grid and interpolation
- Define local reference b-values (no use of background b for Δb)
- Compute Δb and absolute changes in Mw 7.1 region
- Temporal evolution and timing toward Mw 7.1
- Figures for anomaly evolution and localization
```

Box B.4.7 Main Visualization Results (Raw Output)



Box B.4.8 Analysis Summary

```
Quantify analysis of the b-value temporal distribution for aftershock of 2019 ridgecrest Mw 6.4.

1. Key observations and findings
- Regional background b-value: From the 2-year pre-Mw 6.4 background catalog, the maximum-curvature method yields a regional completeness magnitude M_c \approx 0.8 and a Gutenberg-Richter b \approx 0.77 with a smooth FMD above M_c.
    - Mechanism: A background b \lesssim 1 indicates a relatively high proportion of larger events, consistent with a moderately high differential stress and heterogeneous faulting environment in the Ridgecrest sector of the Eastern California shear zone.
- Time-varying b in the Mw 6.4 rupture region (control, 5 km): The 5 km Mw 6.4 region has 2,529 events between Mw 6.4 and Mw 7.1, enabling 94 sliding windows (200 events, step 25). Completeness evolution: Immediately after Mw 6.4, M_c is high (\sim 2.1), then decays to \sim 1.0 within ~0.2 days and eventually to \sim 0.3-0.6 close to Mw 7.1. Thus, late-time b-values are based on a well-resolved, nearly complete local catalog. b-value evolution: Windowed b stays mostly in 0.65-0.80, with no sustained trend; fluctuations are of order 0.05-0.1 and always within bootstrap 5-95 % intervals. Relative to the regional reference b \approx 0.77, the Mw 6.4 region is regionally typical and shows no persistent low-b anomaly.
```

```
7       - Mechanistic interpretation: In the immediate Mw 6.4
          rupture zone, the post-mainshock stress field and
          fault network evolve in a way that keeps the effective
           stress/strength heterogeneity balance roughly
          stationary, yielding a stable size distribution of
          aftershocks (no progressive concentration of larger
          events).
8     - Time-varying b in the future Mw 7.1 rupture region (target,
         10 km): The 10 km Mw 7.1 region contains 2,721 events
        between Mw 6.4 and Mw 7.1, supporting 101 sliding windows.
         Completeness: M_c starts near \sim 1.8 immediately after
        Mw 6.4, falls to \sim 0.9-1.0 within ~0.5 days, and
        stabilizes at \sim 0.4-0.6 during the last ~0.4-0.5 days
        before Mw 7.1. Absolute b-values: Early post-6.4 b is \sim
         0.7-0.8 (similar to regional). Later, oscillatory
        behavior includes: transient high-b episodes (b \sim 0.9-
        1.0), repeated low-b dips to \sim 0.5-0.6 in the last ~0.4
         days before Mw 7.1.
9       - Mechanistic interpretation: The Mw 7.1 source area
          experiences evolving local stress and fault-zone
          damage, producing alternating phases of relatively
          more small events (high b) and relatively more larger
          events (low b), consistent with episodic stress
          concentration and partial relaxation on the impending
          rupture plane.
10    - Localized b-value change in the Mw 7.1 region (absolute and
         relative): A local reference b-value for the Mw 7.1
        region, based only on early post-6.4 windows (first 0.5
        days), is b_{\text{ref},71} = 0.672 \pm 0.055 (1$\sigma$).
        Interpolated absolute b-values b(t) in the Mw 7.1 region
        lie mostly in 0.6-0.8, with a minimum b_{\min} \approx
        0.54 occurring at t \approx -0.7 days relative to Mw 7.1.
        Corresponding $\Delta$b(t) = b(t) - b_{\text{ref},71} reaches ~-
        0.13 to -0.15 at this minimum, and remains mildly negative
         (~-0.05 to -0.15) over much of the last ~0.5 days before
        Mw 7.1. Bootstrap 95 % intervals often overlap $\Delta$b = 0, but
         consistently show a negative bias during these times.
11      - Mechanistic interpretation: Relative to its own early
          post-6.4 state, the Mw 7.1 region evolves toward a
          modestly lower b-value, indicating a temporarily
          increased proportion of larger events. This can be
          interpreted as localized stress concentration or
          progressive weakening on the to-fail fault segments.
12    - Spatial comparison: Mw 6.4 vs Mw 7.1 regions: After
         interpolation to a common time axis, the Mw 6.4 (5 km) and
         Mw 7.1 (10 km) regions show broadly similar absolute b
        ranges (\sim 0.65-0.85) over 0-1.4 days after Mw 6.4. The
        inter-regional difference fluctuates between roughly -0.2
        and +0.15 with typical $\sigma$($\Delta$b) $\approx$ 0.06-0.1. There is no
        sustained interval where $\Delta$b is strongly negative and its
        uncertainty band lies entirely below zero; negative
        excursions are short-lived and modest, comparable to their
         uncertainties.
13      - Mechanistic implication: Any low-b tendencies in the Mw
           7.1 region are not sharply localized relative to the
          Mw 6.4 control region at the tested scales. The two
          zones share similar regional stress and structural
          controls, and the Mw 7.1 area does not develop a
          uniquely deep, long-lasting low-b patch in the window
          between the mainshocks.
```

```
- Overall answer to the triggering question: The Mw 7.1
  future rupture region does show moderate, time-dependent b
  -value lowering relative to its own early post-6.4 state,
  but this reduction is modest, intermittent, and not
  strongly distinct from the behavior of the Mw 6.4 rupture
  region. The catalog data therefore do not provide strong
  evidence that Mw 6.4 promoted Mw 7.1 primarily via a
  pronounced, localized low-b anomaly.

2. Overview and method context
- The study uses only catalog data to track time-dependent b-
  values in two spatial windows between the 2019 Mw 6.4 and
  Mw 7.1 Ridgecrest earthquakes. First, catalogs are
  harmonized and clipped to the Mw 6.4-Mw 7.1 interval, and
  events are tagged by distance to each mainshock to define
  a 5 km control region around Mw 6.4 and a 10 km target
  region around Mw 7.1. A two-year pre-event catalog
  provides a qualitative regional reference b-value and
  magnitude of completeness Mc via SeismoStats maximum
  curvature. For each region, sliding windows of N = 200
  events (step 25) are constructed; in each window, Mc is re
  -estimated with MAXC and a classic Gutenberg-Richter b-
  value is computed above Mc, with uncertainty quantified by
   bootstrap resampling. Finally, the window-based b-value
  series are interpolated onto a common time grid, early "
  local reference" b-values are defined in each region, and
  anomalies Δb(t) and inter-regional differences $b_{\text{
  target}}(t) - b_{\text{control}}(t)$ are computed and
  summarized as functions of both absolute time and time to
  the Mw 7.1 mainshock.

3. Summary of figure-based results
Diagnostic A - Spatial distribution and region definitions
Observations:
- Geometry of the sequence
    - Events between the Mw 6.4 and Mw 7.1 mainshocks form a
      well-defined, bilinear fault system:
        - A NW-SE trending band running roughly through the
          Mw 6.4 epicenter.
        - A WNW-ESE to NW-SE band extending through the Mw
          7.1 epicenter.
        - The Mw 6.4 (red star) lies near the northwestern
          segment of the aftershock cloud.
        - The Mw 7.1 (orange star) sits closer to the
          southeastern cluster, along the main NW-SE trend.
    - Research region placemen
        - Mw 6.4 control region (radius 5 km, red dashed
          circle):
            - Encloses a compact cluster around the Mw 6.4
              epicenter.
            - This region captures activity mainly on (or
              immediately adjacent to) the Mw 6.4 rupture
              plane.
            - Its smaller radius reduces mixing with more
              distant segments of the aftershock zone,
              making it a good spatial control.
        - Mw 7.1 target region (radius 10 km, orange dash-dot
          circle):
```

- Encompasses a broader portion of the southeastern part of the sequence.
- A substantial length of the NW-SE aftershock trend leading toward the central part of the sequence.
- The larger radius ensures enough events for stable b-value estimation while still focusing on the future Mw 7.1 rupture area.

Diagnostic B,C,D - Time-varying b-values for the Mw 6.4 rupture region (5 km radius) and Mw 7.1 rupture region (10 km radius)

Observations:

- Mw 6.4 rupture region (control)
  - b generally fluctuates between ~0.65-0.85, with occasional peaks approaching ~0.9-0.95.
  - No obvious long-term monotonic trend; variability appears moderate and roughly stationary over the analyzed interval.
  - The confidence bands are relatively wide (reflecting finite window size and Mc variability), but the central values remain mostly $\geq$ ~0.7.
- Future Mw 7.1 rupture region (target)
  - b-values are broadly in the same range as the Mw 6.4 region: mostly ~0.6-0.85, with a transient peak near ~1.0 around ~0.7 days.
  - The temporal pattern differs in detail (e.g., peaks and troughs do not always align with the Mw 6.4 region), but there is no persistent downward shift to systematically lower b.
  - Uncertainty bands are similar to, or slightly larger than, those of the Mw 6.4 region, indicating comparable statistical robustness.
- Differential behaviour:
  - Δb oscillates between roughly -0.2 and +0.15.
  - For much of the sequence, the Δb median is close to zero, and the $\pm 1\sigma$ band crosses or straddles zero.
  - There are short intervals where:
    - Δb is slightly positive (Mw 7.1 region having marginally higher b than Mw 6.4), e.g., near ~0.2 and ~0.5-0.7 days.
    - Δb becomes negative (Mw 7.1 region lower b than Mw 6.4), e.g., some dips around ~0.4, ~0.8-0.9, and ~1.1 days.
  - However, even during negative excursions, the -1σ band often overlaps zero, and the amplitudes ($|\Delta b| \lesssim 0.2$) are modest. Crucially, there is no sustained period where: Δb remains consistently negative, and the entire $\pm 1\sigma$ band lies well below zero (which would indicate a robust, localized low -b anomaly in the 7.1 region relative to the 6.4 control). Instead, the spatial difference fluctuates around zero with relatively small magnitude.

Implications:

```
1. No clear evidence of a persistent low-b state in the Mw
   7.1 region: Absolute b-values in the 7.1 region are
   comparable to or slightly higher than those in the 6.4
   region at various times. When the 7.1 region does show
   lower b than the 6.4 region, the effect is short-lived and
    modest (Δb magnitude typically ≲ 0.1-0.2).
2. Spatial contrast is weak and intermittent. Δb(t) spends
   substantial time near zero, with uncertainty intervals
   overlapping zero. This pattern is more consistent with
   shared regional variability in stress/heterogeneity and
   catalog statistics than with a strong, localized precursor
    in the Mw 7.1 area.
3. Within this dataset and methodology, the Mw 7.1 region
   does not exhibit a robust, uniquely low-b anomaly between
   Mw 6.4 and Mw 7.1. The results do not strongly support the
    hypothesis that Mw 6.4 promoted Mw 7.1 via the
   development of a pronounced, localized low-b patch around
   the future Mw 7.1 rupture, at least at the spatial scales
   (10 km) and temporal resolution sampled here.
```

B.5 Stage-Dependent Behavior of the Omori-Utsu Decay Relation

To examine dynamical differences between fault units during the inter-mainshock stage, this section constructs separate Omori-Utsu (OU) decay models for $M \geq 3.0$ earthquake sequences occurring after the M_w 6.4 event along the two principal fault orientations. The decay exponent p, magnitude evolution characteristics, and spatial organization patterns are systematically compared. In the OU formulation, the exponent p quantifies the temporal decay rate of seismic activity. Its physical interpretation is commonly associated with stress relaxation efficiency, damage evolution, and the system's memory of the initial perturbation. Consequently, inter-regional differences in p values and their evolutionary patterns provide a critical basis for distinguishing between two dynamical regimes: passive aftershock decay and active nucleation preparation.

The results indicate that seismicity along the M_w 6.4 rupture segment (Region A) exhibits a typical relaxation-type aftershock sequence. Following the mainshock, the maximum magnitude rapidly declined to $M < 4.2$, and no sustained moderate-magnitude activity was observed thereafter, implying that the majority of accumulated stress was effectively released during the mainshock. The corresponding OU decay exponent p ranges from approximately 1.0 to 1.6, within the standard aftershock decay regime, indicating rapid attenuation of activity rate and progressive weakening of the system's response to the initial disturbance. The b value in this region is approximately 0.7, with small to moderate events dominating the magnitude-frequency distribution, consistent with a stress relaxation environment. Collectively, the dynamical behavior of Region A can be interpreted as post-mainshock regression toward a low-stress steady state. In contrast, Region B, located along the conjugate fault system, displays markedly different statistical characteristics. Moderate-magnitude events (M 4-5) persisted throughout the inter-mainshock stage and continued until the eve of the M_w 7.1 mainshock, without evidence of progressive magnitude ceiling decay. The b value in this region is approximately 0.58, lower than that of Region A, indicating a relatively higher proportion of larger events and reflecting a fault system approaching instability under elevated differential stress. In terms of temporal decay structure, the OU exponent p in Region B ranges from approximately 0.5 to 0.8, representing a

slow decay process. This behavior suggests a pronounced memory effect of the M_w 6.4 perturbation, with seismic activity rates maintained at relatively high levels over extended timescales. More importantly, during the final stage preceding the M_w 7.1 event, the observed occurrence rate in Region B significantly exceeded the extrapolated OU decay trend, exhibiting a clear rate surplus. This deviation indicates that the region was not undergoing passive attenuation, but rather continued stress accumulation and reorganization.

The evolution of spatial organization further reinforces this contrast. In Region A, post-mainshock seismicity remained concentrated around the established rupture segment, without evident migration. In Region B, however, seismic activity progressively converged toward the eventual M_w 7.1 nucleation site. The centroid of activity contracted from a dispersed distribution at approximately 6-8 km scale to a localized zone within $\leq$ 3 km. Concurrently, the continuous reduction in nearest-neighbor distances indicates strengthening clustering intensity, suggesting that cascading triggering processes may have progressively amplified local stress concentration within specific fault segments. Taken together, the systematic differences between Regions A and B in OU decay behavior, magnitude structure, and spatial organization reveal two fundamentally distinct dynamical states. Region A reflects a classical passive aftershock decay regime, in which stress release is followed by gradual stabilization through distributed small events. Region B, by contrast, evolved toward a foreshock-type sequence following the perturbation induced by the M_w 6.4 event. Its characteristics-slow decay, rate surplus, and spatial convergence-are consistent with a nucleation preparation process initiated by external perturbation and sustained loading toward critical instability. These stage-dependent differences in OU behavior provide key constraints for understanding the stress evolution pathway and dynamical transition mechanisms linking the two mainshocks.

Box B.5.1 User Request

```
1 Investigate the triggering mechanism of the Mw 7.1 earthquake
      by the Ms 6.4 earthquake within the Ridgecrest earthquake
      sequence. Identify the difference magnitude decay of the
     two regions (one for Mw 6.4 rupture and another for the Mw
      7.1 rupture). Identify is the new triggered earthquake in
      specific region is influenced by the previous triggered
     earthquakes distribution.
2 Requirements:
3 1. Data Source: earthquake catalog is locate at "~/
     ridgecrest_catalog.csv", main-shock events is locate at "~
     /main_shock_events.csv"
4 2. Catalog preprocessing: only use the catalog with magnitude
      greater than 3.0
5 2. Regional Definition: Two rectangular regions are defined
     along the fault direction:
6 - Region A: along the NE-SW fault direction, coordinates:
7 [-117.62120049,   35.52601731],
8 [-117.66574867,   35.57056548],
9 [-117.47482793,   35.76148622],
10 [-117.43027975,   35.71693805]
11 - Region B: along the NW-SE fault direction, coordinates:
12 [-117.49103561,   35.7507739 ],
13 [-117.55467585,   35.68713365],
14 [-117.77105269,   35.90351049],
```

```
[-117.70741244,   35.96715074]
3. Time-Dependent Omori-Utsu Parameter Analysis for both region
```

Box B.5.2 Final Experimental Plan

```
Experimental Plan: Use the M > 3 catalog of the 2019 Ridgecrest sequence to test whether the Mw 7.1 mainshock was preferentially "prepared" by the Mw 6.4 sequence in its future rupture region (Region B), by:
- Quantitatively comparing time-dependent Omori-Utsu decay and magnitude decay between Region A (Mw 6.4 fault) and Region B (Mw 7.1 fault).
- Assessing whether new events in each region preferentially occur where previous triggered earthquakes have already concentrated.
- Focusing on the interval between Mw 6.4 and Mw 7.1, using only the specified catalog and mainshock files.

1. Catalog loading, time reference, and region assignment
- Load catalogs and define time reference
    1. Read mainshock file
    2. Read Ridgecrest catalog
    3. Compute relative times to Mw 6.4
    4. Define the core analysis time interval
    5. QC checks
- Define regions and assign events
    - Region A:
        - `[-117.62120049, 35.52601731]`
        - `[-117.66574867, 35.57056548]`
        - `[-117.47482793, 35.76148622]`
        - `[-117.43027975, 35.71693805]`
    - Region B:
        - `[-117.49103561, 35.7507739 ]`
        - `[-117.55467585, 35.68713365]`
        - `[-117.77105269, 35.90351049]`
        - `[-117.70741244, 35.96715074]`

2. Spatiotemporal overview and magnitude decay (descriptive): This module satisfies the map and time-magnitude visualization requirements and provides a first, quantitative look at magnitude decay differences between A and B.
    - Map view with regions and mainshocks
    - Time-magnitude plots for each region
    - Quantitative magnitude decay comparison

3. Time-dependent Omori-Utsu fitting in expanding windows: This is the core Omori analysis exactly matching the user's specification: expanding cumulative windows from Mw 6.4 to Mw 7.1, separately in each region.
- Define expanding windows
    - Load: `catalog_regionA_Mgt3.csv`, `catalog_regionB_Mgt3.csv`, `T_total_hours` from Script 1.
    - Define window endpoints:
        - `t_n_hours = 1, 2, 3, ..., floor(T_total_hours)`.
        - For each `t_n`, window is `[0, t_n]`.
    - For each region R and each window `t_n`:
```

```
        - Select events with `0 < t_rel_hr ≤ t_n`.
        - Exclude the Mw 6.4 origin time itself.
        - Record `N_events(t_n, R)`.
    - Only proceed with Omori fitting for windows where `N_events ≥ N_min`, e.g., `N_min = 15-20` to ensure stability.
- Omori-Utsu model and MLE
    - Use the rate model: n(t) = \frac{K}{(t + c)^p}, \quad t > 0,
    - with t in hours since Mw 6.4, For window `[0, t_n]` with events at times \{t_i\}:
        - Log-likelihood:
        \[
            \log L(K,c,p) = \sum_i \log n(t_i) - \int_0^{t_n} n(t)\,dt.
        \]
        - Integral:
        \[
              \int_0^{t_n} \frac{K}{(t + c)^p} dt =
              \begin{cases}
              \frac{K}{1-p}\left[(t_n + c)^{1-p} - c^{1-p}\right], & p \neq 1,\\
              K \log\left(\frac{t_n + c}{c}\right), & p = 1.
              \end{cases}
        \]
- Bootstrap uncertainty for K, c, p
- Visualization - time evolution of Omori parameters

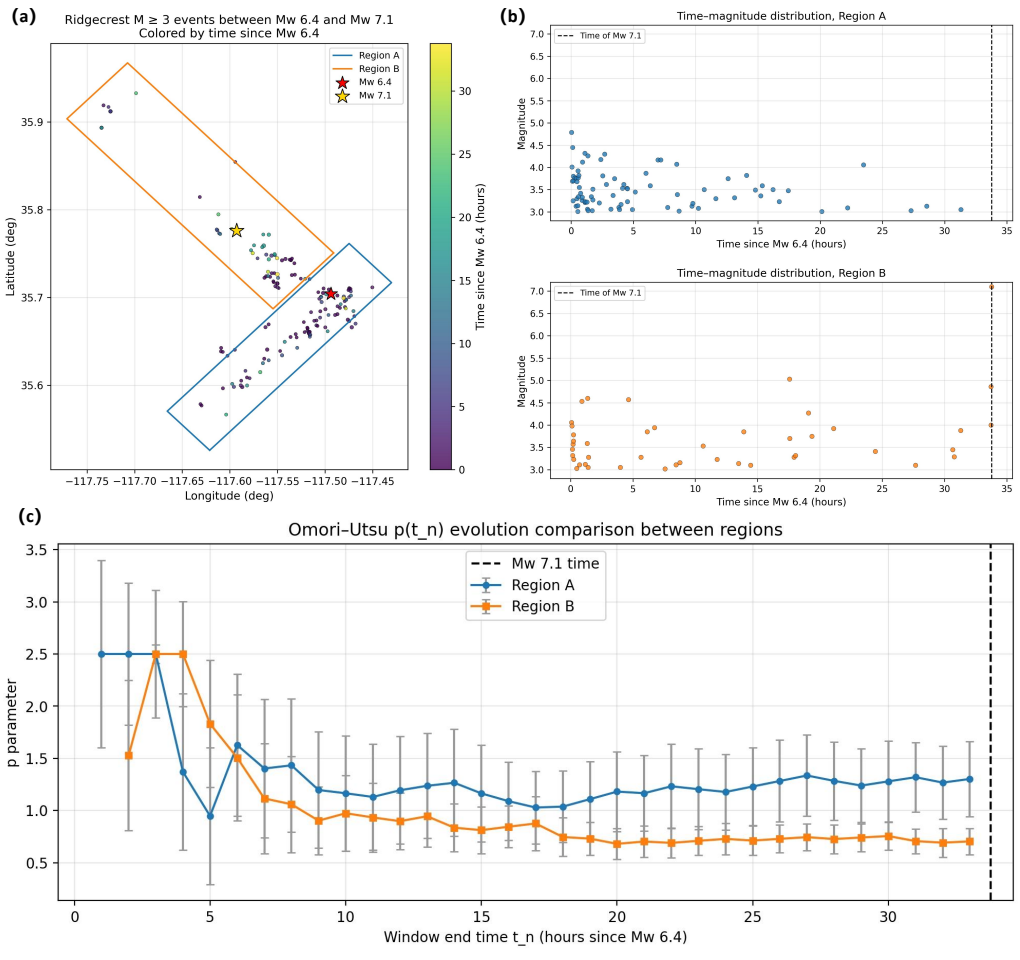
4. Rate vs early-time Omori extrapolation and standardized residuals
- Observed seismicity rate in fixed bins
- Early-time Omori fit (0-6 hours)
    - For each region:
        - Select events with `0 < t_rel_hr ≤ 6` hours.
        - Fit Omori-Utsu model on `[0, 6]` hours using same MLE framework.
        - Perform bootstrap (e.g., 1000 resamples) to estimate uncertainty of `K_early`, `c_early`, `p_early`.

- Omori extrapolation and confidence bands
    - For each region and each time bin center `t_center` in `[0, T_total_hours]`:
        - For the point estimate `(K_early, c_early, p_early)`:
            - Compute predicted rate:
              \[
              n_{OU}(t_center) = \frac{K_{early}}{(t_{center} + c_{early})^{p_{early}}}.
              \]
        - Approximate expected count per bin:
              \[
              \mu_j \approx n_{OU}(t_{center,j}) \cdot \Delta t_{rate}.
              \]
    - Using bootstrap samples of `(K_early, c_early, p_early)`:
- Observed rate vs Omori extrapolation
- Standardized residuals vs time
```

- Regional comparison of p(t_n) and residuals

5. Additional triggering diagnostics (spatio-temporal influence of prior events: "Identify is the new triggered earthquake in specific region is influenced by the previous triggered earthquakes distribution."
   - Distance to mainshock and to Mw 7.1 epicenter
     - Load: ‘catalog_regionA_Mgt3.csv‘, ‘catalog_regionB_Mgt3.csv‘, and Mainshock coordinates (‘latR64‘, ‘lonR64‘, ‘latR71‘, ‘lonR71‘).
     - For each event in Region B (and separately A) with ‘0 < t_rel_hr ≤ T_total_hours‘, compute:
       - Epicentral distance to Mw 6.4: ‘d_64‘.
       - Epicentral distance to Mw 7.1: ‘d_71‘ (in km, using local planar approximation or spherical formula).
     - Plot for Region B:
     - For comparison, do the same for Region A.
   - Distance to previous earthquakes (nearest-neighbor clustering)
   - Density-following analysis (are new events drawn to early clusters?)
   - Combined indicators and summary

Box B.5.3 Main Visualization Results (Raw Output)



Box B.5.4 Analysis Summary

```
Quantify analysis of the b-value temporal distribution for
   aftershock of 2019 ridgecrest Mw 6.4.

1. Key observations and findings
- Contrasting magnitude decay and size-frequency statistics
   between Regions A and B: From the descriptive analysis,
   time-magnitude plots and binned statistics show that in
   Region A (Mw 6.4 fault) the maximum magnitude drops
   rapidly after Mw 6.4 and remains ≤ M 4.2 beyond ~8 h,
   whereas Region B (future Mw 7.1 fault) continues to host M
    4-5 events up to ~18 h and then Mw 7.1 itself. Hourly
   magnitude statistics show similar mean magnitudes in both
   regions, but clearly higher and more persistent maxima in
   Region B. Gutenberg-Richter fits give \(b_A \approx 0.7\)
   and \(b_B \approx 0.58\), indicating a relatively higher
   proportion of larger events in Region B.
    - Physical interpretation: Region A behaves like a
      conventional aftershock zone of Mw 6.4: rapid release
      of stress on the Mw 6.4 rupture and nearby patches
      produces early moderate aftershocks, after which the
      remaining stress heterogeneity supports mainly smaller
       events. Region B's lower b-value and persistence of
      moderate events imply a fault segment closer to
      failure, with a stress state that continues to favor
      larger ruptures under the combined tectonic and Mw 6.4
      -induced loading. In terms of fault mechanics, this is
       consistent with a near-critical asperity on the Mw
      7.1 fault that was nudged toward instability rather
      than fully relaxed by the Mw 6.4 sequence.

- Different Omori-Utsu decay between regions: Region A
   follows a near-standard aftershock decay, Region B decays
   more slowly and exhibits rate excess: Time-dependent Omori
   -Utsu fits in expanding windows show that after the first
   few hours, Region A stabilizes at \(p_A \approx 1.1-1.3\)
   with \(c_A \sim 0.7-1.3\) h, whereas Region B evolves
   toward \(p_B \approx 0.5-0.8\) with \(c_B \sim 0.1-0.2\) h
   . Productivity \(K\) decreases smoothly in both regions,
   but is much larger in Region A initially and modest in
   Region B; Region B's lower \(p\) implies slower relative
   decay despite lower absolute counts. Early-time (0-6 h)
   Omori fits extrapolated to the full 0-34 h window show
   that Region A's observed rates remain within the 95%
   confidence band of the extrapolated decay, whereas Region
   B displays a clear late-time rate burst just before Mw 7.1
    that lies well above the extrapolated band.  Standardized
    residuals confirm this: Region A's residuals fluctuate
   around zero with no sustained positive trend, whereas
   Region B shows more frequent and higher positive residuals
    at early-intermediate times and a pronounced late-time
   excess when viewed in rate space.
```

```
8       - Physical interpretation: The Omori-Utsu law \(n(t)=K/(t
          +c)^p\) describes stress-controlled decay of triggered
          seismicity. Region A's \(p>1\) and moderate \(c\) are
          characteristic of a sequence relaxing efficiently
          toward a lower-stress state on the Mw 6.4 rupture.
          Region B's \(p\lesssim 1\) and very small \(c\) imply
          slow decay and effective "memory" of the Mw 6.4
          perturbation from very early times; combined with the
          late rate excess, this behavior indicates that the Mw
          7.1 fault segment remained highly stressed and
          continued to accumulate micro-failures rather than
          relaxing, consistent with progressive preparation of
          the Mw 7.1 rupture patch rather than a passive,
          uniformly decaying aftershock field.
9
10    - Spatial localization toward the Mw 7.1 epicenter and
        strengthening clustering, especially in Region B: Distance
        -time plots to the Mw 7.1 epicenter show that Region A
        events remain ~10-20 km from the Mw 7.1 epicenter
        throughout, whereas Region B events start 6-8 km away and
        progressively migrate inward, with many late events
        occurring within $\lesssim$1-3 km of the future epicenter. Nearest-
        neighbor (NN) distances within each region decrease with
        time in both A and B, reflecting increasing clustering,
        but Region B shows particularly strong tightening of NN
        distances in the 6-24 h and pre-Mw 7.1 windows. Early-
        period kernel density estimates (KDEs) reveal that early
        Region B activity is initially concentrated south of the
        Mw 7.1 epicenter; later events progressively occupy and
        reinforce zones that become dense near the epicenter.
11        - Physical interpretation: The inward migration of Region
            B seismicity toward the Mw 7.1 epicenter is
            consistent with stress transfer (static Coulomb and/or
            dynamic) from Mw 6.4 and subsequent aftershocks
            focusing loading on the future nucleation patch.
            Strengthening clustering (shorter NN distances)
            reflects cascade triggering: each event increases
            local stress perturbations and weakens nearby patches,
            consistent with an ETAS-like cascade embedded in a
            larger-scale stress change. In Region B, because this
            cascade unfolds around the Mw 7.1 epicenter, it
            effectively tracks the approach to large-scale failure
            on that segment.
12
13  2. Overview and method context
```

- The workflow began by constructing an Mw > 3 catalog with times referenced to Mw 6.4 (T = 0), then assigning each event to one of two fault-parallel polygons: Region A (Mw 6.4 rupture) and Region B (future Mw 7.1 rupture). Descriptive spatiotemporal analysis quantified when and where $M \geq 3$ events occurred between Mw 6.4 and Mw 7.1, including time-magnitude diagrams, hourly magnitude statistics, and regional b-values. The core temporal analysis fit the Omori-Utsu law in cumulative expanding windows [0, tn] for each region using maximum likelihood, with bootstrap uncertainties for K, c, p, and then compared observed binned rates to an early-time (0-6 h) Omori fit extrapolated to the full ~34 h interval, computing standardized residuals per bin. Finally, spatial triggering diagnostics-distances to the Mw 7.1 epicenter, nearest-neighbor distances, early KDE maps, and density-following tests-were applied to assess how late events relate to earlier clusters and whether these patterns differ between the Mw 6.4 and Mw 7.1 fault segments.
- Physical Principle
    - Aftershock decay (Omori-Utsu law): Seismicity rate modeled as $n(t)=K/(t+c)^p$, with t in hours since Mw 6.4, where K is productivity, $c>0$ an effective early-time offset (accounting for short-time saturation / catalog incompleteness), and p the decay exponent. MLE fits maximize $\log L = \sum_i \log n(t_i) - \int_0^{t_n} n(t)\,dt$, and bootstrap resampling provides uncertainties on K, c, p.
    - Size-frequency distribution (Gutenberg-Richter): Magnitude-frequency statistics in each region follow $\log_{10}N(M\ge m)=a-bm$ for $m\ge M_c=3$; lower b in Region B indicates relatively more large events, reflecting a different stress or strength distribution compared with Region A.
    - Rate extrapolation and residuals: Early-time Omori parameters (0-6 h) define a reference decay; predicted counts per bin are $\mu_j \approx n(t_{c,j})\Delta t$. Standardized residuals $r_j = (N_{\text{obs},j}-\mu_j)/\sqrt{\mu_j}$ assess deviations from this reference, highlighting localized rate excess not explained by simple aftershock decay.
    - Spatial clustering and density-following: Nearest-neighbor distances quantify evolving clustering; shrinking NN distances indicate increasing local triggering. Kernel density estimates of early events define a continuous spatial "stress proxy"; if late events sample systematically higher early KDE values than random points, this indicates that prior localized triggering patterns strongly condition where later events occur.

3. Summary of figure-based results

Diagnostic A - Spatial distribution and temporal coloring of events

Observations:

- Geometry of regions and mainshocks
    - Region A (blue rectangle) trends roughly NW-SE and coincides with the Mw 6.4 rupture zone.
    - Region B (orange rectangle) trends NE-SW and encompasses the Mw 7.1 epicentral area.

```
28      - The Mw 6.4 epicenter (red star) lies along the southern
            part of Region A.
29      - The Mw 7.1 epicenter (yellow star) lies near the
            central-northern portion of Region B.
30  - Early versus late activity
31      - Colors map time since Mw 6.4 (0-~34 h). Dark colors are
            early, light colors late.
32      - Immediately after the Mw 6.4, aftershocks cluster
            strongly along Region A, forming a dense, elongated
            cloud following the Mw 6.4 fault.
33      - Region B hosts fewer very-early events but does begin
            to light up within the first few hours, with a small
            cluster surrounding the future Mw 7.1 epicentral area.
34      - As time progresses, events occur throughout both
            regions, but by ~20-30 h the activity appears somewhat
            more spread out along both fault trends.
35  - Implication for triggering
36      - The Mw 6.4 sequence rapidly activates its own fault (
            Region A) and, somewhat more sparsely, the conjugate
            Mw 7.1 fault system (Region B).
37      - The presence of early post-Mw 6.4 activity in Region B,
            including near the eventual Mw 7.1 epicenter,
            supports the notion that the 6.4 event dynamically or
            statically loaded the future 7.1 fault.
38
39  Diagnostic B - Time-magnitude distributions
40  Observations:
41  - Region A
42      - Magnitudes range from ~3.0 to just below 4.8.
43      - The largest events occur in the first $\lesssim$1-2 h after Mw
            6.4.
44      - Beyond ~5-10 h, most events are M3-3.7; no very late
            moderate events ($\geq$M4.5) appear before Mw 7.1.
45      - After ~20 h, only a few small (M$\approx$3) events occur.
46  - Region B
47      - Magnitudes span from ~3.0 up to the Mw 7.1 mainshock at
            ~34 h.
48      - Several M4-4.6 events appear within the first few hours
            .
49      - Unlike Region A, Region B exhibits intermittent
            moderate events (M$\approx$3.5-5.0) through much of the 6-24 h
            window, including an M$\approx$5 at ~18 h.
50      - In the last several hours before Mw 7.1, Region B
            continues to host M$\geq$3 events, culminating in the Mw
            7.1 itself.
51  - Implications
52      - Region A shows a fairly classic monotonic magnitude
            taper: large aftershocks confined to early times, with
            later seismicity dominated by smaller events.
53      - Region B, in contrast, maintains episodic moderate-
            magnitude activity for >24 h, and ultimately produces
            a much larger mainshock. This is a first indication
            that magnitude decay is slower or more irregular in
            Region B.
54
55  Diagnostic C - Time evolution of the Omori \(p(t_n)\)
        parameter
56  Observations:
57  - Early windows (first ~5 h):
```

```
58      - Both regions start with high p-values (~2-2.5),
          reflecting the very rapid early decay dominated by
          immediate aftershocks of the Mw 6.4.
59      - Error bars are large, so differences between regions
          are not yet meaningful.
60  - Intermediate windows (~5-10 h)
61      - Region A (blue):
62        \(p\) decreases to ~1.3-1.5 and then stabilizes.
63      - Region B (orange):
64        \(p\) decreases more strongly, dropping below 1 (≈0.9)
            by ~9-10 h.
65  - Late windows (~10-34 h, up to Mw 7.1)
66      - Region A:
67        - \(p(t_n)\) remains near ~1.0-1.6, slowly increasing
            toward the end.
68        - This is close to a "classical" Omori decay (\(p \
            approx 1\)).
69      - Region B:
70        - \(p(t_n)\) stabilizes at significantly lower values,
            ~0.5-0.8.
71        - Error bars overlap somewhat but are consistently
            lower than Region A's.
72        - A lower p indicates a slower long-term decay or
            comparatively stronger late activity.
73  Implications:
74  - The Omori decay is systematically shallower in Region B
      than in Region A once the first few hours are included.
75  - Because Region B lies along the future Mw 7.1 rupture, this
        suggests that the part of the fault that will later host
      the Mw 7.1 retains relatively higher levels of seismic
      activity, rather than quieting as quickly as the Mw 6.4
      fault segment (Region A).
```

B.6 Multi-Perspective Synthesis and Agent-Based Integrated Assessment

After conducting independent analyses from the perspectives of spatiotemporal organization, magnitude-frequency distribution, and Omori-Utsu decay behavior, this section integrates the evidence obtained across these analytical dimensions. Relying on the multi-perspective analysis module of the TRACE platform, we perform cross-evidence correlation and internal consistency testing to reconstruct, at the causal-structural level, the dynamical evolution pathway linking the M_w 6.4 and M_w 7.1 events.

The integrated results indicate that the M_w 6.4 earthquake did not directly trigger the M_w 7.1 event through instantaneous dynamic perturbation. Neither the early post-mainshock epicentral expansion pattern nor the OU decay structure reveals evidence of immediate cascading propagation along the NW-SE direction. Instead, multiple lines of evidence consistently support a progressively evolving loading process initiated by static Coulomb stress redistribution. Specifically, the geometry and kinematics of the M_w 6.4 rupture are mechanically compatible with the NW-SE trending fault segments, imparting a favorable static stress increment to that structure and thereby increasing the feasibility of subsequent rupture nucleation. During the approximately 1.4-day inter-mainshock interval, the NW-SE fault system did not exhibit synchronous activation. Rather, it underwent a structurally controlled and temporally asynchronous

evolutionary process. Persistent fault-parallel seismicity, the development of a low-b corridor, and slowly decaying OU behavior collectively indicate progressive stress redistribution and localized weakening within this fault segment. This process does not appear to have been dominated by a single strong event. Instead, it is more consistent with a delayed nucleation mechanism within the rate-and-state friction framework. Under initial static loading, the fault likely evolved gradually through distributed microfracture growth and possibly aseismic slip modulation, enabling potential rupture patches to progressively approach the critical instability threshold.

At the causal level, this integrated model simultaneously explains multiple independent observations. First, the spatial formation of a low-b concentration belt and seismic convergence along the future rupture corridor. Second, the presence of an approximately day-scale delayed response rather than immediate triggering. Third, statistically significant deviations from standard aftershock decay, including rate surplus and slow decay behavior. Accordingly, purely instantaneous dynamic triggering mechanisms or simple aftershock relaxation models are insufficient to account for these multi-scale features. The 2019 Ridgecrest earthquakes sequence can therefore be interpreted as a near-field cascading triggering process initiated by static stress loading and dynamically expressed through delayed nucleation. This process reflects the coupled interaction among structural geometry, stress transfer, and frictional evolution, and provides a unified explanatory framework for inter-mainshock triggering mechanisms within complex fault systems.

Box B.6.1 User Request

```
Evaluate the interaction between the M6.4 and M7.1 seismic
    events.
Task Requirement: Integrate the most plausible physical
    explanation based on independent analysis reports.
    - Geometric Compatibility: Does the rupture geometry of
      the M6.4 event create a favorable stress condition for
      the M7.1 nucleation site?
    - Temporal Signature: Does the delay between events align
      with immediate mechanical triggering or a time-
      dependent process (e.g., afterslip or fluid diffusion)
      ?
    - Seismicity Statistics: What do the b-value and Omori-
      law fluctuations reveal about the state of stress and
      criticality before the M7.1 mainshock?
    - Background Information: Is there any background
      information that can help us understand the
      interaction between the M6.4 and M7.1 seismic events?

1. Regional Geological Background:
```

Southern California's high level of seismic activity is a result of tectonic motion, which causes the northward progress of the Pacific plate (on the west) relative to the North American plate (on the east). The main plate-boundary fault is the San Andreas Fault, which stretches 1,200 km (745 mi) from the Salton Sea in the south to offshore Cape Mendocino in the north. The southern San Andreas Fault crosses through the largest mountains in southern California and runs near communities including Parkfield, Frazier Park, Palmdale, Wrightwood, San Bernardino, Banning, and Indio. This right-lateral strike-slip fault moves at different rates along its trace, from about 35 mm per year (1.4 in/yr) near Parkfield to a low of about 18 mm/year (0.7 in/yr) in the south. The San Andreas Fault can generate the region's largest magnitude earthquakes (up to about M8.2). The most recent 'Big One' on this fault in southern California was the M7.9 Fort Tejon earthquake of 1857, which was strongly felt throughout Los Angeles.

To the west of the San Andreas, several other right-lateral, strike-slip faults accommodate plate-boundary motion. The San Jacinto, Elsinore, Newport-Inglewood, and Rose Canyon Faults are the most prominent. There are also right-lateral faults offshore, including the faults of the San Diego Trough Fault Zone. Among these faults, the San Jacinto moves the fastest, at a rate of about 14 mm/year (0.6 in/yr), but all of these faults are capable of major earthquakes. There have been large, historical earthquakes on the San Jacinto (1918, M6.7) and the Newport-Inglewood Faults (1933, M6.4). The Rose Canyon Fault is an important source for seismic hazard in San Diego because of its proximity to the city. Just south of the Salton Sea, deformation from the San Jacinto and San Andreas Faults merge onto a single fault, known as the Imperial Fault. This fault has a high slip rate (>30 mm/yr, 1.2 in/yr) and two large historic earthquakes in 1940 (M6.9) and 1979 (M6.5).

The faults of the Eastern California Shear Zone (ECSZ) accommodate about a quarter of the Pacific-North American tectonic plate boundary motion. This network of faults runs north from the southern San Andreas Fault to the California-Nevada border. The ECSZ has hosted nearly all of the major earthquakes in southern California over the past few decades, including the M7.2 1992 Landers earthquake, M7.1 1999 Hector Mine earthquake, and the M7.1 2019 Ridgecrest earthquake sequence. Most faults of the ECSZ exhibit strike-slip motion.

```
15      Many of the mountains of southern California are bounded
           by reverse faults. Between Palm Springs and Santa
           Barbara, the San Andreas Fault bends to the west, and
           plate-boundary motion creates compressive forces.
           Reverse fault slip accommodates these forces and the
           Transverse Range mountains, including the San
           Bernadino, San Gabriel, and Santa Monica Mountains,
           are lifted as a result. The Cucamonga, Sierra Madre,
           and Hollywood Faults are prominent examples, but not
           all of these faults reach Earth's surface. The
           damaging M6.7 Northridge earthquake in 1994 occurred
           on a blind fault beneath greater Los Angeles and
           highlighted the potential hazard from faults that have
            no visible scarp. The Puente Hills Fault is an
           important blind fault that has been identified since
           the 1994 Northridge earthquake. Although many southern
            California reverse faults are short compared to the
           San Andreas, they are still quite dangerous. Moderate
           earthquakes on these faults, including the 1994
           Northridge and M6.6 1971 Sylmar, have caused over 100
           deaths and thousands of casualties. Moreover, multiple
            faults may rupture together in a major earthquake in
           close proximity to population centers.
16
17      Very few southern California faults exhibit primarily
           left-lateral slip. The Garlock Fault is an example
           that is highly visible in the landscape and capable of
            large earthquakes. The Garlock fault slips at about 8
            mm/year (0.3 inches/year). Other left-lateral faults
           tend to be much less active
18
19      Southern California is also home to small areas of
           volcanic and geothermal activity, including Coso,
           north of Ridgecrest, and in the area south of the
           Salton Sea. In these areas, hot fluid or magma is
           moving through the crust, causing local stresses and
           fracture movement. These areas frequently experience
           seismic swarms, which are clusters of earthquakes that
            have no clear mainshock. They may consist of many
           thousands of events and can last for hours, days, or
           years. Seismic swarms are also observed elsewhere in
           southern California, indicating localized movement of
           crustal fluids.
20
21  2. Independent Research Results
22      - Spatiotemporal Analysis1: PATH_TO_TECHNIQUE_REPORTS
23      - Spatiotemporal Analysis2: PATH_TO_TECHNIQUE_REPORTS
24      - Fault Triggering Mechanism1: PATH_TO_TECHNIQUE_REPORTS
25      - Fault Triggering Mechanism2: PATH_TO_TECHNIQUE_REPORTS
26      - Fault Triggering Mechanism3: PATH_TO_TECHNIQUE_REPORTS
27      - Temporal Evolution of Directional Clusters:
           PATH_TO_TECHNIQUE_REPORTS
28      - Quantitative Analysis of Fault Segmentation:
           Differences in Propagation at the Fault Scale:
           PATH_TO_TECHNIQUE_REPORTS
29      - B-value time-varying: PATH_TO_TECHNIQUE_REPORTS
30      - B-value spatial-varying: PATH_TO_TECHNIQUE_REPORTS
31      - Regional Omori-Utsu law: PATH_TO_TECHNIQUE_REPORTS
```

Box B.6.2 Analysis Summary

```
1. Scientific Story
The 2019 Ridgecrest sequence posed a deceptively simple question to seismologists: did the Mw 7.1 mainshock simply happen to follow the Mw 6.4 event, or did the smaller rupture actively prepare and promote the larger one along a specific fault strand of the Eastern California Shear Zone? Independent analyses of the relocated TRACE catalog, mapped surface faults, and time-dependent seismicity statistics converged on a striking narrative. A nearly quiet fault system in the Mojave Desert was first jolted by the Mw 6.4 event, which instantaneously lit up a dense, fault-controlled aftershock cloud, then progressively organized that cloud into a NW-SE corridor linking the two eventual mainshocks. Over tens of hours, KDE hotspot tracking, directional Ripley analyses, and along-fault projections revealed the principal locus of seismicity migrating and sharpening along this corridor, even as the overall envelope of seismicity spread and fragmented across multiple strands. In the same interval, Omori-Utsu inversions showed the Mw 6.4 fault segment relaxing as a textbook aftershock zone, while the future Mw 7.1 segment departed dramatically from a single Omori decay, entering a late, quasi-steady high-rate regime tightly clustered around earlier events. Spatially resolved b-value mapping further exposed a narrow, low-b corridor along part of the future Mw 7.1 rupture, embedded within a broader field that lacks a compelling time-persistent anomaly when viewed at coarse scale. Together with fault-distance statistics that confine most seismicity to within ~1-2 km of mapped traces, these patterns outline a physically coherent scenario: within the tectonically loaded, right-lateral fabric of the Eastern California Shear Zone, the Mw 6.4 rupture imposed a favorable Coulomb stress change and immediate high-rate activation on the connected NW-SE fault, after which time-dependent processes-plausibly aseismic slip and rate-and-state frictional evolution-progressively weakened a pre-stressed patch that finally failed as the Mw 7.1 earthquake.

2. Abstract
Southern California's Eastern California Shear Zone accommodates a substantial fraction of Pacific-North America plate motion and frequently hosts multi-fault earthquake sequences, raising fundamental questions about how moderate events condition subsequent large ruptures. Here we examine the causal link between the 2019 Ridgecrest Mw 6.4 and Mw 7.1 earthquakes by integrating independent spatiotemporal clustering analyses, fault-referenced kinematics, Omori-Utsu inversions, and spatially and temporally variable b-value estimates from the relocated TRACE catalog.
```

Using time-sliced epicentral maps, directional Ripley functions, kernel density hotspot tracking, and along-fault projections, we show that the Mw 6.4 event rapidly activates a multi-armed aftershock system that is tightly confined to mapped strike-slip faults and progressively organizes into a NW-SE corridor that directly links the Mw 6.4 and Mw 7.1 epicenters. Gridded onset-time statistics, change-point analyses of regional rates and energy, and region-specific Omori fits reveal that while the Mw 6.4 rupture segment exhibits normal, rapidly decaying aftershock behavior with high Omori exponents, the NW-SE segment that hosts the Mw 7.1 mainshock undergoes a delayed rate surge ≈18 h after Mw 6.4, a pronounced drop of the Omori exponent to ≈0.5, and strong positive rate residuals, indicating a localized, late-time acceleration inconsistent with a single homogeneous Omori law. Spatially averaged, time-varying b-values within a 5-10 km radius of the Mw 7.1 hypocenter do not show a statistically persistent low-b anomaly relative to a Mw 6.4 control region, yet adaptive kernel mapping over the full inter-mainshock window delineates a narrow, low-b corridor along the future Mw 7.1 rupture, bounded by higher-b off-fault and conjugate structures.

Here we show that these geometric, temporal, and statistical signatures together support a triggering mechanism in which the Mw 6.4 earthquake imparts favorable static stress changes on a structurally compatible NW-SE fault, immediately seeds that fault with aftershocks, and then, over ~1.4 days, progressive fault-parallel clustering, aseismic slip, and evolving rate-and-state conditions drive the Mw 7.1 nucleation patch toward critical failure. This integrated picture reconciles seemingly discordant seismicity metrics, rules out purely instantaneous system-wide triggering, and underscores that large ECSZ earthquakes can emerge from spatiotemporally organized cascades within pre-existing, plate-boundary strike-slip networks.

3. Research Findings

The observational foundation across the independent analyses is remarkably consistent: between Mw 6.4 and Mw 7.1, seismicity is strongly fault-bound, anisotropic, and gradually focused along the future Mw 7.1 rupture. Distance-to-fault calculations demonstrate that nearly three-quarters of inter-mainshock events nucleate within 2 km of mapped faults, and directional Ripley L-functions show an early phase of multi-azimuth clustering that evolves into a dominant NW-SE orientation matching the mapped right-lateral system that hosts Mw 7.1. Time-colored epicenter maps and KDE fields reveal that the first hours after Mw 6.4 are dominated by activity near the Mw 6.4 fault intersection and its conjugate strand, while the eventual Mw 7.1 fault remains comparatively subdued; yet over the subsequent tens of hours, hotspot maxima and density ridges migrate north-northwest, forming a continuous seismic corridor between the two epicenters and culminating in persistent hotspots within a few kilometers of the Mw 7.1 hypocenter. Gridded onset-time and fault-segment activation analyses further indicate that activation is highly non-synchronous: cells and segments switch on over almost the entire ~34 h interval, with the 10-90 % activation span occupying most of the inter-mainshock window, and along-strike regression slopes of onset time versus distance indicating only diffuse, slow migration rather than a sharp front. Regionally, the fault segment that hosted Mw 6.4 displays broadly synchronous, high-rate activation along strike immediately after the foreshock, whereas the NW-SE segment that later ruptures in Mw 7.1 activates more heterogeneously, with earliest sustained activity and highest cumulative counts clustering around the eventual Mw 7.1 nucleation zone.

Mechanistically, these patterns support a physically coherent scenario in which geometric compatibility and static stress transfer from the Mw 6.4 rupture establish favorable conditions for Mw 7.1, while time-dependent processes govern the observed delay. The mapped fault network around Ridgecrest forms part of the Eastern California Shear Zone, where right-lateral strike-slip faults link the southern San Andreas system to the Walker Lane; in this setting, the Mw 6.4 rupture on a NE-SW-oriented strand intersected and loaded a structurally connected NW-SE fault that is kinematically consistent with regional shear. The immediate concentration of aftershocks in narrow, fault-parallel corridors, and the rapid emergence of a NW-SE lineation between Mw 6.4 and Mw 7.1, are consistent with positive Coulomb stress changes along that through-going strike-slip fault. However, the ~33.8 h delay, the prolonged, multi-stage activation of grid cells and fault segments, and the pronounced late-time rate acceleration confined to the future Mw 7.1 region argue against a purely instantaneous trigger and instead implicate aseismic slip and rate-and-state evolution. Omori-Utsu inversions highlight this contrast: along the Mw 6.4 fault (Region A) the aftershock sequence decays rapidly, with Omori exponents p stabilizing at $\gtrsim 2$ and residuals that are negative or near zero, consistent with efficient stress relaxation; along the Mw 7.1 segment (Region B) the sequence first mimics this behavior, but then, ~17-20 h after Mw 6.4, transitions into a low-p (≈ 0.5), high-residual state in which observed rates exceed early-time Omori predictions by up to an order of magnitude. Spatial nearest-neighbor statistics, KDE hotspot focusing, and along-strike migration analyses all show that this anomalous regime is tightly clustered on the same NW-SE patch that ultimately ruptured, suggesting that continued aseismic slip or slow redistribution of stress concentrated failure onto a pre-stressed asperity rather than nucleating a new orientation or activating a previously quiescent volume.

```
Validation across diverse seismicity statistics reinforces this interpretation while clarifying the role of b-values. Time-dependent, disc-based b-value estimates within 5-10 km of the Mw 7.1 and Mw 6.4 epicenters show no robust, long-lived low-b anomaly unique to the Mw 7.1 region; instead, both regions fluctuate around background levels, with the most pronounced deviation in the Mw 7.1 circle being a transient high-b episode, and confidence intervals never clearly separating between the two areas. Yet an independent, spatially adaptive kernel mapping of b-values over the full inter-mainshock window reveals a narrow low-b corridor (b≈0.55-0.7) along the NW-SE rupture path, bounded by higher-b off-fault and conjugate domains, and low-b clusters whose centroids lie within the near-fault corridor. Consistent with the Omori anomalies, this suggests that while broad, time-persistent low-b precursors are absent at coarse scale, the future Mw 7.1 rupture is embedded within a spatially focused, magnitude-biased regime that is only resolved when b-values are analyzed along the actual fault geometry. The convergence of fault-distance statistics, anisotropic clustering metrics, onset-time distributions, Omori inversions, and spatial b-value mapping-all derived from independent workflows-therefore yields a statistically robust and geophysically plausible explanation: in the tectonically loaded Eastern California Shear Zone, the Mw 6.4 earthquake immediately reorganized a multi-fault system into a strongly fault-parallel, NW-SE-dominated network, imposed favorable static stresses on the connected Mw 7.1 fault, and initiated localized high-rate and low-b clustering there; over the following day, this segment evolved through an anomalous, slowly decaying foreshock regime that culminated in the Mw 7.1 mainshock, exemplifying how moderate events within plate-boundary strike-slip systems can act as dynamically evolving precursors to larger ruptures rather than as isolated shocks.
```

C Global Seismicity Characterization through Structured TRACE Reasoning

This section describes the automated and modular analysis of global seismicity conducted by TRACE. The analysis focuses on critical dimensions, including earthquake completeness, magnitude distribution laws, spatiotemporal evolutionary behavior, and focal physical mechanisms. The primary dataset is the Global CMT (1980–2023) catalog [6], supplemented by the ISC-Bulletin (1900–2024) [7] to enhance the coverage of focal depth analysis. Aligning with the criteria established by Petruccelli et al. (2019) [8], the core analytical sequence focuses on 56,832 seismic events with depths shallower than 50 km.

C.1 Spatiotemporal Evolution of Catalog Completeness and Observational Capacity

The completeness magnitude (M_c) serves as both a fundamental statistical constraint for seismicity analysis and a direct metric for the evolution of global seismic network

observational capacity. TRACE systematically evaluates the completeness of the Global CMT (1980–2023) catalog by integrating diverse statistical estimation methods. Within this analytical framework, TRACE robustly quantifies M_c and its associated uncertainties by employing the Maximum Curvature (MAXC) method coupled with bootstrap resampling. The analysis reveals a pronounced step-wise declining trend in global M_c since 1980, with a cumulative reduction of approximately 0.5 magnitude units. Leveraging change-point detection techniques, the agent precisely identifies significant transitions in observational capacity around 1988, 2006, and 2015, which physically correspond to the global deployment of digital seismic networks and the phased expansion of broadband stations.

Spatially, TRACE identifies substantial heterogeneity in global monitoring capabilities. In regions with superior observational infrastructure, M_c remains stable below 5.05; conversely, in remote or sparsely instrumented areas—such as mid-ocean ridges and polar regions—M_c exceeds 5.3. By correlating local completeness magnitudes with station density distributions, TRACE further elucidates the dominant role of local monitoring infrastructure in governing the quality of the global catalog. The agent automatically identifies critical observational "weak zones" in regions including Peru-Ecuador, Central Chile, Luzon, and East Siberia. Strategic station deployment in these tectonically active but undersampled zones is identified as the optimal strategy to mitigate global M_c fluctuations and enhance the overall statistical integrity of the seismic catalog.

Box C.1.1 User Request

```
Perform an analysis of the magnitude of completeness (Mc) for
    a global earthquake catalog.
Requirements:
1. Data Source
- A global earthquake catalog from CMT (1980-2023): "./data/
  Catalog_1980_2023_Depth50.txt"
- Global seismic station distribution: "./data/stations_info.
  csv"
2. Estimate the magnitude of completeness (Mc) using more
   than one method (e.g. Maximum Curvature, K-S distance, Mc
   by b-value stability)
3. Validate the Stability and Consistency Analysis of
   estimated Mc
4. Estimate the Temporal Evolution of the Magnitude of
   Completeness (Time-Varying Mc)
5. Estimate the Spatial Variation of the Magnitude of
   Completeness
6. Give some suggestions for the station deployment for
   further based on the station distribution and the spatial
   variation of the magnitude of Completeness.
```

Box C.1.2 Final Experimental Plan

```
Experimental Plan: Global Magnitude of Completeness (Mc)
    Analysis
1. Top level Goal: Quantify and analyze the magnitude of
   completeness (Mc) of the Global CMT earthquake catalog
   (1980-2023) by
     - Estimating static (whole-catalog) Mc with multiple
       methods
     - Assessing uncertainty via bootstrap
```

```
    - Tracking temporal evolution of Mc
    - Mapping spatial variation of Mc at each epicenter
    - Relating spatial Mc to station coverage and proposing
      future station deployment

2. Load, clean, and standardize earthquake and station data
   for all downstream analyses.
    - Read Global CMT catalog
    - Read station distribution
    - Build spatial indices
    - KD-tree on event epicenters; KD-tree on station
      coordinates
    - Save cleaned data

3. Compute a global static Mc using multiple established
   methods and compare results.
    - Define magnitude binning: Bin width ΔM = 0.1; magnitude
      range [min(mag) - 0.05, max(mag) + 0.05]
    - Estimate Mc by each method (parallel over methods): a)
      Maximum curvature (MAXC)
    b) Kolmogorov-Smirnov distance (KS) c) b-value stability
      (MBS) d) (Optional) Gutenberg-Richter goodness-of-fit
      at 90% (GFT-90)
    - Collate results

4. Quantify uncertainty of static Mc estimates via bootstrap
   with early-stopping.
    - For each method in step3 (parallel over methods):
      1) Initialize bootstrap (default N=50, max=100)
      2) At each iteration: resample magnitudes with
         replacement, recompute Mc via method
      3) Track running standard deviation; stop if Δ(std) <
          0.02 units over last 10 iterations 4)If total
         events < 500, skip bootstrap and flag '
         insufficient data'
    - Summarize per method

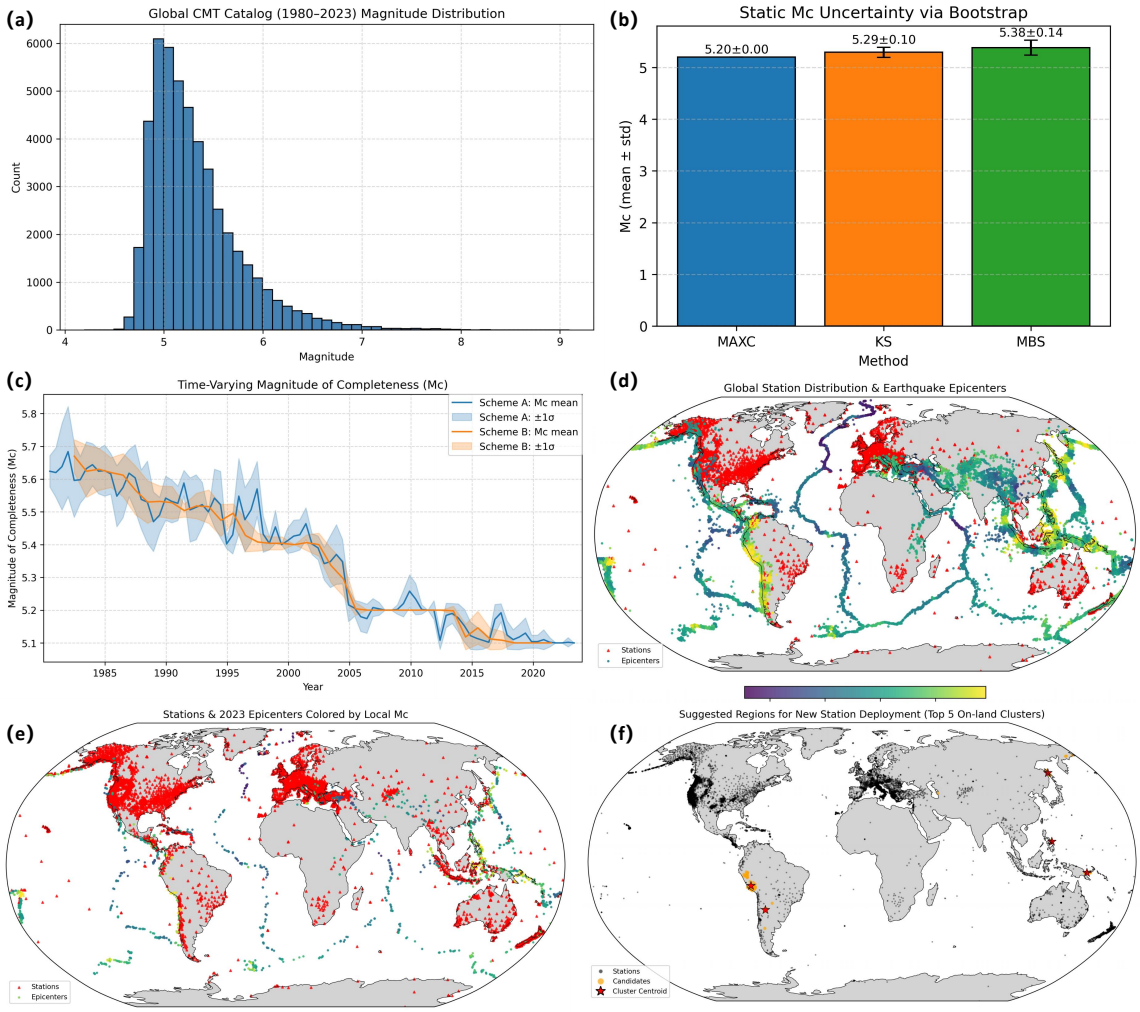
5. Estimate time-varying Mc using sliding and fixed windows,
   quantify uncertainty, and detect change-points.
    - Define window schemes:
      - Scheme A: fixed = 1 year, slide = 0.5 year
      - Scheme B: fixed = 5 years, slide = 1 year
    - Generate window list
      - From 1980-01-01 to 2023-12-31; compute window_start
        times at slide interval
    - For each window and scheme (parallel over windows)
      - Extract events in [start, start+fixed]
      - If n_events < 200, skip window
      - Estimate Mc via MAXC; bootstrap N=50 (max=100) with
        early-stop (Δ(std)<0.02 over 10 iters)
      - Record: window_center, scheme, Mc_mean, Mc_std,
        n_events
    - Detect change-points
      - Apply PELT algorithm on Mc_mean time series per
        scheme
      - Identify dates where significant shifts occur

```

```
6. Compute local Mc at each epicenter using adaptive cylindrical sampling volumes.
- Set sampling radii: [200,300,..,1500] km
- For each event node (parallel over nodes)
    a) For each radius in ascending order:
        - Query KD-tree for events within horizontal distance ≤ radius
        - If total_events ≥200 and (after Mc estimation) events_above_Mc ≥100, select radius; else continue
    b) If no radius qualifies, mark node as 'insufficient data' and skip bootstrap
    c) At selected radius:
        - Estimate Mc_initial via MAXC
        - Apply conservative correction: Mc_corrected = Mc_initial + 0.2
        - Bootstrap N=100 (max=200) with early-stop (Δ(std) <0.02 over 20 iters); if total_events < 300, skip bootstrap (σ=NaN)
    d) Record per node: node_id, lon, lat, Mc_corrected_mean, Mc_corrected_std, total_events, radius_used, bootstrap_iters

7. Analyze relationship between station distribution and spatial Mc; recommend future station placements.
    - Plot global overlay and last-year overlay
    - Compute station density vs. Mc
        - For each node in spatial_mc_results: count stations within 300 km; record station_density
        - Compute Spearman correlation between station_density and Mc_corrected_mean
        - Build table: node_id, station_density, Mc_corrected_mean
    - Recommend deployment regions
        - Identify top 5 geographic clusters (e.g., via DBSCAN) where station_density low (< P10) and Mc_high (> P90)
        - Summarize cluster centroids and recommended station count
```

Box C.1.3 Main Visualization Results (Raw Output)



Box C.1.4 Analysis Summary

```
summary of magnitude of completeness (Mc) for a global
    earthquake catalog.

1. Key findings
- Global static Mc estimates cluster tightly between 5.2 and
    5.6: Completeness arises where the observed frequency-
    magnitude distribution departs from the Gutenberg-Richter
    linear trend due to detection limits.
- Bootstrap-derived uncertainties differ by method:
    Resampling magnitudes reveals that the MAXC curvature
    method is highly stable (σ ≈ 0), whereas KS (σ ≈ 0.10) and
     b-value stability (σ ≈ 0.14) reflect differing
    sensitivities to distributional fluctuations.
- Temporal decline of Mc by ~0.5 units since 1980: Global
    network expansions (digital instrumentation in late 1980s,
     broadband roll-out ~2000, densification in 2010s) lower
    the detection threshold over time, yielding significant
    change-points around 1988, 2006, and 2015.
```

- Spatial heterogeneity: Mc $\lesssim$ 5.05 in well-instrumented regions vs. Mc $\gtrsim$ 5.3 in remote areas: Local station density dictates sampling volume completeness; sparse networks (e.g., mid-ocean ridges) raise Mc due to reduced detection capability.
- Identification of top-5 under-instrumented clusters for station deployment: Regions with low station density and high Mc (e.g., Peru/Ecuador, Central Chile, Luzon, PNG/ Solomon Islands, Eastern Siberia) will benefit most from added stations to reduce local detection thresholds and improve seismic catalogs.

2. Overview and method context

- We first cleaned and indexed the Global CMT catalog and ISC station list (1980-2023), then computed a global static Mc via multiple estimators, quantified bootstrap uncertainties, tracked Mc evolution through fixed/sliding temporal windows with change-point detection, mapped spatial Mc by adaptive cylindrical sampling around each epicenter, and finally correlated local Mc with station density to propose optimal new station sites.
- Key physical and algorithmic principles:
  - Gutenberg-Richter frequency-magnitude relation: log10 N (>M)=a-b M; Mc is where the observed N(M) departs from linearity.
  - MAXC: detect peak curvature in the binned magnitude distribution (d^2N/dM^2 maximum).
  - KS: minimize Kolmogorov-Smirnov distance between empirical and ideal exponential tail.
  - MBS: select Mc where the estimated b-value stabilizes within a tolerance.
  - Bootstrap uncertainty: resample magnitude catalog with replacement to derive σ(Mc).
  - Temporal windows: fixed duration T and slide ΔT to capture Mc(t), change-points via PELT.
  - Spatial sampling: for each node, increase cylindrical radius until N_total $\geq$200 and N_{>Mc} $\geq$100, then apply MAXC+0.2 correction.
  - KD-tree queries for efficient neighbor searches and parallel processing (n_jobs=64).

3. Summary of figure-based results

Diagnostic A - Magnitude Distribution

- The catalog contains earthquakes with magnitudes from about 4.5 up to 9.0.
- There is a clear peak in event counts around M $\approx$ 5.0, with over 6,000 events in that bin.
- Counts decline steadily for M > 5.0, indicating fewer large events.
- The distribution is right-skewed: the vast majority of events cluster between M 4.8 and M 5.5.
- The steep drop below M 4.8 suggests the onset of catalog incompleteness near that magnitude.

Diagnostic B - Static Magnitude of Completeness (Mc) Uncertainty via Bootstrap

- The global catalog's magnitude of completeness lies in the range 5.2-5.4 depending on the chosen method (MAXC, KS, MBS).

- For most applications, adopting Mc ≈ 5.3 (e.g., from the KS method) strikes a compromise between under- and over-estimation.
- If one requires maximum conservatism (minimizing false completeness), use Mc ≈ 5.4 from MBS.
- The near-zero σ for MAXC suggests over-confidence; cross-validation with other techniques is advisable.

Diagnostic C - Temporal Evolution of Magnitude of Completeness (Mc)

- Both schemes show a clear decreasing trend in Mc over the last four decades:
  - Early 1980s: Mc ≈ 5.6-5.7
  - Late 2020s: Mc ≈ 5.1-5.2
  - Scheme A (1-year fixed window, 0.5-year slide).
  - Scheme B (5-year fixed window, 1-year slide).
- Change point detection indicate the successive expansions and technological upgrades of the global seismic network
  - ~1988: First significant drop in Mc
  - ~2004: Second step decrease

Diagnostic D and E - Spatial Variation of Magnitude of Completeness (Mc)

- Well-instrumented continental regions (e.g., Japan, California, central Europe) exhibit the lowest completeness thresholds (Mc $\lesssim$ 5.05).
- Active continental margins (e.g., Mediterranean, western South America, Java-Sumatra) show intermediate Mc values (≈ 5.1 - 5.25), reflecting moderate station coverage.
- Remote oceanic plate boundaries (mid-ocean ridges, southern Pacific arcs, central Indian Ocean Ridge) consistently have higher Mc (>= 5.3), indicative of sparse seismic networks and/or lower event rates.
- Subduction zones display spatial variability within the same system:
  - The Aleutian arc and Kurile trench attain Mc ≈ 5.0-5.1 near well-covered segments, rising to ≈ 5.3 further offshore.
  - The Andean margin shows Mc increasing from ≈ 5.15 in Chile's central coast to ≈ 5.35 beneath Peru and Ecuador.
- Deep-ocean ridges (East Pacific Rise, Southeast Indian Ridge) cluster around Mc ≈ 5.2-5.35, reflecting both distance from land stations and generally lower earthquake rates.

Diagnostic F - Suggested Regions for New Station Deployment

- There is a clear inverse correlation between station density and local Mc: remote offshore and poorly instrumented onshore regions exhibit Mc bumping up toward 5.3-5.4, while well-covered areas achieve Mc ≈ 5.0-5.1.
- Prioritizing station installations in the five identified clusters will significantly improve the global magnitude of completeness and support more reliable seismicity and b-value studies.
- Next steps:
  - Validate candidate sites for logistics, power, and telemetry.

```
- Plan deployments in phases, starting with the most
  seismically active clusters (Peru/Ecuador and Central
  Chile).
- Re-evaluate local Mc after installation to quantify
  improvement.
```

C.2 Magnitude–Frequency Scaling and Multi-dimensional *b*-value Heterogeneity

C.2.1 Magnitude-Frequency Modeling

The Gutenberg-Richter (G-R) relation constitutes the cornerstone of earthquake statistics and probabilistic seismic hazard analysis [9]. TRACE constructs an end-to-end automated statistical inference workflow for global seismic catalogs, designed to eliminate circular reasoning biases by evaluating model performance without pre-assuming a fixed completeness magnitude (M_c). By applying Maximum Likelihood Estimation (MLE) and bootstrap resampling to seismic sequences shallower than 50 km in the Global CMT catalog, the agent systematically compares the fitting performance of exponential (G-R law), truncated exponential, Gamma, and Weibull distributions across multiple magnitude thresholds. Comprehensive evaluations using AIC/BIC information criteria and likelihood ratio tests demonstrate that while non-linear models (e.g., Gamma) offer marginal improvements in the low-to-intermediate magnitude range ($M \approx 5.0$–5.5), the traditional exponential model remains the most robust choice globally, consistent with the parsimony principle. Furthermore, TRACE employs Lilliefors and runs tests to reveal the intrinsic stochasticity of the magnitude sequence. Significant positive autocorrelation at lower thresholds highlights temporal clustering driven by aftershock triggering; however, as the threshold increases beyond 6.5, the sequence converges toward an independent Poisson process, validating the spatiotemporal decoupling of major seismic events in a statistical sense.

Box C.2.1 User Request

```
Use the given global earthquake catalogue to model the
    magnitude-frequency relationship and test the magnitude
    independence and exponentiality.
Requirements:
1. Data Source:
- A global earthquake catalog from global CMT (1980-2023): '
    ./data/Catalog_1980_2023_Depth50.txt'
2. Setting threshold list for the magnitude-frequency
    distribution analysis
3. Fitting Magnitude-frequency distribution using exponential
     (standard Gutenberg-Richter model), Truncated Exponential
    , Gamma and Weibull distribution
4. Goodness-of-Fit (GoF) Evaluation for the fitted model
    using 1) K-S test, χ^2 test, and Anderson-Darling test (
    absolute fit); 2) Information Criterion (AIC/BIC) and
    Akaike weights (relative model ranking); 3) Likelihood-
    ratio tests (LRT) forg nested models (e.g. exponential vs.
     tapered exponential)
5. Magnitude independence & exponentiality (Stochastic
    Process) Tests using Lilliefors test and Coefficient of
    Variation (CV) Test for Exponentiality (Distributional
    Shape)
```

Box C.2.2 Final Experimental Plan

```
Experimental Plan: Magnitude-Frequency Relationship Modeling of the Global CMT Catalog (1980-2023, Depth ≤ 50 km)

1. Top-Level Plans: Systematically characterize the magnitude-frequency distribution (MFD) of global shallow earthquakes (Depth ≤ 50 km) in the CMT catalog (1980-2023), comparing multiple parametric models, quantifying parameter uncertainties, evaluating goodness-of-fit, and testing the fundamental stochastic assumptions (exponentiality and independence) of magnitudes above threshold.

2. Data Preparation: Load the raw catalog, filter by depth, sort chronologically, and export cleaned data.
- Read whitespace-delimited file at "./data/Catalog_1980_2023_Depth50.txt"
- Assign columns in exact order
- Retain events with Depth ≤ 50 km
- Timestamp Construction & Sorting

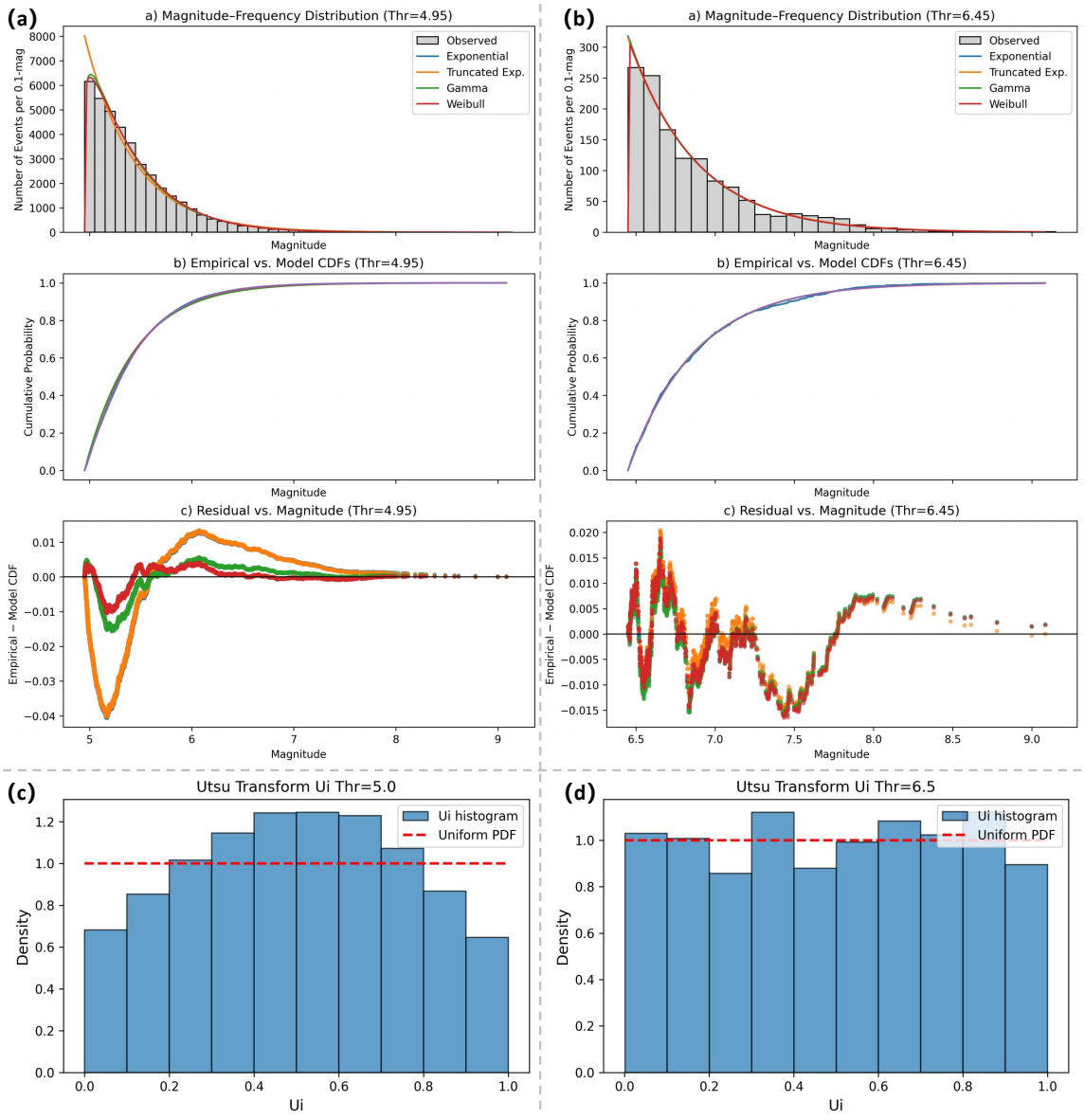
3. Completeness Magnitude & Threshold Definition: Estimate the catalog completeness magnitude (Mc) via the MAXC method and define analysis thresholds, enforcing N > 50.
- Estimate Mc (MAXC) with bin width = 0.1, bootstrap iterations = 100, and early stopping when Mc change < 0.02 over 10 consecutive iterations
- Define Thresholds: Compute thresholds: [Mc, Mc + 0.5, Mc + 1.0, Mc + 1.5]

4. Distribution Fitting & Goodness-of-Fit: For each valid threshold, fit four candidate MFD models, estimate parameters (±SE), evaluate absolute and relative fit quality, and produce diagnostic figures.
- Data Subsetting: Load magnitudes ≥ T from `01_magnitudes.csv`
- Candidate Models: Exponential (Gutenberg-Richter), Truncated Exponential (upper bound Mmax via MLE), Gamma distribution (shape k, scale θ), Weibull distribution (shape k, scale λ)
- Parameter Estimation: Perform MLE for each model using seismostats.fit_distribution or scipy.optimize and Estimate standard errors via bootstrap:
- Goodness-of-Fit Tests
    - Absolute:Kolmogorov-Smirnov (seismostats.ks_test), Chi-square test: bin width = 0.1; merge bins with expected < 5 events, Anderson-Darling (seismostats.ad_test)
    - Relative: Compute log-likelihood, AIC, BIC, Derive ΔAIC and Akaike weights across models at this threshold, Likelihood-ratio test (Wilks' theorem) for nested pair : Exponential vs. Truncated Exponential

6. Stochastic Assumptions Tests: For each valid threshold, test whether exceedance magnitudes are independent and exponentially distributed, and verify uniformity of Utsu transforms.
- Compute Variables
    - Exceedance Xi = Mi - T for i = 1.N (chronological order)
```

```
    - Utsu transform Ui = Xi / (Xi + Xi+1), for i = 1.N-1
- Exponentiality Tests on Xi:
    - Lilliefors test: seismostats.lilliefors(Xi, dist='expon')
    - Coefficient of Variation (CV) test: CV = σ/μ; p-value via bootstrap (100 iterations, cores = 8)
- Serial Independence Tests on Xi
    - Runs test: seismostats.runs_test(Xi)
    - Autocorrelation coefficient at lag 1: compute ρ1; p-value via Monte Carlo permutations (1 000 max, early stop if p < 0.01)
    - CV test on inter-event exceedance differences (reuse bootstrap settings)
- Uniformity Test on Ui
    - Kolmogorov-Smirnov test vs. Uniform(0,1)
    - Chi-square test with 10 equal-width bins
```

Box C.2.3 Main Visualization Results (Raw Output)



Box C.2.4 Analysis Summary

summary of magnitude-frequency relationship modeling of the global CMT catalog

1. Key findings

- The global magnitude-frequency distribution follows the Gutenberg-Richter exponential law above thresholds, with truncated exponential, gamma, and Weibull models yielding marginal improvement around M ≈ 5.0-5.5
- At higher thresholds (5.95, 6.45) the reduced sample size (N≈4 350 and 1 332) makes model discrimination weak; the simple exponential model remains preferred for parsimony.
- Exceedance magnitudes (Xi = Mi - Mc) conform to an exponential law in the central quantiles but exhibit heavy -tail deviations at the highest magnitudes, especially above threshold 6.5.
- Significant positive autocorrelation at lag 1 is detected for thresholds ≤ 6.0, indicating violation of strict independence; independence is recovered at threshold 6.5. Observed serial correlation at moderate thresholds reflects temporal clustering (aftershock sequences) superimposed on a Poissonian background.

2. Overview and method context

- We processed the global CMT catalog (1980-2023, depth ≤ 50 km) by (1) cleaning and chronological sorting, (2) estimating completeness magnitude Mc via the MAXC method with bootstrap, (3) fitting exponential, truncated exponential, gamma, and Weibull models above multiple thresholds using MLE and bootstrap uncertainty quantification, (4) evaluating goodness-of-fit through K-S, χ^2, Anderson-Darling tests, AIC/BIC comparisons and likelihood-ratio tests, and (5) testing stochastic assumptions (exponentiality via Lilliefors/CV tests, independence via runs/autocorrelation, and uniformity of Utsu transforms), all accelerated with parallel computing and early-stopping.
- Key Principles
  - Gutenberg-Richter law: P(M ≥ m) ∝ 10^(-b m) -> exponential tail in exceedance X.
  - Maximum likelihood estimation with bootstrap for parameter uncertainties.
  - Model selection via information criteria: AIC, BIC, and likelihood-ratio tests.
  - Exponential memoryless property: u_tt=v$^2\nabla^2$u analogy for stress-release process; leads to Ui ∼ Uniform(0,1).
  - Autocorrelation function and runs test for serial dependence diagnostics.

3. Summary of figure-based results

Diagnostic A - Magnitude-Frequency Distribution Diagnostics with M > 4.95

- Observations:
  - The observed frequency histogram falls off roughly exponentially from M=4.95 to M≈7.0.

- In the FMD panel, all four models nearly coincide beyond M≈5.5, but the Truncated Exponential slightly overpredicts the count immediately above the threshold.
- Empirical vs. Model CDFs are nearly indistinguishable for all models, indicating excellent overall fit.
- In the residual-magnitude plot, residuals remain within ±0.05 for all magnitudes; the Truncated Exponential shows a small systematic positive bias around M≈5.2-5.5.

- Conclusions:
  - The classical Gutenberg-Richter (Exponential) model is adequate at this threshold.
  - At lower thresholds (4.95, 5.45), more flexible models (Truncated Exponential, Gamma, Weibull) yield marginal improvements in fitting the low-magnitude curvature immediately above the completeness cutoff.

Diagnostic B - Magnitude-Frequency Distribution Diagnostics with M > 6.45

- Observations:
  - At high threshold, N is small (≈1 300), leading to larger scatter in the histogram.
  - Model curves (especially Truncated Exp. and Gamma) overlap closely, though minor deviations appear around M≈7.0-7.2.
  - Empirical vs. Model CDF panel still shows good alignment but with slight jitter due to low N.
  - Residuals vs. Magnitude fluctuate within ±0.07; no strong bias.
- Conclusions:
  - Model discrimination is difficult at this threshold because of limited data.
  - As threshold increases, sample size declines sharply, reducing power to distinguish models; all fits converge towards the Exponential form.
  - Statistical uncertainty is highest here; results should be interpreted with caution.

Diagnostic C and D - Serial Exponentiality and Independence test with M > 5 and M > 6.5

- Observations:
  - At thresholds 5.0, 5.5 and 6.0, the lag-1 ACF and PACF bars exceed the 95% bounds, indicating statistically significant positive serial correlation in exceedance magnitudes.
  - higher lags (2-5) show smaller but still borderline significant correlations at these lower thresholds.
  - At threshold 6.5, all ACF/PACF coefficients lie within the confidence interval, consistent with serial independence for the reduced sample of large events.
  - For all thresholds, the Ui histograms are approximately flat and center around the uniform-density line.
  - No systematic peaks or troughs are seen that would indicate a departure from uniformity.
  - K-S and χ^2 tests (not shown) confirm that the Utsu transforms are consistent with Uniform(0,1) at the 5% level.
- Summary of Conclusions

```
- Exponentiality: Exceedance magnitudes Xi are well described by an exponential distribution in the central quantile range for thresholds up to 6.0. There is a modest heavy-tail deviation at the highest magnitudes, especially above threshold 6.5.
- Independence: Significant positive autocorrelation at lag 1 for thresholds 5.0-6.0 violates strict independence. Independence appears to hold for the largest-magnitude subset (threshold = 6.5).
- Uniformity (Utsu Transform): The Utsu-transformed variables Ui follow the expected Uniform(0,1) distribution across all thresholds, supporting the lack of strong local clustering in exceedance magnitudes.
```

C.2.2 Multi-dimensional b-value Heterogeneity

As a critical parameter characterizing the scaling of earthquake magnitudes, the spatiotemporal variation of the b-value directly maps the heterogeneity of crustal stress states and rock mechanical properties. TRACE implements a multi-dimensional inversion of the global b-value under unified statistical constraints, effectively mitigating estimation uncertainties arising from small-sample sensitivity and zonation bias. In the spatial domain, the agent employs an adaptive local sampling strategy to uncover the profound coupling between b-values and tectonic settings. Extensional regimes, such as mid-ocean ridges, consistently exhibit high b-values, reflecting the dominance of small-scale ruptures under low differential stress. Conversely, strongly coupled, high-stress regions—including subduction zones and major strike-slip faults—display significantly lower b-values, indicating a higher proportion of large-magnitude events within the seismic rupture hierarchy.

In the depth dimension, TRACE characterizes the non-monotonic evolution of the b-value. Independent estimations via overlapping bins reveal that b-values are elevated in the shallow crust, decrease with depth to a minimum in the mid-crust (proximal to the brittle-ductile transition zone), and subsequently exhibit a moderate rebound in deeper intervals. This "V-shaped" depth profile is statistically significant and aligns closely with the non-linear evolution of shear stress with depth observed in rock mechanics experiments. These analytical results demonstrate that TRACE can automatically extract complex geophysical laws with clear physical significance without human intervention, providing robust quantitative support for discussing the tectonic control of earthquake size distributions.

Box C.2.5 User Request

```
Estimate the spatial and depth-dependent b-values using the provided global earthquake catalogue.
Requirements:
1. Data Source:
- Use the Global CMT catalogue (1980-2023) located at: './data/Catalog_1980_2023_Depth50.txt'
2. Depth-Dependent b-value Estimation (Depth-Varying b-value): Partition the catalogue into depth bins (e.g., 5 km intervals). Calculate the b-value and its associated uncertainty for each bin to resolve depth-varying characteristics.
```

```
3. Spatial-Dependent b-value Estimation (Spatial-Varying b-value): Treat each earthquake epicenter as a spatial node. Calculate the local b-value at each node to map the spatial variations across the study area.
```

Box C.2.6 Final Experimental Plan

```
Experimental Plan: Depth- and Spatial-Dependent b-Value Estimation from Global CMT Catalog

1. Top-Level Plans: Quantify how the Gutenberg-Richter b-value varies with depth and space using the 1980-2023 global CMT catalog (depth ≤50 km). For each depth bin and for each earthquake epicenter (node), estimate completeness magnitude (Mc) and b-value with uncertainty via bootstrap (≤200 iterations, early stopping)
- Run 01_data_preparation.py first to load and filter the catalog.
- 02_utils.py provides shared functions for Mc and b-value estimation, bootstrap control, spatial sampling, and parallel mapping.
- Run 03_depth_bvalue_analysis.py (next) to process depth bins (depends on data prep + utils).
- Run 04_spatial_bvalue_analysis.py (last) to process spatial nodes (depends on data prep + utils).

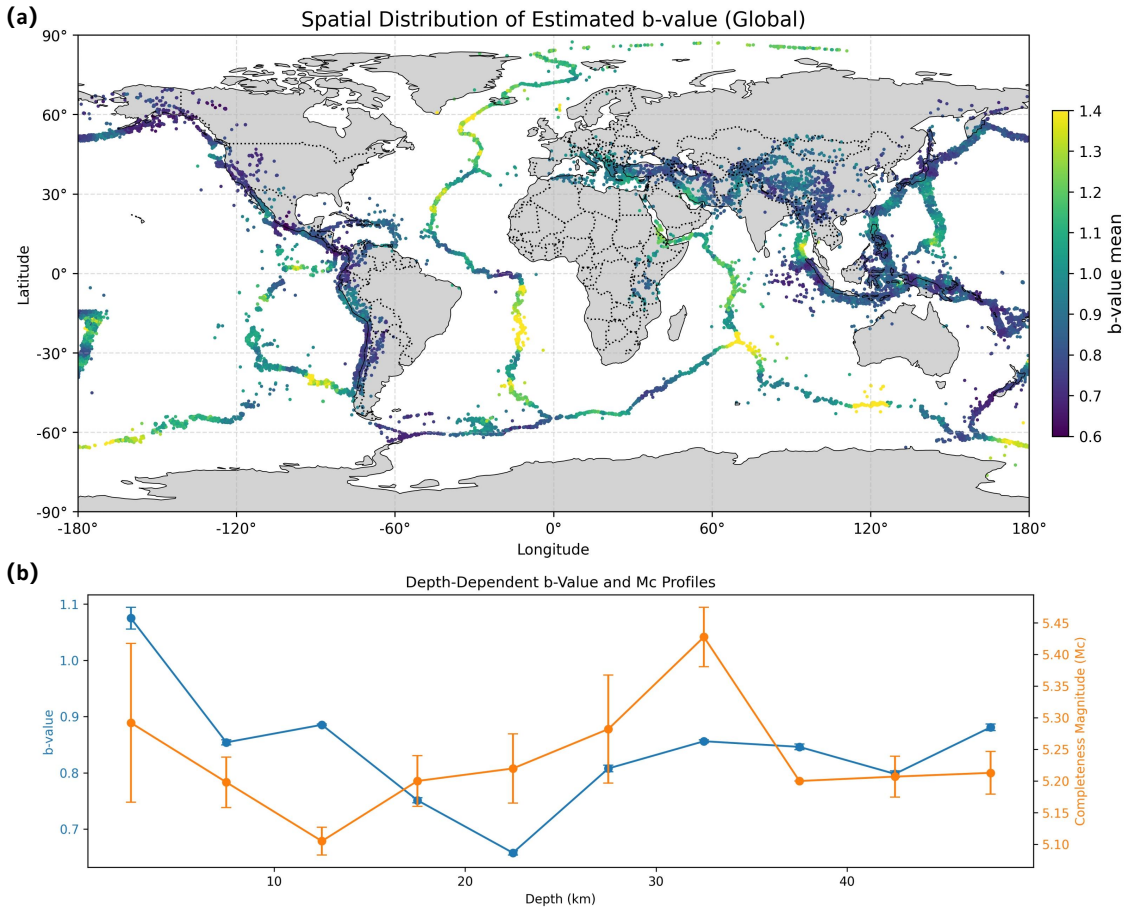
2. data preparation: Load the raw CMT catalog, filter to depth ≤50 km, create timestamps, and produce initial QA outputs.
- Load Raw Catalog: Read whitespace-delimited text from:'./data/Catalog_1980_2023_Depth50.txt'
- Filter Depth: Retain only events with Depth ≤ 50 km.
- Construct Datetime: Combine Year/Month/Day/Hour/Minute/Second into a single pandas datetime column.

3. utils wrapper Provide reusable routines for Mc and b-value estimation (with bootstrap and early stopping), parallel execution, and spatial sampling.
- Mc Estimation Wrapper: Function compute_maxc(magnitudes, nboot=100, max_boot=200, tol=1e-3)
- b-Value Estimation Wrapper: Function compute_bvalue_mle(magnitudes, Mc, nboot=100, max_boot=200, tol=1e-3)
- Spatial Sampling: Function select_within_radius(df, lon, lat, radius_km)
- Parallel Mapping: Function parallel_map(func, iterable, n_cores=64)

4. depth bvalue analysis: Estimate Mc and b-value for sequential 5 km depth bins, record bootstrap uncertainties, and plot depth profiles.
- Define Depth Bins: Create bins: [0-5), [5-10),.., [45-50] km; bin centers at 2.5, 7.5,.., 47.5 km.
- Loop over Depth Bins:
    a. Subset magnitudes in bin.
    b. If n_events < 50: skip bin and log warning.
    c. Mc Estimation: Call compute_maxc(...) on all magnitudes in bin
    d. Filter for magnitudes ≥ Mc_mean
```

```
27      e. b-value Estimation: Call compute_bvalue_mle(...) on
           filtered magnitudes
28      f. Record results: depth_min, depth_max, n_events,
           Mc_mean, Mc_std, Mc_bootstrap_used, b_mean, b_std,
           b_bootstrap_used
29
30  5. spatial bvalue analysis: For each epicenter node,
       adaptively choose sampling cylinder, estimate Mc and b-
       value with bootstrap uncertainty, and map spatial
       distribution.
31  - Load Catalog & Define Nodes
32  - Read catalog_prepared.csv; each event (lon, lat) is a node.
33  - Parallel Node Processing (64 cores, via parallel_map), for
       each node:
34      a. Adaptive Radius Selection
35          - Radii = [200,300,...,1500] km
36          - For each r: subset = select_within_radius(df, lon,
              lat, r), if n_subset ≥ 200 → final_r = r; break
37          - If none meets ≥200, record NaNs and skip bootstrap
38      b. Mc Estimation
39          - If n_subset ≥ 200: call compute_maxc(subset.
              magnitudes,.)
40          - Else: Mc_mean=NaN, Mc_std=NaN, Mc_bootstrap_used=0
41      c. b-value Estimation
42          - If n_subset ≥ 200: filter mags ≥ Mc_mean, then call
              compute_bvalue_mle(...)
43          - Else: b_mean=NaN, b_std=NaN, b_bootstrap_used=0
44      d. Record for node:
45          - node_id, lon, lat, final_r, n_subset, Mc_mean,
              Mc_std, Mc_bootstrap_used, b_mean, b_std,
              b_bootstrap_used
```

Box C.2.7 Main Visualization Results (Raw Output)



Box C.2.8 Analysis Summary

```
summary of spatial and depth-dependent b-values distribution investigation.

1. Key findings
- Spatial b-Value Variations
    - Observations: Extensional mid-ocean ridges exhibit elevated b (~1.1-1.3), whereas subduction zones and transform faults show lower b (~0.7-0.9), with back-arc/collision regions intermediate (~0.9-1.1).
    - Mechanism explanation: Extensional settings have widespread small fractures under low differential stress (high b); convergent/transform zones concentrate high stress and larger events (low b); mixed tectonics yield intermediate values.
- Depth-Dependent Completeness and b-Value Patterns:
    - Observations of completeness magnitude varying with depth: Mc is lowest (~5.10) in the 5-10 km bin, increases to ≈ 5.43 at 25-30 km, then falls to ≈ 5.20 at 45-50 km.
    - Mechanism explanation of Mc variation: near-surface detection efficiency is high (low Mc), mid-crustal attenuation and sparser small events elevate Mc, deeper improved signal-to-noise reduces Mc again.
```

```
10    - Observations of Gutenberg-Richter b-value varying with
        depth: peaks (~1.07) in 0-5 km, declines to a minimum (
        ~0.66) at ~20-25 km, and recovers to ~0.85-0.90 at 45-
        50 km.
11    - Mechanism explanation of b-value variation: Shallow
        crust hosts abundant micro-ruptures (high b), mid-crust
         under higher stress yields larger ruptures (low b),
        deeper fluid/heterogeneity effects raise b.
12
13 2. Overview and method context
14 - All earthquakes (1980-2023, depth ≤ 50 km) were filtered
     and time-stamped, then analyzed in two parallel streams:
15    - Spatial analysis: each epicenter defines a node;
        cylindrical volumes with radii 200-1500 km adaptively
        sampled until ≥ 200 events; same bootstrap-based Mc
        and b-value workflow applied in parallel across 64
        cores.
16    - Depth analysis: data binned in 5 km intervals; in each
        bin, Mc estimated via maximum curvature with ≤ 200
        bootstrap iterations and early stopping; events ≥ Mc
        used to compute b by maximum-likelihood.
17 - Key principles:
18    - Gutenberg-Richter relation: log_{10}N(M) = a - bM.
19    - Maximum-curvature Mc detection and bootstrap
        uncertainty control.
20    - MLE for b: b = ln10/(M - (Mc - ΔM/2)).
21    - Great-circle (Haversine) sampling for spatial node
        volumes.
22    - Early-stop bootstrap when parameter variance change <
        tol.
23
24 3. Summary of figure-based results
25 Diagnostic A - Spatial-Dependent b-Value Analysis
26 - Observations:
27    - Along mid-ocean ridges (East Pacific Rise, Mid-Atlantic
         Ridge, Southeast Indian Ridge) the b-values are
        systematically higher (≈ 1.1-1.3). This is consistent
        with relatively open, extensional tectonic settings
        where smaller ruptures dominate.
28    - Subduction zones and major transform faults (e.g. the
        Chilean trench, Japan trench, San Andreas and North
        Anatolian fault) exhibit lower b-values (≈ 0.7-0.9).
        These regions are associated with higher differential
        stress and larger characteristic earthquakes.
29    - Back-arc and diffuse continental collision regions (e.g
        . eastern Mediterranean, Tibetan plateau margins) show
         intermediate b-values (≈ 0.9-1.1), reflecting a
        mixture of stress regimes and crustal heterogeneity.
30    - Sampling sizes (marker area) are largest beneath well-
        instrumented, seismically active belts-e.g. Pacific
        Rim-leading to robust local estimates. In remote ocean
         basins or cratonic interiors, smaller sample sizes (
        and larger radii) yield greater uncertainty, but still
         capture first-order regional trends.
31 - Conclusions:
```

```
32      - These spatial patterns provide insight into stress
          states and fracture properties at the global scale and
           underscore the utility of depth- and space-dependent
          b-value mapping for seismic hazard studies.
33      - Tectonic control: b-value spatial variations correlate
          strongly with known tectonic environments-higher in
          extensional settings, lower in high-stress convergent
          and transform zones.
34      2. heterogeneity indicator: Elevated b-values at ridge
          and back-arc regions likely reflect more fractured,
          fluid-rich media.
35      3. Method robustness: The adaptive cylinder-sampling
          approach captures global trends with ≥ 200 events per
          node, balancing resolution and statistical reliability
          .
36
37  Diagnostic B - b-Value/Mc vs. Depth
38  - Observations:
39      - Mc is lowest (≈ 5.10) in the shallowest bin (5-10 km).
40      - Mc increases to a maximum of ≈ 5.43 around 25-30 km
          depth.
41      - Below 30 km, Mc gradually decreases to ≈ 5.20 at 45-50
          km.
42      - Bootstrap uncertainties grow in mid-crustal bins (20-35
           km), reflecting fewer events near completeness.
43      - The shallowest bin (0-5 km) shows the highest b-value (
          ~1.07), suggesting prolific small-magnitude events.
44      - b-value decreases with depth, reaching a minimum (~
          0.66) at ~20-25 km.
45      - Below ~25 km, b-value recovers to ~0.85-0.90 in the mid
          -lower crust and ≈ 0.87 at 45-50 km.
46      - Error bars are largest in the shallowest and deepest
          bins, due to limited event counts near Mc.
47  - Conclusions:
48      - These depth-dependent patterns in Mc and b-value
          highlight changes in earthquake detectability and
          rupture physics through the crust. Further spatial
          analysis will investigate lateral variations in these
          parameters.
49      - Shallow Crust (0-10 km): Lowest Mc and highest b-value
          indicate strong detection capability and a relative
          abundance of small events.
50      - Mid Crust (10-30 km):Gradual rise in Mc suggests
          decreasing network sensitivity and fewer small-
          magnitude events. b-value minimum at ~20-25 km may
          reflect a transition to more brittle, higher-stress
          conditions.
51      - Deep Crust (30-50 km): Mc decreases again, possibly due
           to lower event densities but improved signal-to-noise
           at depth. b-value rebound implies a return to more
          heterogeneous or fluid-influenced rupture regimes.
```

C.3 Temporal Seismicity Dynamics and Stochastic Point-Process Characterization

The temporal stochasticity of earthquake sequences is the fundamental basis for seismic hazard assessment and the development of forecasting models. Although traditional probabilistic seismic hazard analysis often assumes that earthquakes follow a stationary Poisson process, factors such as non-stationarity, aftershock clustering, and stress interactions frequently lead to deviations from this ideal hypothesis in observational catalogs. TRACE addresses this by constructing a multi-dimensional point-process statistical testing framework designed to systematically evaluate long-term trends in earthquake occurrence rates, the overdispersion of counting statistics, and the intrinsic randomness of inter-event times.

TRACE utilizes change-point detection based on the PELT (Pruned Exact Linear Time) algorithm, constrained by a logarithmic penalty, to identify abrupt transitions in annual earthquake counts across multiple magnitude thresholds ($M > 5.0, 5.5, 6.0, 6.5$). The analysis reveals pronounced step-wise increases in global earthquake occurrence rates during the mid-1990s and mid-2000s, showing high consistency across different magnitude levels. By integrating the previously established evolutionary patterns of completeness magnitude (M_c), the agent automatically determines that these frequency shifts do not originate from systematic changes in tectonic stress release modes. Instead, they represent observational effects introduced by the global transition to digital seismic networks and improved catalog completeness. This finding underscores the necessity of filtering non-physical "artificial increments" resulting from network evolution when constructing long-term predictive models.

In modeling earthquake counts, TRACE employs a model competition mechanism to compare the descriptive power of Poisson, Negative Binomial, and Generalized Poisson distributions for annual seismic frequencies. The results indicate that at lower magnitude thresholds ($M \leq 5.5$), earthquake counts exhibit significant overdispersion, deviating sharply from the stationary Poisson assumption due to pronounced clustering effects from aftershock sequences. In these cases, the Negative Binomial distribution, with its higher degrees of freedom, demonstrates superior fitting robustness. However, as the magnitude threshold increases beyond 6.5, the variance-to-mean ratio converges toward unity, and temporal correlation weakens substantially. This indicates that on a global annual scale, the occurrence of major seismic events essentially degrades into an independent Poisson process, validating the quasi-stochastic nature of large earthquakes over macroscopic timescales.

For the distribution of inter-event times, TRACE conducts an in-depth renewal process analysis. By comparing Exponential, Gamma, Weibull, and Brownian Passage Time (BPT) models, the agent finds that the Gamma and Weibull distributions exhibit excellent fitting performance across all magnitude thresholds. In contrast, the classic exponential distribution—representing the memoryless property of a Poisson process—fails to capture the observed interval patterns. Notably, the BPT model lacks significant statistical support in the globally aggregated catalog. This suggests that global-scale earthquake sequences are primarily governed by short-term clustering and weak memory effects rather than being dominated by a single, cyclic stress accumulation-and-release process. This automated workflow not only elucidates the temporal statistical signatures shaped by aftershock triggering and stress transfer but also proves the reliability of physical model selection within a unified framework

using statistical uncertainty assessments (e.g., χ^2 testing and bootstrap resampling), providing a quantitative reference for the temporal measures of global earthquake dynamics.

Box C.3.1 User Request

```
Statistic the temporal evolution of global earthquak and modeling the distribution of yearly counts and interevent-time
Requirements
1. Data Source:
    - Use the Global CMT catalogue (1980-2023) located at: './data/Catalog_1980_2023_Depth50.txt'
2. Seismicity Rate Statistics for each magnitude threshold (5, 5.5, 6 and 6.5)
3. Annual Earthquake Counts Distribution Modeling for each magnitude threshold using poisson distribution, negative-binomial distribution and generalized poisson distribution.
4. Interevent-Time Distribution Modeling for each magnitude threshold using exponential distribution, gamma distribution, weibull distribution and brownian passage time distribution.
```

Box C.3.2 Final Experimental Plan

```
Experimental Plan: Estimating Seismicity Rates and Testing Poisson-Process Assumptions with the Global CMT Catalog

1. Top-Level Plans: Estimate annual and inter-event-time statistics of global shallow (≤ 50 km) earthquakes from the CMT catalog (1980-2023) at multiple magnitude thresholds, detect seismicity-rate change-points, fit and compare count-based and time-interval models, quantify departures from Poisson expectations, and assess serial dependence.
- We organize the work into four cohesive Python scripts. Data and intermediate results flow top-down; computationally intensive tasks are parallelized and support bootstrapped uncertainty estimates with early-stopping.

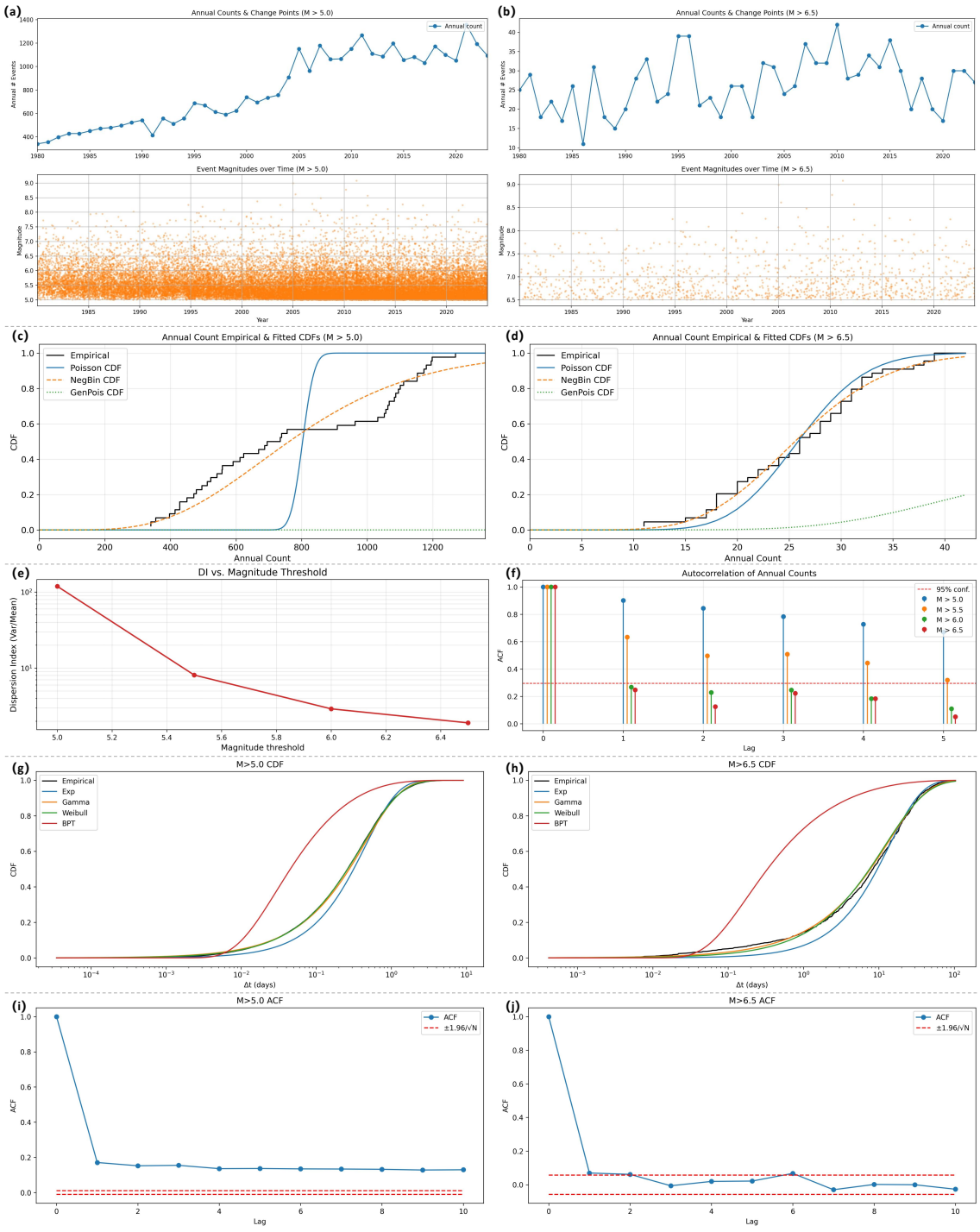
2. data preparation: Load the raw CMT catalog, filter by depth, construct event-time arrays for each magnitude threshold.
- Read raw catalog and Assign columns, finally Cast Year-Second to integers, Magnitude/Depth to floats.
- Filter by depth: Retain records with Depth ≤ 50 km.
- Generate per-threshold event-time arrays, for each T in [5.0,5.5,6.0,6.5].

3. seismicity rate analysis: Compute annual and monthly counts for each magnitude threshold and detect change-points in the annual series.
- Load event_times_M{T}
- Count aggregation: Annual counts and Monthly counts
- Change-point detection on annual counts
```

4. annual count modeling: Fit discrete distributions to annual counts, evaluate fit, compute dispersion and serial dependence.
- Load annual counts from rate_stats_M{T} and get array C
- Compute summary statistics: μ = mean(C), σ^2 = var(C), DI = σ^2/μ
- MLE fitting of count models
  - Poisson: $\lambda = \mu$
  - Negative-Binomial: estimate (r, p) via custom MLE
  - Generalized Poisson: estimate (λ, θ) via custom MLE
  - Use scipy.optimize.minimize (parallel across models)
- Model comparison
  - Chi-square test: group counts so E_i ≥ 5; compute p-values for each model
  - AIC and BIC for each model; compute normalized AIC weights
- Serial dependence: Compute ACF up to lag 5 with statsmodels.tsa.acf; test significance via Bartlett formula
- Bootstrap CIs (parallel, up to 200 iters, early-stop): Resample C with replacement; refit each model; record parameters and DI; derive 95% CI
- Aggregate results: Build one row per T with: λ(CI), r/p (CI), λ/θ(CI), DI (CI), χ^2(p-values), AIC, BIC, AIC_weights, ACF_lags

5. interevent time modeling: Model inter-event-time distributions, assess goodness-of-fit, independence, and clustering.
- Load event_times_M{T} and sorted times; compute Δt_i = diff(times) in days
- Compute CV and summary: μ_Δt, σ_Δt, CV = σ_Δt/μ_Δt
- MLE fitting of continuous models
  - Exponential (λ), Gamma (k,θ), Weibull (k,λ), Brownian Passage Time (μ,σ)
  - Use scipy.stats or custom log-likelihood; parallel across models
- Goodness-of-Fit tests
  - KS and Anderson-Darling tests for each model
  - Empirical CCDF vs. model CCDF plotted in log-log
- Diagnostics & independence tests
  - Q-Q plots vs. each model
  - ACF of Δt up to lag 10; Ljung-Box test p-value
  - Runs test on 'above/below median sequence
- Bootstrap CIs (parallel, $\leq$200 iters, early-stop)
  - Resample Δt with replacement; refit; record parameters, CV; derive 95% CI
- Aggregate results
  - One row per T with: model parameters (CI), KS/AD p-values, Ljung-Box p, Runs p, AIC, BIC, CV (CI)

Box C.3.3 Main Visualization Results (Raw Output)



Box C.3.4 Analysis Summary

```
Summary of Estimating Seismicity Rates and Testing Poisson-
    Process Assumptions with the Global CMT Catalog

1. Key findings
- Abrupt Increases in Annual Seismicity Rates
```

- All magnitude thresholds (M > 5.0, 5.5, 6.0, 6.5) exhibit one or more statistically significant change-points in annual counts, notably around the mid-1990s and mid-2000s.
- These jumps coincide with enhancements in global seismic network coverage and catalog completeness rather than true shifts in tectonic stress release.

- Over-Dispersion and Serial Correlation in Yearly Counts
  - Strong Over-dispersion at low magnitude thresholds (M > 5.0, 5.5) invalidates the simple Poisson model; Negative-Binomial provides a much better fit in CDF and PMF comparisons.
  - Dispersion Decreases rapidly with higher thresholds: by M > 6.5 the annual-count variance is only twice the mean, making the Poisson assumption progressively more tenable.
  - Temporal Dependence (ACF) is significant for lower thresholds, violating the i.i.d. assumption; it weakens substantially for M > 6.0 and above.
  - Model Selection
    - For M > 5.0 & 5.5: use Negative-Binomial (or Generalized Poisson) to account for over-dispersion and memory effects.
    - For M > 6.0: Poisson may suffice as a baseline, but NB/Gen-Poisson still marginally improve fit.
    - For M > 6.5: Poisson is an adequate approximation; additional complexity yields minimal gains.
- Renewal-Type Inter-event times distributions
  - Inter-event times deviate from the Exponential distribution, exhibiting over-dispersion and weak short-term memory.
  - Gamma and Weibull models provide the best overall fit to both CDF and PDF across thresholds.
  - The BPT model is not supported by the observed Δt statistics.
  - Clustering (CV > 1 and positive ACF at lag-1) is strongest at lower magnitude thresholds and weakens as the threshold increases.
  - Short-interval clustering (aftershocks) and stress transfer generate over-dispersed, non-renewal behavior.

2. Overview and method context

- We loaded the shallow ($\leq$ 50 km) global CMT catalog (1980-2023), filtered events by four magnitude thresholds, and branched into three analyses: (1) change-point detection on annual counts via PELT, (2) count-distribution modeling with Poisson/NB/Generalized Poisson fitted by MLE and compared by χ^2/AIC/BIC, (3) inter-event-time modeling with Exponential, Gamma, Weibull, and Brownian Passage Time fitted by MLE and validated via KS/AD tests, CV, ACF, Ljung-Box, and runs tests. Bootstrapped CIs were obtained with $\leq$ 200 iterations and early stopping.
- Key principles:
  - Dispersion Index DI = σ^2/μ measures deviation from Poisson.
  - Change-point detection: minimize cost + penalty ~ log(n)$\cdot\sigma^2$ (PELT algorithm).

- Count models: Poisson ($\lambda = \mu$), NB (r,p), Generalized Poisson (λ, θ) via log-likelihood maximization.
- Inter-event distributions:
  - Exponential: f(t)=λ.e^{-λt}
  - Gamma: γ(k,θ)
  - Weibull: f(t)=kθ^k.t^{k-1}e^{-(θt)^k}
  - Brownian Passage Time
- Temporal dependence: autocorrelation ρ(k), Ljung-Box and runs tests for serial correlation.

3. Summary of figure-based results

Diagnostic A & B - Annual Counts & Change Points (M > 5.5 & M > 6.5)

- Observations of M > 5.5
  - Change-points occur near 1990 and 2006.
  - Counts increase from ~220 events/year in the early 1980 s to ~260 by 1990, then to ~315 after 1990, and to ~360-390 after 2006.
  - As with M > 5.0, the magnitude distribution remains uniform over time, suggesting improved detection/ completeness rather than physical changes in seismicity.
- Observations of M > 6.5
  - A single change-point is detected around 2000.
  - Counts rise modestly from ~25 events/year in the 1980s to ~32-40 afterwards, with larger fluctuations due to the smaller sample size.
  - Magnitude-time plot remains stationary, reinforcing that rate changes likely reflect catalog and network factors.
- Conclusions:
  - Consistent Rate Increases: All thresholds show one or more abrupt increases in annual counts, typically in the mid-1990s to mid-2000s.
  - Stationary Magnitude Distribution: In each case the scatter of magnitudes over time is uniform, ruling out a physical shift toward larger earthquakes.
  - Catalog/Detection Effects: The timing of rate increases aligns with enhancements in global seismic networks and catalog completeness; real physical changes in global seismicity are less likely.
  - Threshold-Dependent Sensitivity: Lower thresholds detect earlier and larger rate jumps (e.g., M > 5.0, 5.5), while higher thresholds (M > 6.5) exhibit fewer, less pronounced shifts due to lower counts.

Diagnostic C & D - Annual Earthquake Count Modeling (M > 5 & M > 6.5)

- M > 5.0
  - The empirical CDF (black) is much wider than the Poisson CDF (blue), indicating strong over-dispersion.
  - The Negative-Binomial CDF (orange) better captures the heavy tails, while the Generalized Poisson (green) remains near zero.
- M > 6.5
  - Poisson CDF closely follows the empirical CDF. NB and Gen-Poisson produce almost indistinguishable fits, suggesting dispersion is now mild.

```
57
58 Diagnostic E – Dispersion Index vs. Magnitude Threshold
59 – The Dispersion Index (variance/mean) falls steeply with
     increasing magnitude threshold:
60     – ~120 for M > 5.0
61     – ~8 for M > 5.5
62     – ~3 for M > 6.0
63     – ~2 for M > 6.5
64 – Values >> 1 at low thresholds confirm large over–dispersion
     ; as threshold increases, DI approaches 1 (Poisson
     expectation).
65
66 Diagnostic F – Annual Earthquake Count Modeling
67 – M > 5.0: Very strong positive autocorrelation at lags 1–5
     (>0.7), indicating significant temporal dependence (memory
      effect).
68 – M > 5.5: Moderate autocorrelation (lag 1 ~0.63, lag 5 ~
     0.31), still above the 95% significance threshold.
69 – M > 6.0: Weak autocorrelation (lag 1 ~0.26), near the
     significance bound, suggesting counts become more
     independent year–to–year.
70 – M > 6.5: Autocorrelations fall below or near the threshold
     at most lags, consistent with a near–Poisson renewal
     behavior.
71
72 Diagnostic G & h – Empirical CDF & CCDF vs. Fitted Models (M
     > 5 & M > 6.5)
73 – Gamma and Weibull distributions (orange & green) closely
     follow the empirical CDF across all thresholds, capturing
     both short and long Δt behavior.
74 – The Exponential model (blue) systematically underestimates
     the frequency of short intervals (Δt ≲ 0.1 day) and over–
     predicts longer intervals, indicating departure from a
     memoryless process.
75 – The BPT model (red) strongly overestimates very short Δt
     and deviates from the empirical tail, suggesting its
     assumed recurrence mechanism is not well supported by the
     data.
76
77 Diagnostic I & J – Autocorrelation Function (M > 5 & M > 6.5)
78 – ACF at lag–1 is consistently positive (≈0.06–0.17),
     exceeding the ±1.96/√N confidence bounds, indicating weak
     but significant short–term correlation in Δt.
79 – higher lags (≥2) quickly fall within noise bounds, showing
     no strong long–range memory.
80 – The strongest serial dependence occurs for M>5.0 (lag–1 ≈
     0.17) and decreases for larger thresholds, suggesting that
      clustering effects (e.g., aftershock sequences) are more
     pronounced for smaller magnitudes.
```

C.4 Spatial Distribution Patterns and Plate-Tectonic Modulation

C.4.1 Epicenter Coupling with Plate Boundaries

The surface geometric distribution of global shallow earthquakes is a macroscopic manifestation of stress accumulation and brittle rupture driven by plate motion. Through a joint analysis of the Global CMT catalog and the global plate boundary

system, TRACE quantitatively evaluates the spatial non-stationarity of seismic activity and its response intensity to tectonic boundaries. To characterize the transition from local fault structures to large-scale tectonic zones, the agent constructs multi-resolution gridded density fields and applies adaptive Gaussian smoothing to mitigate sampling stochasticity. Analysis reveals that primary tectonic boundaries, such as the Circum-Pacific Belt, exhibit exceptionally high spatial clustering across all resolutions.

Further geodesic distance statistics uncover the dominant control of plate boundaries on stress release: the median distance from global epicenters to the nearest plate boundary is approximately 40 km, compared to over 600 km for a random distribution. This robust spatial correlation exhibits systematic variations across boundary types. Along divergent boundaries (e.g., mid-ocean ridges), seismicity is highly concentrated in the immediate vicinity of the boundary line. In contrast, subduction and collision zones show a broader statistical tail in their distance distribution, a feature attributed to the expanded deformation zones of the upper plate and the inclined geometry of the subducting slabs. These automatically extracted spatial parameters not only validate the statistical foundations of plate tectonic theory but also provide quantitative criteria for identifying non-typical intra-plate seismic activity.

Box C.4.1 User Request

```
Analyze the spatial distribution and plate tectonic context
    of the global earthquake catalog
Requirements
1. Data Source:
     - Use the Global CMT catalogue (1980-2023) located at:
        './data/Catalog_1980_2023_Depth50.txt'
     - Load the global plate boundaries located at './data/
        plate_boundaries.shp'
2. Estimate the spatial distribution of global earthquake
    epicenters using a gridded density representation followed
     by spatial smoothing.
3. Nearest Plate Boundary Distance Calculation and Statistic
    for Each Earthquake.
4. Baseline Comparison with a Spatially Random Reference
    Distribution
5. Group and Compare earthquakes by the type of their nearest
     plate boundary
```

Box C.4.2 Final Experimental Plan

```
Experimental Plan: Spatial Distribution and Plate-Tectonic
    Context of Global Earthquakes

1. Top-Level Plans: Characterize the global spatial patterns
    of shallow, large earthquakes (Mw ≥ 5.0, depth ≤ 50 km;
    1980-2023 CMT catalog) and quantify their relationship to
    plate boundaries. This involves (1) preparing and
    visualizing the data, (2) mapping gridded density with
    multi-scale smoothing, (3) computing nearest-boundary
    distances for both earthquakes and a matched random
    catalog, (4) comparing distance statistics between real
    and random points, and (5) examining distance
    distributions by boundary type.
```

```
- We divide the analysis into five cohesive Python scripts.
  Each script has a clear role with minimal overlap.
  Parallel tasks use 128 cores with progress reporting.

2. data preparation: Load and clean the earthquake catalog;
   load and harmonize plate boundaries; produce an overview
   map.
- Load and Clean Earthquake Catalog
- Load and Standardize Plate Boundaries
- Overview Map Visualization

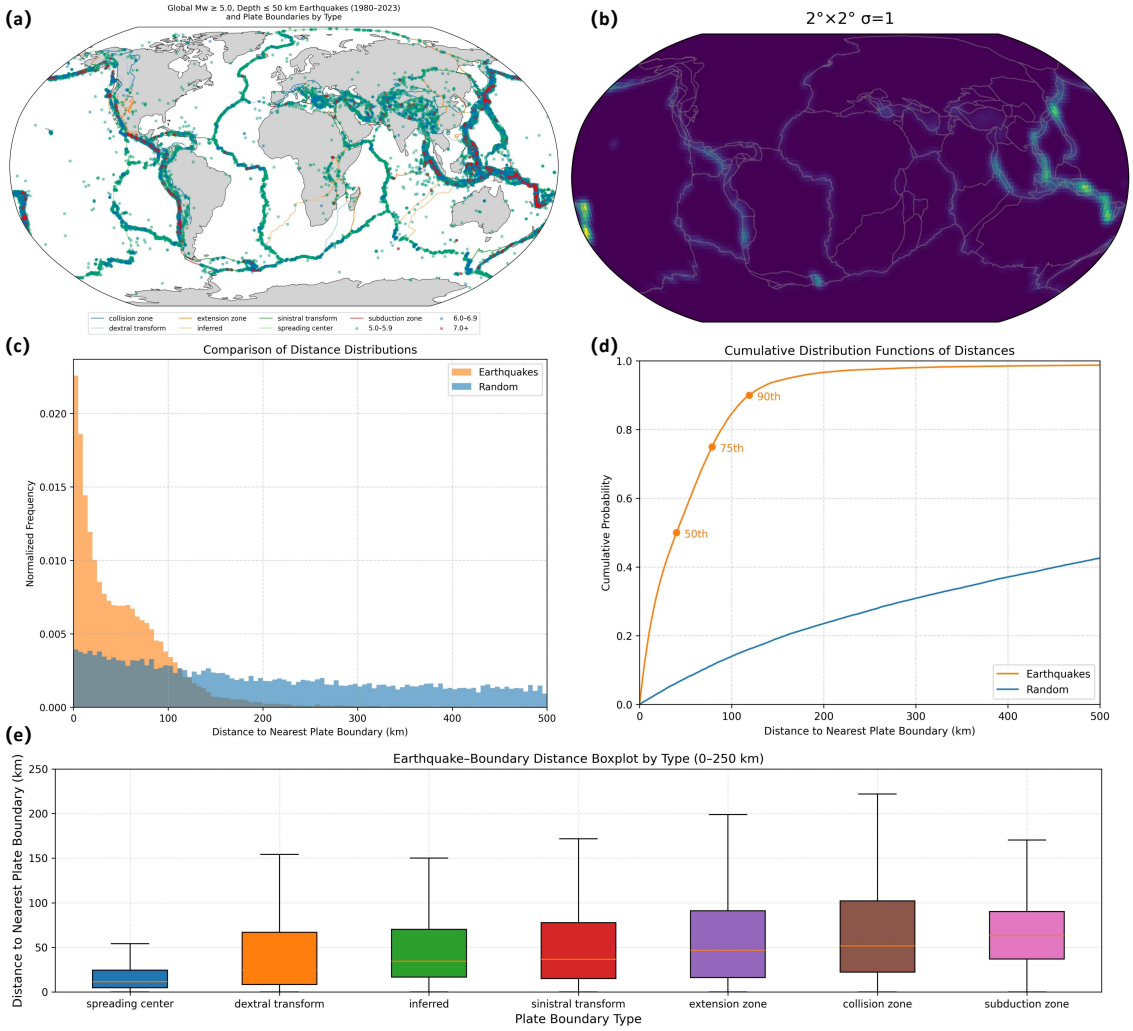
3. spatial density calculation: Construct gridded earthquake
   density at two resolutions and apply multi-scale Gaussian
   smoothing.
- Define Global Grids
- Count Events per Cell
- Gaussian Smoothing
- Density Visualization

4. boundary_distance_calculation: Compute nearest-plate-
   boundary distances for both earthquake epicenters and a
   matched random reference catalog.
- Prepare Spatial Data and Random Catalog
- Distance Computation

5. distance statistics comparison: Compute and compare
   distance statistics and distributions for earthquakes vs.
   random points.
- Descriptive Statistics
- Distribution Visualization

6. boundary type analysis:Examine how earthquake-to-boundary
   distances vary by boundary type.
- Grouping and Statistics by Type
- Comparative Visualization
```

Box C.4.3 Main Visualization Results (Raw Output)



Box C.4.4 Analysis Summary

```
Summary of Spatial Distribution and Plate-Tectonic Context of
    Global Earthquakes

1. Key findings
- Earthquake epicenters align tightly with global plate
  boundaries. This clustering reflects stress accumulation
  and brittle failure driven by relative plate motions at
  convergent, divergent, and transform interfaces.
- Multi-scale gridded density maps highlight the Pacific "
  Ring of Fire" as the dominant seismic belt and reveal
  resolution-dependent detail: fine smoothing (σ=1)
  preserves narrow ridge-parallel bands, coarse smoothing (σ
  =3) emphasizes broad tectonic belts. These patterns arise
  from heterogeneous fault density and slip rates along
  different plate boundaries.
- Earthquakes occur significantly closer to mapped plate
  boundaries than a spatially random reference. Median
  distance is ~40 km for earthquakes versus ~664 km for
  random points, underscoring the primary role of plate-
  boundary stress concentrations.
```

- Distance-to-boundary distributions vary systematically by boundary type. Spreading centers show the tightest clustering (<10 km median), transforms and inferred faults display intermediate dispersion (∼30-45 km), and subduction/collision zones exhibit the broadest tails (>70 km median) due to complex upper-plate deformation and dipping megathrust geometries.

2. Overview and method context

- A global catalog of Mw $\geq$ 5.0, depth $\leq$ 50 km earthquakes and a WGS84 plate-boundary shapefile were cleaned and merged, then used to build 2°×2° and 1°×1° gridded seismicity fields with Gaussian smoothing at σ=1 and σ=3 cells. Great-circle distances from both real and uniformly sampled random points to the nearest boundary were computed in parallel via STRtree indexing and geodetic inversion. Statistical comparisons of histograms and CDFs quantified clustering strength and boundary-type effects.
- Key principles:
  - Grid-based density estimation: count per cell + Gaussian convolution (σ in cells).
  - Great-circle distance d=R$\Delta\sigma$ computed via geodetic inverse (pyproj.Geod).
  - Uniform spherical sampling: latitude ϕ=arcsin(u), u \ sim U(-1,1) for reference catalog.
  - Statistical metrics: mean, median, p75, p90; histograms and CDFs to compare empirical vs. random distributions.

3. Summary of figure-based results

Diagnostic A - Overview spatial Map Analysis

- Observations
  - Earthquakes concentrate almost exclusively along plate boundaries, confirming the strong link between large-magnitude, shallow earthquakes and plate-tectonic processes.
  - Subduction zones (red lines) around the Pacific "Ring of Fire" host the densest clusters of events, including the largest magnitudes (red dots, Mw $\geq$ 7.0).
  - Spreading centers (green lines) along mid-ocean ridges exhibit a more continuous but lower-magnitude seismicity (mostly 5.0-5.9).
  - Collision zones (blue lines) in continental regions (e.g., himalaya, Alpine-Himalayan belt) show significant clustering of moderate-to-large events.
  - Transform faults (light blue and dark green lines; e.g., San Andreas, North Anatolian) also display aligned epicenters, though with fewer Mw $\geq$ 7.0 shocks.
  - The global map is largely devoid of large-magnitude events in intraplate regions, indicating effective catalog filtering (depth $\leq$ 50 km, Mw $\geq$ 5.0) and good data coverage along active boundaries.
- Conclusions: The overview map confirms that our filtered catalog reliably captures plate-boundary seismicity patterns. This successful data preparation step sets the stage for detailed density analysis and quantitative distance-to-boundary calculations in subsequent scripts.

```
Diagnostic B – Spatial Density Analysis
– Observations
    – Plate–boundary concentration:
        – The highest densities follow the Pacific "Ring of Fire," notably: West coast of the Americas (Chile, Cascadia, Alaska); Eastern Asia (Japan–Kurils, Taiwan, Philippine Sea); Indonesia and New Zealand regions.
        – Secondary concentrations appear along the Mid–Atlantic Ridge and Indian Ocean ridges.
    – Effect of grid resolution and smoothing scale
        – Fine smoothing (σ=1) preserves narrow, high–contrast bands along plate boundaries, especially visible at 1° resolution.
        – Broad smoothing (σ=3) merges adjacent high–density cells into continuous belts, highlighting the global geometry of major tectonic boundaries.
        – The 1° grid with σ=1 captures more localized clusters (e.g., East African Rift, Alpine–Himalayan belt), whereas the 2° grid emphasizes broader trends.
    – Intraplate and diffuse seismicity
        – Residual low–density spots correspond to intraplate or continental rift zones (e.g., Eastern Turkey, East Africa, interior of Australia).
        – These features are more apparent in the 1°–σ=1 panel, confirming that finer grids and light smoothing better resolve isolated seismic clusters
– Conclusions:
    – Earthquake epicenters are strongly localized along active plate boundaries, with the Pacific margins dominating the global Mw ≥ 5, depth ≤ 50 km seismicity.
    – Choice of grid resolution and smoothing scale affects the clarity of fine–scale seismic patterns versus broad tectonic trends. A 1° grid with minimal smoothing best resolves localized clusters, while a 2° grid with larger smoothing highlights overarching boundary geometries.
    – The combination of multi–scale smoothing across two resolutions provides a robust depiction of both sharp boundary–parallel seismic belts and diffuse intraplate seismicity.

Diagnostic C – Comparison of Distance Distributions (Histogram)
– Observations & Conclusion
    – Earthquake epicenters cluster strongly very close to plate boundaries, with the highest normalized frequency in the 0–20 km range.
    – The frequency of earthquakes falls off rapidly beyond ~50 km and becomes negligible past ~100 km.
    – In contrast, the random reference points show a much flatter distribution across the entire 0–500 km range, indicating no inherent preference for proximity to plate boundaries.

Diagnostic D – Cumulative Distribution Functions of Distances (CDF)
```

```
- Observation:
  - Median (50th percentile) distance to the nearest plate boundary:
    - Earthquakes: ~50 km
    - Random points: ~200 km
  - 75th percentile distance:
    - Earthquakes: ~100 km
    - Random points: ~300 km
  - 90th percentile distance:
    - Earthquakes: ~130 km
    - Random points: ~400 km
- Conclusion:
  - The histogram and CDF comparisons demonstrate that global seismicity is far more tightly clustered near plate boundaries than would be expected from a random spatial distribution. This strong proximity underscores the fundamental role of plate-boundary processes in generating large earthquakes.

Diagnostic E - Box-and-Whisker Summary of earthquake-to-plate distance
- Observation:
  - Median distance increases in the order: spreading center < transform faults (dextral ≈ sinistral) < inferred < extension < collision < subduction.
  - Interquartile ranges and whisker lengths grow steadily from spreading centers to subduction zones, highlighting more diffuse seismicity away from well-defined plate margins in collision and subduction settings.
  - A few outliers in each category reach distances >200 km, especially for subduction and collision types.
- Conclusion:
  - Spreading centers host the most tightly confined seismicity (<20 km), consistent with focused brittle failure along mid-ocean ridges.
  - Transform faults show moderately tight clustering (~30-40 km median) but a longer tail, reflecting both along-strike seismicity and off-fault deformation.
  - Extension zones and collision zones display broader distance distributions, likely due to distributed faulting and deformation away from a single structural fabric.
  - Subduction zones have the largest median and 90th-percentile distances, indicating that large shallow earthquakes in these settings often occur on dipping megathrusts or upper-plate structures located tens to hundreds of kilometers from the surface trace of the slab interface.
```

C.4.2 Tectonic Modulation of b-values

Beyond spatial localization, the statistical scaling of earthquake size distributions (b-values) is profoundly modulated by the tectonic environment. Under unified statistical criteria, TRACE performs a categorical inversion of global seismic sequences based on plate boundary types, aiming to reveal the scaling laws of rupture proportions under varying mechanical regimes. The analysis indicates that while global monitoring

capacity for $M_w \geq 5.0$ is spatially balanced—with M_c stabilized between 5.25 and 5.70—b-values demonstrate a pronounced and systematic dependence on the plate-tectonic setting.

Statistical results show that extensional regimes, such as mid-ocean ridges, generally correspond to high b-value distributions, reflecting the dominance of small-scale ruptures under low differential stress. In sharp contrast, subduction zones, collision belts, and strike-slip faults exhibit significantly lower median b-values, indicating stronger stress coupling and a higher probability of large-magnitude events. This plate-type dependence of b-values remains highly stable globally, directly mapping the systematic constraints of fault geometry and thermodynamic states on the rupture process. TRACE's ability to precisely extract and quantify these tectonically dependent seismic features—through adaptive neighborhood aggregation and maximum likelihood estimation without prior hypotheses—provides critical statistical evidence for understanding global-scale stress heterogeneity.

Box C.4.5 User Request

```
Analyze the plate type-dependent b-value characteristics of the global earthquake catalog
Requirements
1. Data Source:
    - Use the Global CMT catalogue (1980-2023) located at: './data/Catalog_1980_2023_Depth50.txt'
    - Load the global plate boundaries located at './data/plate_boundaries.shp'
2. Global Mc and b-value Estimation: 1) Use each earthquake epicenter as a spatial node, 2)select the smallest radius that contain at least 200 events and 100 events above Mc, 3) estimate the Mc and b-value.
3. Plate Boundary Analysis based on the calculated global b-value distribution: 1) associate nodes to nearest boundary (<200 km), 2) compute and save the summary statistics by boundary time, including the boundary type, the number of nodes used, the MC and b value.
```

Box C.4.6 Final Experimental Plan

```
Experimental Plan: Plate type-dependent b-value characteristics of the global earthquake catalog

1. Top-Level Plans: Quantify how seismic b-values and completeness magnitudes (Mc) vary with proximity to different plate-boundary types by: 1) Estimating local Mc and b-value (with uncertainties) at every shallow (≤ 50 km), Mw ≥ 5.0 earthquake epicenter in the global CMT catalog (1980-2023). 2) Assigning each sampling "node" to its nearest plate boundary (within 200 km). 3) Aggregating and comparing Mc/b-value statistics by boundary type. We implement three cohesive Python scripts, executed in sequence. Intermediate CSVs and figures feed forward, and heavy loops are parallelized over 128 cores with progress bars (tqdm). Dependencies:

2. Data Preparation & Quality-Control Mapping: Load, clean, and filter the earthquake catalog and plate-boundary shapefile; produce a global overview map.
```

```
- Load & Clean Earthquake Catalog
- Load & harmonize Plate Boundaries
- QC Global Map

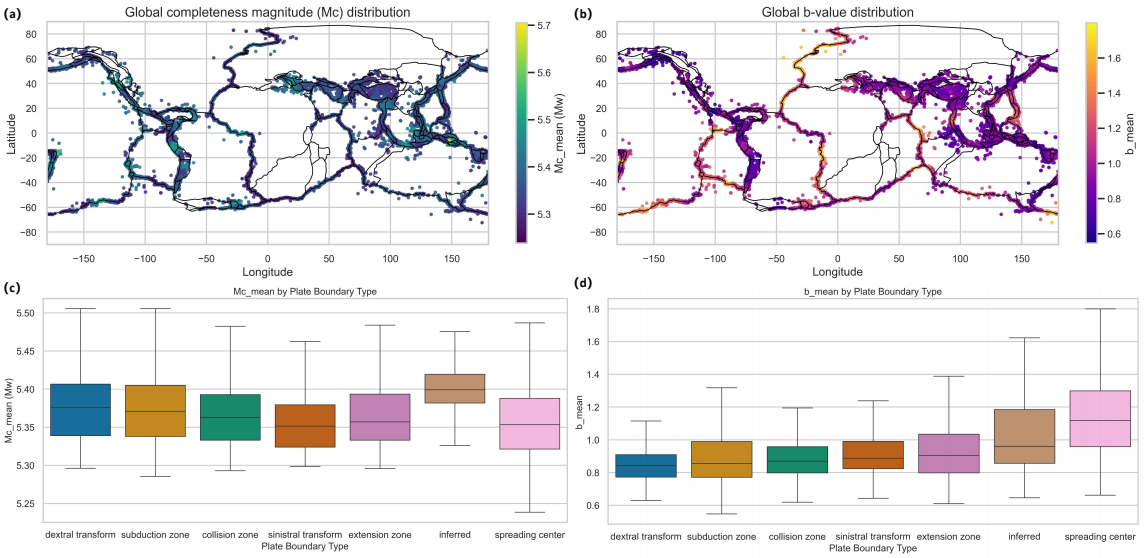
3. Local Mc & b-Value Computation: For each event location ("node"), determine the minimal cylindrical sampling radius that yields robust Mc and b-value estimates, then compute Mc and b with bootstrap-estimated uncertainties.
- Define Sampling Parameters
    - Radii (km): 200, 300, .., 1500
    - Minimum total events for Mc: 200
    - Minimum events above Mc for b-value: 100
    - Bootstrap settings for Mc/b:
        - max_iter = 200
        - early_stop variance threshold = 0.01 (1%) over a 20-iteration window
        - skip bootstrap if sample size marginal (<250 for Mc; <120 for b)

- Per-Node Routine: For each node i at (lon_i, lat_i):
    a. Compute great-circle distances to all filtered catalog events (haversine or pyproj.Geod).
    b. Loop through radii R:
        - Select events with distance ≤ R. Let N_total = count.
        - If N_total < 200: continue to next R.
        - Estimate Mc via seismostats.maximum_curvature on selected magnitudes: Obtain Mc_mean, Mc_std, used_bootstrap_iters_Mc
        - Count N_above_Mc (M ≥ Mc_mean).
        - If N_above_Mc ≥ 100: break and accept R; else continue.
    c. If no R satisfies both thresholds, mark node "insufficient_data" and skip Mc/b steps.
    d. For accepted sample: Estimate b-value via seismostats.bvalue_mle on M ≥ Mc_mean: Obtain b_mean, b_std, used_bootstrap_iters_b
    e. Record node result: node_id, lon, lat, sampling_radius_km, N_total, N_above_Mc, Mc_mean, Mc_std, used_bootstrap_iters_Mc, b_mean, b_std, used_bootstrap_iters_b


4. Plate-Boundary Assignment, Statistics & Visualization: Assign each node to its nearest plate boundary, compute Mc and b-value statistics by boundary type, and generate summary visualizations.
- Nearest-Boundary Assignment
    - Load nodes and boundaries as GeoDataFrames.
    - Project both to a metric CRS (e.g., EPSG:3857) for distance computations.
    - For each node, find nearest boundary segment:
        - Compute min distance (km).
        - Record boundary feature_id and type.
    - Exclude nodes with min_distance > 200 km.
    - Save assigned nodes
- Outlier Filtering & Clipping
    - In assigned nodes, clip b_mean to [0.5, 1.8].
```

```
    - Remove any node with b_mean outside this range from
      further statistics.
- Summary Statistics by Boundary Type. For each unique
  boundary type:
    - number_of_nodes
    - Mc: mean, std, 25th, 50th, 75th percentiles
    - b-value: mean, std, 25th, 50th, 75th percentiles
    - Fractions of nodes in Mc low (<25th), mid (25th-75th),
      high (>75th)
    - Fractions of nodes in b low/mid/high bins similarly
- Visualizations
    - Global Mc map: nodes colored by Mc_mean
    - Global b-value map: nodes colored by b_mean
    - Boxplot of Mc by boundary type
    - Boxplot of b-value by boundary type
    - Scatter plot: Mc_mean vs b_mean, colored by type
```

Box C.4.7 Main Visualization Results (Raw Output)



Box C.4.8 Analysis Summary

```
Summary of Plate type-dependent b-value characteristics of
   the global earthquake catalog

1. Key findings
- Global completeness magnitude Mc is remarkably uniform
    - Mc ranges from ~5.25 to 5.70, with lower values along
      well-instrumented, high-activity boundaries (ridges,
      subduction fronts) and higher values in remote or
      poorly covered zones.
    - Uniformity stems from similar network sensitivity at Mw
      ≥5.0, modulated locally by station density and
      background seismicity.
- Systematic b-value variations by tectonic setting
    - b-values span ~0.6-1.8: lowest in major subduction and
      collision zones, highest at mid-ocean ridges and
      extensional areas.
```

```
    - Reflects differing stress regimes: locked megathrusts favour larger events (low b), extensional/ridge environments produce abundant small ruptures (high b).
- Statistical summaries confirm plate-type dependence
    - Median Mc is narrowly 5.30-5.40 across types, peaking in "inferred" boundaries.
    - Median b: spreading centers (~1.12) > extension (~0.93) > inferred (~0.95) > subduction/collision/transforms (~0.85-0.90).
    - Differences arise from variation in crustal stress, faulting style, and event-size distributions in each tectonic regime.

2. Overview and method context
- We loaded and cleaned a global CMT catalog (1980-2023, Mw≥5.0, depth≤50 km) and a global plate-boundary shapefile, converted to common EPSG:4326. Each earthquake epicenter served as a spatial node: we performed neighbor queries in cylindrical volumes (radii 200-1500 km) to secure ≥200 total events for Mc estimation and ≥100 events above Mc for b-value estimation. Completeness magnitude was determined via the maximum-curvature method, and b-value via maximum-likelihood, both with bootstrap uncertainty (≤200 iterations, adaptive early stopping). Nodes beyond 200 km of any boundary were excluded; remaining nodes were binned by boundary type to compute summary statistics. Finally, we generated global maps, boxplots, and scatterplots to visualize spatial and tectonic trends.
- Key principles:
    - Gutenberg-Richter frequency-magnitude law: log10N(m) = a - b m
    - Completeness via maximum-curvature on magnitude histogram to find Mc
    - MLE b-value: b = ln(10)/(M - (Mc - ΔM/2)) with bootstrapping
    - Cylindrical sampling volumes adapt radius r to meet event-count thresholds
    - Nearest-boundary assignment using spatial join within 200 km

3. Summary of figure-based results
Diagnostic A - Global Completeness Magnitude (Mc) Distribution
- Observations
    - Estimated Mc varies between about 5.25 and 5.70 globally.
    - Lower Mc values (≈ 5.25-5.35) occur along well-instrumented and highly active plate boundaries (e.g., mid-ocean ridges, active subduction fronts).
    - higher Mc (≈ 5.50-5.70) is seen in regions with sparse seismicity or poorer network coverage (e.g., portions of the Indian Ocean, remote continental interiors).
- Conclusions:
    - Fairly uniform across major boundary types (5.30-5.40), with higher values in inferred or poorly instrumented zones.

Diagnostic B - Global b-Value Distribution
```

```
- Observations
  - b-values range from about 0.6 up to 1.8.
  - Low b-values (0.6-0.8) are concentrated in major subduction zones (e.g., Marianas, Peru-Chile) and some continental collision belts.
  - high b-values (1.2-1.8) align with mid-ocean spreading centers and certain extensional settings, suggesting relatively more small events in those environments.
  - Transform and inferred segments exhibit intermediate b around 0.8-1.2.
- Conclusions:
  - Maps confirm plate-wide trends: high b along ridges, low b along deep subduction trenches.

Diagnostic C  - Mc_mean by Plate Boundary Type
- Observations
  - Median Mc across all boundary types lies in a narrow band of 5.30-5.40.
  - "Inferred" boundaries have the highest median Mc (~5.40), consistent with these segments often being less well instrumented.
  - Convergent (subduction, collision) and transform (dextral, sinistral) zones cluster around 5.34-5.38.
  - Spreading centers and extension zones show slightly lower median Mc (~5.33-5.36).

Diagnostic D  - b_mean by Plate Boundary Type
- Observations
  - Spreading centers exhibit the highest median b (~1.12) and the widest interquartile range, reflecting abundant small-magnitude events.
  - Extension zones and inferred boundaries have moderately high medians (~0.90-0.95).
  - Subduction zones, collision zones, and sinistral transforms show lower median b (~0.85-0.90).
  - Dextral transforms have the lowest median (~0.85) and the tightest distribution.
- Conclusions:
  - Systematic differences by boundary type:
    - highest at spreading centers and extension zones.
    - Lowest at subduction and collision zones, especially along slick subduction interfaces.
  - Reflects differing stress regimes and rupture processes.
```

C.5 Vertical Structure of Global Seismicity and Discrimination of Depth Artifacts

The vertical distribution of focal depths not only elucidates the stress-release mechanisms within the lithosphere and the boundaries of the brittle-ductile transition zone but also serves as a fundamental indicator for distinguishing tectonic environments and rupture modes. However, constrained by the limitations of global-scale focal parameter inversion algorithms, seismic catalogs frequently exhibit significant discretization artifacts at specific depths. TRACE addresses this by constructing an automated parallel control-analysis framework for the Global CMT (1980–2023,

$M_w > 5.2$) and ISC-Bulletin (1900–2024) catalogs, designed to disentangle genuine tectonically controlled depth structures from complex observational noise.

Through anomaly detection on original depth histograms with 1 km resolution, TRACE automatically identifies two non-physical high-frequency clusters near 10 km and 33 km. These quasi-impulse-like distribution features lack physical support and typically originate from initial parameter settings or default boundary conditions in the inversion process. To eliminate the interference of these artifacts on statistical inference, the agent generates a control catalog by filtering the identified depth artifacts. By synchronously tracking spatial density, annual frequency, and representative statistics across both the original and control catalogs, TRACE demonstrates a robust ability to distinguish geophysically real signals from inversion-induced systematic errors, particularly in mitigating the banding depth bias commonly observed in oceanic plate regions.

Analysis after artifact removal reveals that global seismic activity exhibits an exceptionally stable "primary-secondary" bimodal clustering structure in the vertical dimension. The primary peak is located within the shallow lithosphere (approximately 6–56 km), with a peak focal depth of roughly 11 km, accounting for over 70% of the global seismic energy release. The secondary peak remains stable near the mantle transition zone (approximately 550–650 km), corresponding to deep-focus earthquake clusters within cold subducting slabs. This stratification feature shows excellent spatial consistency within the range of statistical uncertainty, directly mapping the global dynamical patterns of mantle convection and plate subduction.

In the temporal dimension, TRACE's multiscale trend analysis uncovers a significant evolutionary signature: since 1980, the average depth of global seismic activity has exhibited a shallowing migration trend. Statistical results indicate that the proportion of shallow earthquakes continues to rise, while the ratio of intermediate- and deep-focus events has decreased accordingly. Because this trend is highly synchronized in both the original and control catalogs, TRACE concludes that these long-term changes are not driven by depth artifacts but likely reflect the dynamic redistribution of the global tectonic stress field across different structural layers. This finding not only validates TRACE's capability to automatically extract multi-dimensional geophysical features but also provides critical quantitative constraints for investigating the modulation of shallow seismicity by deep tectonic processes.

Box C.5.1 User Request

```
1 Analyze the depth distribution of global earthquakes with
    magnitude Mw > 5.2 using the Global CMT catalog.
2 Requirements
3 1. Data Source:
4      - Use the Global CMT catalogue (1980-2023) located at:
         './data/Catalog_full.csv'
5 2. Perform systematic depth-quality diagnostics prior to
    statistical analysis: Identify abnormal depth clustering
    by examining fine-bin depth histograms. Record depth
    levels with unusually high frequencies and their relative
    proportions.
6 3. Analysis the spatial patterns of the global depth
    distribution: find and analyze the spatial patterns in the
     global depth distribution.
```

```
4. Analysis the temporal patterns of the global depth
   distribution: Partition the catalog into temporal windows
   (annual). Analyze yearly changes in the global depth
   distribution. Track temporal variations in the relative
   proportions of shallow, intermediate, and deep earthquakes
   .
```

Box C.5.2 Final Experimental Plan

```
Experimental Plan: Comprehensive Global Earthquake Depth
   Statistics Analysis

1. Top-Level Plans: Conduct a multi-scale, systematic
   investigation of earthquake depth statistics using the
   GCMT catalog (1980-2023) for events with magnitude > 5.2.
   The study comprises five major modules: data preparation,
   depth-quality diagnostics, spatial pattern mapping, depth-
   distribution clustering, and temporal evolution analysis.
   Each module runs as an independent script, produces CSV
   summaries and figures, and leverages up to 64 CPU cores
   with progress reporting.

2. Data Preparation & Filtering: Load the raw GCMT CSV, apply
    magnitude and basic quality filters, and export a
   standardized event catalog.
- Read Input
    - File: `./data/Catalog_full.csv`
    - Parse columns: year, month, day, hour, minute, second,
       longitude, latitude, depth_km, magnitude.
- Magnitude Filter: Select events with magnitude > 5.2.
- Datetime Construction: Combine year-month-day-hour-minute-
   second into a single UTC datetime column.
- Coordinate & Depth Validation: Ensure longitude ∈ [-180,
   180], latitude ∈ [-90, 90], depth_km ≥ 0. Flag and drop
   any outliers or NaNs.

3. Depth Quality Control & Artifact Diagnostics: Quantify
   discretization- or inversion-induced depth artifacts via
   fine-bin histograms and define artifact depth intervals
   for downstream filtering.
- Load Filtered Catalog
- Fine-Bin histogram: Bin width = 1 km; depth range = 0-700
   km; compute global counts.
- Anomaly Detection
    - Compute mean (μ) and standard deviation (σ) of bin
       counts.
    - Flag bins where count > μ + 3σ.
    - For each flagged bin, record: bin_center (km), count,
       proportion of total events (%).
- Artifact Interval Definition
    - Merge adjacent flagged bins into continuous intervals (
       start_km, end_km).
    - For each interval, compute total count and aggregate
       proportion.

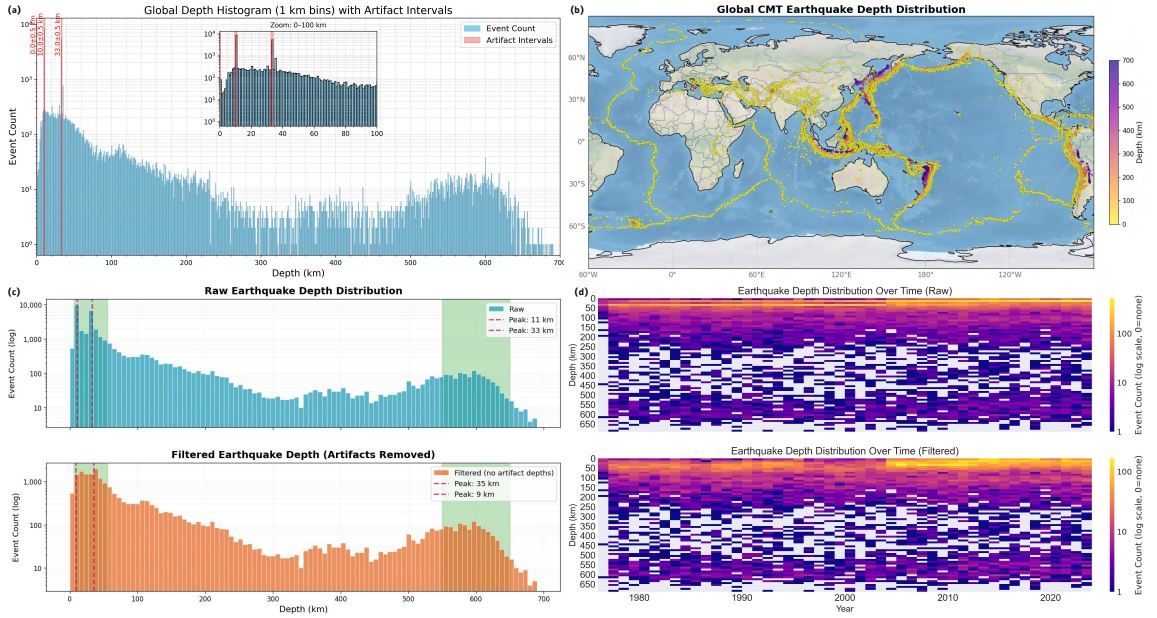
4. Global Spatial Patterns of Depth: Map epicenter
   distributions colored by depth before and after artifact
   filtering to reveal spatial clustering.
- Load Data
```

- Define Subsets
  - Raw: all events.
  - Filtered: exclude events whose depth_km $\in$ any artifact interval.
- Map Generation (for each subset)
  - Basemap: Cartopy NaturalEarthFeature('physical','land','50m', facecolor='lightgray', alpha=0.4).
  - Scatter epicenters: marker size = 5 pt; color = depth_km; cmap = plasma_r; zorder = 1.
  - Add coastlines and gridlines.

5. Global Depth-Distribution & Clustered Depth Ranges: Compute and compare global depth histograms (raw vs. filtered) with two binning schemes, identify major and secondary peaks, and define clustered depth ranges.
- Load Subsets: Reload raw/filtered sets from Module 3.
- histogram Computation
  - Diagnostic bins: 1 km width, 0-700 km.
  - Interpretation bins: 2 km width, 0-700 km.
  - Compute counts and proportions for each binning scheme.
- Peak Identification & Cluster Definition
  - Smooth interpretation-bin counts with Gaussian kernel (σ = 2 bins).
  - Find local maxima with prominence $\geq$ 1% of total events.
  - For each peak:
    - Peak_depth = bin_center at maximum.
    - Cluster_range = contiguous bins where smoothed count $\geq$ 50% of peak count.
    - Event_count and percentage within cluster.
  - Label peaks as "dominant" (highest percentage) or "secondary."

6. Temporal Evolution of Depth Distribution: Track annual changes in depth distributions and class proportions (shallow/intermediate/deep) with heatmaps and time series.
- Load Filtered Catalog
- Annual Partitioning: Years = 1980-2023; assign each event to its calendar year.
- Per-Year histograms & Proportions, for each year in parallel:
  - Compute 1 km-bin histogram over 0-700 km.
  - Compute shallow% (depth < 70 km), intermediate% (70-300 km), deep% (> 300 km).
  - Compute mean_depth and median_depth.
- Depth-Time Matrix
  - Assemble matrix (years $\times$ depth_bins) of normalized counts (per-year normalization).

Box C.5.3 Main Visualization Results (Raw Output)



Box C.5.4 Analysis Summary

```
Summary of Comprehensive Global Earthquake Depth Statistics Analysis

1. Key findings
- Identification of Depth Artifacts
    - Two narrow depth-bins at 10 km and 33 km exhibit anomalously high counts (≈25 % and 16 % of events) indicating inversion/discretization artifacts.
    - Mechanism: GCMT focal-depth inversion employs fixed nodal-plane discretization that artificially anchors many solutions at preferred depths.
- Clarified Tectonic Depth Patterns After Filtering
    - Raw epicenter map shows spurious depth "stripes" on oceanic plates; filtered map reveals continuous dipping slabs in subduction zones and ubiquitous shallow seismicity on ridges/transforms.
    - Mechanism: Plate-boundary geometry governs hypocenter depth: transform/ridge faults produce shallow (<70 km) seismicity, while slab dehydration and phase transformations in subduction zones generate intermediate (70-300 km) and deep (>300 km) earthquakes.
- Dominant Shallow and Secondary Deep Clusters
    - Depth histogram (1 km bins, log-scale) shows a dominant cluster at 6-56 km (peak ~11 km, >70 % of events) and a secondary cluster at 550-650 km (peak ~600 km, ~3-5 %). Artifact filtering does not alter these tectonic features.
    - Mechanism: Crustal stress release concentrates in upper crust; deep-slab seismicity reflects dehydration embrittlement and high-pressure phase changes in subducting slabs.
- Long-Term Shift Toward Shallower Seismicity
```

- From 1980 to 2023, shallow fraction rose from ~74 % to ~80 %, intermediate declined from ~20 % to ~12 %, and median depth fell from ~33 km to ~12–20 km.
- Mechanism: Likely combined effects of improved detection of shallow events, evolving catalog completeness, and potential changes in faulting depth due to geodynamic or thermal structure variations.

2. Overview and method context

- We ingested the GCMT global catalog (1980–2023, Mw > 5.2), applied quality filters, and constructed fine-bin (1 km) depth histograms to identify artifact intervals (μ+3σ criterion). After excluding these intervals, we generated raw vs. filtered spatial depth maps, computed diagnostic (1 km) and interpretation (2 km) bin histograms, smoothed the latter to locate dominant and secondary clusters, and finally tracked annual depth distributions, class proportions (shallow/intermediate/deep), and summary metrics across 1980–2023 using parallel processing.
- Key principles:
  - Anomaly detection via statistical threshold: flag bins where count > μ + 3σ.
  - Depth classification: shallow (<70 km), intermediate (70–300 km), deep (>300 km).
  - Normalized histograms: pi = Ni/Ntotal and per-year matrix normalization.
  - Smoothing & peak detection: Gaussian kernel (σ=2 bins); peaks with prominence $\geq$ 1% of total.
  - Tectonic control: slab dehydration and phase transitions determine deep-focus seismicity.

3. Summary of figure-based results

Diagnostic A – Depth QC histogram Analysis

- Observations
  - Two depth bins exhibit exceptionally high counts compared to the surrounding distribution:
    - 10 km depth bin
    - Count $\approx$ 10000 events
    - Proportion $\approx$ 25.1 % of the entire catalog
  - 33 km depth bin
    - Count $\approx$ 5000 events
    - Proportion $\approx$ 16.2 % of the entire catalog
  - These two peaks together account for over 40 % of all events and stand out as clear discretization or inversion-constraint artifacts.
  - The rest of the depth distribution shows the expected decay of event frequency with depth up to ~200 km, a minor bump around 150 km (possible intermediate-depth cluster), a trough near 300–400 km, and the characteristic deep-focus cluster between 500–650 km associated with major subduction zones.
- Conclusions:
  - Artifact Intervals: Define narrow intervals around the flagged bins for downstream filtering: 9.5–10.5 km and 32.5–33.5 km

```
40      - Data Cleaning: Exclude or flag all events whose
          reported depth falls within these intervals to remove
          modeling-induced clustering artifacts.
41      - Impact on Analysis: Removing these two artificial
          clusters will reduce nearly half of the raw event
          count but yield a more geophysically meaningful depth
          distribution for spatial, clustering, and temporal
          analyses.
42
43  Diagnostic B - Spatial Pattern Mapping of global catalog
44  - Observations
45      - Epicenters clearly outline the major plate boundaries,
          especially the Pacific Ring of Fire:
46          - Western Americas (Chile-Peru trench, Cascadia/
              Aleutians)
47          - Eastern Asia (Japan-Kuril, Kamchatka, Philippines-
              Mariana)
48          - Southwest Pacific (Tonga-Kermadec, New Zealand)
49      - Shallow events (< 70 km; yellow) dominate transform and
          spreading centers (e.g., mid-Atlantic ridge, San
          Andreas).
50      - Intermediate (70-300 km; orange) and deep (> 300 km;
          purple) earthquakes cluster in subduction zones.
51      - A few isolated "stripes" of intermediate-depth events
          appear on oceanic plates-likely inversion-induced
          discretization artifacts (e.g., at ~100 km and ~300 km
          steps).
52  - Conclusion:
53      - Tectonic Control: The global depth distribution
          faithfully traces plate interfaces: shallow
          earthquakes along faults and ridges, deeper events
          within dipping slabs.
54      - Artifact Identification & Removal: Fine-bin QC
          highlighted artificial peaks at discrete depths (e.g.,
          100 km increments). Filtering preserves meaningful
          seismicity patterns and removes inversion
          discretization noise, especially on oceanic plates
          away from trenches.
55      - Spatial Clustering: Deep (>300 km) and intermediate (70
          -300 km) events are confined to subduction zones;
          shallow seismicity is widespread along all plate
          margins. No significant deep seismicity occurs in
          continental interiors, confirming slab-bound behavior
          of deep earthquakes.
56
57  Diagnostic C - Depth histogram Filter & Clusters
58  - Observations
59      - Shallow Cluster (Dominant)
60          - Depth range: ~6 - 56 km
61          - Peak at 11 km (highest event count ≈10000)
62          - Secondary summit at 33 km
63          - Accounts for the vast majority (> 70 %) of global
              events.
64      - Intermediate Depths
65          - Depths between 70 km and 300 km show relatively low
              counts (order 10^1-10^2 per bin).
66          - No pronounced, narrow peaks-reflects sparser
              seismicity in slab interiors.
```

```
    - Deep Cluster (Secondary)
      - Depth range: ~550 - 650 km
      - Peak around 600 km
      - Represents subducting-slab seismicity (~3-5 % of total).
- Conclusion
    - Global seismicity for large (Mw > 5.2) earthquakes is overwhelmingly dominated by shallow crustal events concentrated between 6 km and 56 km.
    - A clear secondary deep-slab cluster at ~600 km depth reflects subduction-zone seismicity.
    - Intermediate-depth events are comparatively scarce, yielding a smooth, low-amplitude background.
    - Artifact diagnostics and filtering do not alter the primary cluster characteristics, validating their geophysical significance.

Diagnostic D - Depth-Time Density heatmap
- Observations
    - A persistent high-density band at shallow depths (10-30 km) in every year.
    - Intermediate depths (50-200 km) show weaker, more diffuse signals, especially after 2000.
    - Deep seismicity (> 300 km) remains sparse across all years, with occasional minor intensifications (visible as faint stripes around 400-600 km in specific years, e.g., 2002 and 2021).
- Conclusions
    - There is a clear long-term migration toward shallower seismicity in the global Mw > 5.2 catalog since 1980.
    - Intermediate-depth and deep earthquakes have steadily become less frequent in relative terms.
    - The heatmap confirms that most seismic energy release occurs at depths shallower than 50 km, with little change in the deeper signal.
    - The concurrent declines in mean and median depth underscore a systematic shift in the global depth distribution, possibly reflecting improvements in detection, catalog completeness, or genuine geodynamic changes in subduction and crustal faulting processes.
```

Supplementary Information References

[1] Ross, Z.E., Idini, B., Jia, Z., Stephenson, O.L., Zhong, M., Wang, X., Zhan, Z., Simons, M., Fielding, E.J., Yun, S.-H., Hauksson, E., Moore, A.W., Liu, Z., Jung, J.: Hierarchical interlocked orthogonal faulting in the 2019 Ridgecrest earthquake sequence. Science **366**(6463), 346–351 (2019) https://doi.org/10.1126/science.aaz0109

[2] Sheng, S., Meng, L.: Stress Field Variation During the 2019 Ridgecrest Earthquake Sequence. Geophysical Research Letters **47**(15), 2020–087722 (2020) https://doi.org/10.1029/2020GL087722

[3] Zhu, W., Beroza, G.C.: PhaseNet: A Deep-Neural-Network-Based Seismic Arrival Time Picking Method. Geophysical Journal International (2018) https://doi.org/10.1093/gji/ggy423

[4] Zhu, W., McBrearty, I.W., Mousavi, S.M., Ellsworth, W.L., Beroza, G.C.: Earthquake Phase Association Using a Bayesian Gaussian Mixture Model. Journal of Geophysical Research: Solid Earth **127**(5), 2021–023249 (2022) https://doi.org/10.1029/2021JB023249 arXiv:2109.09008 [physics]

[5] Waldhauser, F.: A Double-Difference Earthquake Location Algorithm: Method and Application to the Northern Hayward Fault, California. Bulletin of the Seismological Society of America **90**(6), 1353–1368 (2000) https://doi.org/10.1785/0120000006

[6] Ekström, G., Nettles, M., Dziewoński, A.M.: The global CMT project 2004–2010: Centroid-moment tensors for 13,017 earthquakes. Physics of the Earth and Planetary Interiors **200–201**, 1–9 (2012) https://doi.org/10.1016/j.pepi.2012.04.002

[7] Centre, I.S.: ISC Bulletin. International Seismological Centre (2022). https://doi.org/10.31905/D808B830

[8] Petruccelli, A., Schorlemmer, D., Tormann, T., Rinaldi, A.P., Wiemer, S., Gasperini, P., Vannucci, G.: The influence of faulting style on the size-distribution of global earthquakes. Earth and Planetary Science Letters **527**, 115791 (2019) https://doi.org/10.1016/j.epsl.2019.115791

[9] Gutenberg, B., Richter, C.F.: Magnitude and Energy of Earthquakes. Nature **176**(4486), 795–795 (1955) https://doi.org/10.1038/176795a0